

**Nanoscale EUV Microscopy on a Tabletop: A General
Transmission and Reflection Mode Microscope Based on
Coherent Diffractive Imaging with High Harmonic
Illumination**

by

Matthew Donald Seaberg

B.S., Bethel University, 2007

A thesis submitted to the
Faculty of the Graduate School of the
University of Colorado in partial fulfillment
of the requirements for the degree of
Doctor of Philosophy
Department of Physics

2014

This thesis entitled:
Nanoscale EUV Microscopy on a Tabletop: A General Transmission and Reflection Mode
Microscope Based on Coherent Diffractive Imaging with High Harmonic Illumination
written by Matthew Donald Seaberg
has been approved for the Department of Physics

Margaret M. Murnane

Henry C. Kapteyn

Date _____

The final copy of this thesis has been examined by the signatories, and we find that both the content and the form meet acceptable presentation standards of scholarly work in the above mentioned discipline.

Seaberg, Matthew Donald (Ph.D., Physics)

Nanoscale EUV Microscopy on a Tabletop: A General Transmission and Reflection Mode Microscope Based on Coherent Diffractive Imaging with High Harmonic Illumination

Thesis directed by Prof. Margaret M. Murnane and Prof. Henry C. Kapteyn

A new scientific frontier exists at the intersection of the nanoscale and the ultrafast. In order to explore this frontier, new tools with unique capabilities for imaging with nanometer spatial and femtosecond temporal resolution are critical. This thesis describes the development of such a tool, combining coherent diffractive imaging (CDI) with an extreme ultraviolet (EUV) high harmonic generation (HHG) light source to produce a compact, accessible, high-resolution microscope. Here, this microscope is used to demonstrate 22 nm resolution in transmission, a record for any full-field tabletop light-based microscope. Further, this microscope is used to demonstrate the most general reflection mode implementation of CDI to date, enabling image reconstruction at any angle of incidence.

Chapter 2 describes the optimization of the HHG source for use with CDI. A pulse shaper is implemented to produce transform-limited pulses at 800 nm for increased HHG conversion efficiency. Furthermore, the long-term stability of the HHG source is improved by an order of magnitude through the pointing stabilization of the kHz driving laser. Chapter 3 develops the ideas necessary for the data processing techniques that enable general reflection mode CDI. Chapter 4 describes enhancements to the microscope to produce images with record 22 nm resolution in addition to extension of the microscope to image more complex, transmissive samples. Chapter 5 presents the most general implementation of reflection mode CDI to date. In chapter 6, the route towards dynamic femtosecond imaging of complex nanosystems is outlined, which includes potential for simultaneous hyperspectral EUV imaging across multiple absorption edges.

Dedication

For my parents.

Acknowledgements

First, I need to thank my advisors Margaret Murnane and Henry Kapteyn, who have been extremely supportive, generous and encouraging, and who enable an amazing breadth of scientific research. It has been a pleasure to work in such a friendly, collaborative lab environment with access to so many technical resources. I also need to thank Richard Sandberg and Daisy Raymondson, who helped to get me started with EUV coherent imaging and who had already achieved a great deal before I started on the project. Daisy in particular was instrumental in teaching me the basics of ultrafast laser amplifier systems. I also want to thank Ethan Townsend, who always made the lab a fun place to be, and who I have missed very much since his life was cut short.

Of course, I need to acknowledge and thank the current KM group “imaging team,” consisting of Dan Adams, Bosheng Zhang, Dennis Gardner, and Liz Shanblatt. Dan has been a great leader and motivator, has pushed and helped me to accomplish things that I wouldn’t have otherwise, and has had a hand in most of the work presented in this thesis in some way or other. He also manages to combine a joking attitude with an eye towards serious progress, making the lab a fun and productive place to work. Bosheng has also been an invaluable partner in the lab, with his tremendous work ethic (as long as it doesn’t conflict with dinner) and his ability to always bring a smile to my face. His unique approach to and tremendous ability in physics have enabled many new ideas in addition to stimulating discussions. While Dennis and Liz are relative newcomers to the team, they have both been valuable additions. They have both contributed to the fun, productive lab environment. In relation to this thesis work, they both contributed to the EUV reflection imaging project; Dennis helped with the experiment and the image reconstructions, and

Liz fabricated the test pattern. They are off to a great start in carrying this project forward. I have also been very fortunate to work and interact in a variety of ways with the rest of the KM group over the past six years.

Finally, I want to thank all my friends and family for the support they've provided during my graduate career. I have been very fortunate to have wonderful roommates during my time in Boulder, with whom I have shared adventures in the mountains as well as in the backyard roasting goats etc. These people include Nathan Lemke, Tavi Semonin, Paul Arpin, Jia Wang, Mike Foss-Feig, Michael Gerrity, Will Kindel, Jen Harlow, Adam Kaufman, Andy Gisler, Joe Britton, and Colin Lindsay. I want to thank my mom, my dad, and my brothers, Jonathan and Stephen, for all the love and support they have provided over the years. Finally, I want to thank my amazing fiancée, Maasa Hosotani, for her love, support and encouragement.

Contents

Chapter

1	Introduction	1
1.1	Visualizing the nanoworld	1
1.2	Imaging with extreme ultraviolet and X-ray light	4
1.2.1	Real-space Imaging Techniques	5
1.2.2	Coherent Imaging Techniques	10
1.3	Coherent EUV and X-ray sources	14
1.3.1	Third-generation synchrotrons	15
1.3.2	Free electron lasers	18
1.3.3	EUV/Soft X-ray lasers	20
1.3.4	High harmonic generation	21
1.4	Overview of this thesis	22
2	High Harmonic Generation Driven by Ultrafast Lasers	24
2.1	Introduction to ultrafast light sources	24
2.2	Compact chirped pulse amplification laser technology	28
2.3	High harmonic generation	31
2.3.1	Three step model	32
2.3.2	HHG phase matching	34
2.3.3	Experimental parameters for HHG phase matching	39

2.4	Complete control of the HHG driving laser	40
2.4.1	Pulse shaping for temporal control	41
2.4.2	Beam pointing stabilization for stable HHG sources	48
2.5	Future prospects for HHG	66
3	Coherent Diffractive Imaging with Ultrafast High Harmonic Sources	67
3.1	Diffraction theory	68
3.1.1	EUV/X-ray scattering	68
3.1.2	EUV/X-ray diffraction	69
3.2	Principle of CDI	80
3.2.1	Oversampling in CDI	80
3.2.2	Coherence requirements	83
3.2.3	Phase retrieval in CDI	86
3.3	HHG as a source for CDI	90
4	Table-top CDI with HHG Sources in Transmission	93
4.1	High resolution CDI using 13 nm HHG	93
4.1.1	Flux improvements to enable CDI at 13 nm	93
4.1.2	Data collection and image reconstruction	100
4.1.3	Analysis	106
4.1.4	Simulation of diffraction from a thick, absorbing object	113
4.2	Tabletop keyhole CDI	115
4.2.1	Extended objects	115
4.2.2	Transparent objects	122
4.3	Conclusions	129
5	Coherent Diffractive Imaging in a Reflection Geometry	133
5.1	First attempts at tabletop reflection mode imaging	133

5.1.1	Reflection keyhole data	136
5.2	Ptychography in reflection mode	138
5.2.1	Experimental geometry	139
5.2.2	Sample fabrication	140
5.2.3	Results and Discussion	143
5.2.4	High Harmonic Beam Characterization Through Ptychography	148
5.2.5	Comparison between CDI reconstruction and SEM and AFM images	150
5.3	Conclusions	153
6	Future Work	154
6.1	Methods for dynamic imaging experiments	155
6.2	Imaging with keV harmonics	159
6.3	Concluding remarks	159
	Bibliography	162

Tables

Table

2.1	Ionization energies of noble gases	35
2.2	Standard deviations of focus position and angle	55
3.1	Formulas to calculate successive iterations for ER, HIO, DM and RAAR algorithms	88
4.1	“Rejector” mirror reflectivity measurements at 13 nm	95

Figures

Figure

1.1	Schematic of a Fresnel zone plate	7
1.2	Schematic of femtosecond slicing principle	17
2.1	Schematic of a typical Ti:sapphire oscillator	26
2.2	Schematic of a chirped pulse amplification system	29
2.3	Tunnel ionization in argon	33
2.4	Absorption-limited phase matching of HHG	37
2.5	Schematic of a general frequency-domain pulse shaper	43
2.6	Schematic of SLM-based pulse shaper	44
2.7	Through-focus simulation of the pulse shaper output	46
2.8	Spectral phase introduced by the pulse shaper	46
2.9	Pulse shaper results	49
2.10	Geometry for active beam pointing feedback	52
2.11	Short-term centroid data	56
2.12	Long-term centroid data	57
2.13	Allan deviations of centroid data	58
2.14	Amplitude spectral densities of centroid data	60
2.15	Measured and theoretical closed-loop sensitivity	61
2.16	High harmonic beam images, stabilized and unstabilized	63

2.17	Integrated harmonic beam stability	65
3.1	Illustration of the source of the obliquity factor for <i>s</i> -polarized light	74
3.2	Illustration of conical diffraction	76
3.3	Illustration showing the implications of finite temporal coherence	85
4.1	“Rejector” mirror reflectivity at 13 nm	95
4.2	“Rejector” mirror reflectivity at 800 nm	97
4.3	13 nm waveguide gas pressure schemes	99
4.4	Waveguide end section transmission at 13 nm	101
4.5	Coherent diffractive imaging 13 nm transmission geometry	103
4.6	Image reconstructions at 13 nm, test pattern J409	104
4.7	Image reconstructions at 13 nm, test pattern J407	105
4.8	Phase retrieval transfer function	108
4.9	Image reconstruction from 30 second exposure	110
4.10	Ankylographic reconstruction, test pattern J407	112
4.11	Simulation of diffraction from a thick, absorbing object	114
4.12	Schematic of initial experimental geometry for tabletop keyhole CDI	117
4.13	Extended test pattern imaged with keyhole CDI	119
4.14	First tabletop keyhole CDI results	121
4.15	Simulated and measured beam profiles for keyhole CDI	124
4.16	Revised keyhole CDI experimental geometry	126
4.17	Reconstructed illumination	127
4.18	Tabletop keyhole results with a transparent object	130
4.19	3D information from keyhole CDI	131
5.1	Schematic for initial reflection mode experiments	134
5.2	Initial reflection mode results	135

5.3	Diffraction from 1 μm pillars in reflection	137
5.4	Reflection ptychography schematic	141
5.5	Reflection ptychography data and reconstruction	142
5.6	Height profile comparison between reflection CDI and AFM	147
5.7	HHG beam reconstruction using ptychography	149
5.8	HHG beam comparison at the detector plane	151
5.9	Comparisons between reflection CDI, SEM and AFM	152
6.1	Keyhole reconstruction using knowledge of probe	156
6.2	First EUV hyperspectral images based on ptychographical information multiplexing	158
6.3	HHG spectra for a variety of driving laser wavelengths	160

Chapter 1

Introduction

Many of the most important technological breakthroughs result from the exploration of new frontiers in science. The frontiers of science can be found in hard-to-reach places such as outer space, the depths of the ocean, and remote regions of Antarctica, but scientific frontiers also exist all around us at length- and time-scales that are difficult to access.

One such current frontier exists at the nanoscale, that is, the regime of materials with dimensions on the nanometer (nm) scale. The nanoscale is inextricably linked to another current frontier in science: the ultrafast (picosecond to attosecond) timescale. As physical systems shrink, the timescales of dynamics typically shrink as well. Indeed, the speed of light is 300 nm/fs. Examples of this effect can be seen in spin and heat transport in nanomaterials, which can occur on femtosecond (fs) and picosecond (ps) timescales, respectively [1,2]. The link between nanoscale dimensions and ultrafast timescales provides the motivation for the work presented in this thesis, which describes the development of a new microscope that enables the study of systems at nm spatial scales and fs timescales simultaneously. Such a technology will ultimately push the limits of our physical understanding of these exciting regimes.

1.1 Visualizing the nanoworld

The quest to understand structure, dynamics, and function at the nanoscale drives the development of new ultrahigh-resolution imaging technologies. Microscopy techniques that have access to nm (and below) spatial scales can be based on photon, electron, neutron, and atom (in scanning

probe microscopy) probes. In the case of atomic probes, the high spatial resolution is typically achieved by scanning a tip whose width consists of only one to several atoms at the point of interaction. Examples of atomic probes include atomic force microscopy (AFM) [3] and scanning tunneling microscopy (STM) [4]. Electron microscopy techniques, such as scanning electron microscopy (SEM) [5] and transmission electron microscopy (TEM), detect scattered electrons with de Broglie wavelengths that are shorter than the desired resolution. Super-resolution techniques in the visible region of the spectrum are also capable of nm-scale resolution when certain criteria are met. Finally, extreme ultraviolet (EUV) and X-ray microscopy are extensions of visible light microscopy, where high energy (short wavelength) scattered photons are detected. While all of these techniques are capable of nm-scale resolution, each offers different benefits and limitations, as discussed in the following paragraphs.

Microscopies which use atomic probes are typically grouped under the umbrella term scanning probe microscopy (SPM). These microscopy techniques rely on interactions with surfaces in the “near field”; the surface is typically only separated from the probe tip by several angstroms. While these techniques can be capable of atomic resolution [6, 7], they can only be used to image surfaces. Some of these techniques have recently been extended to be capable of fs temporal resolution [8, 9]. However, these techniques are point-by-point scanning methods, meaning that raster scans must be performed in order to capture full images.

Electron microscopy is well established as a powerful method for obtaining images with sub-nm resolution, but cannot penetrate thick (i.e. > 100 nm) samples, and can suffer from a relatively low image contrast. SEM images only contain surface information, and TEM imaging, which can access 3D information, requires thin samples due to the strong interaction between electrons and matter. While the resolution of electron microscopes is fundamentally limited only by the de Broglie wavelength of the electrons (often < 10 pm), the practical resolution of these microscopes is usually aberration-limited to > 1 Å. However, recent work has resulted in ≈ 50 pm resolution using high-order aberration correction in a scanning TEM (STEM) [10]. Most electron microscopes have poor temporal resolution, although stroboscopic techniques have recently been developed which allow

for sub-ps resolution [11]. However, these techniques require that only a single electron is detected at a time, meaning that many measurements must be made to build up a single image.

Super-resolution optical imaging techniques such as multiphoton microscopy [12], stimulated emission depletion microscopy (STED) [13,14], photo-activated localization microscopy (PALM) and stochastic optical reconstruction microscopy (STORM) have made impressive progress using visible light for super-resolution imaging [15,16]. However, these techniques rely on scanning or on sparsely emitting labeled samples, where the centroid of single fluorescent molecules in the sample can be located down to 10 nm precision. Techniques that require labeling are useful when functional groups can be reliably and selectively labeled. However, this approach is invasive, time-consuming, and requires considerable prior knowledge of the system. Powerful and widely-used label-free techniques such as multiphoton [17] or CARS microscopy [18] avoid these issues, but require scanning and yield only modestly higher spatial resolution than conventional techniques such as confocal microscopy.

EUV/X-ray microscopy is a general-purpose nanoscale imaging technique that complements scanning probe, electron, and visible wavelength microscopies because it can penetrate thick samples (allowing for 3-D imaging) and achieve very high spatial resolution with the added advantages of elemental and chemical specificity. To date, X-ray microscopy has been implemented primarily using light from synchrotron radiation facilities, with demonstrated spatial resolutions down to 15 nm using zone plate based microscopes [19]. X-ray microscopy has also proven to be uniquely capable of 3-D tomographic imaging of whole, 5 μm diameter, single cells with 50 nm spatial resolution [20,21] and in 2-D with 11 nm resolution [22].

There are a variety of EUV/X-ray sources used for microscopy, including third generation synchrotrons [23], free electron lasers (FELs) [24], EUV lasers [25–27], laser-produced plasma emission sources [28,29], and high-harmonic generation [30,31]. Each source has its own unique characteristics, such as temporal resolution, coherence and brightness, which affect what imaging modalities can be performed. In the following section, a variety of the imaging techniques that make use of this type of nanoscale probe will be described.

1.2 Imaging with extreme ultraviolet and X-ray light

Taking advantage of the short wavelengths of extreme ultraviolet (EUV) and X-ray light to access information at the nm spatial scale (and below) is an old idea. X-ray crystallographers have been using X-ray diffraction to probe crystal structure ever since Laue's discovery of X-ray diffraction peaks more than 100 years ago [32]. However, it wasn't until much later that X-ray microscopy took hold with the development of Kirkpatrick-Baez (KB) glancing incidence reflective focusing systems in the 1940's [33] and EUV and X-ray Fresnel zone plates in the 1970's [34–36]. Both of these types of EUV/X-ray focusing elements are limited in resolution by the numerical aperture (NA) and fabrication quality of the optics. Additionally, Fresnel zone plates require high flux light sources due to poor diffraction efficiency.

A new technique known as coherent diffractive imaging (CDI) has more in common with X-ray crystallography; in order to retrieve a high-resolution image, the intensity of the diffraction pattern of an object, rather than a direct image, is recorded. This technique was first demonstrated in the visible region of the spectrum [37], and only demonstrated in the X-ray region of the spectrum 15 years ago [38]. The advantage of CDI over more conventional forms of imaging lies in the fact that the resolution of the images obtained with this technique is only limited by the wavelength of light and the NA of the detector used to collect the scattered light. Images can be retrieved via the Fourier transform relationship between a scatterer and its diffraction pattern.

The advantage in resolution comes with a price. The reduced optical complexity of this type of “imaging” system is replaced with increased computational complexity. While specific techniques such as Fourier transform holography (FTH) and its variants allow images to be retrieved through a single Fourier transform of the recorded diffraction pattern, the most general implementation of CDI requires phase retrieval of the measured diffraction intensity [39]. Below, the differences between direct real-space imaging and coherent techniques is discussed in more detail.

1.2.1 Real-space Imaging Techniques

Traditional refractive lenses are impossible to manufacture in the EUV and X-ray spectrum, due to the fact that the index of refraction of most materials is very close to unity for photon energies above 30 eV [40]. Thus, forming a direct image using EUV/X-ray light requires either reflective or diffractive optics. In this section, strengths and limitations of objective-based, full-field imaging methods will be discussed.

Multilayer mirrors can be manufactured in the EUV region of the spectrum with relatively high reflectivities at normal incidence [41]. This is the basis for the semiconductor industry's choice of 13.5 nm as the next lithography wavelength candidate to increase computer chip pattern density [42, 43]. The lithography process involves a mirror-based, $4\times$ demagnification system from mask to wafer. However, while it is possible to fabricate normal-incidence mirrors in the soft X-ray region, tolerances are stricter and reflectivities are lower ($\approx 70\%$) than for visible optics [44]. In the hard X-ray region, materials are only reflective at glancing incidence, meaning that mirror-based imaging requires the use of KB-type systems [45, 46].

As with any linear imaging system, the highest resolution, d_{\min} , of a mirror-based imaging system is limited by the wavelength and numerical aperture (NA) of the system via the Abbé diffraction limit to

$$d_{\min} = \frac{\lambda}{2n \sin \theta} = \frac{\lambda}{2\text{NA}}, \quad (1.1)$$

where λ is the illumination wavelength, n is the index of refraction of the medium between the sample and the imaging optic, and θ is the collection angle of the imaging optic. Whereas for visible light microscopy, the index of refraction, n , can be increased using oil immersion techniques in order to increase resolution, EUV/X-ray microscopy typically requires light propagation to occur in vacuum, so that in Eqn. (1.1) $n = 1$. The diffraction limit represents the best possible resolution a linear imaging system can achieve.

In practice, the diffraction limit is very difficult to achieve due to imperfections in the imaging optics, which cause aberrations in the resulting image and worsen the achievable resolution. Some

aberrations, such as spherical aberration, are inherent to spherical mirrors. This type of aberration can be reduced using aspherical optics such as elliptical and hyperbolic mirrors. Other aberrations such as astigmatism, coma, and defocus come from imperfect alignment and from mirror imperfections. For instance, in order to achieve the diffraction limit, the shape of the mirror surface must typically be correct to length scales smaller than the desired resolution. This is particularly difficult, and expensive, to achieve at hard X-ray wavelengths. For this reason, most mirror-based imaging systems in the X-ray region do not achieve very high resolution. However, these systems still have advantages over visible-light microscopes because of the elemental contrast and long penetration depths of X-ray light [45, 47, 48]. Nevertheless, mirror-based full field microscopes with resolution below 50 nm are possible and are under development [46, 49].

Due to the difficulties of alignment and fabrication of mirror-based EUV/X-ray imaging systems, much effort has been put towards the development of Fresnel zone plate-based microscopes. A Fresnel zone plate is a diffraction-based imaging optic, and is essentially an approximation to a Fresnel lens. In contrast to a traditional (or Fresnel) lens, a zone plate has additional, high order foci as well as an unfocused zeroth order. These additional orders are the result of high order diffraction (higher-order foci) and undiffracted light (zeroth order). A zone plate consists of many concentric rings, or “zones”; in the simplest case the zones alternate between transparent and opaque, with radii such that the transparent zones interfere constructively at the focus (depicted in Fig. 1.1). This type of zone plate has a theoretical efficiency of only 10% at the first-order focus. In order to achieve higher efficiency, the opaque zones can be replaced with material of the correct thickness such that these zones impart a phase shift of π relative to the transparent zones. Assuming there is no absorption in the phase-shifted zones, the first-order efficiency is increased to 40%.

The radius of the n th zone, r_n , can be calculated geometrically by determining the transverse distance from the optical axis at which the phase will shift by $n\pi$ (equivalent to an optical path length difference of $\lambda/2$) at a distance f along the optical axis, as shown in Fig. 1.1. Simply making

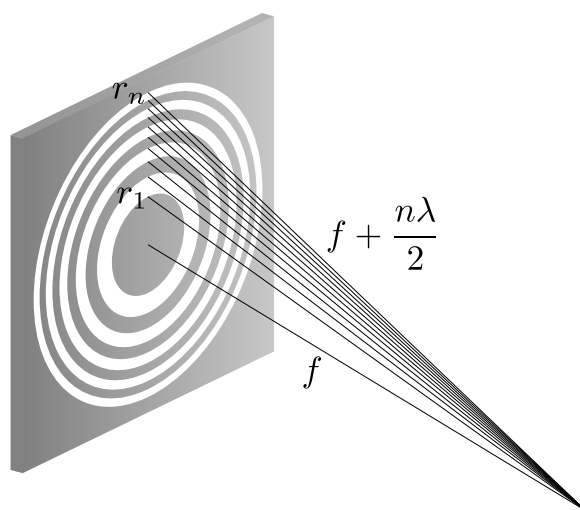


Figure 1.1: Schematic of a Fresnel zone plate. The radius of each zone is chosen such that adjacent zones have a path length difference of $\lambda/2$ to the focus, as depicted in the figure. Figure adapted from Attwood [50].

use of the Pythagorean theorem, this condition can be expressed as

$$r_n^2 + f^2 = \left(\frac{n\lambda}{2} + f \right)^2. \quad (1.2)$$

Upon solving for the radius of the n th zone, Eqn. 1.2 becomes

$$r_n = \sqrt{n\lambda f + \left(\frac{n\lambda}{2} \right)^2}. \quad (1.3)$$

In order to gain an understanding of what is required to obtain high resolution in a zone plate imaging system, it is instructive to calculate the outermost zone width of a zone plate “lens” described by Eqn. (1.3) and relate this to the NA of that lens, which limits the resolution as in Eqn (1.1). When the approximation that the focal length is large compared to the zone plate diameter is made (meaning NA is small), Eqn. (1.3) can be rewritten as

$$r_n \approx \sqrt{n\lambda f}. \quad (1.4)$$

This approximation simplifies the calculation of the outermost zone width, Δr_N , which can be obtained directly as

$$\Delta r_N = \sqrt{N\lambda f} - \sqrt{(N-1)\lambda f}. \quad (1.5)$$

Squaring both sides of Eqn. (1.5) yields

$$\Delta r_N^2 = \left(2N - 2\sqrt{N(N-1)} - 1 \right) \lambda f. \quad (1.6)$$

If we make the further approximation that $N \gg 1$, then to lowest order the outermost zone width is

$$\Delta r_N^2 = \left(2N - \left[2N - 1 - \frac{1}{4N} + \dots \right] - 1 \right) \lambda f \approx \frac{\lambda f}{4N}. \quad (1.7)$$

If we insert r_N in place of N using Eqn. (1.4), we have

$$\Delta r_N \approx \frac{\lambda f}{2r_N}. \quad (1.8)$$

Rearranging Eqn. (1.8) gives an expression for the NA of the system (here defined as r_N/f for the low-NA case) in terms of the outermost zone width,

$$\text{NA} \approx \frac{\lambda}{2\Delta r_N}. \quad (1.9)$$

Finally, this allows us to calculate the diffraction-limited resolution of a given zone plate using Eqn. (1.1), which turns out to simply be

$$d_{\min} \approx \Delta r_N. \quad (1.10)$$

This simple relation implies that fabrication quality must be extremely high in order to achieve high resolution using a zone plate objective. Indeed, record zone plate-based image resolution of 10-15 nm has only been achieved through complex multi-step fabrication processes. One such process involves two patterning steps in which an overlay must be performed with few-nm accuracy [19, 51, 52], to obtain outer zone widths down to 12 nm. The other process involved an e-beam patterning step followed by a deposition step that effectively doubles the number of zones, and decreases the outer zone widths by a factor of two [53, 54].

The above discussions have been related to traditional absorption-contrast imaging. However, sometimes absorption contrast in semi-transparent samples (such as biological cells) is weak [55]. In this case, phase contrast imaging ideas which were originally developed for visible light microscopy [56] have been applied to zone plate microscopy as well, with phase contrast resolution as high as 25 nm through relatively simple modifications to the imaging system [57, 58]. Quantitative phase information is still difficult to obtain in these systems, even though phase differences are the source of image contrast [55].

A major difference between mirror-based and zone plate-based full field microscopes is the sensitivity to chromatic aberrations, which come from changes in focal length as a function of wavelength. Fully reflective systems have focal lengths independent of the wavelength of light, whereas zone plates are strongly chromatic. This can be seen by solving for the focal length from Eqn. (1.8), which is

$$f \approx \frac{2r_N \Delta r_N}{\lambda}, \quad (1.11)$$

showing that for a given zone plate design, the focal length is inversely proportional to wavelength. While designs have been proposed to slightly reduce the chromaticity of zone plate optics [59], they have yet to be demonstrated experimentally. However, the relative ease of alignment of on-axis zone

plate objectives in contrast to glancing-incidence mirror systems means zone plates are much more widely used in EUV/X-ray microscopes. Both mirror-based and zone plate full-field microscopes are limited in resolution by the manufacturability of the optics. In order to take full advantage of the high resolution potential of short wavelength light, coherent imaging techniques are needed.

1.2.2 Coherent Imaging Techniques

The direct imaging techniques described above are necessary when using incoherent light sources, and are still useful for coherent sources as well. However, the availability of spatially coherent light sources enables alternative approaches for high resolution EUV/X-ray microscopy. These alternative approaches can be classified as either point scanning techniques or diffraction-based techniques. As will be described below, there is some overlap between these two classes of coherent imaging techniques.

1.2.2.1 Scanning X-ray transmission microscopy

Scanning X-ray transmission microscopes (STXM) take advantage of highly spatially coherent sources to focus X-rays to extremely small spots. Focusing can be accomplished using KB mirror systems [60], condenser zone plates (CZPs) [53], multilayer Laue lenses (MLLs) [61], and, at high photon energies, compound refractive lenses [62, 63]. Images are formed pixel by pixel by scanning the object across the beam focus, with resolution limited by the focused spot size of the EUV/X-ray beam and by the scanning step size.

Resolution for KB systems and CZP systems is limited in the same ways as what is described above in the case of full-field imaging, based on Eq. (1.1) for the KB case and Eq. (1.10) for the CZP case. This is clearly the case due to the reciprocity theorem (first attributed to Helmholtz), which states that the source and observation points in optical systems are interchangeable [64]. Essentially, conversion from a full field microscope to a scanning microscope consists of performing this interchange in addition to reversing the direction of light propagation through the optical

system. More simply put, the object and image distances, d_o and d_i , in the lens maker's equation,

$$\frac{1}{f} = \frac{1}{d_o} + \frac{1}{d_i}, \quad (1.12)$$

where f is the focal length, are interchangeable. In STXM, the source is demagnified at the beam focus by the same amount as an object would be magnified if it were placed at the beam focus position and illuminated from the opposite direction, with its image formed at the location where the source would be in STXM. Interestingly, this equivalence was recently taken advantage of to achieve Zernike phase contrast in a STXM geometry [65].

MLLs are a new type of diffractive optic, and are essentially one-dimensional versions of zone plates [66]. While focusing in two dimensions requires two MLLs, their potential advantage over CZPs comes from a simpler fabrication process. Typically, zone plates require lithographic patterning, whereas MLLs can be fabricated via sputtering. The simplified process offers promise of smaller zone widths relative to what is possible with zone plate fabrication, causing speculation that MLLs are the way towards focusing to 1 nm spot size [67,68]. Thus far the best resolution obtained was 11 nm [61]. Other work has shown possibilities for zone plate fabrication via deposition, allowing for high aspect ratios combined with 5 nm outer zone width [69]. The zone plate is coated layer by layer on a rotating wire, and sliced to the desired thickness afterwards using a focused ion beam (FIB). While this fabrication technique shows promise, the zone plates manufactured in this way have not yet been applied to imaging.

While it is stated in the previous section that traditional refractive lenses are impossible to fabricate for EUV/X-rays, this statement needs some qualification. The fact that the index of refraction is very close to one for all materials across the EUV/X-ray range means that any refractive lens must be very thick in order to achieve any significant amount of focusing. This means that this type of refractive lens can only be made for hard X-rays, because materials are too absorbing at lower photon energies. The first demonstration of a refractive X-ray lens was a compound lens consisting of 30 adjacent 300 μm -diameter cylinders bored in an Al-Cu alloy [62]. This first demonstration was not overly ambitious and produced an 8 μm focus size. More recent demonstrations have

produced focus diameters as small as 50 nm, using parabolic compound lenses [63]. As with MLLs, most refractive X-ray lenses produced thus far focus in only one dimension, so that to focus in both dimensions two lenses oriented perpendicularly to each other are needed. Recent work has also resulted in initial demonstrations of 3D lenses capable of focusing in two dimensions [70, 71].

While coherent scanning techniques are capable of achieving very high resolution, they are unable to provide simultaneous amplitude and phase information about the object under study. In order to measure this kind of information, phase retrieval techniques such as holography or coherent diffractive imaging are needed. These techniques are capable of retrieving the complex-valued electric field scattered by an object, rather than simply providing amplitude or phase contrast separately.

1.2.2.2 Coherent diffractive imaging

The other main class of coherent imaging in the EUV/X-ray region is based on measurement of scattered, or diffracted, light. Coherent diffractive imaging (CDI), as it is known, encompasses a relatively broad range of techniques, connected by measurement of diffraction intensities with no optics between the object being studied and the detector. Thus, the geometry is very similar to STXM, with the exception that the point detector used for STXM is replaced with a pixel detector, typically a charge-coupled device (CCD). The CCD detector measures the intensity, but not the phase, of the light scattered by the object. In order to recover an image of the object, the phase of the scattered light must be retrieved using one of a number of techniques. These phase retrieval techniques can be classified as either direct or iterative, where direct techniques require some form of holographic measurement and iterative techniques rely on one or more constraints to solve the two-dimensional (2D) phase retrieval problem [72, 73].

In contrast to STXM, high resolution is achieved by the collection of diffraction at high angles (high NA, as in Eq. (1.1)) instead of being limited to the size of a nano-focused X-ray beam [38], thus removing the need for reliance on high resolution optical elements. Additionally, CDI is a full-field imaging technique, so while the experimental geometry is similar to STXM,

the resulting image shares more similarity with objective-based techniques, with the 2D phase retrieval algorithm replacing the imaging optic. Images reconstructed using CDI contain both amplitude and phase contrast, similar to the Zernike approaches discussed above. A significant difference, however, is that both the amplitude and phase information in the reconstructed image are necessarily quantitative as a result of the 2D phase retrieval process. Finally, because there are no optics between the object and the detector, virtually no aberrations are introduced into the imaging system. As a result, researchers have already achieved resolutions below 10 nm in two and three dimensions using CDI [74–76].

The limitations of the technique include the necessity of a fully spatially coherent light source as well as the need to satisfy one or more constraints, which can be enforced during the iterative reconstruction by projecting the solution onto sets defined by these constraints in a generalized Gerchberg-Saxton scheme [77]. The original Gerchberg-Saxton algorithm involved retrieving the phase by enforcing a modulus constraint in both the image and diffraction space [78]. Enforcing a modulus constraint means requiring the solution to be consistent with measured intensities, while leaving the current solution to the phase unchanged.

Most CDI phase retrieval techniques involve applying a modulus constraint in the diffraction space and one of a variety of types of support constraints in the image space. This means that, with a couple of exceptions [79], either the object or the illumination must be confined to a limited size specified by the geometry of the experiment. The requirement of a finite support is equivalent to requiring that the diffraction pattern must be “oversampled” [80]. Oversampling refers to sampling the diffraction amplitude at a spatial frequency beyond the Nyquist frequency. The various available constraints and phase retrieval algorithms will be described in detail in Ch. 3.

Finally, traditional CDI requires the illumination to be monochromatic. However, one of the clear strengths of CDI is that by introducing additional computational steps, experimental requirements can be relaxed. For instance, CDI can be extended for use with broadband sources simply by numerically propagating each part of the spectrum independently between the object and detector planes [81]. Additional work has shown that the spatial coherence requirements can

also be relaxed to allow for partial coherence [82–84].

It was stated above that there is some overlap between STXM and CDI. As a result of the similarity in experimental geometry between the two techniques, many STXM microscopes have been upgraded to have pixel detectors in order to be compatible with a new branch of CDI called ptychography CDI [85,86]. Ptychography CDI is an extension of an imaging technique developed for TEM starting in the 1970's [87, 88]. Ptychography involves scanning an object across the illuminating EUV/X-ray beam, similarly to the STXM procedure. However, rather than being limited by the illumination size and distance between scan positions, the resolution is only limited by the NA of the recorded diffraction patterns at each position. Ptychography solves for the object and illumination functions independently; thus any non-uniformity in illumination is factored out during the image reconstruction [89]. Due to the wealth of information present in a ptychographic dataset, many generalizations to the technique have been proposed and demonstrated since the initial demonstration of ptychography, including but not limited to extension to 3D imaging [90] and extension to broadband sources [91]. Some of these generalizations will be described in Ch. 3.

CDI clearly has much to offer in terms of nanoscale imaging capabilities. Similarly to holography, CDI techniques enable reconstruction of the complex amplitude of the scattered electric field. However, CDI removes limitations on resolution which are typically imposed by holographic techniques. In order to take advantage of this new class of techniques, light sources with both high temporal and spatial coherence are needed.

1.3 Coherent EUV and X-ray sources

Despite the clear potential for EUV/X-ray CDI microscopes to enable rapid advances in the nano- and bio-sciences, accessibility to these microscopes is limited, because they are primarily located at a small number of large synchrotron or x-ray free electron laser (FEL) light sources. Fortunately, in recent years rapid advances in compact coherent short wavelength light sources based on high harmonic generation (HHG) [31,92] and EUV and soft X-ray lasers [26,27,93] have opened up new capabilities in tabletop EUV/soft X-ray microscopy. Brief descriptions of these four

types of coherent light sources follow.

1.3.1 Third-generation synchrotrons

Historically, the first source of coherent X-rays was the synchrotron, which was pioneered in the 1950's. The original synchrotrons were developed originally for the study of particle physics [94], with X-ray emission as a byproduct [95]. These original synchrotron facilities are classified as first-generation sources. Some of these facilities were converted completely to light sources, moving away from particle physics research; these facilities are classified as second-generation sources. In the 1990's, new synchrotrons were designed specifically as dedicated high brilliance light sources, ushering in the era of third-generation facilities [96].

A third-generation synchrotron facility consists of several components. The main component is the storage ring, which is a roughly circular tube which the electrons traverse at relativistic speeds. Bending magnets spaced around the circumference of the storage ring serve to bend the trajectory of the electrons along the storage ring, as well as produce broadband X-ray beams due to the centripetal acceleration of the electrons at these points. Finally, so-called insertion devices are placed in the straight sections between the bending magnets. One type of insertion device, called an undulator, is the main source of high-brilliance X-ray beams at third generation synchrotrons. Each undulator sends an X-ray beam to an end station set up for a particular type of scientific measurement. A typical synchrotron facility has 50 or fewer of these end stations.

Undulators consist of periodic arrays of magnets which induce transverse oscillation in the electron beam that produce narrow-band, coherent X-ray radiation. The wavelengths that are radiated can be calculated from the following equation, (see Jackson for derivation [97]):

$$\lambda = \frac{\lambda_0}{2n\gamma^2} \left(1 + \frac{K^2}{2} + \gamma^2\theta^2 \right), \quad (1.13)$$

where λ_0 is the spatial period of the magnet array, n is the harmonic number, γ is the relativistic factor based on the electrons' energy, θ is the emission angle, and K is a dimensionless deflection parameter based on the magnetic field strength and the geometry. K is equal to $eB\lambda_0/2\pi mc^2$,

where e is the charge of an electron, B is the magnetic field amplitude in the lab frame, m is the mass of an electron, and c is the speed of light. Thus for small deflection parameters K , the on-axis emission is simply at harmonics of $\lambda_0/2\gamma^2$, which is purely geometric after taking into account the Lorentz transformations from the lab frame to the electron frame and back again. As can be seen from Eq. (1.13), the peaks can be tuned by adjustment of the magnetic field strength. This can also be understood geometrically via the fact that the axial velocity of the electrons is decreased as the deflection parameter is increased.

The simplest type of undulator induces roughly sinusoidal electron trajectories, generating linearly polarized light. However, the magnet arrays can be arranged in such a way to induce helical trajectories, providing light sources with circular polarization. This can be useful for studies where materials respond differently depending on the helicity of light, as in the case of X-ray magnetic circular dichroism (XMCD). In terms of coherent flux, a typical undulator can provide on the order of 10^{11} photons/s in a 0.1% bandwidth. While undulator light sources provide tunable, high brilliance X-ray sources (meaning high photon flux in a narrow bandwidth and narrow divergence angle), these sources have relatively poor temporal resolution in comparison to fs timescales needed for ultrafast studies; typical pulse durations are 10's of picoseconds long [23].

Techniques such as fs slicing exist for achieving better temporal resolution. The principle of fs slicing is depicted schematically in Fig. 1.2. A ≈ 50 fs, 2 mJ laser pulse propagates collinearly with the electron bunch through an undulator, modulating the energy of some of the electrons at the center of the bunch by up to 1% of their initial energy due to the high electric field of the laser pulse. The electron bunch is then sent into a bending magnet, which angularly disperses the electrons of different energy. This bending magnet is followed by a second undulator which produces X-ray radiation. The “sliced” bunch of electrons produces an X-ray pulse of ≈ 100 fs duration, which is separated from the main ≈ 50 ps pulse with an aperture. However, this process is very inefficient, resulting in $10^{-4} \times$ fewer photons than are produced by the unmodulated bunch, greatly reducing the total X-ray flux. Furthermore, this technique dramatically increases the complexity of the system, requiring high-precision synchronization between the fs laser and the electron bunches.

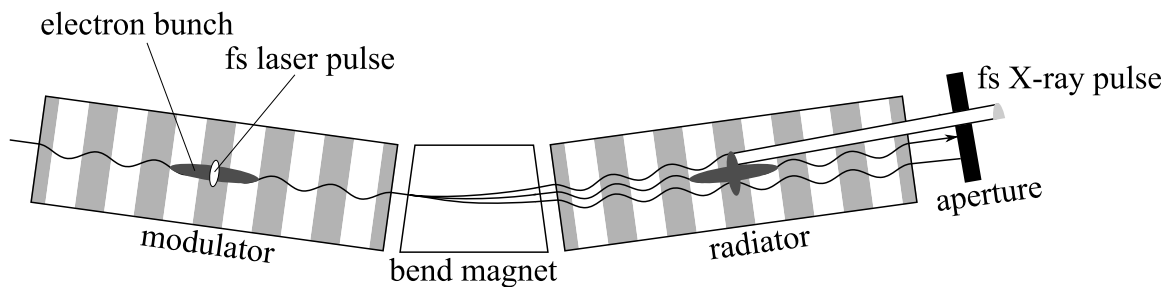


Figure 1.2: Schematic of the fs slicing principle. A fs laser pulse propagates collinearly with the electron bunch through an undulator, modulating the energy of electrons at the center of the bunch. Hence this undulator is termed the “modulator” as labeled above. The electron bunch then passes through a bend magnet, which angularly disperses the electrons according to energy. A second undulator, termed the “radiator”, produces X-ray radiation. An aperture placed beyond the radiator selects only the radiation from the “sliced” electrons. The main electron bunch continues along the trajectory of the storage ring. The alternating dark and light zones in the undulators represent alternating magnetic field directions. Figure adapted from [98].

1.3.2 Free electron lasers

Recent years have seen the introduction of a new coherent EUV/X-ray source: the FEL, which has been called the fourth-generation synchrotron. FELs build on the ideas that are the foundation for undulator light sources. Namely, relativistic electrons produce radiation due to sinusoidal trajectories induced by an alternating magnetic field. The difference lies in the fact that in an FEL, the electron bunch can be considered to act as a gain medium due to its interaction with the collinearly propagating electromagnetic wave (see Saldin et al. [99] for details). The first experimental observation of amplification by stimulated emission using relativistic electrons as a gain medium dates as far back as the 1970's, with the amplification of a 10.6 μm CO₂ laser [100]. However, it wasn't until 2005 that FELs were pushed to soft X-ray wavelengths for the first time at DESY (Deutsches Elektronen-Synchrotron) [24].

FELs operating in the visible and infrared (IR) can operate as amplifiers or oscillators in the traditional sense, due to the availability of resonant optical cavities in this wavelength range. In the case of an oscillator, electron bunches from an external source such as a linear accelerator or storage ring are synchronized to the round trip time of the cavity in order to overlap in time with the laser pulse. However, in the EUV/X-ray region, FELs can only be operated in a single-pass mode. This can mean either operation as an amplifier or as a self-amplified spontaneous emission (SASE) FEL. In order to reach gain saturation, the undulator in a SASE FEL must be much longer (5-10 \times) than what is typical for undulators used as insertion devices [24].

In a SASE FEL, "spontaneous emission" at the front end of the undulator stimulates further emission along the undulator. At the output of the undulator, the resulting pulses contain $10^{12} - 10^{13}$ photons [101]. Operating at 120 Hz, this corresponds to $10^3 - 10^4$ times the average photon flux of a third-generation synchrotron. Additionally, these photons arrive in pulse widths < 50 fs, in contrast to ≈ 50 ps from an undulator source.

While the spatial coherence of these X-ray beams is very high, the temporal coherence is limited due to the fact that the SASE amplification process starts from noise. This means that the

temporal and spectral profiles of the pulse from shot-to-shot exhibit large variations [102]. This situation can be improved by injecting a seed pulse into the undulator, effectively using the FEL as an amplifier. Seeding can be accomplished in a variety of ways. One option is to produce the seed pulse with a separate source, such as using HHG. Preliminary demonstrations of HHG seeding at EUV wavelengths show promise, but are plagued by difficult technical challenges such as timing jitter between the seed and the electron bunch [103–105]. Another type of external seeding is called high gain harmonic generation (HG) [106]. In HG, an external seed laser is used to modulate the energy of the electron beam in a modulator undulator (similar to what is described above for fs slicing). The electron beam is then sent through a dispersion section, resulting in spatial bunching of the electrons along the direction of propagation spaced by the laser wavelength. Finally, the electron beam is sent into a second, very long, undulator (analogous to the radiator used in fs slicing) tuned to a harmonic of the seed laser. The resulting EUV or X-ray beam produced from this type of seeded FEL has much better temporal coherence properties than what is produced in the SASE process [107]. So far, HG seeding has been successfully demonstrated at EUV and soft X-ray wavelengths at the FERMI FEL in Italy [108].

Another option for producing a temporally coherent X-ray FEL beam is to use a process called self-seeding. This type of seeding again involves two undulators as in HG, except in this case both undulators are tuned to the same wavelength. Here, the first undulator operates using SASE in order to generate the seed. The seed is then spectrally filtered using a monochromator which is placed between the two undulators. This spectrally narrow seed in addition to the electron beam are then sent into the second undulator, which is used as an FEL amplifier. This type of seeding has been demonstrated at hard X-ray wavelengths at the Linac Coherent Light Source (LCLS), with drastic improvement of the spectral purity of the resulting 8 keV X-ray beam [102].

While the potential of EUV/X-ray FEL light sources is enormous due to their capability to produce extremely bright beams, to-date only four facilities are in operation at these short wavelengths. Additionally, each of these facilities can currently handle only one user at a time. In the future, switching stations will likely be installed in order to slightly increase the user accessibility

of these light sources.

1.3.3 EUV/Soft X-ray lasers

The coherent light sources described in the two preceding sections operate at large facilities. Users must submit proposals to obtain beam-time at these facilities; beam-time typically ranges from several days to 2 weeks at a time during which the users can attempt their experiment. Two other types of coherent EUV/X-ray sources exist on a smaller-scale: EUV/soft X-ray lasers and HHG sources. These sources are compact and inexpensive enough to operate in a typical laboratory.

EUV/soft X-ray lasers, similar to FELs, operate in a single-pass geometry. However, in contrast to FELs, the gain medium consists of multiply ionized atoms rather than relativistic electrons, and photons are emitted at energies corresponding to atomic transitions similarly to lasers operating in the visible range. The first EUV laser was demonstrated in the early 1980's at wavelengths near 20 nm, using Ne-like selenium (Se XXV) as a gain medium using a high-power, facility-scale picosecond laser as the pumping mechanism [109]. The reason for the long gap in time between the first visible laser in 1960 and the first EUV laser is due to the unfavorable scaling of required pump power density, P , with wavelength, which scales as $P \propto \lambda^{-5}$ [26]. It wasn't until 1994 that the first tabletop-scale EUV lasers were demonstrated because of this unfavorable scaling.

Thus far, two pumping mechanisms have been demonstrated that can produce this type of pump power density on a tabletop scale. First, as high-power ultrafast lasers have become more compact, they now have the power density necessary to pump ions to the upper level of EUV/soft X-ray laser transitions to wavelengths less than 8 nm [110]. Second, EUV lasers have also been demonstrated using fast capillary discharges as the pumping mechanism, most successfully for Ne-like argon as the gain medium with laser output at 46.9 nm [25,111].

EUV/soft X-ray lasers are capable of producing from 10 μJ up to 1 mJ, at several Hz to 100 Hz repetition rates, with very narrow spectral bandwidth [26]. This is comparable to the average power of a typical X-ray FEL, albeit limited to mostly EUV wavelengths. The other caveat is that the pulse durations produced by this type of laser are in the picosecond range, comparable to that

produced by an undulator. Also, while these lasers exhibit very narrow spectral bandwidths, the temporal and spatial coherence is limited since, similar to FELs, the laser output is produced by a SASE process. However, as with FELs, they can instead be used to amplify a seed pulse in order to improve coherence properties. Initial demonstrations have been performed that HHG can be used to seed these lasers to be used in an amplifier mode. Similar to FELs, however, the synchronization between the seed pulse and the gain medium excitation is technically challenging [112–114].

1.3.4 High harmonic generation

The final currently available coherent EUV/X-ray light source is HHG. Dramatic advances in the past 15 years have greatly increased the usability of HHG as a light source for a wide variety of scientific studies. HHG was first observed in the 1980's [30,115], but it wasn't until the 1990's that the process could be considered to be fully understood with a quantum theory of the process [116]. HHG is an extreme nonlinear process, and, while it shares some similarities with low-order harmonic generation, a description of HHG requires fundamentally different physics than that which is involved in ordinary nonlinear optics.

The HHG process involves the production of coherent radiation at integer harmonics of an ultrafast driving laser. The process can be understood classically in a 3-step model. In step one, a noble gas atom located in a strong, oscillatory electric field (produced by the driving laser) is field-ionized. In step two, the ejected electron is then accelerated in the electric field, first away from the parent ion and, after the electric field reverses sign, back towards the ion. In step three, the electron has a finite probability of recombination with the parent ion, after which the extra energy it gained in the laser field can be emitted as a high-energy photon [117].

The above simple description describes the high harmonic process for a single atom at a time. However, to gain a full understanding of HHG as a light source, radiation from all of the noble gas atoms involved must be taken into consideration macroscopically, and ideas such as phase matching between the fundamental laser and the harmonic beam taken into account [118,119]. The result is a fully spatially and temporally coherent light source, with the EUV/X-ray beam essentially taking

on the coherence properties of the driving laser [31, 92]. Additionally, pulse durations are in the attosecond to femtosecond range. Isolated attosecond pulses are possible when photons above a certain energy are only generated during a single half-cycle of the driving laser [120]. In general, EUV/X-ray photons are produced in attosecond bursts, once every half-cycle of the fundamental laser.

Currently, bright HHG beams can be produced in the EUV and soft X-ray region of the spectrum, with wavelengths ranging from $\approx 1 - 30$ nm. While these compact sources are nowhere near as bright as FELs (typically 10^8 photons per shot can be produced in a single harmonic at repetition rates of several kHz [92]), the temporal resolution of these sources is unmatched. Furthermore, while traditionally HHG beams exhibit linear polarization, recent work has shown that it is also possible to generate circularly polarized HHG light, which should prove to be very useful for ultrafast magnetism studies [121]. Due to the above desirable characteristics, HHG was chosen as the light source for the work in this thesis.

1.4 Overview of this thesis

This thesis will present the further development of a CDI-based coherent EUV microscope, using HHG as the light source. This microscope will be applied to dynamic imaging studies at the nm- and fs-scales, taking advantage of the short wavelength and ultrafast properties of HHG, in order to address important scientific questions at the nanoscale. These questions include how function is related to nanoscale inhomogeneities in catalytic, biological and energy-conversion systems, how heat dissipates in next-generation data storage devices, and how to design and characterize next generation integrated circuits in support of the relentless drive to shrink device dimensions.

In Ch. 2, HHG based on compact, ultrafast chirped pulse amplification (CPA) technology will be described in detail. This description will include improvements to the specific laser/HHG source used for this work. Ch. 3 will provide an overview of coherent scattering in the EUV/X-ray region. Additionally, this chapter will describe available CDI techniques which can be applied for use with this microscope. Ch. 4 will describe imaging results obtained with this microscope in

transmission mode, as well as improvements to the HHG source and microscope which enabled these results. These results include the demonstration of a record tabletop full-field resolution of 22 nm. Recent imaging results in reflection geometry will be presented in Ch. 5. These results represent the most general reflection CDI imaging to date. Finally, Ch. 6 will present ideas for the further development of the microscope, with the goal of dynamic imaging studies in mind.

Chapter 2

High Harmonic Generation Driven by Ultrafast Lasers

This chapter will focus on a discussion of the HHG light source used for the CDI-based microscope described in this thesis. HHG sources rely on ultrafast lasers that are capable of producing the strong electric fields necessary to drive this extreme nonlinear optics process. The following will first include brief reviews of ultrafast laser technology and the HHG process. Next, improvements to the laser system relevant for its use as an HHG driver, including implementation of a pulse shaper and active laser beam pointing feedback, will be described and the impacts of these improvements will be discussed. The chapter will end with an outlook for the future of HHG sources.

2.1 Introduction to ultrafast light sources

Short pulse lasers have been around almost since the invention of the laser [122, 123], since a simple modification to the cavity of a ruby laser allowed it to be Q-switched only two years later [124]. Q-switching simply refers to a fast way of modifying the finesse, or Q, of the laser cavity. This is essentially a way to quickly turn on and off the optical feedback in a laser, allowing the upper laser state to grow in population in the absence of stimulated emission while the feedback is off before releasing this energy in a short pulse after the feedback is turned back on. These early Q-switched lasers had pulse durations of ≈ 100 ns, but mode-locked lasers capable of producing picosecond pulses followed soon after [125].

Mode-locking simply refers to the situation in which the many longitudinal modes in a laser

cavity have a stable, or “locked”, phase relationship with each other. Simple Fourier analysis predicts that this situation will result in a periodic sequence of pulse structures, with the width of the features in the sequence inversely proportional to the frequency bandwidth covered by the resonating modes. Thus, a laser medium with a large gain bandwidth has potential to produce extremely short pulses. However, in the simplest laser cavity (consisting of a gain medium inside an optical cavity), the various modes are typically independent of each other, with varying phase relationships due to various vibrations and other fluctuations in the laser system.

Coupling between modes can be achieved both actively and passively. Active mode-coupling was demonstrated as early as 1964, and was achieved by modulating the cavity loss at the same frequency as the laser mode spacing [126]. The modulation induces sidebands on each cavity mode, and when these sidebands are coincident with adjacent modes a fixed phase relationship between all modes is formed. Passive mode-locking can be achieved by introducing a nonlinearity into the laser cavity. For instance, passive mode-locking was first demonstrated through the use of saturable absorbers, which introduce intensity-dependent loss into the cavity [127,128]. These materials can be extremely lossy for low intensity light and near-transparent at high enough intensities. The mode-locking process in this passive system can most easily be understood in the time domain. If more than one mode is oscillating in the cavity, the interference between these modes will result in amplitude structure in the time-varying electric field of the laser beam. Low-intensity fields will see more loss in the saturable absorber than higher-intensity fields. This means that any peak-like amplitude structure will become narrower at every pass through the laser cavity. Additionally, low-intensity structure between larger peaks will end up being completely absorbed. In the frequency domain, this peak-narrowing process results in the participation of more and more cavity modes. Again, from Fourier analysis, the end result can be predicted to be pulses which repeat at the mode spacing frequency and have width limited by the bandwidth covered by the participating laser modes. This type of system is exactly analogous to an electronic circuit called a regenerative pulse generator, which was developed before the laser was invented.

While early Q-switching and mode-locking methods resulted in unprecedented peak optical

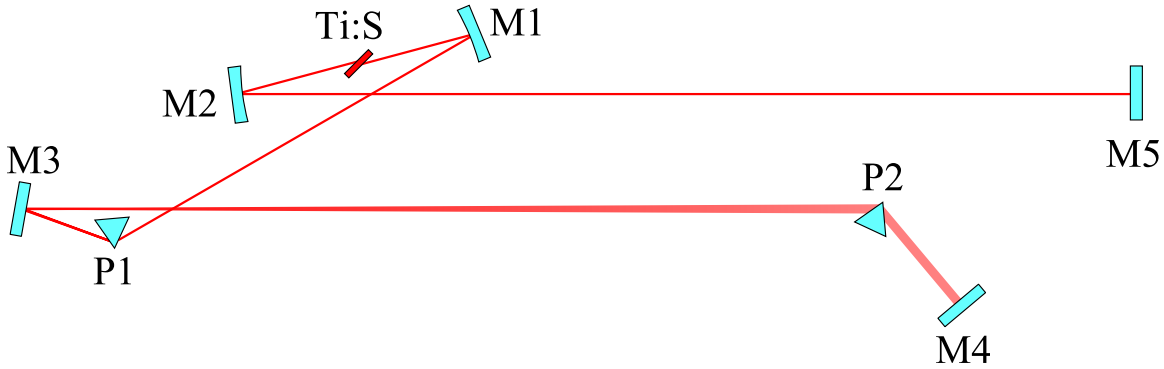


Figure 2.1: Schematic of a typical Ti:sapphire oscillator. M1 and M2 are curved mirrors (10 cm radius of curvature), M3 is a fold mirror, M4 is an end mirror, M5 is an output coupler, P1 and P2 are fused silica prisms, and Ti:S is a Ti:sapphire crystal. The wider beam width between P1 and P2 represents the angularly dispersed spectrum. The spectrum is collimated between P2 and M4.

power and sub-picosecond pulses directly out of an oscillator [129], it wasn't until the discovery of Kerr lens mode-locking (KLM) in Ti:sapphire that the ultrafast revolution really began [130, 131]. Soon after, reduction of the round-trip dispersion in the cavity resulted in sub-10 fs pulses directly out of an oscillator [132]. KLM is a passive mode-locking technique in which the nonlinearity which couples the various cavity modes is a property of the Ti:sapphire gain medium itself. A typical dispersion-compensated Ti:sapphire oscillator is depicted in Fig. 2.1, where negative dispersion due to a pair of fused silica prisms is used to compensate for the positive dispersion in the Ti:sapphire crystal [133].

As with saturable absorber modelocking, KLM can be most easily understood in the time domain. The nonlinearity comes in the form of the nonlinear index of refraction, n , of Ti:sapphire, which can be written as

$$n(I) = n_0 + n_2 I + \dots, \quad (2.1)$$

where n_0 is the normal index of refraction, n_2 is the second-order index of refraction, and I is the instantaneous intensity of the beam in the crystal. The key to understanding the mode-locking mechanism is that the nonlinear index of refraction produces a lensing effect, assuming the laser beam has a Gaussian mode distribution. To give a general idea of why this occurs, we can

approximate the intensity of a Gaussian beam near the optical axis as

$$I(r) = I_0 e^{-\frac{2r^2}{w^2}} \approx I_0 \left(1 - \frac{2r^2}{w^2} \right), \quad (2.2)$$

where I_0 is the peak intensity of the beam, r is the distance from the optical axis and w is the waist size of the beam. Using Eq. (2.1), we see that after propagating a distance d through a (thin) laser crystal, the accumulated phase a distance r from the optical axis relative to the on-axis phase is

$$\Delta\phi(r) = -2k_0 n_2 d I_0 \frac{r^2}{w^2}, \quad (2.3)$$

where k_0 is the free-space wavenumber of the laser. From comparison with the effect of a thin lens, we can approximate the Kerr focal length as

$$f_K = \frac{w^2}{4n_2 d I_0}. \quad (2.4)$$

While the above Kerr focal length is only an approximation, Eq. (2.4) serves the illustrative purpose to show that self-focusing proportional to the instantaneous intensity occurs in the crystal. This effect can introduce an intensity-dependent loss into the cavity via the fact that the Kerr lens changes the stability parameter of the cavity. The intensity-dependent loss can be effected either by placing an aperture in the cavity or by alignment of the cavity such that low-intensity (cw) operation produces a larger beam size in the crystal than does high-intensity (pulsed) operation [134,135]. The latter method takes advantage of a tightly focused pump laser providing the excitation of the gain medium, producing gain only within the width of the pump laser beam (termed soft aperturing) [134]. With an intensity-dependent loss mechanism established, the mode-locking mechanism can be understood exactly as described above for the saturable absorber case.

KLM has clear advantages over mode-locking achieved with the use of a saturable absorber. In the soft aperturing case, no extra losses must be added to the cavity. In addition, the quasi-instantaneous response of the KLM mechanism means that there is no need for long round-trip cavity times to allow for the recovery of a dye or other absorber. Because of the necessary recovery time, there is also less low-intensity loss immediately following the peak of the pulse, which can

limit the achievable pulse duration [136]. Advantages over active mode-locking schemes include the reduced complexity of the laser system and, again, shorter achievable pulse durations [136].

2.2 Compact chirped pulse amplification laser technology

A wide variety of scientific applications have been enabled based on mode-locked oscillator output alone. For instance, frequency-comb metrology and optical clocks are two very important applications that make direct use of the well-defined relationships between all of the modes in a mode-locked oscillator [137]. Additionally, many experiments take advantage of the short pulse durations and strong electric fields directly out of a Ti:sapphire oscillator for time-domain studies and coherent control [138, 139]. However, HHG in a noble gas requires electric fields with strengths much larger than what can be obtained directly from a mode-locked oscillator. In order to produce intensities required for HHG ($> 10^{13}\text{W}/\text{cm}^2$) using a tabletop system, the output of the oscillator can either be coupled into a femtosecond enhancement cavity [140, 141] or amplified at a reduced, usually kHz-level, repetition rate using chirped pulse amplification (CPA) [142], which was the method used for the work in this thesis.

CPA is a method of increasing the pulse energy output of an oscillator by many orders of magnitude, while keeping the peak intensity relatively low during the amplification process. This is important in order to avoid damaging the optical components in the amplifier system, and also avoids nonlinear distortion as the beam passes through material in the amplifier [142]. A schematic of a typical CPA system is depicted in Fig. 2.2. Here, a tabletop, single-stage amplification system based on Ti:sapphire as a gain medium is described. However, the general principle is the same for other gain media as well as for multi-stage amplifiers.

The output from a mode-locked oscillator (similar to that depicted in Fig. 2.1) is sent into a positive-dispersion grating stretcher. The stretcher is shown in Fig. 2.2, and consists of two anti-parallel (with respect to the optical axis) gratings with a telescope placed between them [143]. After the stretcher, the pulse is stretched, or “chirped”, to ≈ 100 ps. The amplifier component shown in Fig. 2.2 includes a pulse picker, or Pockels cell in order to reduce the repetition rate from

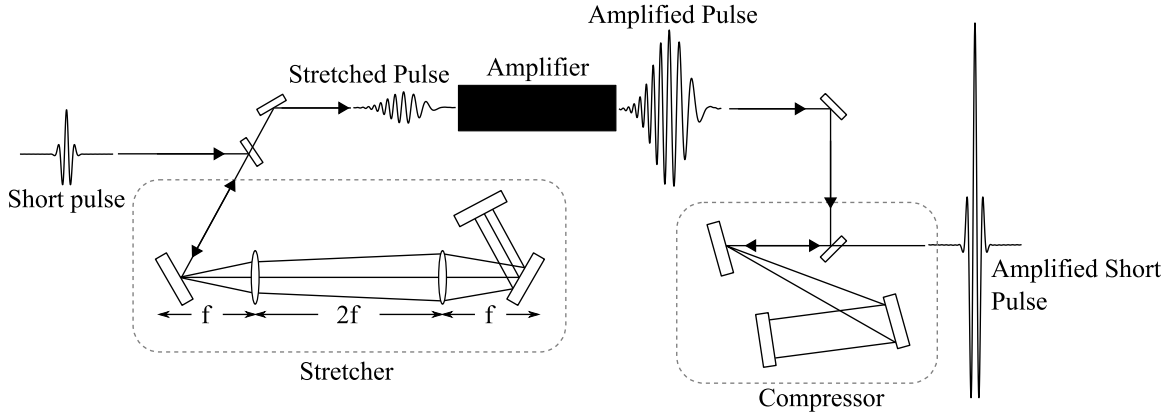


Figure 2.2: Schematic of a chirped pulse amplification system. Figure adapted from [142].

≈ 80 MHz to, in this case, 3-5 kHz. These pulses are then amplified in a Ti:sapphire crystal in a multi-pass scheme, with enough passes to ensure gain saturation. The laser crystal can be pumped with up to 100 W of average power when cryo-cooled with a closed-loop helium system (Cryomech PT90), allowing for multi-millijoule pulse energies at several kHz repetition rate [144]. In this work, the amplifier crystal is pumped by a frequency-doubled Nd:YAG laser operating at 1-10 kHz repetition rate and a maximum average power of 100 W at 532 nm (Lee Laser LDP-200MQG-HP). After amplification, the pulse is sent into a negative dispersion grating compressor, as depicted in Fig. 2.2. With use of blazed reflective gratings, the efficiency of the compressor is typically $\approx 65\%$ due to four grating bounces. Due to the effect of gain narrowing in the amplifier, the compressed pulse duration is typically limited to 20-25 fs full width at half maximum (FWHM) [142].

To get an idea of the peak powers, and when focused, peak intensities, that can be achieved with this amplifier system it is useful to consider the properties of a transform-limited Gaussian pulse. We will consider pulses which are not transform-limited in a later section. For convenience we will also assume a Gaussian spatial distribution. The following properties will be derived in somewhat of a reverse manner. We will consider experimentally measurable parameters and from these, eventually derive the strength of the electric field that can be obtained using a CPA system as described above. We will restrict ourselves to considering a single plane normal to the optical

axis. First, we can define the quasi-instantaneous power of an isolated pulse as

$$P(t) = P_{\max} e^{-4 \ln 2 (t/\tau)^2}, \quad (2.5)$$

where P_{\max} is the instantaneous power at the peak of the pulse and τ is the FWHM pulse duration. In the above definition, the pulse is centered at $t = 0$. The reason this is “quasi-instantaneous” and not simply “instantaneous” is that Eq. (2.5) is representative of the envelope of the pulse and doesn’t account for the fast variations in power due to the presence of optical cycles. This will be taken into account later when writing an expression for the electric field of the pulse. It is convenient to write the peak power in terms of the pulse energy, E_p , and the pulse duration. This expression can be obtained by integrating over the pulse. This allows us to rewrite Eq. (2.5) as

$$P(t) = \frac{2E_p}{\tau} \sqrt{\frac{\ln 2}{\pi}} e^{-4 \ln 2 (t/\tau)^2}. \quad (2.6)$$

From Eq. (2.6) we can immediately calculate the peak power for a given pulse energy and duration. For instance, a laser that produces 2 mJ, 25 fs pulses gives access to a peak power of 75 GW. To provide a sense of scale, the state of Colorado currently uses 50 GW of power on average. However, operating at 5 kHz the average power output of this laser is only 10 W.

If we now assume a Gaussian spatial profile as well, we can write the intensity distribution as

$$I(r, t) = I_0(t) e^{-2(r/w)^2} \quad (2.7)$$

where $I_0(t)$ is the on-axis intensity at time t , r is the radial coordinate, and w is the $1/e^2$ radius of the beam. The on-axis intensity can be related to the instantaneous power by integrating over the beam spatially, with the result that

$$I(r, t) = \frac{2P(t)}{\pi w^2} e^{-2(r/w)^2}. \quad (2.8)$$

Use of Eq. (2.6) allows us to write the intensity as a function of space and time as

$$I(r, t) = \frac{4E_p}{\pi w^2 \tau} \sqrt{\frac{\ln 2}{\pi}} e^{-2(r/w)^2} e^{-4 \ln 2 (t/\tau)^2}. \quad (2.9)$$

If the above-mentioned laser pulse is focused to 100 μm diameter, Eq. (2.9) gives a peak intensity of $1.9 \times 10^{15} \text{ W/cm}^2$.

We can use Eq. (2.9) to write an expression for the electric field of the pulse as a function of time and space, with knowledge of the center frequency of the laser. The amplitude of the electric field is given by

$$|\mathcal{E}(r, t)| = \sqrt{\frac{2I(r, t)}{c\epsilon_0}} \quad (2.10)$$

which gives

$$\mathcal{E}(r, t) = \left(\frac{2}{c\epsilon_0} \frac{4E_p}{\pi w^2 \tau} \right)^{1/2} \left(\frac{\ln 2}{\pi} \right)^{1/4} e^{-(r/w)^2} e^{-2 \ln 2 (t/\tau)^2} \cos(\omega_0 t + \phi_{ce}), \quad (2.11)$$

where ω_0 is the central laser frequency and ϕ_{ce} is the carrier-envelope phase. Unless stabilized experimentally, the carrier-envelope phase varies from one pulse to the next [137]. From Eq. (2.11), it can be seen that the maximum electric field only occurs at the center of the pulse envelope if $\phi_{ce} = n\pi$. This fact can be very important for few-cycle pulses, in the case where τ approaches $2\pi/\omega_0$. For instance, the maximum field strength can vary by 2.5% for a 5 fs pulse. However, the maximum field strength only varies by 0.1% for a 25 fs pulse. For the model pulse that we have been discussing (2 mJ, 25 fs, focused to 100 μm diameter), the maximum electric field amplitude is $1.2 \times 10^{11} \text{ V/m}$. For comparison, the Coulomb field at the position of the bound electron in hydrogen is $5.1 \times 10^{11} \text{ V/m}$.

2.3 High harmonic generation

High harmonic generation requires laser intensities high enough that the ponderomotive energy of the electric field is close to the ionization potential of the atoms used as the harmonic media, in order to promote tunnel ionization [116]. For noble gases, this means that peak intensities $\geq 10^{14} \text{ W/cm}^2$ are necessary. We have seen in the previous section that the laser system discussed above is capable of producing peak intensities on this scale. In order to generate bright, coherent HHG beams, it is possible to match the phase velocity of the fundamental laser to that of the harmonic light to produce coherent buildup of HHG light along the optical axis. The “phase-

matching region” can be extended to long distances (several cm’s) through the use of hollow-core waveguides.

2.3.1 Three step model

Much theoretical work on the mechanism of HHG has been developed over the past 25 years. The process can be well understood semi-classically using the so-called 3-step model [117]. The 3-step model has also been extended to include fully quantum calculations [116]. Here we will restrict ourselves to a brief discussion of the semi-classical model for a noble gas. The three steps include tunneling ionization, acceleration of the electron, and electron recombination. For simplicity, we will at first only consider a single atom in the electric field of the laser pulse.

The first step in the model is tunnel ionization of the electron. With large electric field strengths due to the incident laser pulse, the Coulomb potential of the atom is significantly distorted, but not enough so that the electron is unbound (see Fig. 2.3 for an example in argon). This is the so-called tunneling ionization regime, which is the regime we will typically consider for HHG [117]. In this regime, the rate at which tunneling (or ionization) occurs was first calculated by Ammosov, Delone, and Krainov [145]. Hence, it is called the ADK rate, which we will come back to later.

The next step is the acceleration of the electron in the electric field of the laser. Here, the semi-classical picture simply describes the trajectory of the electron in the oscillating electric field of the laser, whereas the fully quantum picture calculates the wavefunction of the electron as a function of time. The diffusion of the wavepacket is proportional to the amount of time the electron spends in the electric field. The electron is first accelerated away from the parent ion (starting from rest), and when the field switches sign it is accelerated back towards the ion. Both the semi-classical picture and the quantum picture agree on the amount of kinetic energy that the electron can gain in the electric field of the laser before re-encountering the ion, and it is simply a function of the phase of the electric field at the time of the electron’s release. The maximum energy that can be gained is $3.17U_p$, where U_p is the ponderomotive potential of the laser field, which is

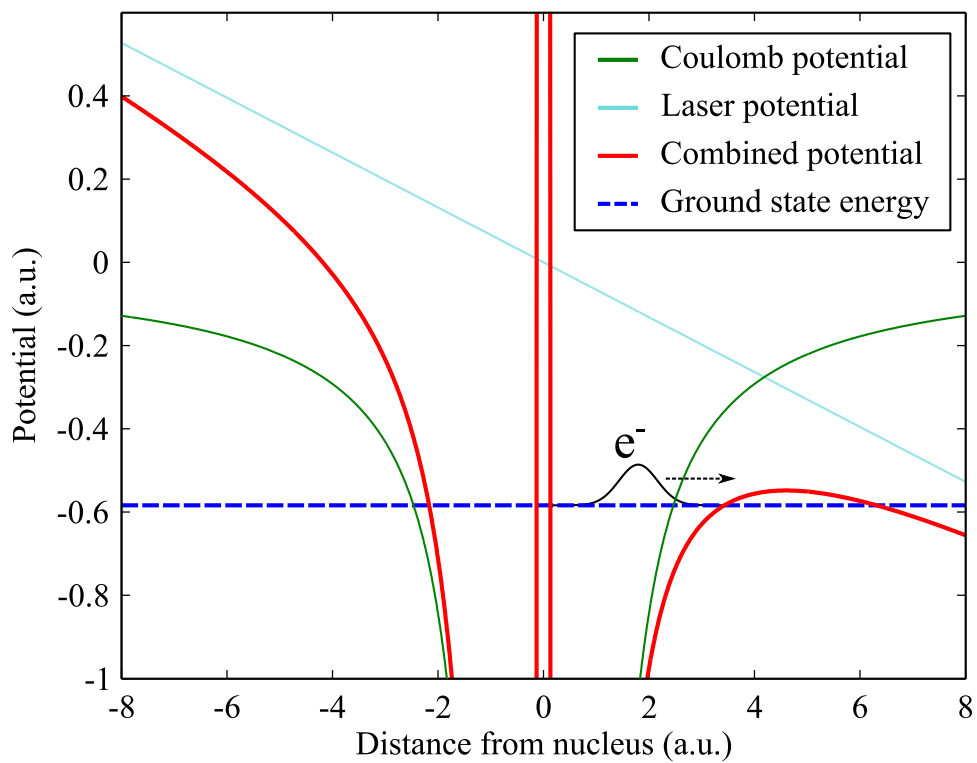


Figure 2.3: Tunnel ionization in argon. The laser has an intensity of $1.5 \times 10^{14} \text{ W/cm}^2$, resulting in a small barrier which is possible for the electron to tunnel through. The Coulomb potential for the outer shell of argon is based on [146].

defined as

$$U_p = \frac{e^2 \mathcal{E}^2}{4m_e \omega^2}. \quad (2.12)$$

This happens when the phase of the electric field is ≈ 0.3 radians at the time of ionization. Electrons having kinetic energy anywhere between 0 and $3.17U_p$ can re-encounter the ion. However, electrons which are ionized at laser phases of $\pi/2 < \phi < \pi$ and $3\pi/2 < \phi < 2\pi$ never re-encounter the ion.

Finally, when the laser re-encounters the ion, there is a chance of recombination with the emission of a photon. The probability for this recombination can be calculated through computation of the expectation value of the dipole transition between the free electron and the ground state of a bound electron. The emitted photon contains the energy that the electron gained due to acceleration in the laser field added to the ionization energy, I_p , of the atom. This leads to the familiar HHG cutoff rule, which states that the maximum photon energy, $h\nu_{\max}$, that can be generated for a given type of atom and laser parameters is given by

$$h\nu_{\max} \approx I_p + 3.17U_p. \quad (2.13)$$

Single ionization energies for the noble gases are listed in Table 2.1. If we assume the harmonics are being generated in a waveguide of inner radius a , the cutoff rule can be rewritten in terms of commonly quoted experimental parameters as

$$h\nu_{\max} \approx I_p + 32.84 \frac{E_p \lambda^2}{\tau a^2}, \quad (2.14)$$

where the cutoff energy, $h\nu_{\max}$, and ionization potential, I_p , are in eV, the pulse energy, E_p , is in mJ, the wavelength, λ , is in nm, the pulse duration, τ , is in fs, and the waveguide radius, a , is in μm . For example, the laser system discussed in Section 2.2, when coupled into a 150 μm diameter waveguide filled with helium, would have a HHG photon energy cutoff of ≈ 230 eV (assuming 70% coupling efficiency).

2.3.2 HHG phase matching

As mentioned above, phase matching the HHG process is extremely important in order to generate bright, coherent EUV and X-ray beams. If the process were to occur in vacuum, the

Element	I_p (eV)
He	24.59
Ne	21.56
Ar	15.76
Kr	14.00
Xe	12.13

Table 2.1: Ionization energies of the noble gases, given in units of eV.

phase velocity of light of any wavelength would be $c = 3 \times 10^8$ m/s. However, in the presence of the gas media and electron plasma there is a significant amount of dispersion. With use of hollow-core waveguides, the beam can be confined to a small area (and hence stay at near-constant high peak intensity) over a much longer distance than in a typical focusing geometry; the waveguide confinement adds an additional term to the dispersion.

Phase-matching is a technique which is borrowed from traditional nonlinear optics and here applied to extreme nonlinear optics [147]. While the HHG process is fundamentally different than, for instance, sum and difference frequency generation which occurs in traditional nonlinear optics, the idea behind phase matching is the same. The goal is to have the harmonic light build up coherently across the entire interaction distance, which will only occur if light generated at one distance along the optical axis is in phase with light generated at any other position along the optical axis. The key to phase matching is to match the phase velocities of two (or more) wavelengths of light. The phase velocity can be defined simply as ω/k , where ω is the angular frequency and k is the magnitude of the wavevector along the direction of propagation. This means that in order to phase-match HHG we simply require the following equality:

$$\frac{\omega_f}{k_f} = \frac{\omega_q}{k_q} = \frac{q\omega_f}{k_q}, \quad (2.15)$$

where f refers to the fundamental laser and q refers to the harmonic number. We have used the simple relation that in the case of harmonic generation, $\omega_q = q\omega_f$. Thus it is clear that for true phase-matching to occur, we require that

$$\Delta k = qk_f - k_q = 0. \quad (2.16)$$

Δk is referred to as the phase mismatch. It is convenient to define a “coherence length” as $L_c = \pi/\Delta k$. The following simple model can further illustrate the importance of phase-matching. In the presence of absorption, the on-axis intensity of the HHG beam in the far field is shown to be proportional to [119, 148]:

$$I_q \propto L_a^2 \frac{1 + \exp(-L_i/L_a) - 2 \exp(-L_i/2L_a) \cos(\pi L_i/L_c)}{(2\pi L_a/L_c)^2 + 1}, \quad (2.17)$$

where L_a is the (1/e intensity) absorption length, L_i is the length of the interaction medium, and L_c is the coherence length. The on-axis intensity as a function of L_i is plotted in Fig. 2.4, showing how the coherence length and absorption length tend to limit the intensity. Note that in order to achieve maximum intensity, the medium length must be several absorption lengths long, and the coherence length must be much longer than the absorption length.

Eq. (2.17) has three interesting limiting cases. In the case where the coherence length is long, $L_c \rightarrow \infty$, the expression for the intensity becomes

$$\lim_{L_c \rightarrow \infty} I_q \propto L_a^2 [1 + \exp(-L_i/L_a) - 2 \exp(-L_i/2L_a)], \quad (2.18)$$

so that with long enough interaction lengths ($L_i \gtrsim 10L_a$) the intensity saturates at a level proportional to the square of the absorption length. The next interesting limiting case is the case where there is no absorption, that is $L_a \rightarrow \infty$. Now Eq. (2.17) reduces to

$$\lim_{L_a \rightarrow \infty} I_q \propto \left[\frac{L_c}{\pi} \sin\left(\frac{\pi L_i}{2L_c}\right) \right]^2. \quad (2.19)$$

Thus it can be seen that in the case of no absorption the output intensity has an oscillatory dependence on the interaction length, with a maximum yield proportional to the square of the coherence length. The final limiting case is the ideal situation in which there is no absorption and perfect phase-matching can be achieved. In this case, the intensity at the output of the waveguide is simply

$$\lim_{L_a, L_c \rightarrow \infty} I_q(L_i) \propto L_i^2. \quad (2.20)$$

This final simplified case is appropriate to use when the interaction length is kept shorter than both the coherence and absorption lengths. Since the absorption is typically not under experimental

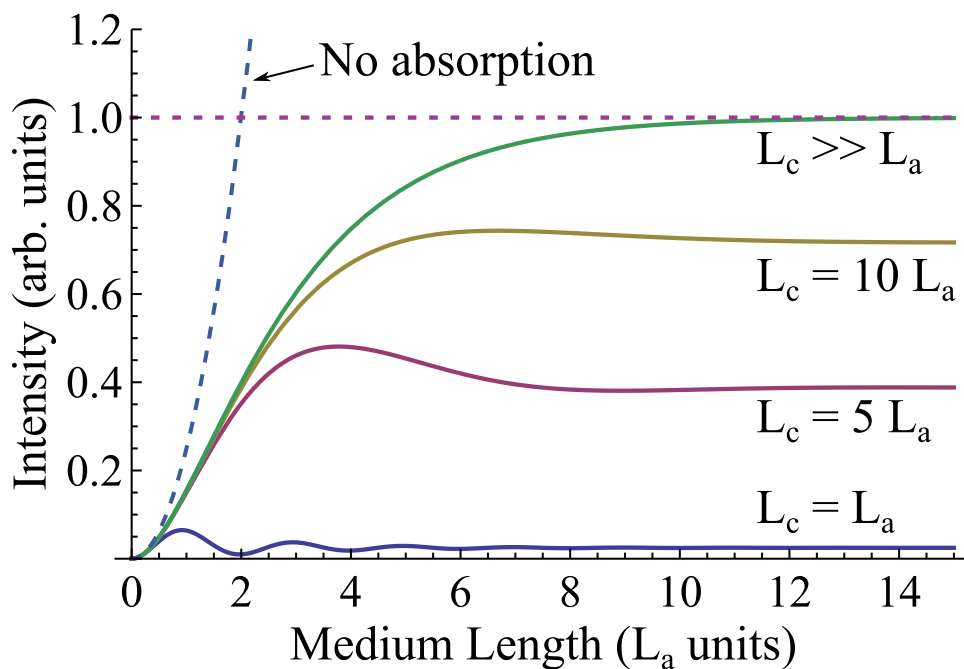


Figure 2.4: On-axis intensity in the case of absorption-limited phase matching, based on Eq. (2.17). Phase-matched growth in the absence of absorption is shown for reference. Note that oscillations as a function of medium length due to finite coherence length disappear for the most part when $L_c > L_a$. However, as shown above, the maximum absorption-limited intensity is only obtained when $L_c \gg L_a$. Figure adapted from [148].

control, it is advantageous to find ways to extend the coherence length to be as long as possible in order to achieve the greatest harmonic yield. Additionally, because the absorption length places a limit on the maximum phase-matched intensity that can be achieved, total power in a harmonic can be increased by use of larger cross-sectional areas. However, in order to generate harmonics efficiently, the peak power of the fundamental laser needs to scale linearly with the cross-sectional area.

With the importance of achieving long coherence lengths, or in other words very good phase-matching, demonstrated above, it is important to understand how phase matching can be achieved. For the most part, this means understanding the various contributions to the index of refraction at the fundamental wavelength and at the q_{th} harmonic. However, when the fundamental beam is confined to a waveguide, there is an additional contribution to the phase velocity as a function of waveguide mode [149]. Here we will assume that the harmonics are generated from a beam that is coupled to the fundamental mode (EH_{11}), of the waveguide. The phase mismatch, Δk , for the q_{th} harmonic can be written as [119, 150]

$$\Delta k \approx q \frac{u_{11}^2 \lambda_0}{4\pi a^2} - qP(1 - \eta) \frac{2\pi}{\lambda_0} (\Delta\delta + n_2) + qP\eta N_a r_e \lambda_0, \quad (2.21)$$

where u_{11} is the first zero of the Bessel J_0 function, λ_0 is the fundamental laser wavelength, a is the waveguide radius, P is the pressure in atmospheres, $\Delta\delta$ is the difference in index of refraction of the neutral gas at the fundamental and harmonic wavelengths, η is the ionization fraction, N_a is the number density of the gas at one atmosphere, and r_e is the classical electron radius. The mismatch is mostly a function of the index of refraction for the fundamental laser; the harmonics propagate at a phase velocity very close to the speed of light in vacuum [118].

From Eq. (2.21) it is clear that the gas pressure provides an convenient experimental tuning parameter in order to achieve phase-matching. Specifically, with no ionization it is clear that there is a specific pressure, depending on the gas species, that will compensate for the waveguide dispersion. As the ionization level increases (due to larger pulse energies and intensities), the pressure necessary to phase-match increases as well. The phase matching pressure can be calculated by solving for

$\Delta k = 0$, and is given approximately by

$$P \approx \frac{u_{11}^2 \lambda_0^2}{4\pi a^2 (2\pi \Delta\delta - \eta N_a r_e \lambda_0^2)}. \quad (2.22)$$

From Eq. (2.22) it can be seen that there is a critical ionization fraction beyond which no amount of pressure increase can achieve phase matching. This effect is reduced somewhat due to the fact that most of the ionization is highest on the optical axis, and the way that the fiber mode propagates results in a modal averaging of the ionization across the spatial distribution of the EH_{11} mode. This means that ionization fractions $\approx 5\times$ higher than the critical ionization level can exist on the optical axis. It is interesting to note the phase-matching pressure dependence on waveguide radius; the harmonics can be phase-matched at a lower pressure for a given ionization fraction, meaning the absorption length, L_a , is extended. As mentioned before, the required pulse energy to generate a given harmonic increases with the cross-sectional area of the waveguide. However, the quadratic scaling of the output with absorption length suggests that this approach can lead to increased harmonic yield [151–153].

2.3.3 Experimental parameters for HHG phase matching

From the understanding of the HHG process gained above, it is useful to get an idea of the required experimental parameters for phase-matched harmonic generation. In the following, we will briefly describe the required conditions for phase matching 29 nm and 13 nm HHG light. Here we will make the assumption that we wish to reach the effective critical ionization level at the temporal and spatial peak of the pulse, so that the single atom yield is maximized but the process can still be macroscopically phase-matched. We will also assume the use of a hollow-core waveguide with an inner diameter of 150 μm , and we will assume 70% coupling efficiency into the lowest order mode.

We saw in Eq. 2.22 that there is a critical ionization level above which phase matching is no longer possible. In addition, we noted that the relevant parameter is the modally averaged ionization level across the EH_{11} mode of the waveguide. In order to calculate this from Eq. 2.22, we need to know the value of $\Delta\delta$ at these two wavelengths. This depends mostly on the neutral gas

dispersion of the gas media at 800 nm, with the contribution from the dispersion at the harmonic wavelength approximately an order of magnitude smaller. For argon at 29 nm, $\Delta\delta_{\text{Ar}} = 3.7 \times 10^{-4}$, and for helium at 13 nm, $\Delta\delta_{\text{He}} = 3.9 \times 10^{-5}$. These values lead to a critical ionization for phase matching of 29 nm in argon of $\approx 5\%$, and a critical ionization for phase matching of 13 nm in helium of $\approx 0.5\%$.

In order to find out what peak intensities we can handle in these two situations before the ionization level is too high for phase-matching, we can use the ADK rates mentioned earlier. If we assume a 25 fs transform-limited pulse at 800 nm, we find that the modally averaged ionization level crosses the critical threshold at the peak of the pulse for peak intensities of $\approx 2.3 \times 10^{14}$ W/cm² in argon, and $\approx 8.5 \times 10^{14}$ W/cm² in helium. In a 150 μm diameter fiber, these peak intensities require pulse energies of 420 μJ and 1.5 mJ, respectively, assuming 70% coupling efficiency into the lowest order mode. At higher pulse energies, phase matching can only be achieved on the leading edge of the pulse. Waveguides with larger diameter can accommodate higher pulse energies, with pulse energy scaling linearly with cross-sectional area.

Based on the peak intensities calculated above in combination with ADK rate calculations, it is interesting to estimate the width of the harmonic beam radius inside the waveguide. This estimate can be made if we assume that the number of emitting atoms is simply proportional to the ionization rate (as a function of time and of the distance from the optical axis), and that the electric field of a given harmonic is proportional to the number of emitters. This type of analysis predicts a Gaussian beam radius of $\approx 20 \mu\text{m}$ when using a 150 μm diameter fiber with peak intensities as calculated above [118], at both 29 nm and 13 nm wavelength. This is consistent with the usual assumption that HHG follows an approximately fifth-order nonlinear field dependence nearly independent of harmonic number [154].

2.4 Complete control of the HHG driving laser

As we have seen in the previous section, extreme nonlinear optics can be used to convert the output of an ultrafast amplifier system to coherent, short-wavelength beams in the HHG process.

However, typical CPA systems are not necessarily fully optimized for use with HHG. In order to achieve the shortest pulse durations, it can be necessary to add a component to the system called a pulse shaper, which is discussed next in Section 2.4.1. Additionally, the stability of an HHG source depends critically on the stability of the fundamental laser. Any pointing or intensity instability of the fundamental laser (typically drift or oscillation) is mapped directly onto the HHG source. Even worse, because HHG is a nonlinear process these instabilities are magnified nonlinearly. First steps towards improving pointing stability of compact CPA systems are discussed in Section 2.4.2.

2.4.1 Pulse shaping for temporal control

In order to achieve phase-matching at the highest possible photon energies, it is important to have short, transform-limited pulse durations [155]. The amplifier systems described in Section 2.2, even when aligned perfectly, typically have 4th-order (and higher) dispersion. In order to achieve transform-limited pulse durations, this extra spectral phase must be compensated for by the insertion of a device called a pulse shaper [156]. While it can be possible to shape pulses in the time domain, for ultrashort pulses it is usually easier to shape them in the spectral domain.

The effect of spectral phase on the time-domain characteristics of the pulse can be understood through the Fourier-transform relationship between the time and frequency domains. From an experimental point of view, it is easier to measure the frequency-domain characteristics of an ultrashort pulse. If the spectral components of the pulse do not all line up in phase, then the frequency-domain representation of the pulse can be written as

$$\tilde{E}(\omega) = \sqrt{\frac{2I(\omega)}{c\epsilon_0}} \exp\left(i\tilde{\phi}(\omega)\right), \quad (2.23)$$

where $I(\omega)$ is proportional to the power spectral density of the pulse and $\tilde{\phi}(\omega)$ is the spectral phase function. $I(\omega)$ can be easily measured with a spectrometer. The spectral phase is typically smoothly varying. For this reason, it can be convenient to expand $\tilde{\phi}(\omega)$ in a Taylor series, so that Eq. (2.23) can be rewritten as

$$\tilde{E} = \sqrt{\frac{2I(\omega)}{c\epsilon_0}} \prod_{n=2}^{\infty} \exp\left(\frac{\tilde{\phi}^{(n)}(\omega_0)}{n!} (\omega - \omega_0)^n\right), \quad (2.24)$$

where $\tilde{\phi}^{(n)}(\omega_0)$ is the n th derivative of $\tilde{\phi}$ evaluated at the central frequency, ω_0 . The first two terms in the series have been omitted, since a constant phase has no effect, and a linear phase simply serves to shift the pulse in time, with no effect on the temporal shape of the pulse. The time-domain characteristics of this pulse can be calculated through an inverse Fourier transform, so that

$$E(t) = \mathcal{F}^{-1} \left\{ \left| \tilde{E}(\omega) \right| \tilde{\Phi}(\omega) \right\} \quad (2.25)$$

where for simplicity the product in Eq. (2.24) is represented by $\tilde{\Phi}(\omega)$. From the convolution theorem, we can see that in the time domain, the electric field of the pulse is a convolution between a transform-limited pulse which is a function of the spectral weights with a function that depends on the spectral phase. This can be written as

$$E(t) = E_{\text{T.L.}}(t) * \Phi(t) \quad (2.26)$$

where $E_{\text{T.L.}}(t)$ represents a transform-limited pulse, and $\Phi(t) = \mathcal{F}^{-1}\{\tilde{\Phi}(\omega)\}$. Since a transform-limited pulse is the shortest possible pulse that can be generated with a given spectrum, any spectral phase function with more than constant and linear terms will produce a spreading of the pulse in the time domain, from Eq. (2.26). Any time the pulse travels through any material that has non-zero dispersion (even air for broad enough spectral bandwidths), this temporal spreading will occur. With grating-based pulse stretchers and compressors it is possible to compensate for up to third-order group delay, which is proportional to the 4th derivative of $\tilde{\phi}$ evaluated at ω_0 [142]. However, for higher-order dispersion compensation it is in general necessary to use other means.

2.4.1.1 Pulse shaper design

As mentioned above, for ultrashort pulses it is usually only possible to achieve transform-limited pulses using frequency-domain pulse shaping. The simplest way of accomplishing this is to spatially disperse the pulse into its constituent colors, apply a spatially-dependent phase retardation on the dispersed pulse, and then spatially recombine the colors back into one beam. What the previous sentence describes is exactly what happens in a pulse stretcher [143], with the

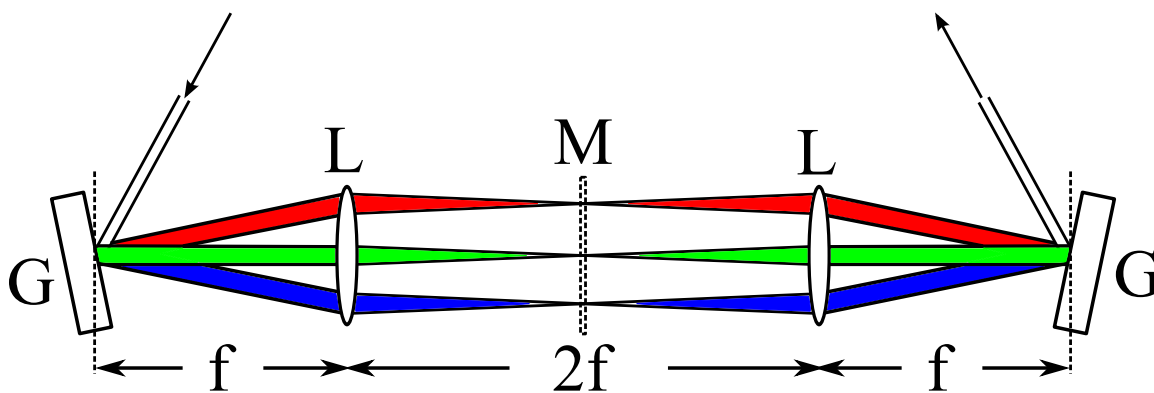


Figure 2.5: Schematic of a zero-dispersion stretcher used as a frequency-domain pulse shaper. As shown, the two lenses, L, have the same focal length, and the two gratings, G, have identical groove spacing. The phase mask M is placed at the Fourier plane of the telescope. The arrows indicate direction of beam propagation. The red, green and blue colors represent the low, middle, and high frequency ranges of the laser spectrum. Figure adapted from [159].

exception that a phase mask can be placed in the Fourier plane of the telescope in order to modify the spectral phase of each color individually. The gratings can then be placed in the zero-dispersion configuration so that the only spectral phase modification occurs due to the phase mask [157,158]. A schematic of this type of apparatus is shown in Fig. 2.5.

The phase masks are often made with liquid crystal spatial light modulators (SLMs). The optical path length through the liquid crystal can be modulated by application of an electric field produced by a series of electrodes, which are typically oriented in an array, forming pixels [160]. If a mirror is placed behind the phase mask in Fig. 2.5, the optical system can be folded in order to improve ease of alignment, make the system more compact, and reduce cost of components. In this folded geometry deformable mirrors have also been used in place of phase masks [161]. A 3D perspective view of such a folded system is shown in Fig. 2.6, with the telescope lens replaced with a spherical mirror at normal incidence.

The pulse shaper design shown in Fig. 2.6 was analyzed using optical design software (Zemax 12). The focal length for mirror M2 was 10 cm, and the grating, G, had 1200 lines/mm. When aligned properly, the output displayed some spectrally-dependent astigmatism. However, as shown in Fig. 2.7, when the input beam was collimated to 2.5 mm diameter, the focus size was very close

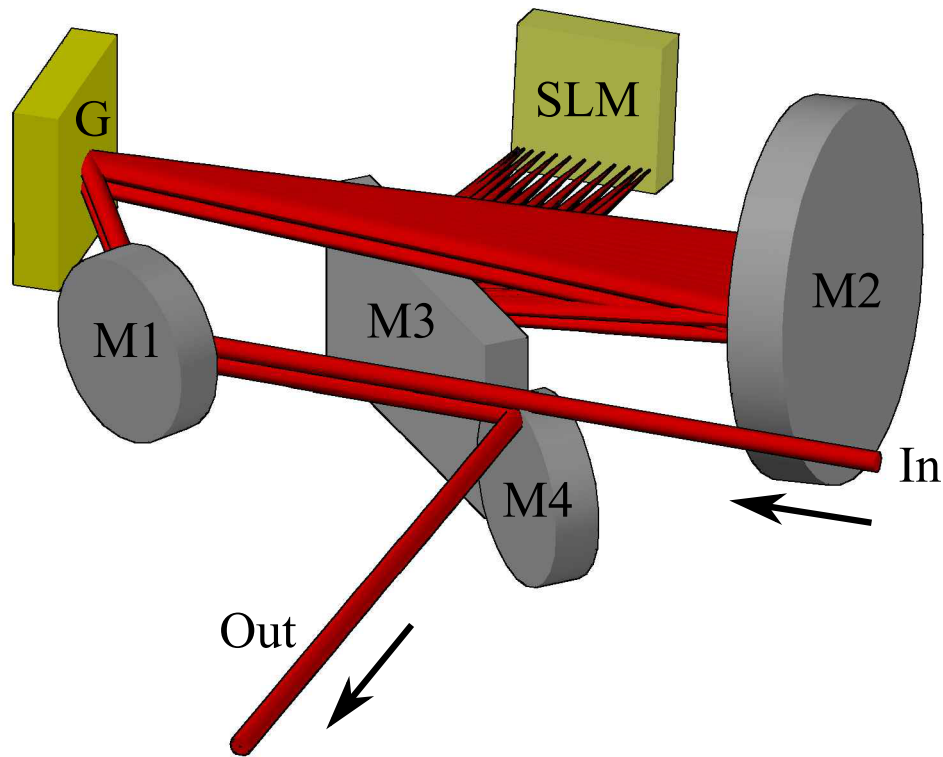


Figure 2.6: Schematic of a folded geometry, SLM-based pulse shaper. The optical path is essentially identical to that described in Fig. 2.5, except that it is made more compact. The beam first travels to M1, and subsequently diffracts from a grating, G. The spectrum is then collimated with a curved mirror, M2, with focal length f , placed a distance f from the grating. Upon reflection from M2 (which is tilted slightly downwards), the spectrum is collimated, while each individual spectral component is focused towards M3. M3 is simply a fold mirror which redirects the spatially dispersed beam towards the SLM. Each spectral component is focused at the plane of the SLM, which is placed in such a way that the optical path length from M2 to the SLM is the focal length, f . A mirror is integrated behind the liquid crystal array of the SLM, so that the beam backtracks its way through the system, with the SLM tilted in such a way that the beam comes out of the system a full beam diameter below the input. The output is then separated from the input at the output mirror, M4.

to diffraction-limited, meaning the astigmatism is only a small effect.

The spectral phase introduced by this pulse shaper design was also calculated using the Zemax model of the system. Minimizing the added spectral phase was the motivation behind using a spherical mirror rather than a lens in this design. The calculated spectral phase as a function of wavelength is shown in Fig. 2.8. Note that across a 150 nm bandwidth, the added spectral phase is less than 1 radian. While the SLM in principle could compensate for spectral phase added due to the passive components of the pulse shaper, the fact that the added spectral phase is small allows for a larger dynamic range of compensation for other sources of dispersion.

2.4.1.2 Experimental implementation

After the Zemax model exhibited good spatial and temporal characteristics for this pulse shaper design, a device was built based on this design for insertion into the amplifier system described in Section 2.2. The SLM used as the phase mask was a 1D array of 12,288 liquid crystal pixels (Boulder Nonlinear Systems Model P12,288), enabling the application of very smooth phase functions with a large possible dynamic range of phase compensation. Large dynamic range is enabled by wrapping the desired phase modulo 2π [159]. The SLM has width 20 mm, so that with the optical design mentioned above (grating with 1200 grooves/mm, 10 cm focal length curved mirror), this pulse shaper can support a bandwidth > 150 nm. The pulse shaper device was placed in the amplifier system directly before the stretcher component (see Fig. 2.2). It is important that this device is placed before the amplification step for two reasons. First, the overall power efficiency is $\approx 60\%$, due to finite reflectivities and diffraction efficiencies. Assuming the oscillator power output is > 450 mW, this efficiency does not reduce the power output of the amplifier. Second, the SLM has a damage threshold well below what would be required if the amplified pulse were sent through the pulse shaper.

In principle, it is possible to measure the spectral phase of the amplifier output using a technique such as frequency resolved optical gating (FROG) [162] and apply the opposite phase on the SLM. However, in practice this is can be a difficult task due to necessary calibration of the

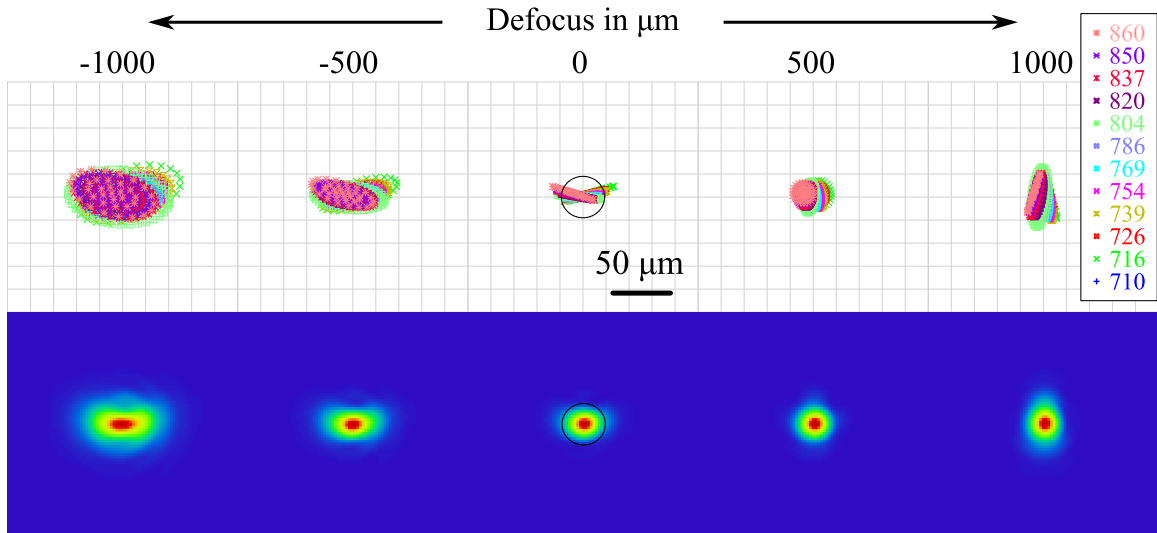


Figure 2.7: The output of the pulse shaper shown in Fig. 2.6 was focused in simulation using Zemax optical design software. A collimated Gaussian beam with 2.5 mm diameter was used as an input to the simulation. The top panels show ray traces as a function of wavelength for 5 positions surrounding the focus. The ray traces show that the pulse shaper adds spectrally-dependent astigmatism. The circle in the panel displaying the rays for zero defocus has diameter of a diffraction-limited Airy radius. The bottom panels are shown on the same scale as the top, and display the spatial beam profiles when the contributions from each wavelength are summed incoherently. Note that the beam profile in focus is near-diffraction-limited. The wavelengths shown in the legend have units of nm.

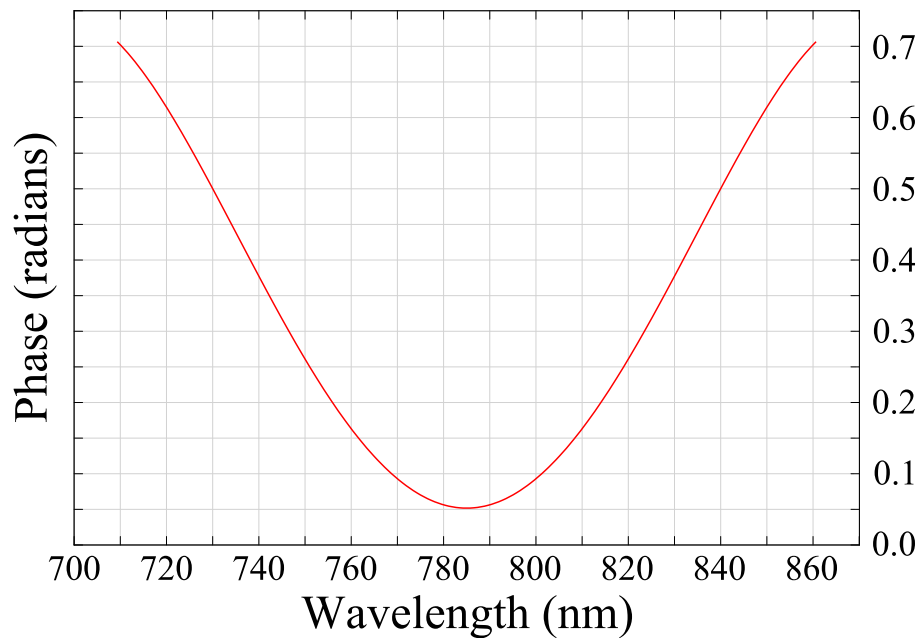


Figure 2.8: Spectral phase introduced by the pulse shaper design shown in Fig. 2.6. The spectral phase was calculated using a Zemax model of the pulse shaper.

spectrum on the SLM, etc. Fortunately, a variety of techniques have been developed which allow one to retrieve the necessary phase to apply in order to achieve transform-limited pulses. These techniques generally rely on some type of nonlinear response similar to that required by FROG techniques, usually through detecting a second harmonic generation (SHG) signal. Assuming the pulse energy stays constant, a flatter spectral phase will always result in higher SHG conversion efficiency [163, 164]. Techniques that have proven to be capable of producing transform-limited pulses include global optimization, for instance genetic algorithms [161, 165], other iterative procedures [166], and direct phase retrieval [167].

Here we have used an iterative procedure known as the freezing phase algorithm (FPA) [166, 168] in order to produce mJ-level transform-limited pulses at 5 kHz repetition rate. The FPA optimizes the phase of each spectral component individually, in relation to the spectral phase of all the other spectral components. The algorithm steps from one spectral component to the next. After every spectral component has been adjusted, the process is repeated a desired number of times. This approach is theoretically guaranteed to always move closer to a transform-limited pulse [166], thus asymptotically approaching the solution. However, there is no guarantee that a set number of iterations will produce the desired accuracy. Nevertheless, simulations and experiments have shown that typically only 3 iterations across the full spectrum are required in order to achieve an accuracy on the level of the phase resolution. The advantage of FPA over a genetic algorithm is that there are no parameters which must be optimized.

The experimental procedure for pulse optimization is as follows. A small portion of the amplifier output is reflected from a wedged window placed near Brewster's angle. The beam is focused (with a spherical mirror rather than lens in order to avoid dispersion) onto a photodiode with wavelength range 150 – 550 nm (Thorlabs PDA25K). The wavelength range of the amplifier output is restricted to 720 – 850 nm, so that only two-photon absorption produces a signal [169]. The two-photon photodiode is used in place of an SHG signal, to reduce measurement complexity. The photodiode signal is measured using an oscilloscope (Tektronix TDS3032) and sent into a computer that also interfaces with the SLM. A typical result of the pulse improvement achieved

after running the FPA is shown in Fig. 2.9. While the pulse is near-transform-limited to begin with (see Fig. 2.9(a)-(c)), the optimized pulse shows significant improvement (Fig. 2.9(d)-(f)). The FWHM time-bandwidth product of the optimized pulse is 0.52, very close to the Gaussian limit of 0.44.

2.4.1.3 Future directions

There is some evidence that HHG can be optimized in the presence of non-zero spectral phase [165,170,171]. However, this optimization has only been demonstrated with pulse durations < 20 fs. With the use of cryo-cooled Ti:sapphire amplifier crystals for high average power, this is a difficult criteria to meet. However, the results obtained by Pfeifer et al. made use of spectral broadening due to self phase modulation (SPM) in argon to achieve 13 fs pulse duration [171]. In their case, the pulse shaper made use of a high-damage threshold deformable mirror, and was inserted into the system after amplification and spectral broadening. Pursuit of HHG optimization with the pulse shaper described here using ≈ 20 fs pulses is a potential future endeavor.

2.4.2 Beam pointing stabilization for stable HHG sources

While compact compared to large laser facilities, the CPA systems described in Section 2.2 are large and complex enough that the beam pointing and average power of the output can be very sensitive to vibrations and thermal drift. However, many experimental techniques rely on the laser source to have stable pointing and average power. In many cases the passive stability of these complex laser systems is not good enough, leading to artifacts in experimental data as well as setting a time limit on certain experiments.

For continuous-wave (cw) laser systems, fast feedback circuits have been developed for beam pointing stabilization using quadrant photodiodes (QPDs) or position sensitive detectors (PSDs) for position detection and piezo-actuated mirrors for position adjustment [172]. With two detectors and two mirrors (two separate feedback loops), both the position and angle of the laser beam can be stabilized at all positions along the beam axis. The difficulty with ultrafast kHz lasers is that

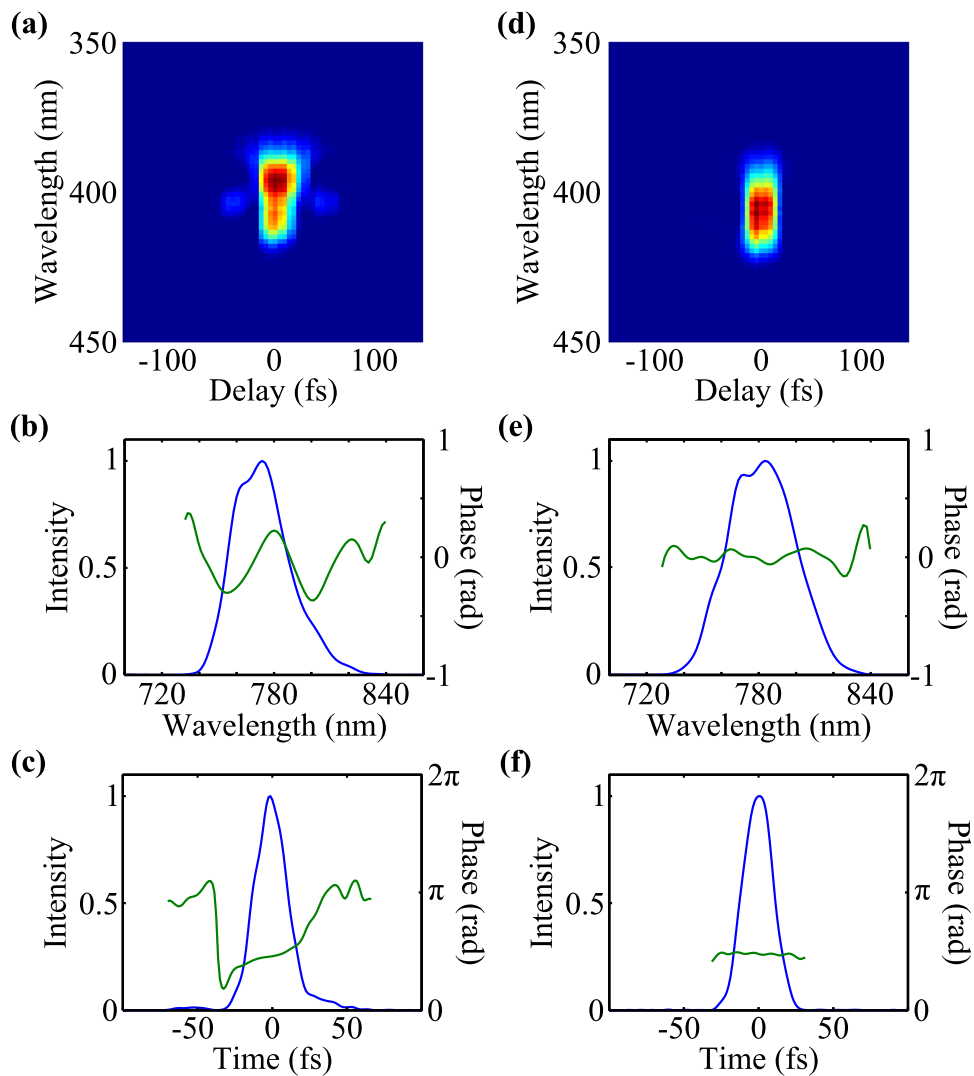


Figure 2.9: Comparison between amplified pulse with and without the pulse shaper. (a) Measured SHG-FROG intensity with the pulse shaper turned off. (b) Retrieved spectral intensity (blue) and phase (green). (c) Retrieved time-domain intensity (blue) and phase (green). (d)-(f) are the same as (a)-(c) except with the pulse shaper turned on. Note that while both pulses in (c) and (f) have duration ≈ 25 fs FWHM, the pulse in (f) has 10% higher peak intensity than (c) for a given pulse energy.

the duty cycle of the pulsetrain is extremely small; if an analog system is to be used for position feedback, a triggered sample and hold circuit must be inserted into the feedback loop. This type of analog system has been previously demonstrated on a kHz laser system, but with only a single mirror and single detector for stabilization of the focus position but not the focus angle [173–175]. Other work has shown that analog feedback systems using a “quasi-cw” oscillator beam collinear with the low-rep rate amplified beam can be measured and stabilized in order to stabilize the pointing of the amplified beam [176]. However, this type of system represents a non-trivial modification to the amplifier system and requires careful alignment to ensure collinearity, in addition to requiring the assumption that the beams stay collinear over time.

A third option for kHz beam pointing stabilization is to use a digital feedback loop, using charge-coupled devices (CCDs) or QPDs for position detection, piezo-actuated mirrors for position correction, and a desktop computer (PC) to close the feedback loop [177–179]. For this type of feedback system, the feedback bandwidth is limited by the relatively low sampling rate of the CCDs, which is typically < 30 Hz. However, the use of CCDs offers several advantages. First, the exposure time can be set to integrate over several laser shots, meaning that there is never a lack of signal. Second, the beam is measured across many pixels, in principle allowing a more accurate calculation of the centroid. Finally, the direct image of the beam can be used for additional beam diagnostics.

Previous implementations of two-detector, two-mirror systems have separated the system into two independent feedback loops. In this case, there are restrictions placed on the possible geometry that can be used. Essentially, the first detector must image the beam position at the second mirror, while the second detector can image the beam position anywhere beyond the second mirror. Here we propose a more general geometry using a digital feedback system, in which the two detectors may be placed at any positions beyond the second mirror position, as long as they are independent. The advantage here is that the detectors can both be placed near the experiment, where the beam stability is most critical. In the following, we will describe the geometry of the feedback system in detail, describe how it is implemented, and compare experimental results to

theoretical performance. Finally, we apply this system to stabilize the driving laser of a high harmonic generation (HHG) source [31], and demonstrate improved intensity and pointing stability of the HHG source as a result.

2.4.2.1 Feedback Geometry

The geometry used for the active pointing feedback is shown in Fig. 2.10. The feedback loop consists of two piezo-actuated mirrors (Thorlabs KC1-PZ mirror mounts with MDT693B piezo controllers) and two CCD detectors (Mightex CGE-B013-U). One piezo-actuated mirror is placed near the amplifier output, while the second is placed directly in front of a lens (here used for coupling into a HHG waveguide). The two mirrors are approximately 2 meters apart. The large distance between the mirrors allows their movements to be decoupled. Intuitively, the first mirror controls the position of the beam on the lens, while the second mirror controls the angle of the beam on the lens.

The transmitted beam through a 99/1 beamsplitter is used for position detection. One detector is placed at the focus, and the other is placed as far past the focus as possible while keeping the beam size small enough to fit completely on the detector. In our case, this corresponds to a 25 cm separation distance between the two detectors. The detectors are externally triggered so that each exposure measures the same number of laser pulses. The horizontal and vertical centroids are monitored at both detector positions at a frame rate of 15-20 Hz, which is functionally equivalent to a measurement of the position and angle of the beam at the focus. While the coupling efficiencies into the waveguide modes are most highly sensitive to beam position at the waveguide entrance, the non-negligible sensitivity to beam input angle necessitates the use of two mirrors and two detectors (see supplementary information for further discussion of waveguide mode sensitivity to position and angle). The centroids are calculated after first subtracting 10% of the maximum value, and setting all pixels less than zero to zero. This measure reduces the influence of detector read noise and beam intensity fluctuations on the centroid calculation.

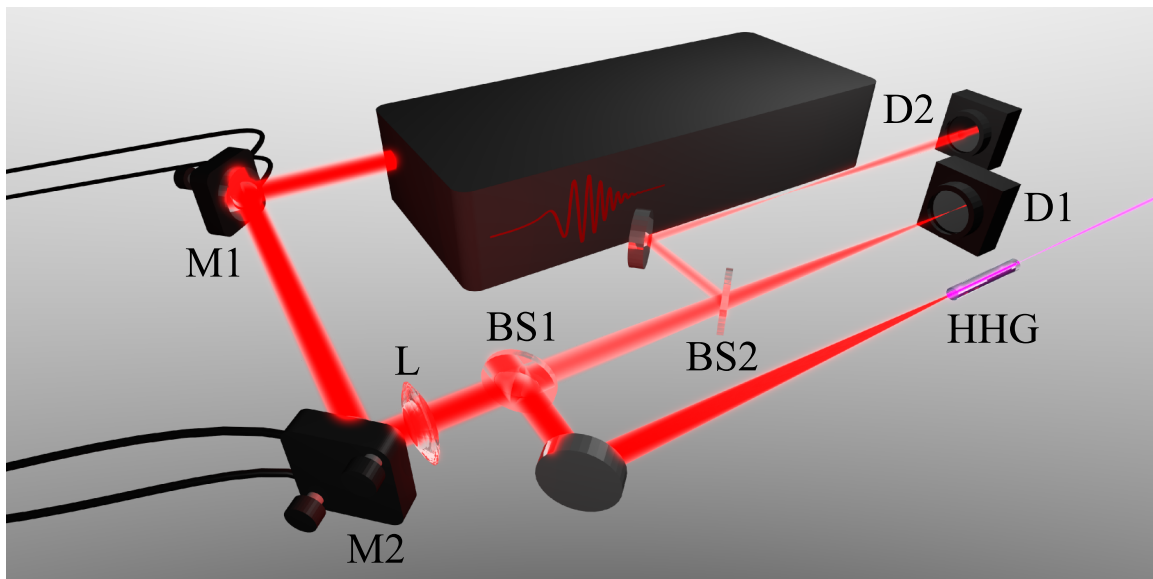


Figure 2.10: Geometry for active feedback. One piezo-actuated mirror (M1) is placed directly at the output of the amplifier system, and the second piezo-actuated mirror (M2) is placed directly before the lens (L) used to couple into a waveguide (HHG). The beam transmitted through a 99/1 beamsplitter (BS1) is used to detect the beam position: this beam is split with a 50/50 beamsplitter (BS2) in order to monitor the beam at both the focus (detector D1) and beyond the focus (detector D2). The feedback loop is implemented on a PC using a custom-written program.

2.4.2.2 Implementation

The feedback loop is closed by a custom PC program which interfaces with the CCD detectors as well as the mirror controllers. The system is treated as a linear system of equations. The four centroid deviations from four target positions are treated as a vector $\delta\vec{X}$, and the changes in applied piezo voltage required to move the beam back to the target position are treated as a vector $\delta\vec{V}$. The system of equations is defined by the matrix A , where

$$\delta\vec{V} = -A \delta\vec{X}. \quad (2.27)$$

While knowledge of all relevant distances between mirrors, detectors and lens would allow direct calculation of A , in practice A is calculated through a calibration routine. The four centroid changes $\delta\vec{X}$ are measured in response to independent movement of each mirror axis. Assuming A is invertible, this measurement populates the columns of A^{-1} one at a time, through the equation

$$\delta\vec{X} = -A^{-1} \delta\vec{V}. \quad (2.28)$$

It is straightforward to show that the invertibility criterion is met as long as the two piezo mirrors are positioned at different points along the beam axis and as long as the two detectors measure different points along the beam axis.

The voltages $\delta\vec{V}$, calculated using Eqn. (2.27), are treated as the error signal in a digital proportional integral (PI) controller implemented in the software program. The PI controller is discretized using the bilinear transform [180], so that the voltage output obeys the following difference equation:

$$\vec{V}_{out}[t] = \vec{V}_{out}[t - \tau] + \left(k_p + \frac{k_i}{2}\right) \delta\vec{V}[t] + \left(-k_p + \frac{k_i}{2}\right) \delta\vec{V}[t - \tau], \quad (2.29)$$

where \vec{V}_{out} is the applied voltage to the piezo mounts, $\delta\vec{V}$ is the error signal calculated from Eqn. (2.27), k_p is the proportional gain, k_i is the integral gain, t is the current time, and τ is the sampling period. The proportional and integral gains are chosen empirically to be as high as possible without introducing instability or degrading short-term stability.

The Z-transform can be applied to Eqn. (2.29) to yield the open-loop transfer function of the feedback system (assuming the piezo mirror response is unity at all relevant frequencies). The result is

$$H(z) = \frac{2k_p(1 - z^{-1}) + k_i(1 + z^{-1})}{2(1 - z^{-1})}, \quad (2.30)$$

where $H(z)$ is the open-loop gain and z is a complex number. The frequency response can be obtained by evaluating z on the unit circle. From the open-loop gain we can define the closed-loop sensitivity as

$$S(z) = \frac{1}{1 + H(z)} \quad (2.31)$$

and the closed-loop complementary sensitivity as

$$CS(z) = \frac{H(z)}{1 + H(z)}. \quad (2.32)$$

The sensitivity is the closed-loop gain on any disturbance to the system (beam drift/oscillation) and the complementary sensitivity is the closed-loop gain on the setpoint (target centroid positions) as well as on any measurement noise (centroid measurements).

2.4.2.3 Results

The performance of the feedback system was tested on the 5 kHz, 2 mJ, 22 femtosecond Ti:sapphire amplifier system described in Section 2.2. In order to fully characterize the system, the beam centroids were monitored on two additional out-of-loop detectors simultaneously with the in-loop detectors. In order to compare the actual performance to the theoretical performance of the PI controller, centroids were monitored with the feedback system both locked and unlocked for several hours in each case.

The short- and long-term stability improvements can be seen immediately by inspection of the raw centroid angle measurements. The beam angles were calculated as

$$\theta_i(z_1) \approx \frac{C_i(z_2) - C_i(z_1)}{z_2 - z_1} \quad (2.33)$$

	Unlocked (in-loop)	Locked (in-loop)	Locked (out-of-loop)
X Centroid (μm)	1.12	0.40	0.44
Y Centroid (μm)	1.90	0.42	0.53
X Angle (μrad)	10.16	6.08	6.82
Y Angle (μrad)	7.81	3.76	4.61

Table 2.2: Standard deviations of focus position and angle, calculated on a one minute timescale for unlocked in-loop, locked in-loop, and locked out-of-loop measurements.

where z_1 is the focus position along the optical axis, z_2 is the position of the second detector along the optical axis, θ_i is the angle of the beam relative to the optical axis, C_i is the centroid of the beam relative to the optical axis, and $i \in \{x, y\}$ represents the transverse coordinates. Examples of short- and long-term centroid and angle measurements are shown in Figs. 2.11 and 2.12, respectively. Quantitatively, the improvements in standard deviation of the focus position and angle on a one minute timescale are displayed in Table 2.2. Further insight into how the stability is improved at a variety of timescales can be gained through calculation of the overlapping Allan deviation [181]. A comparison of the Allan deviations of the centroids and angles at the beam focus for locked and unlocked cases is displayed in Fig. 2.13, for timescales ranging from 70 ms to 5 minutes. Note that above 1 s averaging time, the stability is improved by better than an order of magnitude. The fact that the open-loop measurements show slightly more drift at long timescales is due to thermal drift of the mirror mounts that are not shared between the two measurements. For this reason, it is important to minimize the number of mirrors/mounts that are not shared between the feedback system and the experiment.

The amplitude spectral densities (ASDs) of the centroid measurements are also useful as a measure of feedback system performance. The ASDs of the centroids and angles at the focus are shown in Fig. 2.14. While there is very clear improvement in the locked vs. unlocked case at low frequencies (below 0.5 Hz), there is a slight degradation in the 1-3 Hz region. The likely explanation for this degradation is that a small amount of measurement noise has been written onto the output of the system. The complementary sensitivity function from Eq. (2.32) (through which measurement noise can be written onto the output) is plotted along with the ASDs for the vertical

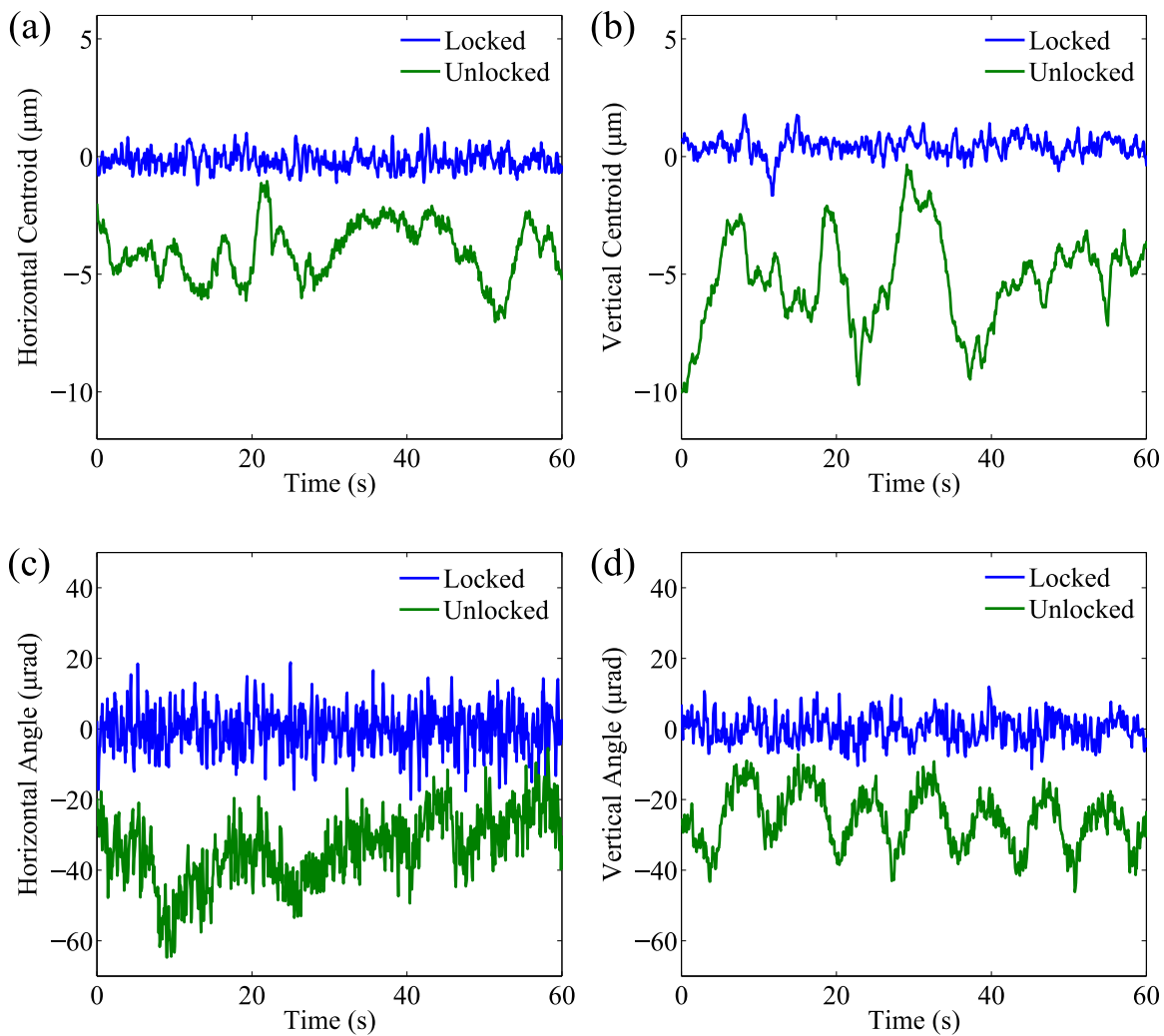


Figure 2.11: Centroids and angles of the beam focus over the course of one minute, locked and unlocked. Note that this is raw data; no smoothing was performed prior to plotting.

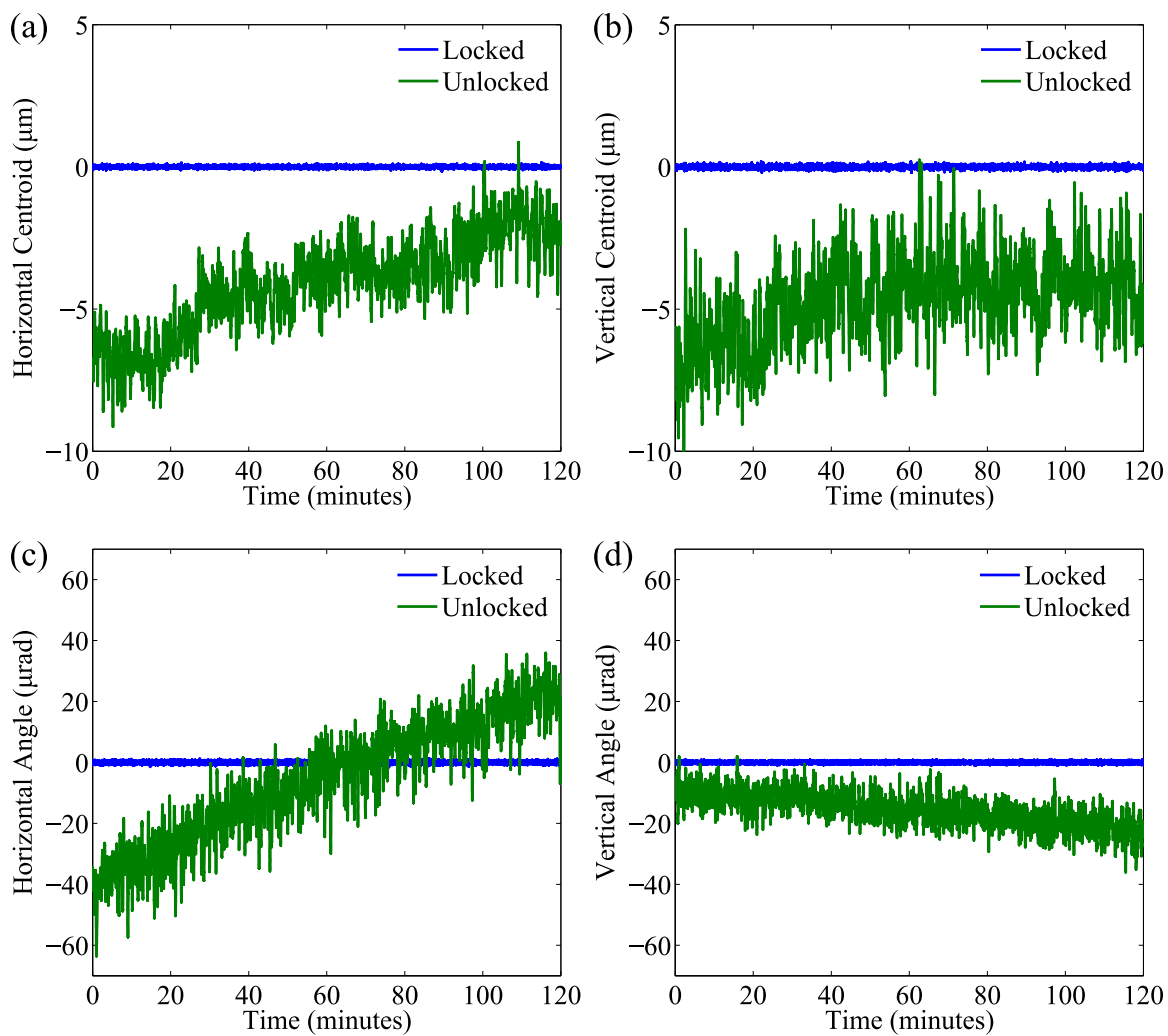


Figure 2.12: Centroids and angles of the beam focus over the course of two hours, locked and unlocked. Note that here the data was smoothed using a boxcar filter with 10 second width.

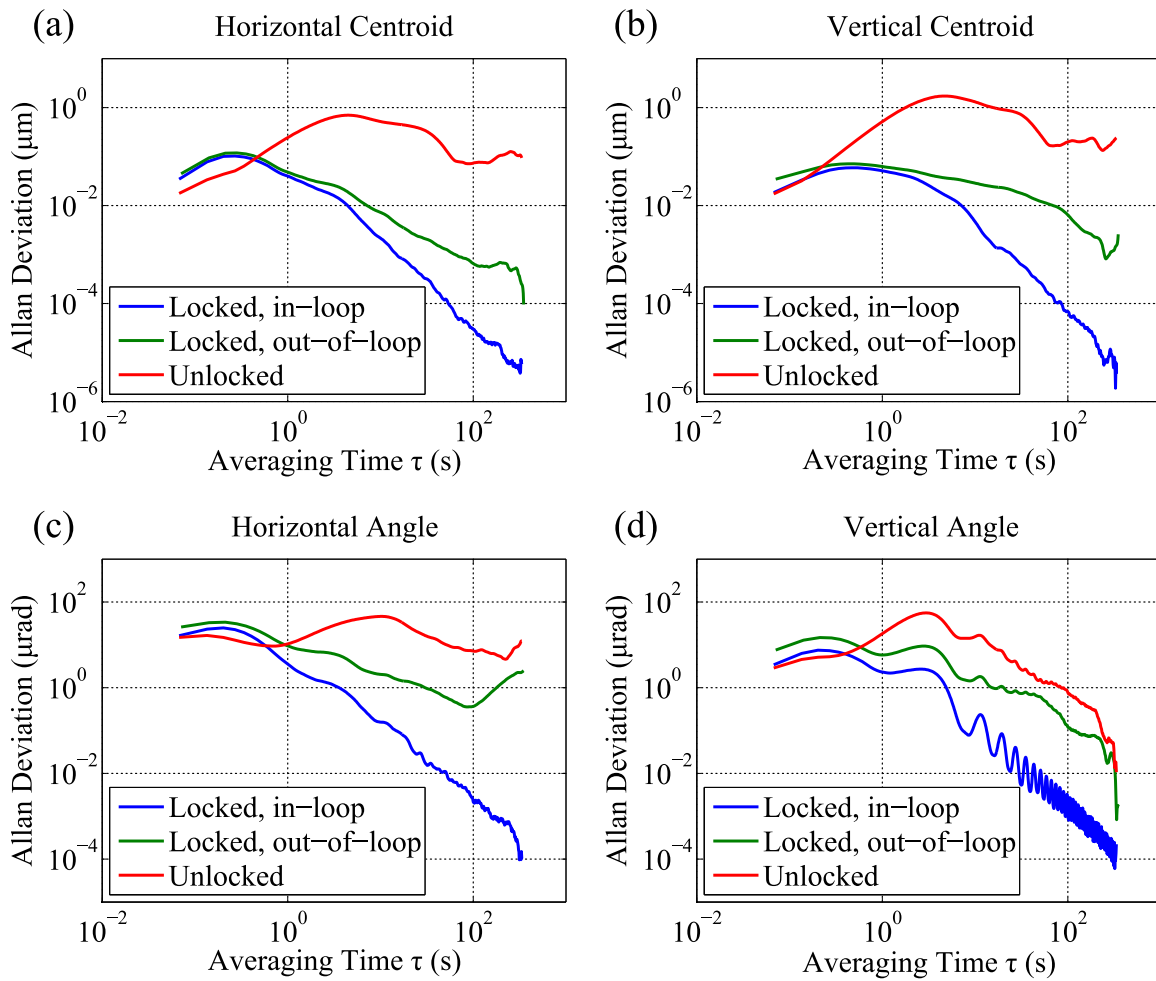


Figure 2.13: Overlapping Allan deviation of the centroids and angles at the beam focus, calculated for locked in-loop, locked out-of-loop, and unlocked cases. The oscillation evident in the vertical angle (d) occurs with a ≈ 7 second period, which has been tracked to the chiller cycle of the amplifier pump laser.

centroid in Fig. 2.14(b), multiplied by a white measurement noise of $0.4 \text{ } \mu\text{m}/\sqrt{\text{Hz}}$. This assumed value of measurement noise is chosen by fitting the complementary sensitivity function to the level of the ASD for the locked case. Additionally, these measurements elucidate the effect amplifier cooling cycles on the beam pointing. In Fig. 2.14(a), the ASD of the horizontal centroid shows clear peaks at 2.4 Hz and 4.8 Hz, which are the lowest two harmonics of the cryocooler (Cryomech PT-90) cooling cycle frequency. These peaks represent a 250 nm peak-to-peak oscillation, and these frequencies are too high to compensate for with the current system. The ASD of the vertical angle (Figure 2.14(d)) shows peaks at 0.13 Hz and 0.26 Hz, which match the cooling cycle of the amplifier pump laser (Lee Laser LDP-200MQG-HP). At these frequencies, Fig. 2.14(d) shows that the stabilization system reduces these peaks by a factor of 5 and 2, respectively.

Additional information can be obtained by dividing the ASD of the locked case by that of the unlocked case, shown again for the vertical centroid of the focus in Fig. 2.15. In a perfect system (no measurement noise), this would be a measure of the sensitivity (Eqn. (2.31)). The theoretical sensitivity function for our feedback system is also plotted in Fig. 2.15. From the figure, it is clear that the system performs as designed below 1 Hz. Further improvements to the system will require reduced measurement noise and a higher sampling rate. Reduction in measurement noise will result in less or no degradation to the stability above 1 Hz. Higher sampling rate will enable more aggressive feedback (reduced sensitivity) at low frequencies, as well as the possibility to broaden the feedback bandwidth to higher frequencies for improved short-term stability.

2.4.2.4 Application to High Harmonic Generation

The utility and reliability of HHG sources is highly dependent on the stability of the laser amplifiers used to drive the HHG process. Here we apply the pointing stabilization technique described above to demonstrate improved short- and long-term stability of a 13 nm wavelength HHG source, driven by the amplifier system described in Section 2.2.

The high harmonics were produced in a helium gas-filled hollow-core waveguide. The waveguide was 5 cm long with an inner diameter of 150 μm . The laser described in Section 2.4.2.3

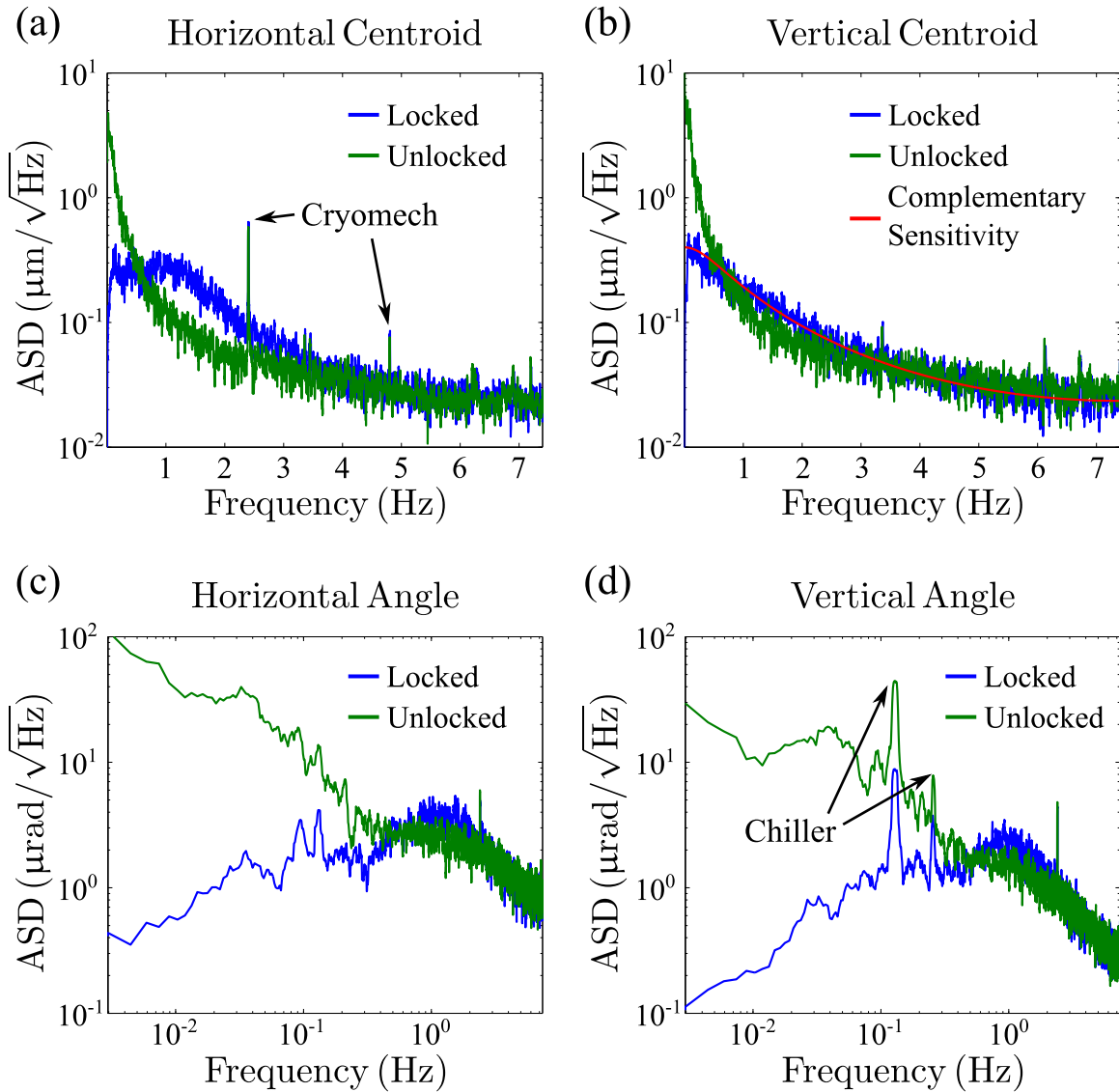


Figure 2.14: The amplitude spectral densities (ASDs) of the centroids and angles at the beam focus, measured in-loop. The locked case is shown in blue while the unlocked case is shown in green. In (a), the horizontal centroid shows very clear oscillations at harmonics of the cryocooler system cycle (Cryomech PT-90). The vertical angle (d) shows strong oscillations at harmonics of the pump laser chiller cycle (Lee Laser LDP-200MQG-HP). The complementary sensitivity multiplied by the noise level is shown in red in (b), with a white noise fit of $0.4 \mu\text{m}/\sqrt{\text{Hz}}$. Note that the amplitude spectral density was smoothed using a boxcar filter with width 1.5 mHz.

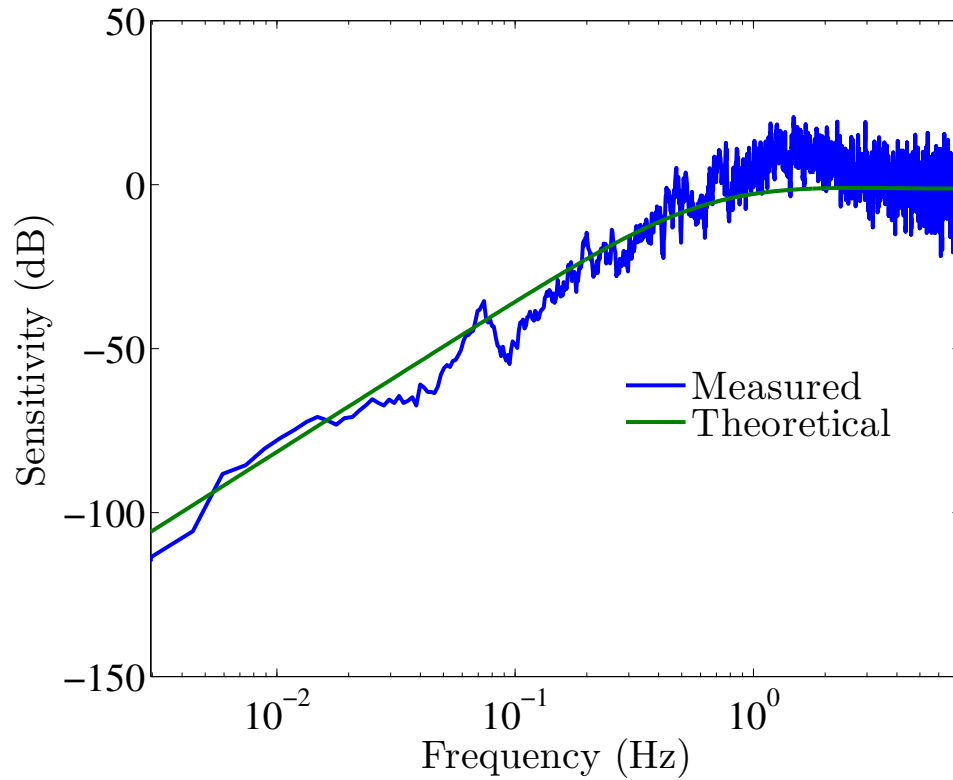


Figure 2.15: The magnitude of the measured and theoretical closed-loop sensitivity for the vertical centroid, measured in-loop. The magnitude of the measured sensitivity is calculated simply by dividing the amplitude spectral density of the locked measurement by the amplitude spectral density of the unlocked measurement. Note that the amplitude spectral densities were smoothed using a boxcar filter with width 1.5 mHz prior to division.

was coupled into the waveguide (as shown in Fig. 2.10) with a waist diameter of approximately 100 μm , in order to couple the majority of the laser energy into the lowest order mode (EH_{11}) of the waveguide [118]. The helium gas was inserted into the final 5 mm of the waveguide, at a phase-matching pressure of approximately 1000 torr. The fundamental laser beam was removed from the collinear high harmonic beam through the use of a pair of ZrO_2 -coated silicon mirrors placed near Brewster's angle for 800 nm, followed by two 200 nm-thick Zr filters. The high harmonic beam was then spectrally filtered by two Mo/Si multilayer mirrors with a reflectivity bandwidth of 4 eV centered at 97 eV (13 nm) for selection of the 63rd harmonic. The 13 nm high harmonic beam was then imaged directly on a EUV-sensitive CCD (Andor iKon), 2 m away from the waveguide. An image of the HHG beam is shown in Fig. 2.16a.

To demonstrate the improvement of high harmonic stability, the driving laser pointing was stabilized into the waveguide as described above. Images of the beam were collected with 1 s exposure time at a rate of ≈ 0.5 Hz for a total of just over 6 hours. For the first 4.5 hours, the pointing feedback was enabled, after which point the feedback was turned off and the HHG beam was monitored for an additional 1.5 hours. Images of the beam at the beginning of measurement, 4 hours into the measurement (feedback still on), and 6 hours into the measurement (feedback off) are displayed in Figs. 2.16a, b and c, respectively. Note that the images of the beam at the 0 and 4 hour points are qualitatively similar, whereas at the 6 hour point the mode shape of the beam has changed considerably. The reason for the change in mode shape is that as the driving laser beam drifts, a significant amount of the energy is coupled into higher-order waveguide modes, resulting in more complicated intensity distributions along the waveguide.

In order to display the entire dataset, each image was summed across the horizontal direction. The result is displayed as a function of time in Fig. 2.17a. A dashed line is placed at the time corresponding to when the feedback was turned off. From the figure, it is clear that the long-term stability of the HHG beam is improved through the use of the pointing feedback system. To more clearly display improvements to the short-term stability of the HHG source, Fig. 2.17b shows a zoomed-in view of the data in Fig. 2.17a for the several minutes surrounding the unlock point.

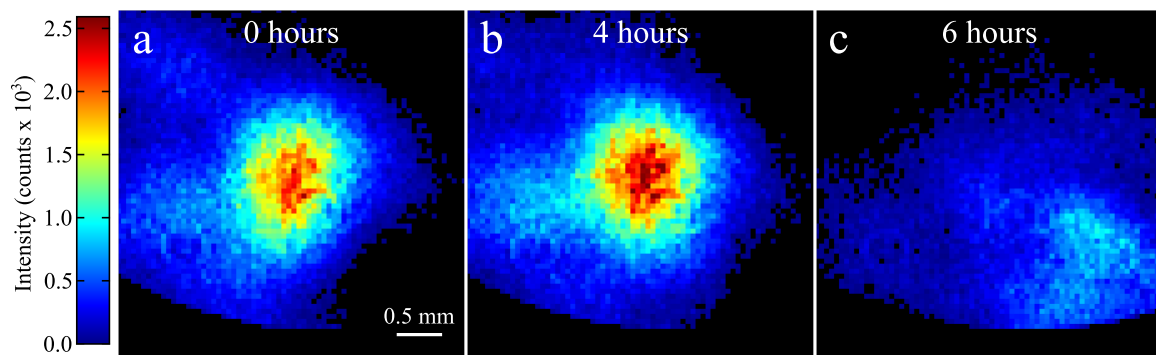


Figure 2.16: Full images of the high harmonic beam at various times, taken from the same raw data as in Fig. 2.17. (a) Beam at the beginning of data collection. (b) Beam after 4 hours with the pointing feedback turned on. (c) Beam 6 hours into data collection, 1.5 hours after the feedback was disabled. Note that the scale bar to the left of (a) is shared among all three images.

Again, the dashed line represents the time at which the feedback was turned off.

Quantitatively, the standard deviation of the horizontal centroid of the HHG beam improved from 29 μrad to 11 μrad and the standard deviation of the vertical centroid improved from 50 μrad to 15 μrad (all calculated on a 5-minute timescale). While locked over 4.5 hours, the maximum deviation of the horizontal centroid was 90 μrad and the maximum deviation of the vertical centroid was 163 μrad . While unlocked over 1.5 hours, the maximum deviation of the horizontal centroid was 915 μrad and the maximum deviation of the vertical centroid was 816 μrad . It is also important to note that, as can be seen from Figs. 2.16 and 2.17, the integrated intensity varied by less than 15% during the time that the feedback system was on, whereas the integrated intensity dropped by almost a factor of 2 after the feedback system had been disabled for just 1.5 hours.

2.4.2.5 Conclusions and future directions

Here we have demonstrated a kHz laser beam pointing feedback system in which the beam position and angle was stabilized in a single feedback system, rather than two independent feedback systems, for the first time. The measured performance of the feedback system is consistent with the design of the feedback loop, and is currently limited by the low sampling rate set by the CCD detectors. However, new CMOS detectors with USB 3.0 communications promise sampling rates up to 350 Hz, which should enable better than an order of magnitude improvement in feedback bandwidth. Additionally, the digital feedback system described here could in principle be implemented with PSDs, which can make measurements at kHz rates and, like CCDs, are capable of sub- μm centroid resolution. Finally, this system provides a way to quantify the sources of noise affecting the beam pointing, so that if possible the noise sources can be tracked down and reduced.

We demonstrated the utility of the digital feedback technique by applying the feedback system to an HHG source. The feedback prevents the driving laser from drifting into higher-order waveguide modes on the many-minute timescale, in addition to improving the short-term (several second timescale) stability of the HHG source. This is an important development for applications of HHG sources. In particular, coherent imaging techniques will benefit, which make use of the full

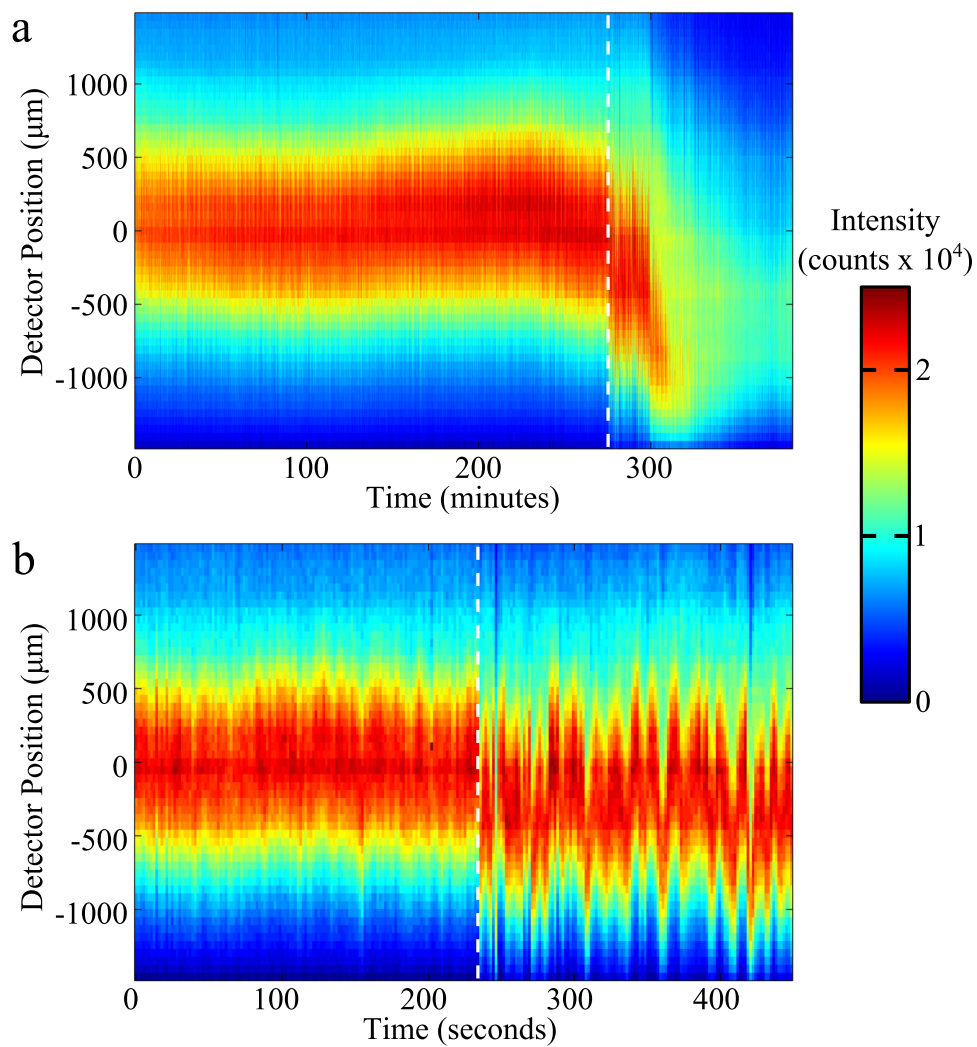


Figure 2.17: High harmonic beam data, integrated along the horizontal direction as a function of time, showing both long- and short-term stability improvement. (a) Long-term harmonic stability data. The dashed line shows the point where the feedback was turned off. (b) Short-term harmonic stability data (zoomed in from (a)). Again, the dashed line shows the point at which the feedback system was turned off.

HHG beam and require high, stable photon flux with stable beam pointing in order to achieve high resolution [182, 183].

2.5 Future prospects for HHG

As discussed in this chapter, HHG is a unique light source that relies on extreme nonlinear optics to produce high energy photons, and macroscopic phase matching to produce bright, coherent EUV beams. This process is highly sensitive to the properties of the fundamental driving laser, including pulse duration and stability. Here we have described the implementation of a frequency-domain, SLM-based pulse shaper which enables mJ-level pulses with transform-limited pulse duration in order to produce very high peak intensities with a compact laser system. Additionally, we have described a beam pointing feedback system to improve the stability of the amplifier system, preventing fundamental laser energy from coupling into higher-order waveguide modes and thus improving the stability of the HHG source.

HHG sources have already been demonstrated which can produce soft X-ray beams with wavelength below 1 nm through the use of longer-wavelength driving lasers [31, 184]. The motivation for using longer wavelength fundamental light to produce short wavelength HHG sources is traced to the λ_0^2 scaling of the HHG cutoff, from Eq. (2.14). Soon, these lasers will likely be available at kHz repetition rates to provide high energy HHG sources bright enough for many scientific applications.

Chapter 3

Coherent Diffractive Imaging with Ultrafast High Harmonic Sources

Dramatic advances in coherent diffractive imaging (CDI) using light in the extreme ultraviolet (EUV) and X-ray regions of the spectrum over the past 15 years have resulted in near diffraction-limited imaging capabilities using both large and small scale light sources [38,185]. In CDI, also called “lensless imaging,” coherent light illuminates a sample, and the scattered light is directly captured by a detector without any intervening imaging optic. Phase retrieval algorithms are then applied to the data set to recover an image. In addition to the absence of aberrations and the diffraction-limited resolution, one of the main utilities of CDI is that due to the necessary phase retrieval, images are reconstructed that have phase and amplitude contrast simultaneously. This feature can provide a wealth of information about objects under study. CDI has already been used to study a variety of biological and materials systems [22,186–189]. Indeed, CDI can be used to study any system which exhibits any type of phase or amplitude contrast.

While CDI has also been applied to visible-light microscopy with interesting applications to biological studies in particular, the discussion here will be restricted to the use of CDI for imaging in the EUV and X-ray regions of the spectrum. The chapter will begin with a brief introduction to scattering theory and available contrast mechanisms in the EUV and X-ray regions of the spectrum. A discussion of the principles behind CDI and its implementation will follow. This section will focus on two-dimensional (2D) phase retrieval and the various CDI algorithms developed thus far. Finally, the chapter will end with a discussion of HHG’s suitability as a light source for EUV and soft X-ray CDI.

3.1 Diffraction theory

In order to understand the basis behind the CDI technique, it is first important to understand the scattering and subsequent diffraction of light. In general, the scattering process is the source of contrast for the image. Most scattering in the EUV and X-ray region can be considered to be due to either elastic scattering from electrons or electron photoabsorption. In CDI, the exit surface wave (ESW) after scattering then diffracts towards the detector where it is measured. Diffraction of light in free space simply obeys the wave equation for electromagnetic fields.

3.1.1 EUV/X-ray scattering

At relatively high photon energies (hard X-rays), far from electronic energy levels in atoms, the amount of scattering is simply proportional to the electron density. At photon energies below the rest mass of the electron, the scattering process is elastic (photon energy-conserving) [97]. Usually in imaging situations these electrons are bound to atoms. Because atomic-level imaging is beyond the scope of the work presented in this thesis, we will restrict the discussion of scattering by electrons to its effect on the effective index of refraction, treating the distribution of atoms as quasi-continuous. In this situation, we can write the index of refraction, n_r , of an atomic distribution as

$$n_r(\mathcal{E}) = 1 - \delta - i\beta = 1 - \frac{r_e}{2\pi} \left(\frac{hc}{\mathcal{E}} \right)^2 \sum_q n_q f_{0q}(\mathcal{E}), \quad (3.1)$$

where δ is the refractive index decrement, β is the absorption index, r_e is the classical electron radius, \mathcal{E} is the photon energy, n_q is the number of atoms per unit volume of type q , and f_{0q} is the complex forward atomic scattering factor for atoms of type q [40]. Note that the sign convention used here is based on the engineering convention of a forward-propagating wave. That is, a plane wave is written as $\exp[i(\omega t - kz)]$. This is important in the case of absorbing materials ($\beta > 0$). We will switch back to the physics convention later.

The atomic scattering factor can be separated into its real and imaginary part as $f_{0q} = f_{1q} + if_{2q}$. The imaginary part, f_{2q} , is proportional to the photoabsorption cross-section of a given

atom, σ_q , which has been measured extensively over a broad photon energy range (30-30,000 eV) for elements with atomic number 92 and below [40]. Explicitly, f_{2q} can be expressed as [190]

$$f_{2q}(\mathcal{E}) = \frac{\mathcal{E}\sigma_q(\mathcal{E})}{2hcr_e}. \quad (3.2)$$

Then, using the Kramers-Kronig relation between the real and imaginary index of refraction, f_{1q} can be calculated as [190]

$$f_{1q}(\mathcal{E}) = Z_q^* + \frac{1}{\pi r_e h c} \int_0^{\infty} \frac{\mathcal{E}'^2 \sigma_q(\mathcal{E}')}{\mathcal{E}^2 - \mathcal{E}'^2} d\mathcal{E}', \quad (3.3)$$

where $Z_q^* \approx Z_q - (Z_q/82.6)^{2.37}$ is a corrected version of the atomic number Z_q , taking into account relativistic effects. Conveniently, the atomic scattering factors have been tabulated and are available online for elements 1 – 92, along with other optical properties courtesy of the Center for X-ray Optics (CXRO) [191]. From Eqs. (3.1) and (3.3), it can be seen that for photon energies far from atomic resonances, δ is simply proportional to the total electron density. Near resonances, electron photoabsorption causes the additional dispersion and absorption terms. There are many element-specific resonances in the EUV region of the spectrum, which leads to element-specific indices of refraction and hence elemental contrast in EUV imaging.

3.1.2 EUV/X-ray diffraction

Diffraction in the EUV and X-ray region of the spectrum can be treated in much the same way as it is treated for visible light. We will start this section by considering exact propagation of light through vacuum through a solution to the Helmholtz wave equation. Next, we will consider non-paraxial, far-field diffraction in transmission and in reflection from a tilted surface. Finally, we will revisit the scattering of light by material with a brief review of the first Born approximation, which can be used to obtain three-dimensional (3D) information under appropriate conditions.

3.1.2.1 The Helmholtz equation and the angular spectrum approach

It is appropriate to begin with the free space wave equation in the absence of source terms, derived from Maxwell's equations [97]:

$$\nabla^2 \mathbf{E} + \frac{\omega^2}{c^2} \mathbf{E} = 0, \quad (3.4)$$

where harmonic time dependence of the field has been assumed, as $\exp(-i\omega t)$. From here, we will assume linear, transverse polarization and a scalar electric field, E . As is often the case in the solution of differential equations, we will start by taking a Fourier transform, in this case in the transverse coordinates. This results in

$$\left[-k_x^2 - k_y^2 + \frac{\partial^2}{\partial z^2} + \frac{\omega^2}{c^2} \right] \tilde{E}(k_x, k_y, z) = 0 \quad (3.5)$$

where we have evaluated the transverse Laplacian by making use of the Fourier transform of a derivative, and where \tilde{E} represents the Fourier transform of E in the transverse coordinates, x and y . We can recognize the solution to Eq. (3.5) immediately as

$$\tilde{E}(k_x, k_y, z) = A \exp(ik_z z), \quad (3.6)$$

where A is a constant that can be determined from knowledge of the field in a given plane and k_z is the propagation constant, which is restricted to $k_z = \sqrt{k_0^2 - k_x^2 - k_y^2}$, where k_0 is defined as $k_0 = \omega/c = 2\pi/\lambda$. This solution allows calculation of the field at any desired plane from knowledge of the field at an input plane. The full solution can be written as

$$E(x, y, z) = \mathcal{F}^{-1} \left\{ \mathcal{F} \{ E(x, y, 0) \} \exp \left(iz \sqrt{k_0^2 - k_x^2 - k_y^2} \right) \right\}. \quad (3.7)$$

From the above equation, it is clear that propagation through free space acts as a kind of low pass filter, attenuating spatial frequencies beyond $1/\lambda$. This is the source of the so-called “diffraction limit”. While the above equation is very useful due to the fact that it is an exact solution to the wave equation in free space (assuming the field goes to zero at infinity in the transverse direction), in practice it can be difficult to use for propagation for large distances due to the highly oscillatory

nature of the exponential for large $z \gg \lambda$. This problem can be solved by splitting a large distance z into N small steps $\Delta z = z/N$ [192].

While not strictly exact, Eq. (3.7) can also be used to propagate through inhomogeneous materials if the propagation step size is small compared to λ , so that diffraction from one step to the next is negligible. This can be done by multiplying the exit wave at each step m , $E(x, y, m\Delta z)$, by a thin “slice” of the material to account for the inhomogeneity of the index of refraction. The slice represents the variation of the index of refraction away from unity, as [192]

$$O_m(x, y) = \exp[-i\delta(x, y, m\Delta z)\Delta z - \beta(x, y, m\Delta z)]. \quad (3.8)$$

This approach is valid for incident plane waves in the case of a weakly scattering object ($\delta, \beta < 1$), since it is incorrect for light propagating any direction but along z . However, this approach was used in Ch. 4 to simulate propagation through a thick object, with good experimental agreement.

As mentioned above, Eq. (3.7) is only practical for propagation over short distances, since further propagation requires splitting the distance into smaller steps. For computationally efficient propagation over large distances, it is useful to make some approximations. The Fresnel approximation can be obtained quickly from Eq. (3.7) when the paraxial approximation is made.

3.1.2.2 Non-paraxial, far-field diffraction, in transmission and reflection

For non-paraxial, far-field calculations, the vectorial Kirchhoff diffraction integral is a good starting point, which is derived through a Green’s function solution to the Helmholtz equation. Here we are assuming that we know the scattered electric field, \mathbf{E}_{sc} , at surface S_1 , consistent with the idea of the ESW mentioned earlier. This can be written as [97]

$$\mathbf{E}_{\text{sc}}(\mathbf{r}) = \frac{e^{ik_0 r}}{i4\pi r} \mathbf{k} \times \int_{S_1} e^{-i\mathbf{k}\cdot\mathbf{r}'} \left[\frac{c\mathbf{k} \times (\mathbf{n}' \times \mathbf{B}_{\text{sc}}(\mathbf{r}'))}{k_0} - \mathbf{n}' \times \mathbf{E}_{\text{sc}}(\mathbf{r}') \right] da', \quad (3.9)$$

where \mathbf{r} represents the far-field coordinates, \mathbf{r}' represents the coordinates of surface S_1 , \mathbf{k} points in the direction of far-field propagation, $\hat{\mathbf{r}}$, with $|\mathbf{k}| = k_0$, and \mathbf{n}' is the normal to surface S_1 . In the absence of surface currents, the first term in the integrand is zero [97]. In the case of a planar surface, \mathbf{n}' can be taken outside the integral.

We will first briefly examine the transmission case. If we assume that the scattered field is weak compared to the incident field, we must write the total electric field in the far field as

$$\mathbf{E}(\mathbf{r}) = \mathbf{E}_{\text{in}}(\mathbf{r}) + i \frac{e^{ik_0 r}}{4\pi r} \mathbf{k} \times \int_{S_1} e^{-i\mathbf{k}\cdot\mathbf{r}'} [\mathbf{n}' \times \mathbf{E}_{\text{sc}}(\mathbf{r}')] da' \quad (3.10)$$

If we assume that the scattered electric field bears information about the scatterer, as we know it does via the ESW, in the case of a thin object at normal incidence we can see that the integral is proportional to the Fourier transform of the scattering surface. Furthermore, we can see that in the case of a weak scatterer, \mathbf{E}_{in} interferes with the scattered light in the far field. In the case of a tightly focused incident beam, this results in a Gabor hologram. An experimental example of this case is found later in this thesis in Section 4.2 [182].

If we go back to Eq. (3.9) and this time consider a reflection geometry, *all* of the light in the domain of the far-field detector can be considered to be scattered. The understanding gained here is critical for the experiments described in Ch. 5 later in this thesis. We will again assume that there are no surface currents, and that the S_1 is a planar surface. We will also assume that \mathbf{E}_{in} has polarization perpendicular to the plane of incidence (*s*-polarized), since this typically results in higher EUV reflectivity. We can now just write this as

$$\mathbf{E}_{\text{sc}}(\mathbf{r}) = i \frac{e^{ik_0 r}}{4\pi r} \mathbf{k} \times \int_{S_1} e^{-i\mathbf{k}\cdot\mathbf{r}'} [\mathbf{n}' \times \mathbf{E}_{\text{sc}}(\mathbf{r}')] da', \quad (3.11)$$

which is the same as Eq. (3.10) except that we have subtracted \mathbf{E}_{in} . In this case, we see that the cross product in the integrand evaluates to a vector that is in the plane of S_1 , as shown in Fig. 3.1. Here we have assumed that on the plane of S_1 , the polarization of \mathbf{E}_{sc} is the same as for \mathbf{E}_{in} . The second cross product between \mathbf{k} and this vector is the source of the so-called ‘‘obliquity factor’’. Thus for *s*-polarized light, the magnitude of the obliquity factor can be calculated as

$$\mathcal{O}_s(\mathbf{r}, \mathbf{n}') = \sqrt{1 - \left(\frac{\hat{\mathbf{x}}' \cdot \mathbf{r}}{r} \right)^2}, \quad (3.12)$$

where the primed (S_1) coordinate system has been defined in Fig. 3.1. An analogous expression for *p*-polarized light can be derived to be

$$\mathcal{O}_p(\mathbf{r}, \mathbf{n}', \theta_i) = \cos \theta_i \sqrt{1 - \left(\frac{\hat{\mathbf{y}}' \cdot \mathbf{r}}{r} \right)^2} \quad (3.13)$$

The introduction of the obliquity factors in Eqs. (3.12) and (3.13), when combined with Eq. (3.11) allow us to write the complex amplitude of the scattered field as

$$\mathbf{E}_{\text{sc}}(\mathbf{r}) = \frac{k_0}{4\pi} \frac{e^{ik_0 r}}{r} \mathcal{O}_j(\mathbf{r}, \mathbf{n}', \theta_i) \int_{S_1} e^{-i\mathbf{k}\cdot\mathbf{r}'} \mathbf{E}_{\text{in}}(\mathbf{r}') O(\mathbf{r}') da' \quad (3.14)$$

where the incident field, \mathbf{E}_{in} , has polarization $j \ni \{s, p\}$, and the scattered field is assumed to be due to the complex, spatially-dependent surface reflectivity $O(\mathbf{r}')$. Here we are assuming that O is truly 2D; later we will see that what really matters is that the exit wave can be factored into a function representing the object, O , and the incident field, \mathbf{E}_{in} [85]. Thus we see that in a reflection geometry, the scattered light is still proportional to the Fourier transform of the “object”. However, at non-normal incidence some care is needed in the evaluation of this Fourier transform. The spatial frequencies at which this Fourier transform is evaluated can be made explicit if we separate the incident field into its amplitude and phase. For the simplest interpretation, we will assume that the incident beam is collimated (\mathbf{k}_{in} constant), so that we can separate the amplitude and the phase of the field as $\mathbf{E}_{\text{in}}(\mathbf{r}') = \psi_{\text{in}}(\mathbf{r}') \exp(i\mathbf{k}_{\text{in}} \cdot \mathbf{r}')$. If we now define the momentum transfer, $\mathbf{q} = \mathbf{k} - \mathbf{k}_{\text{in}}$, we see that we can rewrite Eq. (3.14) as

$$\mathbf{E}_{\text{sc}}(\mathbf{r}) = \frac{k_0}{4\pi} \frac{e^{ik_0 r}}{r} \mathcal{O}_j(\mathbf{r}, \mathbf{n}', \theta_i) \int_{S_1} e^{-i\mathbf{q}\cdot\mathbf{r}'} \psi_{\text{in}}(\mathbf{r}') O(\mathbf{r}') da'. \quad (3.15)$$

Thus we see that the scattered field is proportional to the Fourier transform of the surface object, $O(\mathbf{r}')$, with a position-dependent scaling. Additionally, for the case of non-normal incidence we see that the dot product in the exponential, $\mathbf{q}\cdot\mathbf{r}'$, is not trivial to evaluate. In order to correctly interpret this, we can begin by defining the unprimed (detector) coordinate system such that $\hat{\mathbf{z}}$ points in the direction of the specular reflection. Then we can write the momentum transfer as [193]

$$\mathbf{q}(\mathbf{r}) = k_0 \left[\left(\frac{x}{\sqrt{x^2 + y^2 + z^2}} + \sin 2\theta_i \right) \hat{\mathbf{x}} + \frac{y}{\sqrt{x^2 + y^2 + z^2}} \hat{\mathbf{y}} + \left(\frac{z}{\sqrt{x^2 + y^2 + z^2}} + \cos 2\theta_i \right) \hat{\mathbf{z}} \right], \quad (3.16)$$

where the incident k-vector has been written explicitly in terms of the angle of incidence, θ_i . In order to associate the components of \mathbf{q} with the spatial frequencies of the scattering surface, we must find the components of \mathbf{q} in the primed coordinate system. For the case shown in Fig. 3.1, we

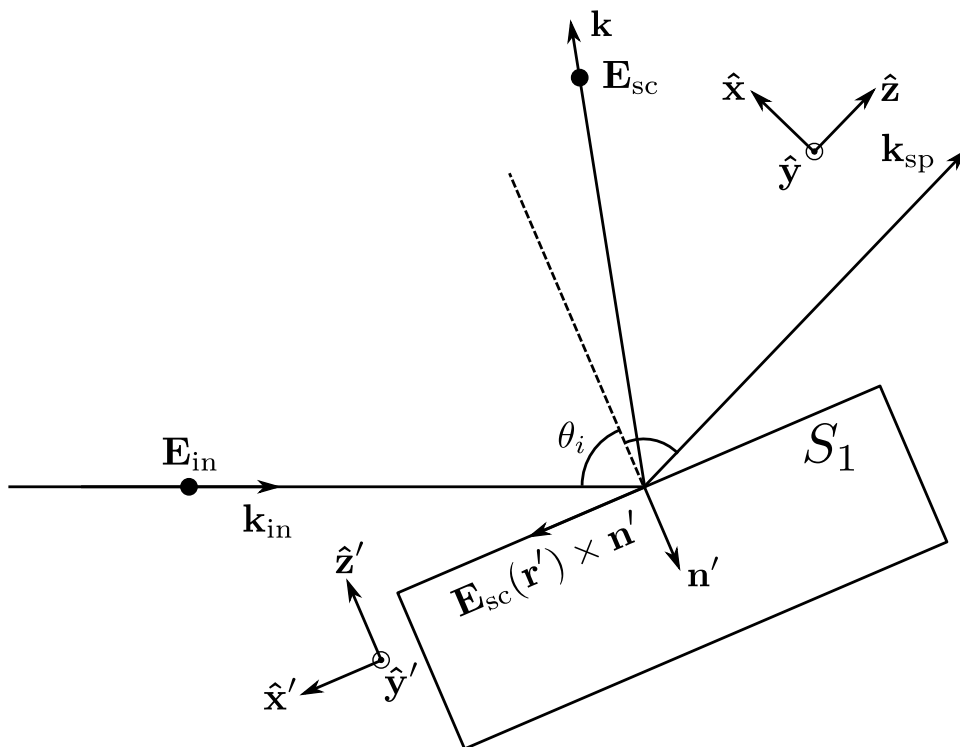


Figure 3.1: Illustration of the source of the obliquity factor for s -polarized light. Only the plane of incidence ($x' - z'$ plane) is shown for simplicity. Here, the angle of incidence is θ_i , the primed coordinate system is aligned with surface S_1 as shown and the unprimed coordinate system is aligned with the specular reflection, \mathbf{k}_{sp} , as shown.

can accomplish this by performing a simple coordinate transformation. Specifically, we can perform a rotation about $\hat{\mathbf{y}}$ by an angle $-\theta_i$. The result is

$$\mathbf{q}(\mathbf{r}') = (q_x \cos \theta_i - q_z \sin \theta_i) \hat{\mathbf{x}}' + q_y \hat{\mathbf{y}}' + (q_x \sin \theta_i + q_z \cos \theta_i) \hat{\mathbf{z}}', \quad (3.17)$$

with q_x , q_y , and q_z defined as the components of \mathbf{q} in the unprimed coordinates, as in Eq. (3.16). With the momentum transfer written in this way the dot product in the Fourier kernel can be evaluated immediately. The coupling of far-field coordinates in $f_x = q_{x'}/2\pi$ and $f_y = q_{y'}/2\pi$ results in a distorted-looking diffraction pattern, termed conical diffraction [194]. An attempt to illustrate this distortion is shown in Fig. 3.2.

In the case of CDI, the far-field intensity is measured with the goal of retrieving the object function, $O(\mathbf{r}')$. This is typically accomplished by relating the far field pattern to the modulus square of the Fourier transform of the object, and fast Fourier transforms (FFTs) are used to propagate between object space and the far field. In the non-normal-incidence reflection geometry, some pre-processing of the measured pattern is required. As we have seen, what is actually measured is

$$I(\mathbf{r}) \propto \frac{\mathcal{O}_s(\mathbf{r}, \mathbf{n}')^2}{r^2} \left| \int_{\mathcal{S}_1} e^{-i\mathbf{q}\cdot\mathbf{r}'} \psi_{\text{in}}(\mathbf{r}') O(\mathbf{r}') da' \right|^2, \quad (3.18)$$

where we have assumed an s -polarized incident wave and $I(\mathbf{r})$ is the intensity of the far-field diffraction pattern. In order to find the magnitude of the 2D Fourier transform of $O(\mathbf{r})$ from the measurement, the measured intensity can be rescaled by $r^2/\mathcal{O}_s(\mathbf{r})^2$. After this rescaling, in order to use the FFT the measurement must be interpolated onto a grid which is linear in $q_{x'}$ and $q_{y'}$ from one that is linear in x and y , using Eqs. (3.16) and (3.17). After this is done, the object function can be retrieved using CDI as usual. This rescaling and interpolation method, termed tilted plane correction (TPC) [193], was used for all the image reconstructions in Ch. 5.

3.1.2.3 First Born approximation with application to 3D imaging

We now turn to the first Born approximation to consider the diffraction pattern produced from a small, weakly scattering 3D object. This is, for instance, a useful approach for 3D imaging of

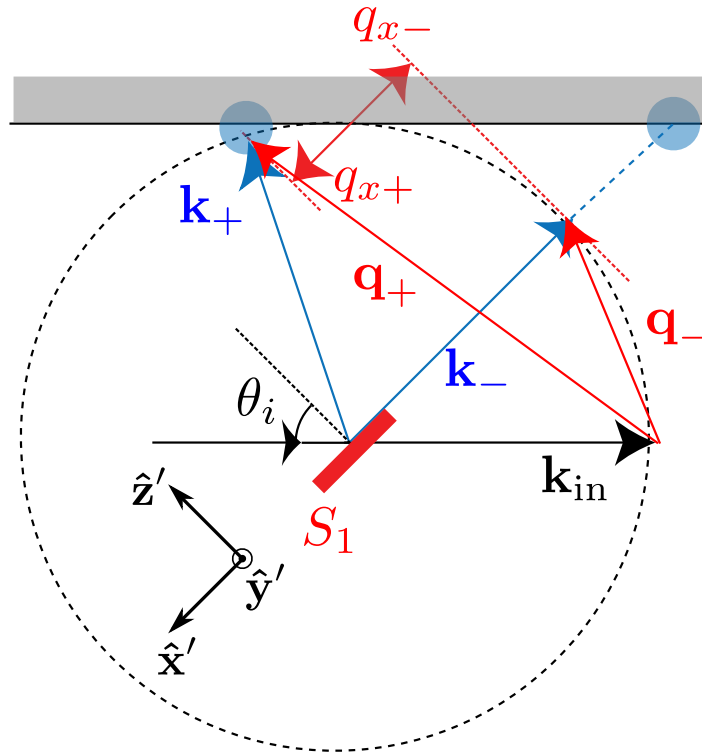


Figure 3.2: Illustration of distortion of the diffraction pattern due to conical diffraction. Two final \mathbf{k} -vectors (\mathbf{k}_+ and \mathbf{k}_-) are shown such that $(\mathbf{q}_+ \cdot \hat{\mathbf{x}}') = -(\mathbf{q}_- \cdot \hat{\mathbf{x}}')$, meaning that these two \mathbf{k} -vectors contain information about the same spatial frequency of the S_1 . However, the locations on the detector where the light scattered to these \mathbf{k} -vectors is measured (at positions shown by the blue dots) are very asymmetric with respect to the position of the specular reflection (not shown) on the detector.

biological cells. Often, it is necessary to use concepts from tomography [74, 186, 189, 195], although some work has been done to develop a technique called ankylography, which requires one to several diffraction patterns to generate a 3D image [196]. Here we will see that when certain conditions are met, limited 3D information can be obtained from a single diffraction pattern.

To begin, we can start from the scalar Helmholtz equation, except this time we will allow for variation of the index of refraction, $n(\mathbf{r})$. This modifies Eq. (3.4) to read as

$$[\nabla^2 + k_0^2 n(\mathbf{r})^2] \mathbf{E}(\mathbf{r}) = 0. \quad (3.19)$$

Now, motivated by the discussion in Section 3.1.1, we will write the index of refraction in the EUV/X-ray region as $n = 1 - \delta$, where for simplicity we are omitting β . However, it can be inserted with δ in the end. As mentioned earlier, for hard X-rays δ is simply proportional to the electron density. If we assume that $\delta \ll 1$, we can approximate $n^2 \approx 1 - 2\delta$. We will also assume that δ is only non-zero in a local region of space, which will become important later. Inserting this for the index of refraction in Eq. (3.19), we have

$$[\nabla^2 + k_0^2 - 2k_0^2 \delta(\mathbf{r})] \mathbf{E}(\mathbf{r}) = 0. \quad (3.20)$$

Now we see that we have an inhomogeneous Helmholtz equation. Our approach to the solution will be to expand \mathbf{E} in a series solution, in orders of δ . This can be written as

$$\mathbf{E} = \sum_{i=0}^{\infty} \mathbf{E}_i \delta^i \quad (3.21)$$

Since we have already dropped orders of δ^2 in Eq. (3.20), upon insertion of this series solution we will keep only zeroth and first order terms. We will also assume that \mathbf{E}_0 is the incident field, and is thus a solution to the homogeneous Helmholtz equation. With those steps taken, we are left with the following equation:

$$[\nabla^2 + k_0^2] \mathbf{E}_1(\mathbf{r}) = 2k_0^2 \delta(\mathbf{r}) \mathbf{E}_0(\mathbf{r}), \quad (3.22)$$

where we have allowed \mathbf{E}_1 to absorb δ . We can now use the Green's function for the Helmholtz equation [97],

$$G(\mathbf{r}, \mathbf{r}') = \frac{e^{ikR}}{4\pi R}, \quad (3.23)$$

with $R = |\mathbf{r} - \mathbf{r}'|$, to solve Eq. (3.22). The assumption that both E_1 and G decay to zero in the limit as $r \rightarrow \infty$ gives the following solution:

$$E_1(\mathbf{r}) = -2k_0^2 \int_V \frac{e^{ik_0R}}{4\pi R} E_0(\mathbf{r}') \delta(\mathbf{r}') d^3r' \quad (3.24)$$

where the limits of integration extend over the region where δ is non-zero. Note that up until this point the only assumption we have made is that $\delta \ll 1$. However, here it is appropriate to make a further assumption that $r \gg D$, where D is the approximate diameter of the scattering object (where δ is non-zero). This allows us to expand k_0R in orders of D/r as [97]

$$k_0R = k_0r - \mathbf{k} \cdot \mathbf{r}' + \frac{k_0}{2r} \left[r'^2 - \frac{(\mathbf{k} \cdot \mathbf{r}')^2}{k_0^2} \right] + \dots \quad (3.25)$$

With this expansion, the magnitude of the n th term is on the order of $(k_0r)(D/r)^n$ in the region where δ is non-zero. At this point a quantity called the Fresnel number should be mentioned, named after Augustin-Jean Fresnel, which is defined as $F = D^2/\lambda r$. The third term of the expansion has maximum magnitude $\approx F$, and when $D \gg \lambda$ can be important to keep even when the field is measured far from the object. Thus F can be used to classify different types of far-field diffraction. The Fraunhofer regime is characterized by $F \ll 1$, the Fresnel regime is characterized by $F \approx 1$, and $F > 1$ is referred to as the near field. For the Fraunhofer case, only the first two terms in the expansion are kept, whereas for the Fresnel case, the third term must also be kept. For the near-field case, the spectrum of plane waves approach can be used, described in Section 3.1.2.1.

Before we continue with the general Fraunhofer case, it is worthwhile to make a comment about the Fresnel case. The coupling between the primed and unprimed coordinates in the third term is in general not possible to deal with using a Fourier transform approach to far-field propagation. However, if the far-field measurement is paraxial, we can assume that $\mathbf{k} \approx k_0\hat{\mathbf{z}}$ and that $z = L$ with L the distance from object to detector, so that the third term becomes $k_0(x'^2 + y'^2)/2L$ and is dependent on only the primed coordinates.

In order to consider the Fraunhofer case, we can take just the first two terms in the expansion

(3.25). After inserting this approximation into Eq. (3.24), we have

$$E_1(\mathbf{r}) = -2k_0^2 \frac{e^{ik_0 r}}{4\pi r} \int_V e^{-i\mathbf{k}\cdot\mathbf{r}'} E_0(\mathbf{r}') \delta(\mathbf{r}') d^3r' \quad (3.26)$$

If we again assume illumination by a collimated beam, and choose $\mathbf{k}_0 = k_0 \hat{\mathbf{z}}$, then we can see that with uniform illumination Eq. (3.26) is proportional to the 3D Fourier transform of $\delta(\mathbf{r}')$, with measurement of the 3D Fourier transform possible at spatial frequencies defined by $\mathbf{q} = \mathbf{k} - \mathbf{k}_0$. Using the same notation as in Eq. (3.15), we can write the final expression for the Fraunhofer Born approximation as

$$E_1(\mathbf{r}) = -2k_0^2 \frac{e^{ik_0 r}}{4\pi r} \int_V e^{-i\mathbf{q}\cdot\mathbf{r}'} \psi_0(\mathbf{r}') \delta(\mathbf{r}') d^3r' \quad (3.27)$$

For a given wavelength λ , we can see that the allowed values for \mathbf{q} exist on a sphere of radius k_0 which is shifted from the origin by \mathbf{k}_0 ; this is called the Ewald sphere.

It is important to note that Eq. (3.26) is non-paraxial. Furthermore, with adjustment of \mathbf{k}_0 the 3D Fourier transform of δ can be measured at additional spatial frequencies. This adjustment can consist of either rotation of the object or by changing the wavelength. With measurement in the forward direction with enough rotations of the object, the magnitude of the 3D Fourier transform can be obtained at most locations within the 3D Fourier cube that has maximum width $2k_0$, which forms the basis for 3D Fourier tomography. In certain cases, with measurement of the scattered intensity at high enough scattering angles, a technique called ankylography can be used to fill in the rest of the 3D Fourier cube to reconstruct a 3D image of the object with a single measurement [196, 197]. Again, in order to use the FFT, an interpolation similar to that described in Section 3.1.2.2, where a pattern measured on a grid that is linearly spaced in \mathbf{r} must be interpolated onto a grid that is linearly spaced in \mathbf{q} .

A final couple of miscellaneous comments concerning Eq. (3.27) are warranted. First, in general the far-field measurement includes the bright incident field, $E_0(\mathbf{r})$, which must be subtracted. Second, the generalization to non-collimated incident fields (e.g. a diverging Gaussian beam) is straightforward and simply consists of multiplying ψ_0 by a phase term dependent only on the primed coordinates. This generalization to non-collimated incident fields can also be applied to the

reflection case in Eq. (3.15).

3.2 Principle of CDI

In the previous section, we have seen that diffraction under certain conditions can provide information about the magnitude of the Fourier transform of a scattering object. In certain cases, the measured intensity must be rescaled and/or interpolated onto a grid that is linearly spaced in spatial frequency before it can be related to the scatterer using a simple FFT. However, once these corrections have been made, we can take advantage of the large body of work that has been devoted to 2D (and 3D) phase retrieval from knowledge of the Fourier modulus of an object (or more generally an ESW). This work began in the 1970's at a time when computational optics was becoming practical due to the introduction of the FFT [78, 198]. As an interesting side note, the FFT algorithm was actually first invented by Carl Friedrich Gauss in 1805.

This section will begin with an explanation of the so-called oversampling requirement, which traditionally limited CDI to small objects. A brief discussion of the traditional coherence (spatial and temporal) requirements for CDI will follow; in the previous section, full spatial and temporal coherence was assumed in order to show that the diffraction pattern of a scatterer is proportional to its Fourier transform. Finally, the various approaches to phase retrieval in CDI which have been developed thus far will be broadly discussed, some of which relax the traditional object size and coherence requirements.

3.2.1 Oversampling in CDI

The oversampling requirement can be understood via the Shannon sampling theorem [199], which states that a band-limited function can be recovered fully if sampled at a high enough rate relative to the band limit. The Nyquist frequency is the 1D version of the generalized N-dimensional sampling rate, in which the sampling rate of a 1D signal must be twice as high as the highest frequency content of the signal in order to be considered Nyquist-sampled. We are concerned with the spatial frequency content of the measurement, which in the case of CDI is the diffraction

amplitude. This may be counter-intuitive, since the diffraction pattern itself represents the spatial frequency content of the scattering object. However, due to the Fourier relationship between the object and its diffracted amplitude, this just means that the band limit of the diffraction pattern depends on the spatial extent of the object.

While it is the diffraction amplitude (and hence electric field) that is proportional to the Fourier transform of the object, it is the diffraction intensity that is actually measured. This is proportional to the square of the amplitude, and from a simple example we will see that sampling the intensity pattern at its Nyquist rate actually corresponds to sampling the diffracted amplitude at *twice* its Nyquist rate, hence the term “oversampling”. For the example, we will use the simple case of a square object as the scatterer, defined by

$$O(x', y') = \text{rect}\left(\frac{x'}{D}\right) \text{rect}\left(\frac{y'}{D}\right), \quad (3.28)$$

which means that the square has sides of length D . Conveniently, the Fourier transform of this object is easily calculated analytically, and is proportional to

$$\mathcal{F}\{O(x', y')\} \propto \frac{\sin(q'_x D/2)}{q'_x D/2} \frac{\sin(q'_y D/2)}{q'_y D/2}. \quad (3.29)$$

From the discussion in the previous section, we know that the far field coordinates in the simple normal-incidence geometry are related to spatial frequency as $\mathbf{q} = k_0(\mathbf{r}/r - \hat{\mathbf{z}})$. Paraxially, this means that in terms of far-field spatial coordinates $q'_x = 2\pi x/\lambda z$, with an analogous expression for q'_y . This means we can rewrite Eq. (3.29) in terms of far-field (detector) coordinates paraxially as

$$\psi(x, y) \propto \frac{\sin(\pi x D/\lambda z)}{\pi x D/\lambda z} \frac{\sin(\pi y D/\lambda z)}{\pi y D/\lambda z}. \quad (3.30)$$

This function is Nyquist-sampled in each dimension if measurements are made with a spacing of $\lambda z/D$ or finer (at least two measurements per period of the sine function). However, what is measured is actually the diffracted intensity, which is proportional to

$$I(x, y) \propto \frac{\sin^2(\pi x D/\lambda z)}{(\pi x D/\lambda z)^2} \frac{\sin^2(\pi y D/\lambda z)}{(\pi y D/\lambda z)^2}. \quad (3.31)$$

From a simple trigonometric identity, we can rewrite this to explicitly reveal the spatial frequency content of the intensity, as

$$I(x, y) \propto \frac{1 - \cos(2\pi x D / \lambda z)}{(\pi x D / \lambda z)^2} \frac{1 - \cos(2\pi y D / \lambda z)}{(\pi y D / \lambda z)^2}. \quad (3.32)$$

In order for the intensity to be Nyquist-sampled, measurements must be made with a spacing of $\lambda z / 2D$ or finer. This requirement is a factor of 2 stricter than that required for the amplitude. This simple example can be made more general by allowing for the object to have internal structure. From the inverse relationship between spatial extent and spatial frequency, we can see that this additional structure only contributes to lower spatial frequency content in the diffraction pattern. Thus from this sample example, we can see that the diffraction intensity typically has twice the band limit that the corresponding amplitude does. For this reason, in CDI the diffraction amplitude must be oversampled by at least a factor of 2. The linear oversampling ratio, OS , can be defined as

$$OS = \frac{\lambda z}{pD} \quad (3.33)$$

where p is the pixel width of the detector used for the measurement. Due to the Shannon sampling theorem, for N dimensions the linear oversampling ratio must be $\geq \sqrt[N]{2}$ [80]; in 2D this is a slight relaxation with respect to the 1D requirement of 2. However, in practice, the presence of measurement noise usually means that $OS \geq 4$ produces better results.

For an intuitive understanding of what the oversampling requirement implies, it is helpful to consider the size of the object relative to the size of the spatial grid supported by the sampling rate of the detector. The answer is simply that the width of the grid, W , relative to the width of the object is simply $W/D = OS$. Thus for a linear oversampling ratio $OS = 2$, the object only takes up 1/4 of the image area. This is the origin for the object isolation requirement in CDI; if the object is not isolated the diffraction pattern will not be sampled appropriately. Fortunately, there are some ways to relax this requirement which will be discussed later.

3.2.2 Coherence requirements

In the consideration of coherence requirements for CDI, it is most convenient to work with spatial and temporal coherence lengths, which we will call l_s and l_t respectively. Spatial coherence is defined transverse to the direction of propagation. The temporal coherence length is defined in the direction of propagation, so it can also be called longitudinal coherence. Coherence lengths are defined in such a way that interference between two waves which are scattered at two points in space (transversely or longitudinally) that are separated by one coherence length have fringe visibility of 88% [200]. The loss of fringe visibility, or coherence, is due to fluctuating phase relationships between points further apart than a coherence length.

Traditionally, CDI treats the diffraction pattern as simply proportional to the Fourier transform of the entire object, meaning that full spatial coherence is assumed. Thus, we must require that $l_s > D$ in the plane of the object. Fortunately, for sources which intrinsically have only partial spatial coherence (such as an undulator), l_s can be increased at the expense of photon efficiency. For instance, a slit (or aperture in 2D) which has width, d , smaller than l_s in the plane can be placed in the beam path. From that point, the light that is transmitted through the slit can be considered to have full spatial coherence between any two transverse points at which there is appreciable intensity. Thus, due to diffraction from the slit, the coherence length l_s grows as $\lambda z/2\pi d$, where z is the distance from the slit.

While CDI also assumes full temporal coherence, the practical requirements on l_t are slightly less strict than for l_s . However, decreased temporal coherence is allowed at the expense of object complexity, which can be defined as the ratio D/r , where r is the resolution of the reconstructed image. This is shown visually in Fig. 3.3. The best attainable resolution is limited by the NA to be

$$r \geq \frac{\lambda}{2 \sin \theta}. \quad (3.34)$$

However, from Fig. 3.3, we see that the temporal coherence length limits the fringe visibility for

scattering angles

$$\sin \theta \geq \frac{l_t}{D}. \quad (3.35)$$

Finite temporal coherence arises when the illumination is not monochromatic. The temporal coherence length can be defined by the coherence time, which is related to the spectral bandwidth of the illumination by the Heisenberg uncertainty principle, so that the coherence time can be defined roughly as $\tau_c = 1/\Delta\nu$. This can be easily understood in the case of pulsed sources from the discussion in Section 2.1. In the case of a pulsed source, the coherence time is just the pulse duration. Two split pulses that are separated in time by more than the pulse duration cannot produce interference (except in the special case when they are separated by an integer multiple of the time between pulses in the pulse train, with stable carrier envelope phase). The coherence length is obtained by calculating how far the wave has traveled during a coherence time, which in the case of light traveling in vacuum means $l_t = c\tau_c$. Written in terms of wavelength, this is

$$l_t = \frac{\lambda^2}{\Delta\lambda}. \quad (3.36)$$

If we combine Eqs. (3.34) - (3.36), we can see that for traditional CDI, the maximum achievable resolution is limited by the temporal coherence length to be

$$r \geq \frac{\Delta\lambda D}{\lambda^2}. \quad (3.37)$$

As predicted earlier, this means that the temporal coherence, which is related to the spectral bandwidth of the source, results in a limit on the maximum image complexity as

$$\frac{D}{r} \leq 2 \frac{\lambda}{\Delta\lambda}. \quad (3.38)$$

As mentioned before, these requirements can be relaxed to a certain extent by modifications to the most basic CDI algorithms. This is accomplished by separating the illumination into either (or both) spatial and spectral modes [83]. For the most part, this relaxation of coherence requirements assumes that the object appears identical to all spatial and spectral modes. However, in the case of ptychography, simulations and measurements with visible light suggest that this assumption is unnecessary, making this a potential hyperspectral imaging technique [91].

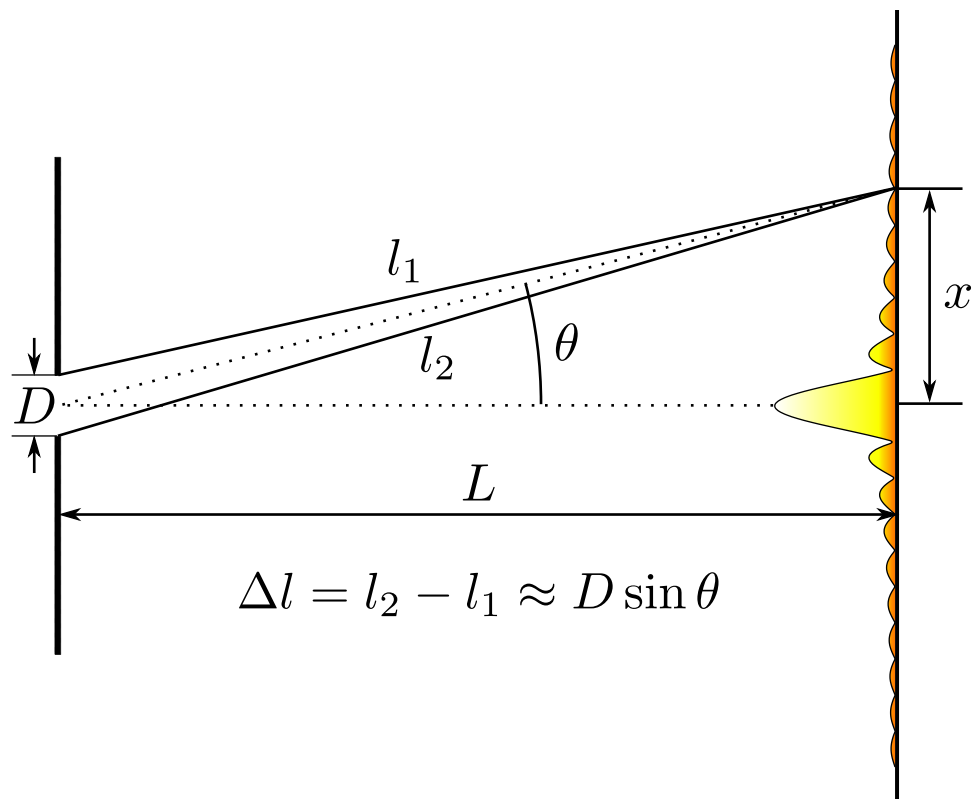


Figure 3.3: Illustration showing the implications of finite temporal coherence. At a scattering angle of θ , light scattered from one side of an object of width D will travel a distance $D \sin \theta$ further to the detector than light scattered from the other side of the object. For temporal coherence lengths less than D , the fringe visibility will be reduced at angles where $\sin \theta > l_t/D$.

3.2.3 Phase retrieval in CDI

Since the first demonstrations of CDI at visible wavelengths [37] and at X-ray wavelengths [38], many extensions to the basic CDI algorithm have been developed. In this section, the basic algorithm will first be discussed followed by a brief discussion of the various extensions. Extensions to CDI which relax the object isolation requirement include keyhole CDI [201], apertured illumination CDI [193, 202], and ptychography CDI [85, 86]. Extensions which relax the coherence requirements involve the separation of the illumination into multiple spatial and temporal modes to account for partial spatial and temporal coherence [81–83, 203]. Recently, ptychography CDI has also shown promise as a particularly powerful method to relax the requirements for temporal coherence, with the possibility of retrieving independent images for each spectral component of the illumination [91].

3.2.3.1 Basic CDI algorithms and projections

The concept of generalized projections is key to understanding all implementations of CDI. Generally, CDI phase retrieval involves projections of the current guess for the solution onto constraint sets that exist in both the object space and its Fourier space [73, 77]. The differences between the various implementations of CDI lie both in which specific constraint sets are used and in how the projections are applied. The various algorithms that lie at the core of CDI are the error reduction (ER) [39], hybrid input-output (HIO) [72], difference map (DM) [77], and relaxed averaged alternating reflections (RAAR) [204] algorithms, which are good starting points before discussing further enhancements to CDI.

Each of the algorithms listed above rely on basic projections, usually consisting of a modulus projection, which acts in the Fourier domain, and support and non-negativity projections, which act in the object domain. The modulus projection, π_m is defined as

$$\tilde{\pi}_m \tilde{\rho}_i(\mathbf{q}) = \sqrt{I(\mathbf{q})} \frac{\tilde{\rho}_i(\mathbf{q})}{|\tilde{\rho}_i(\mathbf{q})|} \quad (3.39)$$

where $\pi_m = \mathcal{F}^{-1} \tilde{\pi}_m \mathcal{F}$, $\tilde{\rho}_i(\mathbf{q}) = \mathcal{F} \rho_i(\mathbf{r})$ represents the Fourier transform of the current guess, $\rho_i(\mathbf{r})$,

and $I(\mathbf{q})$ is the measured diffraction intensity [73]. The effect of this projection is to keep the current guess for the phase of the complex diffraction amplitude, while forcing the magnitude to be consistent with the measured intensity. The support projection, π_s , is simply defined as [73]

$$\pi_s \rho_i(\mathbf{r}) = \begin{cases} \rho_i(\mathbf{r}) & \text{if } \mathbf{r} \in S \\ 0 & \text{otherwise} \end{cases} \quad (3.40)$$

where S constitutes a region in object space known as the support. Use of a support constraint in CDI is motivated by the requirement that the diffraction pattern must be oversampled as discussed earlier, leading to an object which takes up less than half the area of the image. The support can either be pre-defined as a known region, or it can be updated dynamically while the algorithm is running using the shrinkwrap method [205]. Finally, the non-negativity (or positivity) projection, π_p , is defined as

$$\pi_p \rho_i(\mathbf{r}) = \begin{cases} \rho_i(\mathbf{r}) & \text{if } 0 < \phi_i(\mathbf{r}) < \phi_{max} \\ 0 & \text{otherwise} \end{cases} \quad (3.41)$$

where the phase of the object, $\phi_i(\mathbf{r})$, is calculated in the usual way, taking into account which quadrant of the complex plane that $\rho_i(\mathbf{r})$ lies in, and ϕ_{max} can range between 0 and 2π . From here we will assume that the non-negativity projection is applied together with the support projection, so that $\pi_{s+} = \pi_s \pi_p$. In order to describe a single iteration of each of the above-mentioned algorithms, the only other definition needed is that of the “reflector”, which is defined as $R = 2\pi_j - I$, where I stands for the identity and j stands for any of the basic projections.

The projections/reflections necessary to calculate each successive iteration for each algorithm are shown in Table 3.1. Note that each successive iteration for all of the algorithms listed can be written in terms of the projections defined above. The algorithm is said to have converged when $\rho_{i+1} = \rho_i$; that is, the algorithm has reached a fixed point.

3.2.3.2 Relaxation of the object isolation requirement

As mentioned earlier, the traditional CDI algorithm requires the object to be isolated due to the oversampling requirement. Here we will describe the various CDI implementations which relax

Algorithm	$\rho_{i+1} =$
ER	$\pi_{s+\pi_m}\rho_i$
HIO	$\begin{cases} \pi_m\rho_i(\mathbf{r}) & \text{if } \mathbf{r} \in S \text{ and } 0 < \phi_i(\mathbf{r}) < \phi_{max} \\ (I - \beta\pi_m)\rho_i(\mathbf{r}) & \text{otherwise} \end{cases}$
DM	$\{I + \pi_{s+}[(\beta + 1)\pi_m - I] - \pi_m[(\beta + 1)\pi_{s+} - I]\}\rho_i$
RAAR	$[\frac{1}{2}\beta(R_{s+}R_m + I) + (1 - \beta)\pi_m]\rho_i$

Table 3.1: Formulas to calculate successive iterations for ER, HIO, DM and RAAR algorithms. β is an adjustable parameter, usually chosen to be near 1. Adapted from [73].

this requirement. Oversampling of the diffraction pattern is still required; the isolation requirement is simply transferred to the illumination instead.

3.2.3.3 Apertured illumination and keyhole CDI

Both keyhole CDI [201] and apertured illumination CDI [193] allow image reconstruction of non-isolated, extended objects using just a single measured diffraction pattern. Apertured illumination is particularly simple. The beam is sent through an aperture which is imaged onto the sample using a high quality optic, in order to produce sharp-edged illumination in the object plane. While this technique has been demonstrated using visible wavelengths in both transmission and reflection [193], attempts to use this technique in the EUV have not been particularly successful [202]. This is likely due to the lack of high quality optics in the EUV.

Keyhole CDI can be considered to be a generalization to apertured illumination. For this technique, the illumination must be tightly focused; the sample is placed outside the focus of the beam so that the incident wavefront is strongly curved. This geometry produces a so-called “hologram region” on the detector, where interference between light scattered from the sample with the unscattered beam can be used to obtain a direct, low-resolution image of the object. Additionally, the resulting asymmetry in the diffraction pattern strengthens the modulus constraint used in the iterative phase retrieval algorithm. For this technique, precise knowledge of the illumination is necessary. Additionally, the distance from sample to focus must be accurately and precisely known [206]. However, this is the only CDI technique that has been demonstrated in

the EUV/X-ray capable of producing an image of an extended sample using a single diffraction pattern [182, 201, 207].

3.2.3.4 Ptychography CDI

Ptychography CDI is a fundamentally different extension to traditional CDI than apertured illumination and keyhole. This technique shares almost the same experimental geometry and data collection process as STXM, which was described briefly in Section 1.2.2.1. The major difference is that ptychography is not limited in resolution to the spot size of a focused X-ray beam. This comes from the fact that rather than collecting a single data-point per scan position, as in STXM, ptychography involves measurement of a 2D diffraction pattern at each scan position [85, 86]. Thus the resolution is limited in the same way as it is for traditional CDI, by the wavelength and the maximum scattering angle (NA).

One of the major benefits of ptychography is that the object and illumination functions are reconstructed separately, thus dividing out any non-uniformities in the illumination. That is, the exit surface wave at each scan position, ψ_j , is factorized into

$$\psi_j(\mathbf{r}) = O(\mathbf{r})P(\mathbf{r} - \mathbf{R}_j) \quad (3.42)$$

where O and P represent the object and probe functions, respectively, and \mathbf{R}_j represents the relative shift of the j th scan position. A ptychographical dataset involves a vast amount of information; the independent reconstructions of both probe and object are enabled by use of an overlap constraint in the object domain. Typically, adjacent scan positions require $> 70\%$ area overlap [86]. Additionally, high quality reconstructions generally require grids with at least 4×4 scan positions. The factorization in Eq. (3.42) is only valid under certain conditions derived in the supplementary material of Thibault et al. [85]. Intuitively, this validity condition amounts to requiring that the probe must not diffract across the thickness of the object by an amount measurable by the resolution of the system. Written as an equation, this is equivalent to

$$\theta_p \Delta z \leq r \quad (3.43)$$

where θ_p is the divergence angle of the probe (assumed to be small), Δz is the thickness of the object, and r is the resolution of the system as defined in Eq. (3.34). If we assume that the illumination is Gaussian, from this intuitive requirement we recover the same condition as in [85], which is that

$$\frac{r}{\Delta z} \geq \frac{\lambda}{2w_0} \quad (3.44)$$

where w_0 is the radius of the beam waist. Thus for thick objects, the factorization is only valid when the illumination is loosely focused. However, Maiden et al. have shown that in the case where Eq. (3.42) is invalid, the vast amount of information collected in a ptychographical dataset is sufficient to retrieve 3D information about the object [90]. This extension to ptychography involves propagation through the object in the same way as described by Eq. (3.8).

Ptychography has generally been assumed to require the same oversampling requirements as traditional CDI (Eq. (3.33)). However, it can be shown that this requirement can be overcome if the redundancy in the ptychographical dataset is high enough [79, 208]. The potential for information extraction in ptychography may not yet be fully grasped. Recently, it was shown that the temporal coherence requirements described in Section 3.2.2 can be relaxed through ptychography. Furthermore, this relaxation of requirements actually enables hyperspectral imaging, with the capability to reconstruct unique object functions for each component of the illumination spectrum [91]. This is in contrast to the methods described by Chen et al. [83], where the object must be assumed to be identical for each spectral mode. The implications for this are extremely important. This technique may, in fact, enable 3D surface imaging as well as hyperspectral EUV imaging across multiple absorption edges simultaneously.

3.3 HHG as a source for CDI

The results presented in Chs. 4 and 5 are based on CDI using an HHG source. Thus it is worth commenting on the applicability of HHG for use as a light source for CDI. As discussed above, traditional CDI requires light sources that have certain spatial and temporal coherence properties.

We will see that while HHG may not be the perfect source for every implementation of CDI, it may be near-ideal for certain types of measurements.

HHG produced in a waveguide geometry has been shown to exhibit full spatial coherence across a very wide wavelength range [31, 92, 150, 209]. The full spatial coherence comes from phase-matching the HHG process along the waveguide, so that the HHG source takes on the coherence properties of the driving laser. Furthermore, when the laser is coupled into the lowest order mode of the waveguide (EH_{11}), the output is near-Gaussian with full spatial coherence across the entire beam. Thus, in contrast to most other coherent EUV/X-ray sources (with the exception of FEL's), the HHG output does not need to be spatially filtered in order for use as a CDI light source.

In terms of temporal coherence, HHG sources are not intrinsically monochromatic due to the production of multiple phase-matched harmonics simultaneously. However, each harmonic can be considered to be quasi-monochromatic, with $\lambda/\Delta\lambda \approx 200$ under optimized conditions [210]. Thus for the traditional implementation of CDI, the HHG source must be spectrally filtered so that the object is illuminated by only one harmonic. Typically, this has been accomplished through the use of a pair of EUV multilayer mirrors. However, the multiple-harmonic structure of HHG should not be seen as a drawback in terms of its applicability towards use as a light source for CDI. Through knowledge of the incident spectrum, the object can be illuminated with multiple harmonics simultaneously by separating the pattern numerically into its various spectral modes [81]. Furthermore, using ptychography independent images of the object at each wavelength can be obtained simultaneously [91]. Additionally, the short-pulsed femto/atto-second nature of HHG light sources will enable dynamic studies of nanosystems with high spatial and temporal resolution in the near future.

Finally, the compact, inexpensive nature of HHG is another major advantage. This means that, while HHG doesn't necessarily produce the very high flux that is characteristic of facility-scale undulator, and in particular, FEL light sources, HHG provides a very accessible light source for CDI that can be produced in many university-scale laboratories. Thus, the characteristics of HHG make it a uniquely relevant source for high-resolution, dynamic imaging studies using CDI. The

next two chapters describe the development of a unique microscope based on HHG CDI, capable of imaging extended objects in both transmission and reflection geometries and poised to make a critical impact on nanoscale studies with its application to dynamic imaging.

Chapter 4

Table-top CDI with HHG Sources in Transmission

Previous work in this group demonstrated that HHG sources enable high-resolution imaging based on CDI with a laboratory-scale source. However, these initial demonstrations were limited to very simple samples, leaving work to be done to make this microscope into a useful tool for nanoscale studies. Improvements to the CDI microscope began in transmission geometry, in order to increase complexity slowly enough to maintain full understanding of each change to the microscope. The first goal was to improve flux at 13 nm in order to push the resolution of the microscope even lower than the 50 nm resolution that had previously been demonstrated using 29 nm HHG [211]. The next goal involved extending the capability of the microscope to image more complex samples by applying the keyhole CDI technique [201]. The implementation of these improvements is described in this chapter.

4.1 High resolution CDI using 13 nm HHG

Previous work using 13 nm HHG light had been met with limited success due to low flux [212]. In order to remedy the problem of low flux, it was necessary to make several improvements to the source prior to attempting further imaging at this wavelength.

4.1.1 Flux improvements to enable CDI at 13 nm

Traditionally, HHG sources at 13 nm wavelength have been difficult to work with. Relatively high-reflectivity mirror coatings made from Mo/Si stacks are available at this wavelength ($\approx 70\%$)

[42], leading to interest from the semiconductor industry for use in EUV lithography processes [43]. However, a number of issues plague the generation of coherent EUV light at 13 nm using HHG. These issues had to be resolved before high quality imaging was possible at this wavelength.

First, Zr filters are the best available choice in terms of transmission properties for separating the fundamental driving laser light from the high harmonics within the range of 70-100 eV. However, Zr has a very low thermal conductivity of $22.6 \text{ Wm}^{-1}\text{K}^{-1}$ relative to, for instance, Al (another common EUV filter material) which has a thermal conductivity of $237 \text{ Wm}^{-1}\text{K}^{-1}$. Thus, whatever laser light that is absorbed ($\approx 10\%$) by the filter can result in local heating and rapid damage to the filter. Second, in order to generate harmonics in this wavelength range, noble gases with high ionization potentials such as neon or helium must be used, which are highly absorbing between 20-200 eV. Finally, the higher ionization potential of helium and neon relative to argon means that higher laser peak intensities are necessary to drive the HHG process than at lower photon energies, resulting in higher necessary laser pulse energies for a given waveguide diameter [209].

Previously, the problem of low thermal conductivity in Zr was solved by coating a thin, ≈ 20 nm, layer of Ag on the first filter following the HHG waveguide [212]. However, while the Ag layer reflected most of the residual 800 nm light, preventing the Zr filter from burning as quickly, it absorbed $\approx 80\%$ of the 13 nm light. This problem was solved by the insertion of “rejector” mirrors into the beamline between the HHG source and the Zr filters. Silicon was chosen as a substrate for the mirror due to its Brewster angle near glancing incidence (15° glancing) and because of its high surface quality. Good candidates for coating materials needed to be dielectric, to prevent laser absorption and damage, and highly reflective at 13 nm. Previous work showed that NbN was a good candidate [213]. Due to difficulties in locating facilities able to coat NbN, other possible dielectric coatings were considered: ZrO_2 , $(\text{NbTa})_2\text{O}_5$, HfO_2 , and Sc_2O_3 . As shown in Fig. 4.1, ZrO_2 was predicted to have the best 13 nm reflectivity near glancing incidence based on data from the Center for X-Ray Optics (CXRO) [40]. After obtaining samples from generous collaborators at Colorado State University, reflectivity measurements (shown in Table 4.1 and plotted in Fig. 4.1) confirmed that ZrO_2 did indeed have the best reflectivity from among these candidates.

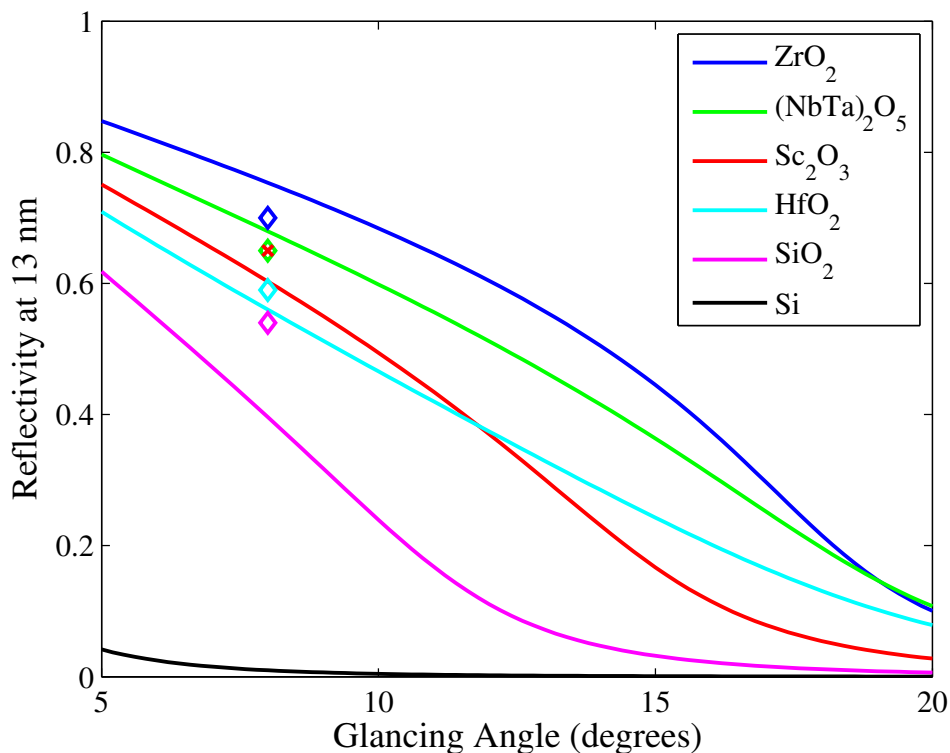


Figure 4.1: Theoretical reflectivity curves for a variety of coating materials at 13 nm wavelength as a function of glancing angle. The coating surfaces are assumed to be perfectly smooth and the 13 nm light is assumed to be p -polarized. The data is taken from the CXRO website [40]. Additional curves for Si and SiO₂ are shown for reference. The measurements using 13 nm light are shown as well, showing reasonably good agreement with the theoretical curves.

Coating Material	Reflectivity	Surface Quality
ZrO ₂	0.70	Excellent
(NbTa) ₂ O ₅	0.65	Excellent
HfO ₂	0.59	Poor
Sc ₂ O ₃	0.65	Excellent
SiO ₂	0.54	Excellent

Table 4.1: Reflectivity measurements of a number of “rejector” mirror coating materials. The reflectivities were measured by comparing total throughput with reflections at 8° glancing incidence to that with the mirror removed. The measurements can be compared with the theoretical reflectivity curves in Fig. 4.1. The measurements show reflectivities in general agreement with the theoretical curves, and are plotted along with the curves in Fig. 4.1. Surface quality is based on subjective analysis of the recorded beam in comparison to the undeflected beam.

A ZrO_2 single-layer anti-reflection coating at 800 nm was optimized numerically using the Fresnel equations, with the result that the coating should be 207 nm thick. As can be seen in Fig. 4.2, the minimum theoretical reflectivity occurs near Si's Brewster angle. However, as seen in Fig. 4.1, the 13 nm reflectivity is higher at smaller glancing angles, leading to a compromise of 12° glancing incidence in the experiment. It is found that even with 5 – 10% reflectivity from the rejector mirror, the Zr filters last indefinitely without damage. However, since the Si substrate is absorbing at 800 nm, the substrate does eventually sustain damage. In the future, since the Zr filters are able to withstand some finite laser power, transparent fused silica substrates coated with ZrO_2 may be used. As shown in Fig. 4.2, the reflectivity of these mirrors at 800 nm will be higher, but the mirrors will likely last much longer before replacement is needed.

In the first implementations of the 13 nm coherent imaging beamline, the high absorption of the gases used as HHG media was somewhat reduced by the use of differential pumping. The differential pumping was implemented by placing a turbopump as close to the HHG waveguide as possible, with a 3 mm aperture placed along the beamline directly after the turbopump. However, this geometry still allowed several cm's of relatively high gas pressure. More recently, with help from the JILA machine shop and Tenio Popmintchev, the differential pumping scheme was improved by placing a roughing pump roughly 2 cm past the end of the HHG waveguide. Roughing pumps are actually more effective than turbopumps for the high-pressure gas loads found in this situation. The aperture placed in the beamline is only 2 mm in diameter and is 2 cm long, providing a much better pressure differential than in the past.

This new differential pumping scheme also allowed a longer phase-matching geometry than previously. Previously, the gas pressure geometry was as shown in Fig. 4.3(a), with only a single gas inlet and two pump-out holes. This type of geometry meant that there was no constant-pressure region along the fiber axis, preventing true phase matching. However, this geometry was necessitated by the fact that the previous differential pumping scheme did not tolerate the larger gas load necessary for allowing a constant-pressure region. The improvement to the differential pumping scheme, which enabled higher gas loads while maintaining lower gas pressures beyond the

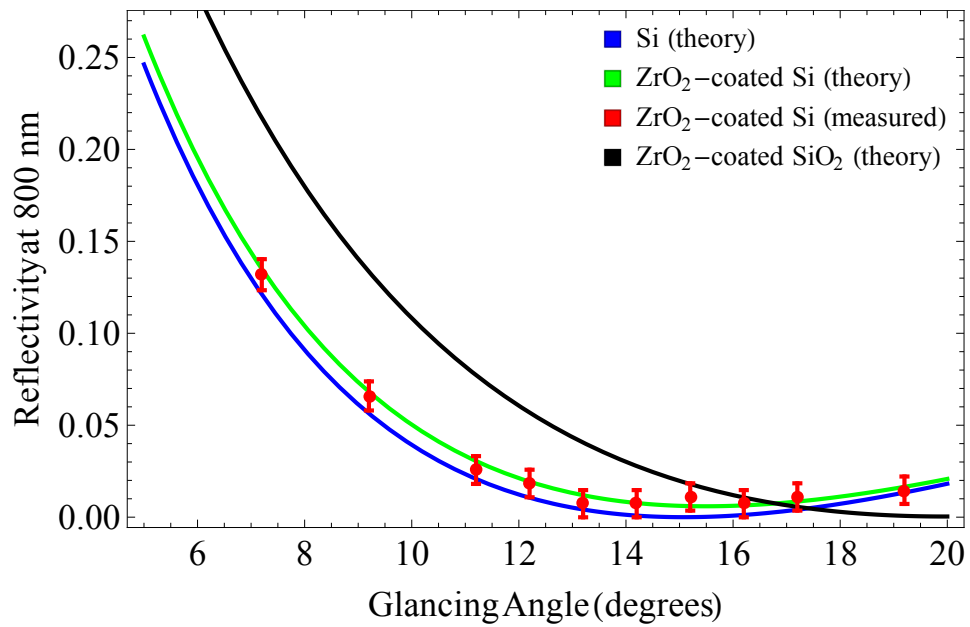


Figure 4.2: Plot showing glancing-incidence reflectivities at 800 nm for a variety of “rejector” mirror designs. The blue curve shows the theoretical reflectivity of bare Si, the green curve shows the theoretical reflectivity of Si coated with 207 nm of ZrO₂, the black curve shows the theoretical reflectivity of SiO₂ coated with ZrO₂, and the red dots show experimental measurements of the reflectivity of Si coated with 207 nm of ZrO₂. The 800 nm light is assumed to be *p*-polarized.

exit of the waveguide, allowed for two pump inlets separated by 5 mm near the exit of the waveguide (see Fig. 4.3(b)). This geometry enabled true phase matching along 5 mm length, limited by the absorption length of helium at 13 nm.

Finally, the laser was upgraded to operate with 2 mJ of pulse energy at a repetition rate of 2 kHz (and later 5 kHz) by replacing the pump laser in the amplifier, a step up from a previous 1.4 mJ at 3 kHz. Previously, due to the lower pulse energy, it was necessary to use waveguides with 100 μm inner diameter in order to achieve high enough intensity for helium ionization [212]. The increase to 2 mJ allowed the use of 150 μm inner diameter waveguides, resulting in harmonic yield that was less sensitive to any laser drift. Additionally, the larger diameter means that the waveguide is easier to align.

The cumulative effect of all of these improvements was to increase the 13 nm high harmonic flux to $> 10^8$ photons/s at the sample, a 100 \times improvement over the previous best shown by our group [212]. However, there is still some room for improvement over the current design. As can be seen in Fig. 4.3(b), there is still 5 mm from the second gas inlet to the exit of the waveguide, across which the phase-matched harmonic beam can be partially absorbed. The length of this “end section” could be reduced through the use of new fiber-mounting designs. A simple estimate for the improvement in transmission of the phase-matched beam through the end section can be calculated using the Beer-Lambert law. The Beer-Lambert law for varying gas density is

$$T(\lambda) = \exp\left(-\sigma(\lambda) \int N(z) dz\right), \quad (4.1)$$

where $T(\lambda)$ is the transmission of the gas at wavelength λ , $\sigma(\lambda)$ is the absorption cross-section of the gas at λ , and $N(z)$ is the gas density as a function of position. Pressure can be traded for density if we assume an ideal gas, allowing us to rewrite Eq. (4.1)

$$T(\lambda) = \exp\left(-\frac{\sigma(\lambda)}{k_B T} \int P(z) dz\right), \quad (4.2)$$

where k_B is Boltzmann’s constant, T is the gas temperature, and $P(z)$ is the gas pressure. If we assume a pressure ramp in the waveguide end section like that shown in Fig. 4.3(b), we can rewrite

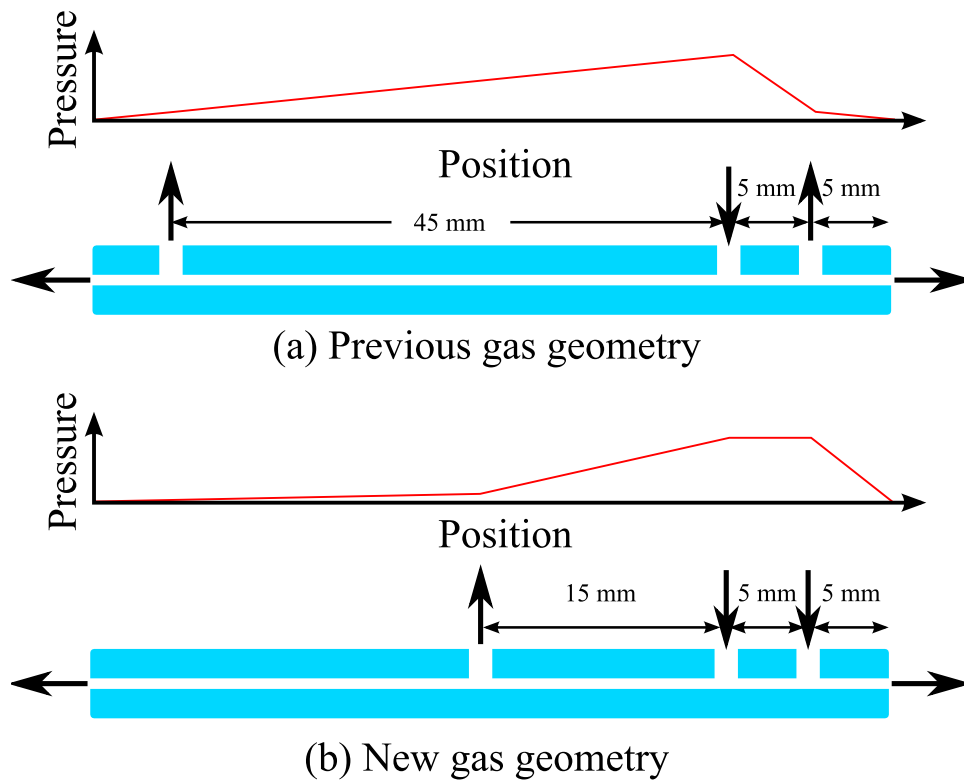


Figure 4.3: Old and new 13 nm waveguide gas pressure schemes. The outward-pointing arrows represent vacuum pump outlets and the inward-pointing arrows represent gas inlets. (a) The previous waveguide design included a vacuum pump outlet 5 mm from the entrance of the waveguide, a gas inlet 1 cm from the exit of the waveguide, and a pump outlet 5 mm from the exit of the waveguide. This geometry resulted in the approximate pressure profile shown above the depiction of the waveguide. (b) The new waveguide design allows for a constant pressure region 5 mm long near the exit of the waveguide, allowing for better phase matching. Additionally, the pump outlet was moved closer to the constant pressure region to prevent extra absorption of the driving laser. Again, the pressure profile shown above the waveguide is approximate.

Eq. (4.2) as

$$T(\lambda) = \exp\left(-\frac{\sigma(\lambda)}{k_B T} \int_0^{z_0} P_0 \left(1 - \frac{z}{z_0}\right) dz\right), \quad (4.3)$$

where P_0 is the pressure at the beginning of the ramp and z_0 is the length of the end section. The integral in Eq. (4.3) is easy to evaluate, resulting in a final expression for the transmission:

$$T(\lambda) = \exp\left(-\frac{\sigma(\lambda)P_0z_0}{2k_B T}\right), \quad (4.4)$$

Based on data found at CXRO's website [40], helium's absorption cross-section is $8.2 \times 10^{-19} \text{ m}^2/\text{atom}$ at 13 nm. The transmission curves shown in Fig. 4.4 were calculated assuming room temperature at peak ramp pressures ranging from 200 – 800 torr, which are in the vicinity of typical experimental phase-matching pressures. As can be seen from the figure, the current 5 mm end sections leave room for another factor of 2 – 10× improvement.

4.1.2 Data collection and image reconstruction

Fig. 4.5 shows a schematic of the tabletop HHG source and microscope used in this work. As described in Ch. 2, light from an ultrafast Ti:sapphire laser-amplifier system (KMLabs DragonTM, 2 mJ pulse energy, 780 nm wavelength, 2 kHz repetition rate, 25 fs pulse duration) is focused into a 5 cm long, 150 μm diameter, helium-filled hollow waveguide to generate fully coherent high-harmonic beams around 13 nm [209]. The 100× increase in high harmonic flux at 13 nm was critical to our experiments, in order to significantly enhance high-angle diffraction with much reduced exposure times. The increase in flux brought the total photon flux at the sample within a factor of 10 of that for a typical 29 nm HHG source [92]. Previous CDI results at 29 nm required exposure times of minutes to hours in order to capture high-angle diffraction data [211], meaning that without this flux improvement high-resolution imaging at 13 nm would have remained out of reach with realistic exposure times.

The waveguide geometry allows a long interaction length to establish excellent laser and HHG modes that can be fully phase matched and fully spatially coherent [92, 118, 209]. Moreover, at 13 nm wavelength, the nonlinear medium (helium) is strongly absorbing, and the gas pressures

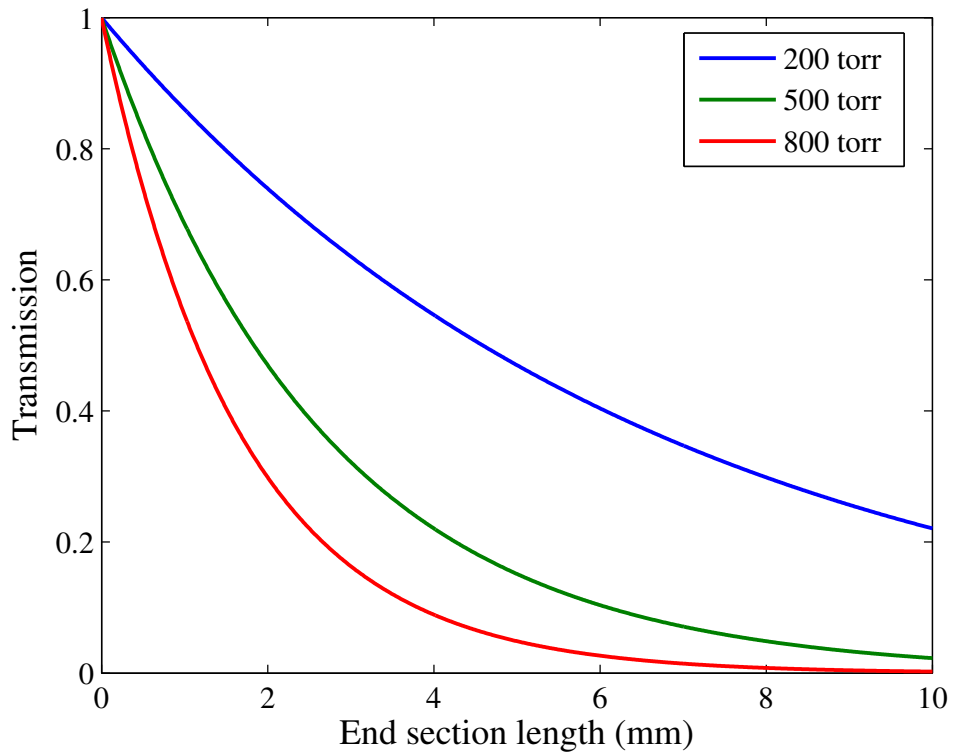


Figure 4.4: Transmission of 13 nm light through a pressure ramp of helium, based on Eq. (4.4). Transmission curves are shown for peak ramp pressures of 200 torr (blue), 500 torr (green) and 800 torr (red) as a function of waveguide end section length. Typical waveguides used for 13 nm HHG have 5 mm end sections, meaning that based on this calculation there is some room for improvement.

required for phase matching are very high (≈ 1 atm). Unless the high harmonic beam emerges into vacuum over a sharp gas density gradient, as discussed in the preceding section, the losses due to phase mismatch and gas absorption in the end sections can be significant.

To reject the laser light that co-propagates with the high harmonic beam, we use a combination of a Brewster-angle silicon substrate coated with 207 nm of ZrO_2 (described in the previous section) [213,214] combined with two 200 nm thick Zr filters. The Brewster mirror absorbs nearly all of the infrared light and reflects $\approx 60\%$ of the HHG beam, while the filters each have a calculated transmission of 50% at 13 nm. The broadband EUV light is then spectrally filtered and refocused onto the sample using a pair of 73% efficient multilayer reflectors centered at 12.8 nm (one flat and one 1 m ROC), resulting in a flux of $> 10^8$ photons/s at the sample. After illuminating the sample, the scattered light is collected in the far field using a back-illuminated, x-ray sensitive CCD detector with $13.5 \mu\text{m}$ square pixels on a 2048×2048 array (AndorTMiKon DO436). In the far field, the diffraction pattern is related to the exit wave of the object by a Fourier transform. Using the Hybrid Input-Output (HIO) phase retrieval algorithm [39], it is possible to recover the phase information and consequently an image of the object.

Two different test objects were used to test the spatial resolution of our tabletop XCDI microscope, shown in SEM images in Figs. 4.6(a) and 4.7(a) (referenced hereafter as J407 and J409). Raw diffraction data are shown in Figs. 4.6(b) and 4.7(b), while reconstructions are shown in Figs. 4.6(c) and 4.7(c). Before reconstructing the image, the raw data must be preprocessed to improve the convergence of the iterative algorithm. First, hot pixels inherent to the CCD chip are removed, and cosmic rays appearing in the final scatter pattern are identified and removed. In some cases, filtering was performed in the Fourier space of the scatter pattern. Finally, the full diffraction pattern was binned by a factor of eight for sample J407 and sixteen for sample J409. The binning process combines photon counts from adjacent pixels into a single pixel, increasing signal to noise and decreasing the overall grid size for the calculation.

After the data was filtered, several well-established iterative phase retrieval algorithms were implemented to reconstruct the amplitude and phase of the images, including the difference map

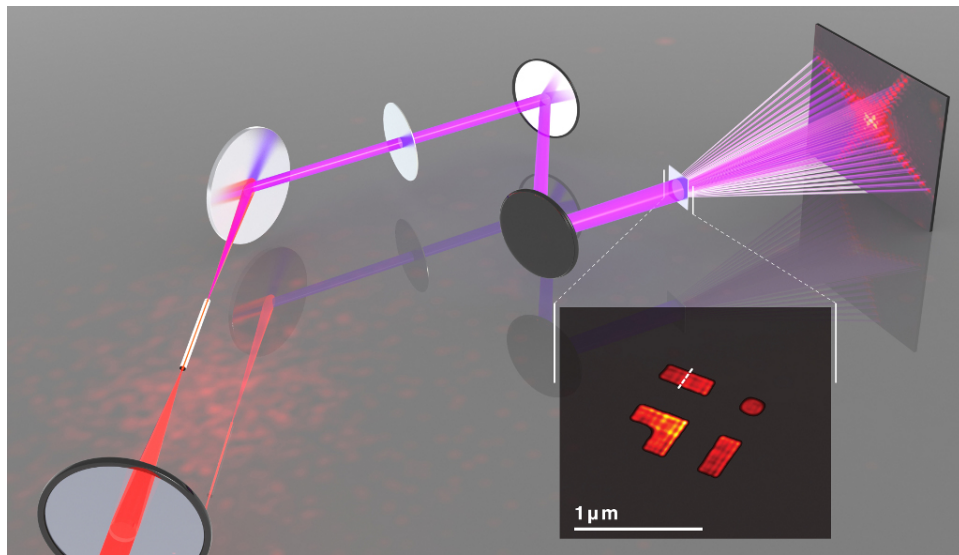


Figure 4.5: A femtosecond driving laser is focused into a helium-filled hollow-core waveguide, producing high harmonics near 13 nm wavelength. A “rejector” mirror removes most of the fundamental laser light while reflecting the majority of the harmonic light. Thin Zr filters are used to remove the rest of the fundamental light while transmitting the HHG light. Finally, a pair of EUV multilayer mirrors select a single harmonic and focus the beam onto a test pattern. The diffracted light is measured on a CCD detector placed only cm’s past the sample. The inset shows an image retrieved using an iterative phase retrieval algorithm. Figure reproduced from Seaberg et al. [185].

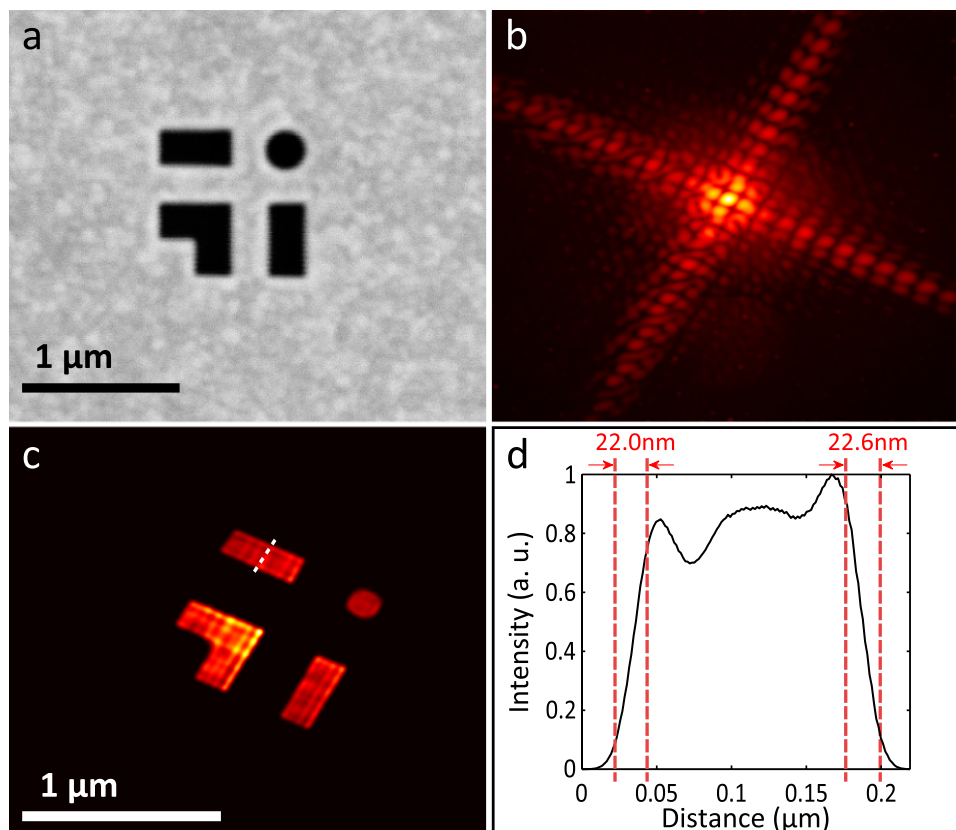


Figure 4.6: (a) SEM image of sample J409. (b) Recorded diffraction pattern using 13 nm light. (c) CDI reconstruction of the test pattern shown in (a). (d) Lineout across the dashed line in (c), demonstrating record 22 nm resolution. Figure adapted from Seaberg et al. [185].

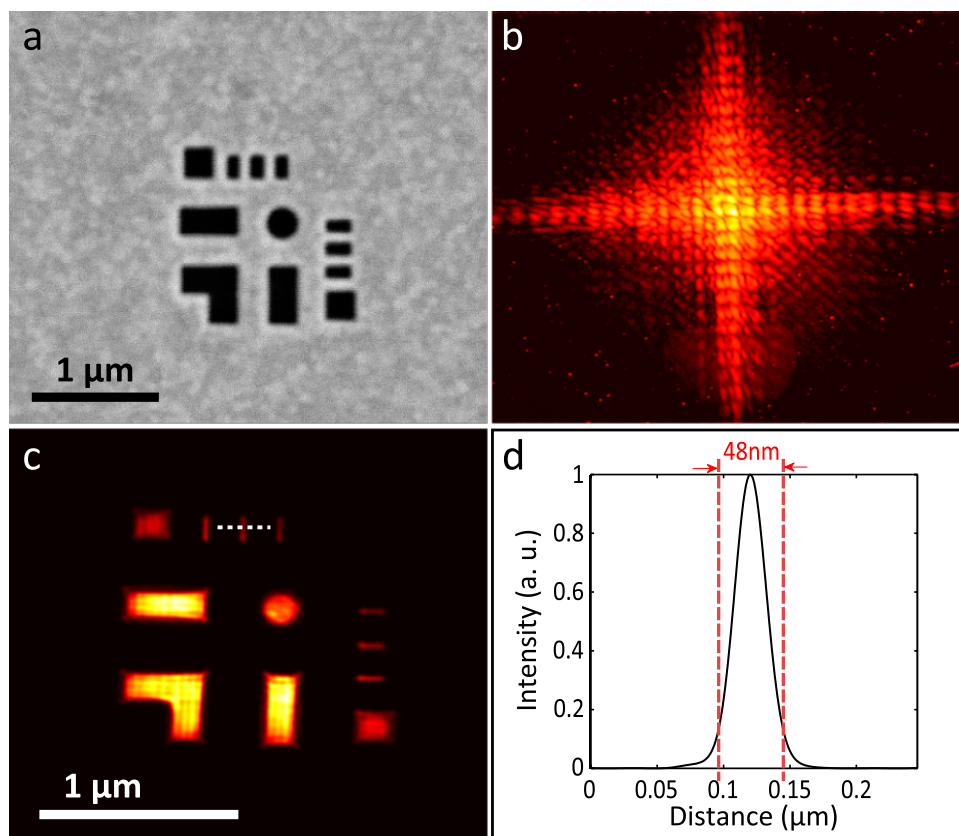


Figure 4.7: (a) SEM image of sample J407. (b) Diffraction pattern produced by sample J407. (c) CDI reconstruction of the test pattern shown in (a). (d) Lineout across the dashed line in (c), demonstrating that 50 nm features in the test pattern are easily resolved. Figure adapted from Seaberg et al. [185].

[215], HIO [39] and RAAR [204]. All of these algorithms converged to the same final object amplitudes. For the results shown in Figs. 4.6 and 4.7, we used the HIO algorithm, replacing the diffraction amplitude with experimental data after each iteration to serve as the Fourier-domain constraint, and a shrinking support [205] as the object-space constraint. The details of the full iterative algorithm are as follows: the HIO algorithm was allowed to converge, after which 1000 final iterations were averaged together to form one independent reconstruction. Thirty such fully independent reconstructions were averaged together to form the solution. Because independent solutions to the phase retrieval are equivalent except for the center positions of the image, independent reconstructions must first be registered with one another using sub-pixel cross-correlation followed by interpolation [216].

4.1.3 Analysis

The data for object J407 (Fig. 4.7) were obtained with the CCD placed 3.6 cm past the object, corresponding to a $NA \approx 0.36$. This allows for a maximum half-pitch resolution using coherent illumination of $\Delta r_{hp} = 0.5 \lambda / NA \approx 18$ nm, calculated using the Rayleigh criterion for coherent illumination. The lineout shown in Fig. 4.7(d) was taken along the profile marked in Fig. 4.7(c) by a white, dashed line. The $1/e^2$ diameter of this nano-fabricated feature is ≈ 50 nm, which provides an upper limit for our imaging resolution. Object J409 (Fig. 4.6) was placed 4.6 cm from the CCD, corresponding to a $NA \approx 0.28$. Using $NA = 0.28$ the half-pitch resolution would be $\Delta r_{hp} \approx 23$ nm. However, Fig. 4.6(b) clearly shows a strong signal to noise ratio out to the corner of the CCD; this increases the NA to 0.4, giving an angle-dependent Rayleigh criterion resolution between 17 nm and 23 nm. The Rayleigh criterion states the maximum resolution of an imaging system, Δr_{hp} , as the ability to resolve two points spaced by $2 \times \Delta r_{hp}$. In our case, however, the sample simply does not contain features this small; the smallest feature is ≈ 50 nm. A conventional alternative to the Rayleigh criterion is to test the distance over which an edge makes a transition from dark to light by measuring the distance between 10% and 90% of the maximum sample intensity. This method is known as the knife-edge test, and the results of such a test are

shown in Fig 4.6(d). Both edges in Fig. 4.6(d) transition from dark to light in a distance ≈ 22 nm, in excellent agreement with the resolution expected based on the NA used to generate this image. We note that the half-pitch resolution calculated using the Rayleigh criterion is usually directly associated with the distance measured using the knife-edge test. However, we point out that the relationship between resolutions measured using the knife-edge test and the Rayleigh criterion is actually closer to $\Delta r_{\text{KE}} \approx 85\% \Delta r_{\text{RC}}$, yielding a resolution of 23 nm. This is in excellent agreement with our data.

After reconstructing the object from its scatter pattern, the pixel area was decreased by a factor of 16 in the images plotted in Figs. 4.6(b) and 4.7(b), in order to accurately ascertain the 10% and 90% points of the intensity across an edge. The pixel size was modified via Fourier transform, zero-padding interpolation. Even though the pixel sizes in Fig. 4.6(b) and 4.7(b) were significantly decreased, no information was added because both objects were originally sampled at a frequency greater than the Nyquist frequency.

While the knife-edge test is convenient and provides an accurate resolution measure of an edge transition, a somewhat more powerful tool is the phase retrieval transfer function (PRTF), defined as

$$\text{PRTF}(f) = \sum_{f=\text{const}} \phi(f). \quad (4.5)$$

The diffraction phases $\phi(f)$ are averaged over constant frequency contours to produce the PRTF, which takes a value of 1 where the iterative algorithm produced perfect convergence consistently, and a value near 0 where the algorithm continually failed to converge. Before using Eq. (4.5) as a measure of the reconstructed image resolution, we constructed a Wiener filter [217] of the form

$$W(f) = \frac{|S(f)|^2}{|S(f)|^2 + |N(f)|^2}, \quad (4.6)$$

where $S(f)$ is the power spectral density of the measured diffraction pattern and $N(f)$ is a measure of the noise trend, taken to be a constant $0 < N < 1$ for our filter. We implemented the Wiener filter to produce an improved measure of image quality as $\text{wPRTF}(f) = W(f)\text{PRTF}(f)$, which is shown in Fig. 4.8.

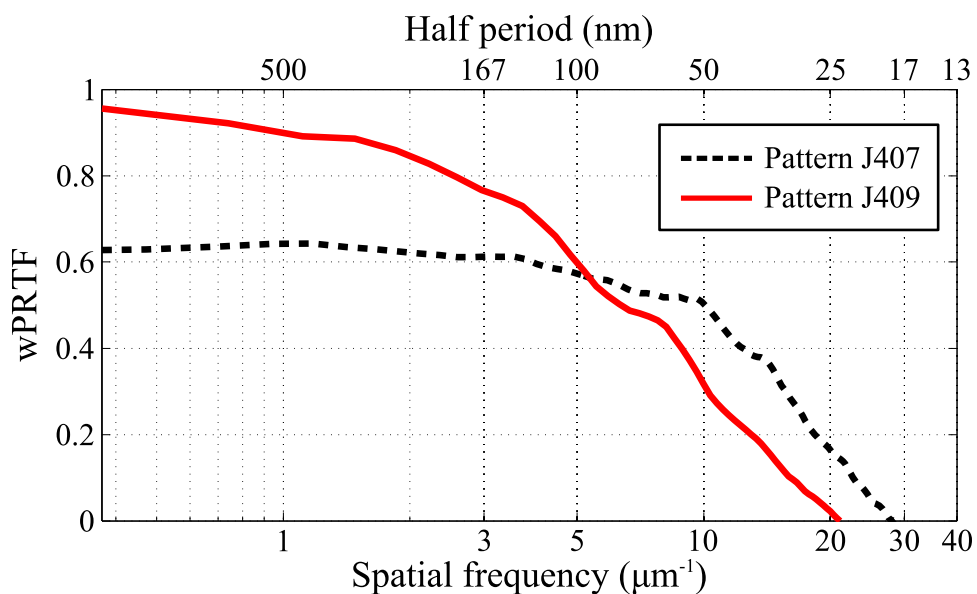


Figure 4.8: Filtered phase retrieval transfer function. Features in the wPRTF provide measures of the smallest sample features and the image resolution of reconstructed images. For example, the wPRTF for sample J407 shows a “knee” structure around 50nm half-period resolution, which corresponds to the feature size of the slots of ≈ 50 nm. The cutoff wPRTF values are between 19 and 22 nm, in excellent agreement with the knife-edge measurements shown in Fig. 4.6. Figure reproduced from Seaberg et al. [185].

Two critical features in the wPRTF can be used to express different types of image resolution. The wPRTF displays a “knee”-type structure where the slope increases rapidly in the negative direction. The point where the slope changes is interpreted as the minimum feature size in the sample. This is evident for sample J407, where the minimum sample feature size from the SEM image and our retrievals is ≈ 50 nm, in excellent agreement with the position of the “knee” in the wPRTF. The second feature is the cutoff value of the wPRTF, which can be interpreted as the maximum resolution achieved in the reconstruction. The cutoff value for sample J407 displays a maximum resolution of ≈ 19 nm, while the cutoff value for sample J409 indicates a maximum resolution of ≈ 22 nm, in excellent agreement with the knife-edge measurement and NA of the imaging system. The variation in brightness over the reconstructed images is explained by diffraction through the thick, absorbing objects. The depth of the nano-patterned holes in the Au test patterns was approximately 400 nm, which is deeper than the depth of field of our imaging system. A comparison with simulation is presented in the following section. Larger-scale variation in brightness may be due to non-uniform illumination, as the sample was placed at the 13 nm beam focus; the diameter of the beam was on the order of the sample size.

While independent reconstructions may only take ≈ 1 minute on a standard personal computer, the limiting factor for near real-time imaging using tabletop high harmonic EUV sources is the limited amount of available photon flux. By increasing the EUV flux at the sample to a value of $> 10^8$ photons/s, sample J409 was reconstructed using significantly shorter exposure times by taking advantage of on-chip binning (performed by the Andor camera) to a grid size of 256×256 pixels to increase the signal to noise ratio of the recorded pattern. The result is displayed in Fig. 4.9. The knife-edge test demonstrates a spatial resolution of ≈ 25 nm in an image acquisition time of only 30 seconds.

Since in our initial experiments the diffraction patterns (Figs. 4.6(b) and 4.7(b)) clearly extended beyond the edges of the CCD chip, we shortened the sample-to-CCD distance to just over 10 mm, corresponding to a $NA = 0.79$. It is well known from diffraction tomography that when collecting a pattern at such large angles, the 2-D pattern can actually be mapped onto

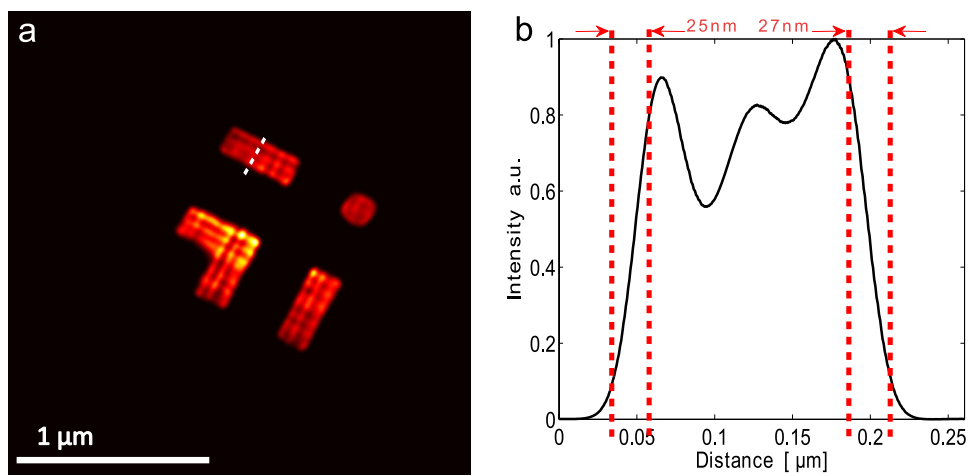


Figure 4.9: Sub-30 nm resolution from a 30 second exposure. Increases in HHG flux enabled by better differential pumping have led to a dramatic decrease in required exposure times. This has enabled 25 nm spatial resolution in an image with only 30 second exposure time. Figure reproduced from Seaberg et al. [185].

a spherical shell of radius $1/\lambda$ in the 3-D Fourier transform space, termed the Ewald sphere. It is important to note that for a thick sample (relative to the 2-D projection of the object in the direction of illumination) in combination with diffraction collection at a high NA, there is modulation in the pattern due to the depth information encoded in the 3-D pattern. In this case, the curvature correction described in previous work [218] does not recover the intensity of the 2-D Fourier transform of the object. To accurately recover the object to the resolution corresponding to the NA, a 3-D reconstruction technique - such as ankylography or tomography - must be employed.

In the 0.79-NA geometry, the diffraction pattern was above the noise level out to an angle corresponding to ≈ 0.6 NA. This data was mapped onto the Ewald sphere as described in Raines et al. [196] and the result is shown in Fig. 4.10(a). In this case the spherical shell is positioned in a 3-D cube, and the points in the cube where data is absent must be retrieved in addition to the phase at the known intensity points. The 0.6 NA imaging allows a best possible resolution Δr_{hp} of 10 nm in the x and y dimensions and 32 nm in the z dimension. An isosurface rendering of the resulting 3-D reconstruction is shown in Fig. 4.10(b). Since the walls of the sample are very absorbing at 13 nm, not all photons initially scattered reach the detector. Thus, this particular sample is not ideal for 3-D image reconstruction. Nevertheless, we are able to see that the sample was tilted by ≈ 10 degrees with respect to the detector (Fig. 4.10(c)) and also extract the relative size difference between features in the sample. This is interesting because the sample was fabricated on a 50-100 nm thick silicon nitride membrane. Thus, the scanning electron microscope images shown in Figs. 4.6(a) and 4.7(a) can only be taken from the front side, where the different etch depths are not apparent. In the future, the robustness of this high-NA 3-D imaging may be improved by illuminating an object with a broad bandwidth (e.g. several adjacent harmonics), thus filling in a significantly larger portion of the cube, using an extension of the technique demonstrated in Chen et al. [81].

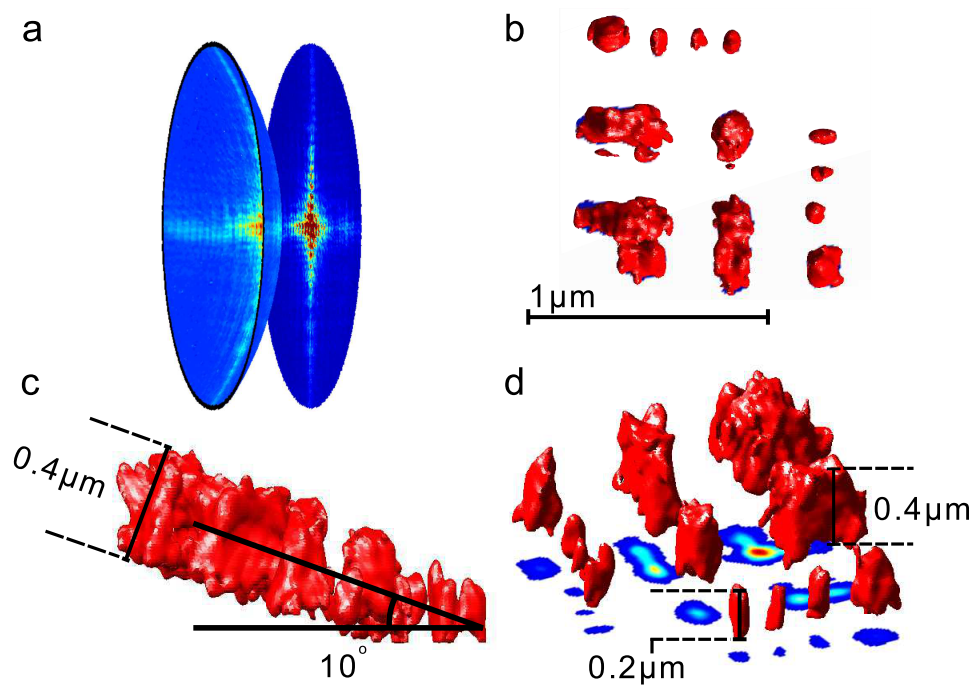


Figure 4.10: Demonstration of ankylography with a high-NA diffraction pattern. (a) Diffraction pattern mapped onto the surface of the Ewald sphere accompanied by a projection onto the plane. (b) Isosurface rendering of the 3-D ankylographic reconstruction. (c) Same as in (b) showing tilt of sample with respect to the detector. (d) Same as in (b) showing the relative size difference between features in the sample with emphasis in the z-direction, accompanied by a projection onto the plane. Figure reproduced from Seaberg et al. [185].

4.1.4 Simulation of diffraction from a thick, absorbing object

Close inspection of the image reconstructions presented in Figs. 4.6 and 4.7 reveals ripples in the intensity of the transmissive regions of the objects. These ripples can be explained by diffraction through a thick, absorbing object. The CDI experiment was simulated via multislice “spectrum-of-plane-waves” propagation through a 400 nm thick pattern etched in gold.

The pattern used for the simulation was an idealized version of the SEM image shown in Fig. 4.6(a). In the simulation, the transverse pixel size was 6.5 nm and the step size between propagation slices was 6.5 nm, in order to properly sample the wave. The complex index of refraction, n , of most materials at EUV and X-ray wavelengths is typically very close to 1, so that it is typically written as

$$n = (1 - \delta) - i\beta. \quad (4.7)$$

For gold at 13 nm, $\delta = 0.091$ and $\beta = 0.040$ [40]. The incident beam was assumed to be a plane wave with unit amplitude.

The magnitude of the simulated field at the exit of the 400 nm thick object, or “exit surface wave” (ESW), is shown in Fig. 4.11(a). This image can be compared directly to the image reconstructions shown in Figs. 4.6(c) and 4.9(a). Note that even the number and locations of the fringes in the simulation are consistent with those found in the image reconstructions. Next, the far-field diffraction pattern was simulated by taking the Fourier transform of the simulated ESW, with the resulting pattern shown in Fig. 4.11(b). For comparison, Fig. 4.11(c) shows the Fourier transform of a single slice of the simulated test pattern, representing an infinitesimally thin object. Finally, diffraction data collected at 0.79 NA is shown in Fig. 4.11(d), after curvature correction was applied [218].

As can be seen from Fig. 4.11(b)-(d), both the simulated diffraction where finite thickness was accounted for and the measured diffraction data do not exhibit centrosymmetry. In contrast, the simulated diffraction from an infinitesimally thin object (single slice) does exhibit centrosymmetry, and is qualitatively very different from the patterns shown in Fig. 4.11(b) and (d). The results of this

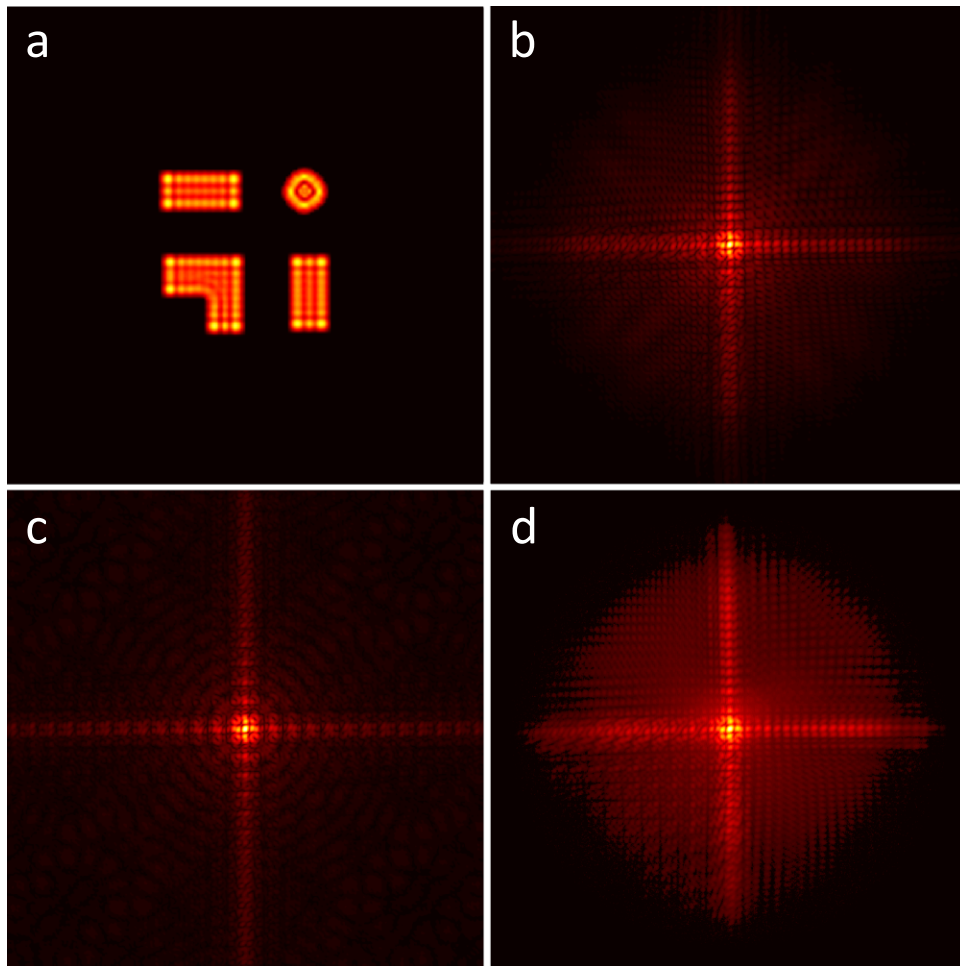


Figure 4.11: (a) Simulated exit surface wave (ESW) resulting from multi-slice propagation through a 400 nm thick gold sample. (b) Simulated far-field diffraction pattern of the thick object, obtained by calculating the Fourier transform of the ESW in (a). (c) Fourier transform of a single-slice object, simulating the diffraction pattern due to a very thin object. (d) Measured diffraction data from test pattern J409, collected at $NA > 0.6$.

simulation indicate that while we were able to attain very high (22 nm) resolution in this experiment, images produced by CDI are not necessarily true representations of thick, absorbing objects. This is because, as opposed to a surface imaging technique such as SEM, the CDI reconstruction is affected by diffraction of light through the object along the direction of propagation. This problem can be partially remedied by moving to a 3-D reconstruction technique, such as ankylography or tomography. However, in the case of a strongly absorbing object, absorption and multiple scattering can occur which lead to artifacts in the reconstruction.

4.2 Tabletop keyhole CDI

After demonstrating the ability to achieve very high 22 nm resolution with 13 nm wavelength, our efforts shifted towards extending the capability of our tabletop CDI microscope to image more complex objects. Initially, this meant moving away from simple “pinhole-like” samples. The difficulty in this step forward lies in the need for an object-plane support as one of the constraints in conventional CDI. For objects that are not “pinhole-like,” the support can be much less well-defined. This is especially true if the sample is too large for the oversampling criterion to be met. Fortunately, a number of generalizations to CDI have been developed that either allow this constraint to be modified in a number of ways. These generalizations include keyhole CDI, apertured illumination CDI, and ptychography CDI, all of which are discussed in detail in Ch. 3. The first successful imaging results of more complex, transparent samples using HHG CDI are presented below, in which keyhole CDI was used for implementation [182]. These first results were obtained using 29 illumination, due to less experimental difficulty at this wavelength.

4.2.1 Extended objects

Our first step towards imaging more complicated objects involved using an extended test pattern, meaning it was too large to illuminate all at once. The utility of keyhole CDI comes from the ability to use the extent of the illumination as the “support” rather than the extent of the object. Small modifications to the experimental setup were necessary in order to use the

illumination as the support. As described in Abbey et al. [201], the goal was to provide a sharply defined, diverging wavefront as the illumination to the sample. The two main modifications made to achieve this goal included replacement of the 50 cm focal length multilayer mirror used previously with a 12.5 cm focal length mirror, and placement of a pinhole in the beam on its way to the focus. These modifications are depicted in Fig. 4.12.

The laser system used in this experiment was the same as that described in Section 4.1.2, configured to run at 3 kHz repetition rate with 1 mJ pulse energy. The laser was focused into a 150 μm ID waveguide filled with argon gas at a pressure near 60 torr, in order to phase-match high harmonics near 29 nm. Two 200 nm thick Al filters were placed between the waveguide and the imaging chamber, in order to block the residual driving laser light. Inside the chamber, the harmonics were reflected off two Mg/SiC multilayer mirrors with peak reflectivity at 43.2 eV (28.7 nm) and full width half maximum (FWHM) reflectivity bandwidth of 2.1 eV. The first mirror was flat while the second had a 25 cm radius of curvature (ROC); these mirrors served to select only the 27th harmonic and refocus the beam. A 50 μm diameter pinhole was placed in the beam ≈ 2 mm before the focus, in order to place a sharp edge on the beam. The X-ray CCD (Andor iKon) was placed 44.6 mm beyond the focus, so that the numerical aperture of the system was approximately 0.3.

Due to the inability to achieve normal incidence on the curved mirror due to geometrical constraints, some astigmatism was introduced into the EUV beam. The vertical and horizontal focus positions were determined by scanning the pinhole across the beam at multiple locations along the beam axis. The separation between foci was determined to be 0.55 mm, with 50 μm precision. The test pattern used in this experiment was fabricated using e-beam lithography, and consisted of etched features in a 100 nm thick gold layer deposited on a thin silicon nitride membrane (shown in Fig. 4.13). The test pattern was first placed 1.3 mm downstream of the circle of least confusion (COLC, the midpoint between the two foci), so that the beam diameter on the sample was approximately 25 μm . The sample was translated so that region I depicted in Fig. 4.13 was illuminated, producing the diffraction pattern shown in Fig. 4.14(a), which was recorded in a 30

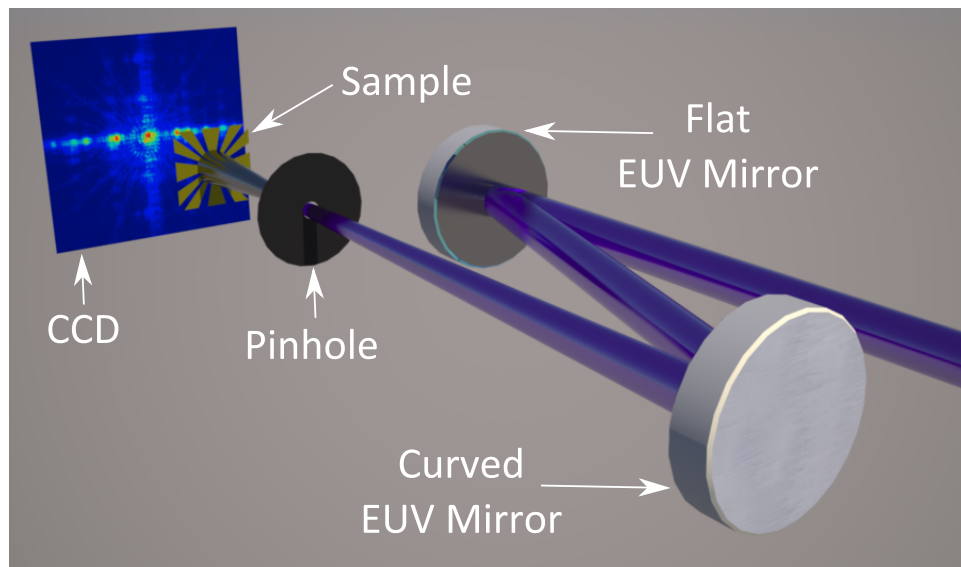


Figure 4.12: Schematic of initial experimental geometry for tabletop keyhole CDI. The 50 cm focal length curved mirror used previously was replaced with a 12.5 cm focal length mirror. Additionally, a pinhole was placed in the beam on its way to the focus, in order to place a sharp edge on the otherwise Gaussian beam. The sample was placed downstream of the focus so that it was illuminated with a diverging wavefront, and, as before, the CCD was placed near the object in order to collect high angle diffraction. Figure adapted from Zhang et al. [182].

minute exposure. Second, the sample was positioned 0.9 mm past the COLC, so that the beam diameter was approximately $18 \mu\text{m}$, and translated so that region II depicted in Fig. 4.13 was illuminated. The resulting diffraction pattern, recorded in another 30 minute exposure, is shown in Fig. 4.14(c).

For this test pattern, only the etched regions of the gold were transparent, whereas the rest of the object was completely opaque to the 29 nm illumination. This meant that all of the light at the detector could be considered to be scattered light; none of the unscattered, incident beam reached the detector unperturbed. Thus, in this case the central region of the diffraction pattern can't be considered to be a "holographic" region as described in the first description of the technique [201]. However, as discussed in Ch. 3, the diffraction pattern is similar (up to a magnification factor) to that which would be recorded in the near field with plane wave illumination. This fact is evident in the asymmetry of the diffraction patterns in Figs. 4.14(a) and (c), particularly near the centers of the patterns. This asymmetry aids in the image reconstruction through the fact that the solution to the phase of the diffraction pattern is unique [219].

Phase retrieval of the diffraction patterns shown in Figs. 4.14(a) and (c) was achieved using the RAAR algorithm [204], in combination with shrinkwrap support [205] and non-negativity object-domain constraints. Use of the non-negativity constraint was made possible by dividing out the phase curvature of the incident beam. The exit surface wave (ESW), ψ_o , can be considered to be the product

$$\psi_o(\vec{r}') = \psi_i(\vec{r}')t(\vec{r}'), \quad (4.8)$$

where ψ_i is the incident illumination, t is the complex transmission of the object, and \vec{r}' represents the sample plane coordinates. The incident illumination ψ_i can be decomposed into its amplitude and phase, as

$$\psi_i(\vec{r}') = |\psi_i(\vec{r}')| e^{i\phi_i(\vec{r}')}, \quad (4.9)$$

where the phase of the incident wave, ϕ_i , is defined as

$$\phi_i = \tan^{-1} \left(\frac{\text{Im}(\psi_i)}{\text{Re}(\psi_i)} \right). \quad (4.10)$$

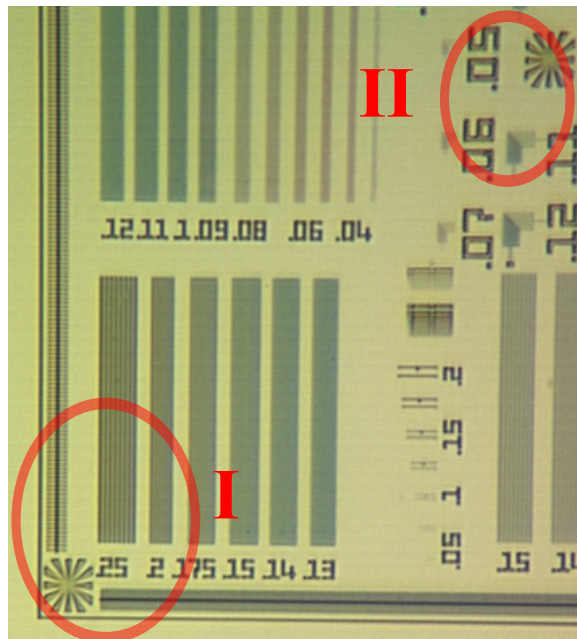


Figure 4.13: Extended test pattern used to demonstrate tabletop keyhole CDI. The regions highlighted by red ovals were both imaged independently, with reconstructions shown in Fig. 4.14. Figure adapted from Zhang et al. [182].

If the incident illumination is approximated as a simple astigmatic Gaussian beam, the phase ϕ_i can be written as

$$\phi_i = \frac{\pi}{\lambda} \left(\frac{x^2}{R(z_c + z_a)} + \frac{y^2}{R(z_c - z_a)} \right), \quad (4.11)$$

where $R(z)$ is the radius of curvature of a Gaussian beam a distance z from its focus, z_c is the distance to the COLC, and z_a is half the distance between horizontal and vertical foci. $R(z)$ is defined as

$$R(z) = z \left[1 + \left(\frac{z_R}{z} \right)^2 \right], \quad (4.12)$$

where z_R is the Rayleigh range. For this experimental geometry z_R was $\approx 250 \mu\text{m}$, based on a focusing NA ≈ 0.01 . This Rayleigh range was long enough relative to the sample-to-focus distances that it had to be taken into account.

In general, we are interested in reconstructing t in Eqn. 4.8. Here what was actually reconstructed, since the phase of the incident beam was divided out, was $|\psi_i(\vec{r}')| t(\vec{r}')$. Thus, non-uniformities in the incident beam were coupled with information about the object. The object reconstructions resulting from illumination of regions I and II are shown in Figs. 4.14(b) and (d), respectively. Note that there is evidence of non-uniform illumination, due to the fact that in keyhole CDI, the field-of-view (FOV) is defined by the entire incident beam rather than the object. Ptychography methods can be used to remove these non-uniformities, since the object and “probe” are reconstructed independently [85, 86]. However, there is a tradeoff in that ptychographic phase retrieval requires the collection of many diffraction patterns for a single image reconstruction, whereas keyhole CDI only requires a single diffraction pattern.

The resolution of this first successful demonstration of keyhole CDI using a tabletop HHG source was approximately 100 nm half-pitch, much lower than that achieved in the previous section. However, the main importance of this result lies in its implications of what will be possible in the future. The fact that nearly the entire HHG beam can be used as the object support for keyhole CDI imaging is further proof of the full spatial coherence of high harmonic generation. Additionally, the fact that the harmonic beam was stable enough over the course of 30 minutes to provide

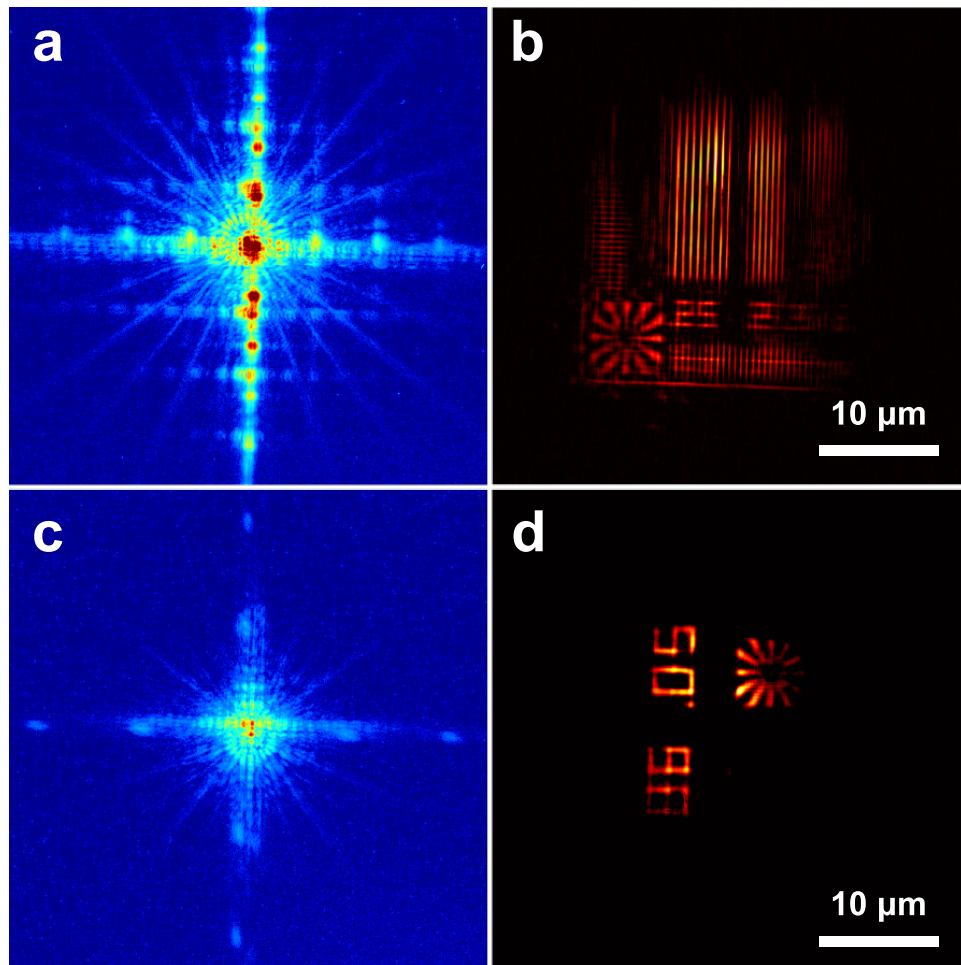


Figure 4.14: (a) Measured diffraction pattern when illuminating the test pattern shown in Fig. 4.13 at region I. (b) Keyhole CDI reconstruction of region I. (c) Measured diffraction pattern when illuminating the test pattern at region II. (d) Keyhole CDI reconstruction of region II. Figure adapted from Zhang et al. [182].

steady illumination across the entire FOV is extremely important for future time-resolved imaging experiments that, in order to obtain quantitative dynamic information, will require the assumption that the illumination doesn't change during the course of the experiment.

4.2.2 Transparent objects

Another challenge not previously addressed successfully using HHG CDI is the imaging of objects that are mostly semi-transparent, with relatively weak contrast. This is an extremely important type of sample from a scientific point of view, in that this type of sample is representative of biological cells. Also, this type of sample is analogous to technologically interesting surfaces which could be imaged in a reflection geometry.

Part of the difficulty in imaging this type of sample is that the scattering efficiency is typically lower due to lower absorption contrast. Thus, any stray light incident on the detector may be brighter than the diffraction from the sample. For instance, there is incoherent atomic line emission (ALE) of HHG gas media [220] at photon energies that fit inside the transmission bandwidths of typical metal filters used to separate the high harmonics from the fundamental laser light. In particular, there are many emission lines from singly ionized argon (Ar II) between 40 and 80 nm wavelength [221,222] which fit inside the transmission bandwidth of aluminum. Neutral helium has several emission lines near 50 nm [222], which fit inside the transmission bandwidth of zirconium filters.

Because this atomic emission is incoherent, it radiates to 4π , which means that compared to laser-like high harmonic beams with typical divergence ≈ 1 mrad, its radiant intensity (power per unit solid angle) relative to the harmonic beam should be relatively small. Empirical data shows that the radiant intensity of HHG is only 10-20 times higher than that for ALE for a 300 μm phase-matching length, so that in a 5 cm waveguide it can be assumed that, in a best case scenario, HHG has spectral radiance $\approx 10^3$ times higher than that of ALE [223]. When compared to sample diffraction, which may be several orders of magnitude less bright than the unscattered harmonic beam, incoherent ALE may be a problem. For this reason, it is extremely important to only allow

light inside the divergence cone represented by the high harmonic beam to reach the detector. This can be accomplished in as simple a manner as placing an aperture in the beam path that has diameter at least as small as the HHG beam at that position, similar to the pinhole described in Section 4.2.1.

Unfortunately, the simple solution of placing a pinhole in the beam path, which seems to fix the problem of incoherent background light, introduces a new problem. Because the pinhole diameter is chosen to be on the order of the HHG beam diameter, there is appreciable diffraction due to the pinhole, as can be seen in Fig. 4.15(a). First attempts to image overall transparent objects made it clear that the scattering from the pinhole was a problem. This is due to the fact that for objects with low contrast, the scattered light from the pinhole obscured scattered light from the sample. Furthermore, in the sample plane this scattered light covered a much larger area than could be oversampled based on the distance between the sample and detector planes. A realistic simulation of the experimental geometry, using the Fresnel diffraction formula for beam propagation, confirmed that the pinhole is causing this diffraction. The simulated beam profile at the detector is shown in Fig. 4.15(b).

The idea of the order sorting aperture (OSA) used to remove unwanted orders when focusing with a zone plate condenser was borrowed as an idea to remove the unwanted pinhole diffraction. A second pinhole was inserted into the simulation, placed closer to the focus and with diameter larger than that of the direct beam. The resulting simulated beam profile at the detector is shown in Fig. 4.15(c). As can be seen from the figure, this second pinhole acts as a spatial filter, removing the unwanted scattered light and providing a very clean illumination. When this idea was implemented in the experimental geometry, the resulting beam profile (shown in Fig. 4.15(d)) agreed very well with the predicted profile from the simulation. The close agreement between experiment and simulation (with no fitted parameters) is further evidence of the excellent Gaussian beam quality and full spatial coherence of the high harmonic source [31,92,210].

Now that we were able to produce a clean, finite beam such as that shown in Fig. 4.15(d), we were ready to image weakly scattering objects. A schematic of the experimental geometry for this

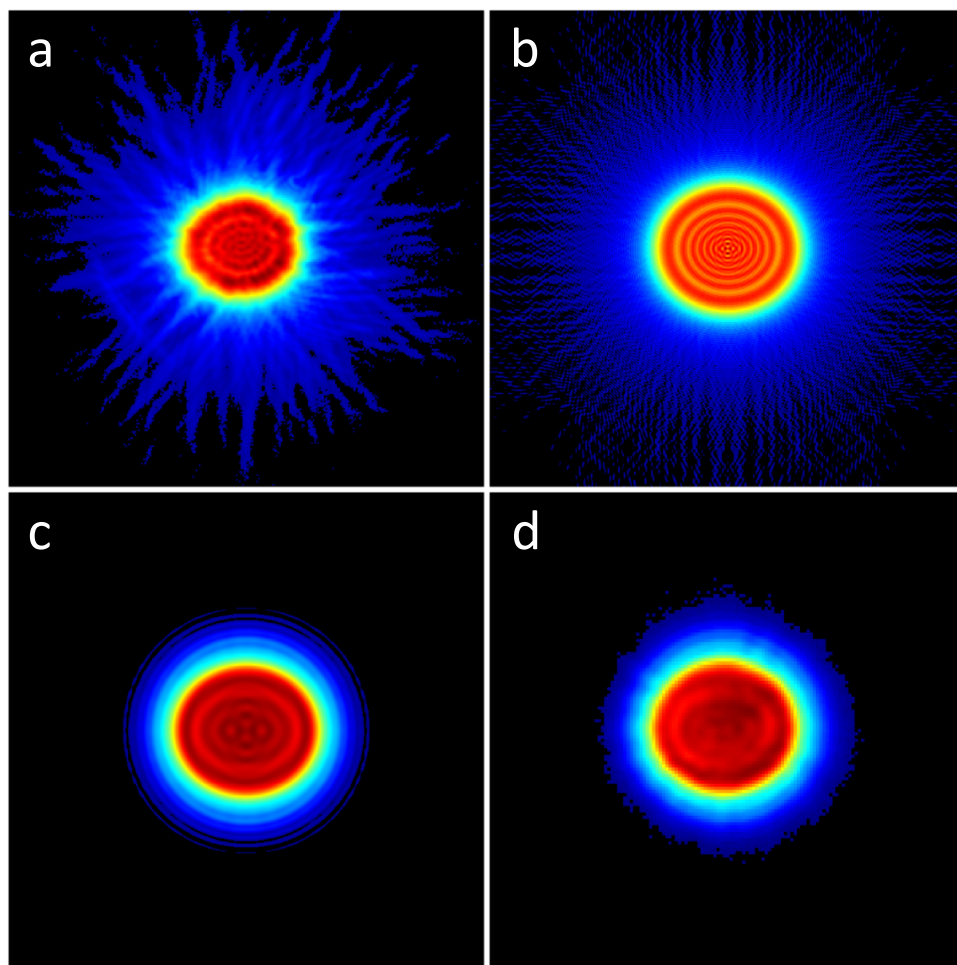


Figure 4.15: Simulated and measured beam profiles at the detector. (a) Measured beam profile at the detector plane with a single pinhole, of diameter approximately that of the beam diameter, placed in the beam path on the way to the focus. Note that there is a considerable amount of scattered light due to the pinhole. This beam profile is representative of that used to obtain the keyhole results shown in Fig. 4.14. (b) Simulated beam profile at the detector for the experimental geometry used to produce the measured beam profile in (a). (c) Simulated beam profile when a second pinhole is placed in the beam path, near the focus. The pinhole diameter is chosen to be larger than the size of the focus, so that it acts as a spatial filter. (d) Measured beam profile after implementing the pinhole “spatial filter.” The beam profiles shown in (a)-(d) are thresholded at 1% of peak intensity.

demonstration is shown in Fig. 4.16. The first pinhole, used to produce a more sharply-defined, finite beam, was placed 16 mm upstream of the COLC and was 200 μm in diameter. The second pinhole, with 50 μm diameter, was placed 1.4 mm upstream of the COLC. As described above, this pinhole was large enough to allow the direct beam to pass, and had the sole function of removing light scattered by the first pinhole. Prior to placing the sample in the beam path, the illumination was characterized as described in Quiney et al. [224], with the small modification that the astigmatism was taken into account. Similarly to the keyhole reconstruction described in the previous section, the wavefront curvature (based on measurements of the horizontal and vertical focus positions) was divided out in the plane of the first pinhole, so that a non-negativity constraint could be applied in this plane. At each iteration, the curvature was added back in after the constraint was applied. The result of this reconstruction is shown in Fig. 4.17, where the sagittal and tangential meridional slices are plotted near the COLC.

In this case, the sample consisted of a 30 nm-thick layer of chromium deposited on a 45 nm-thick silicon nitride membrane. Features were etched in this two layer system using a focused ion beam, shown in Fig. 4.18(a). The sample was placed at the COLC, where the beam diameter was approximately 8 μm . The amplitude and phase of the illumination at the COLC are shown in Figs. 4.17(c) and (d), respectively. The resulting diffraction pattern, as measured on the detector 5.71 cm away, is shown in Fig. 4.18(b) scaled to the 1/4 power. The inset of Fig. 4.18 shows the direct, unscattered beam. As can be seen from the figure, the light scattered by the object is a small perturbation to the unscattered beam. The fact that there is a large amount of unscattered light means that the pattern can be treated as an in-line hologram, with the unscattered beam treated as the reference wave. This can easily be seen in the plane of the sample by examination of the exit surface wave (ESW), ψ_T , which can be written as

$$\psi_T = \psi_0(\vec{r}')t(\vec{r}'), \quad (4.13)$$

where ψ_0 is the incident beam, t is the complex transmission of the object, and \vec{r}' represents the coordinates in the sample plane. In order to separate the object and reference waves, t can be

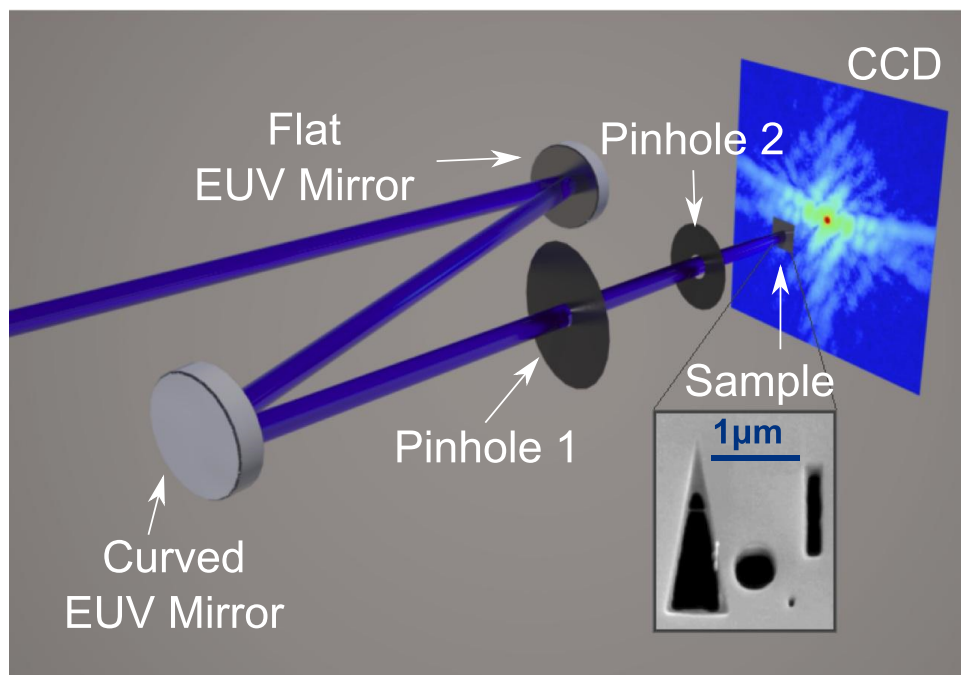


Figure 4.16: Schematic of revised keyhole CDI experimental geometry. The only change from the geometry shown in Fig. 4.12 is the addition of a second pinhole near the focus. The pinhole diameter is chosen to be larger than the size of the beam, so that it simply functions to remove the majority of the scattered light from the first pinhole. The inset shows the sample used to demonstrate keyhole CDI with a semi-transparent object. Figure adapted from Zhang et al. [182].

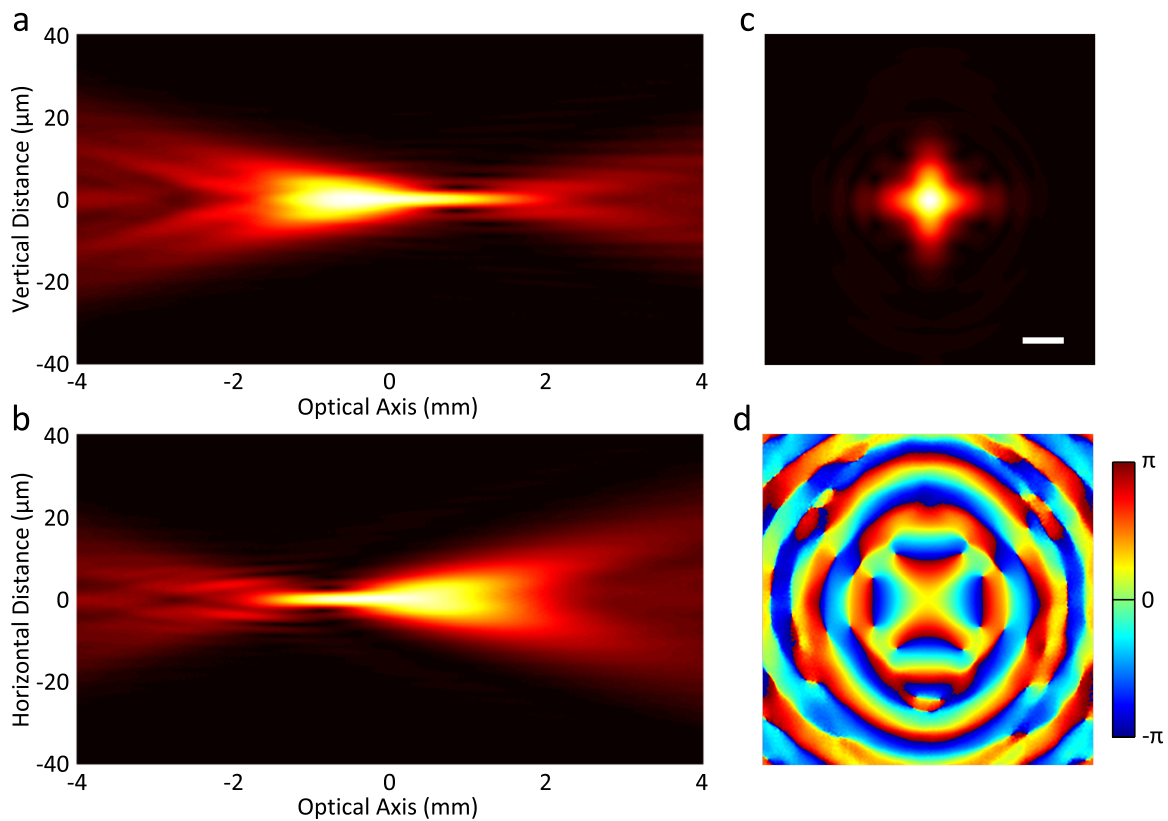


Figure 4.17: (a) Sagittal and (b) tangential meridional slices of the reconstructed illumination surrounding the circle of least confusion. (c) Amplitude of the reconstructed illumination at the circle of least confusion. The scale bar has width $5 \mu\text{m}$. (d) Phase of the illumination at the circle of least confusion, shown at the same scale as in (c).

written as

$$t(\vec{r}') = t_0 \left(1 + \frac{\Delta t(\vec{r}')}{t_0} \right), \quad (4.14)$$

where t_0 is the “background” transmission of the object and Δt is the modification to the object transmission at the “featured” regions. Both t_0 and Δt are in general complex, but for convenience the phase of t_0 can be set to 0. Combining Eqns. (4.13) and (4.14), we can identify the reference wave, ψ_r , as

$$\psi_r = \psi_0(\vec{r}')t_0 \quad (4.15)$$

and the object wave, ψ_o , as

$$\psi_o = \psi_0(\vec{r}')\Delta t(\vec{r}'). \quad (4.16)$$

Note that full knowledge of the reference wave in relation to the object wave requires knowledge of t_0 . Fortunately, t_0 can be measured by comparing the amplitudes of the unscattered beam with and without the Cr/Si₃N₄ layer pair placed in the beam path. The reference wave can be used both to calculate an initial low-resolution image of the object and also to improve the convergence of a CDI reconstruction [225]. The major difference between this approach and that used in traditional CDI involves the way in which the modulus constraint, which enforces consistency with the measured diffraction pattern, is applied. Here, the modulus constraint was applied in the following way: First, the current guess for the object wave was propagated to the detector plane. Second, the reference wave (calculated at the detector plane) was added coherently to the object wave, after which the modulus constraint was enforced. Third, the reference wave was subtracted and the new guess for the object wave was propagated back to the sample plane. Fourth, the phase of the incident wave, ψ_0 , was subtracted from the object wave so that a non-negativity constraint could be applied. Fifth, the phase of the incident wave was added back in, to give the new guess for the object wave which is fed into the next iteration.

Image reconstructions were retrieved using ≈ 100 iterations of the RAAR phase retrieval algorithm [204], followed by 10 iterations of the error reduction algorithm [39]. The reconstructed amplitude and phase of the “features” of the object, Δt defined in Eq. (4.14), are shown in Figs. 4.18(c)

and (d), respectively. Quantitative depth information can be obtained by adding together Δt with t_0 in order to obtain the full transmission function, t , of the object. The phase information contained in t can be combined with knowledge of the material composition of the object (and corresponding indices of refraction) in order to calculate the etch depth as a function of \vec{r}' . Because this sample is composed of two layers of different materials, it is also necessary to know the thickness of the top layer. With the index of refraction written as $n = 1 - \delta + i\beta$, the etch depth, d , can be related to the phase of t , ϕ_t , as

$$d(\phi_t) = \begin{cases} -\frac{\lambda\phi_t}{2\pi\delta_{\text{Cr}}} & \text{for } 0 \leq \phi_t \leq \frac{2\pi}{\lambda}\delta_{\text{Cr}}h_{\text{Cr}}, \\ -\frac{\lambda\phi_t}{2\pi\delta_{\text{Si}}} - \frac{h_{\text{Cr}}}{\delta_{\text{Si}}}(\delta_{\text{Si}} - \delta_{\text{Cr}}) & \text{for } \phi_t > \frac{2\pi}{\lambda}\delta_{\text{Cr}}h_{\text{Cr}}, \end{cases} \quad (4.17)$$

where h_{Cr} is the thickness of the Cr layer, δ_{Cr} and δ_{Si} are known values for δ at 29 nm for the Cr and Si_3N_4 layers, respectively [40], and the depth d is negative where material has been removed. Because the Cr layer was evaporated onto the Si_3N_4 membrane, its density was actually only 91% of the bulk value, as determined by X-ray reflectivity measurements, so that δ_{Cr} was 91% of the tabulated value. The thickness of the Cr layer, h_{Cr} was known to be 30 nm based on the fabrication process. A depth map based on the image reconstruction as well as the above known quantities is shown in Fig. 4.19(b), which can be compared with a depth map obtained from an atomic force microscope (AFM, Digital Instruments Dimension 3100) shown in Fig. 4.19(a).

The depth map results are compared quantitatively along a lineout (dashed line in Fig. 4.19(b)), shown in Fig. 4.19(c), showing very good agreement within error bars (the uncertainty calculation is described in Zhang et al. [182]). Further agreement is found when comparing the depth of the smallest feature in the sample, a 50 nm diameter circle. The etch depth of this circle was found to be 28(9) nm using CDI and 20(5) nm using AFM. The depth maps are also displayed in a 3D perspective in Figs. 4.19(d) and (e) based on AFM and CDI measurements, respectively.

4.3 Conclusions

The results presented in Section 4.1 using 13 nm, along with previous work from our group at 29 nm [211], demonstrate that CDI using HHG allows for near-wavelength-limited resolution.

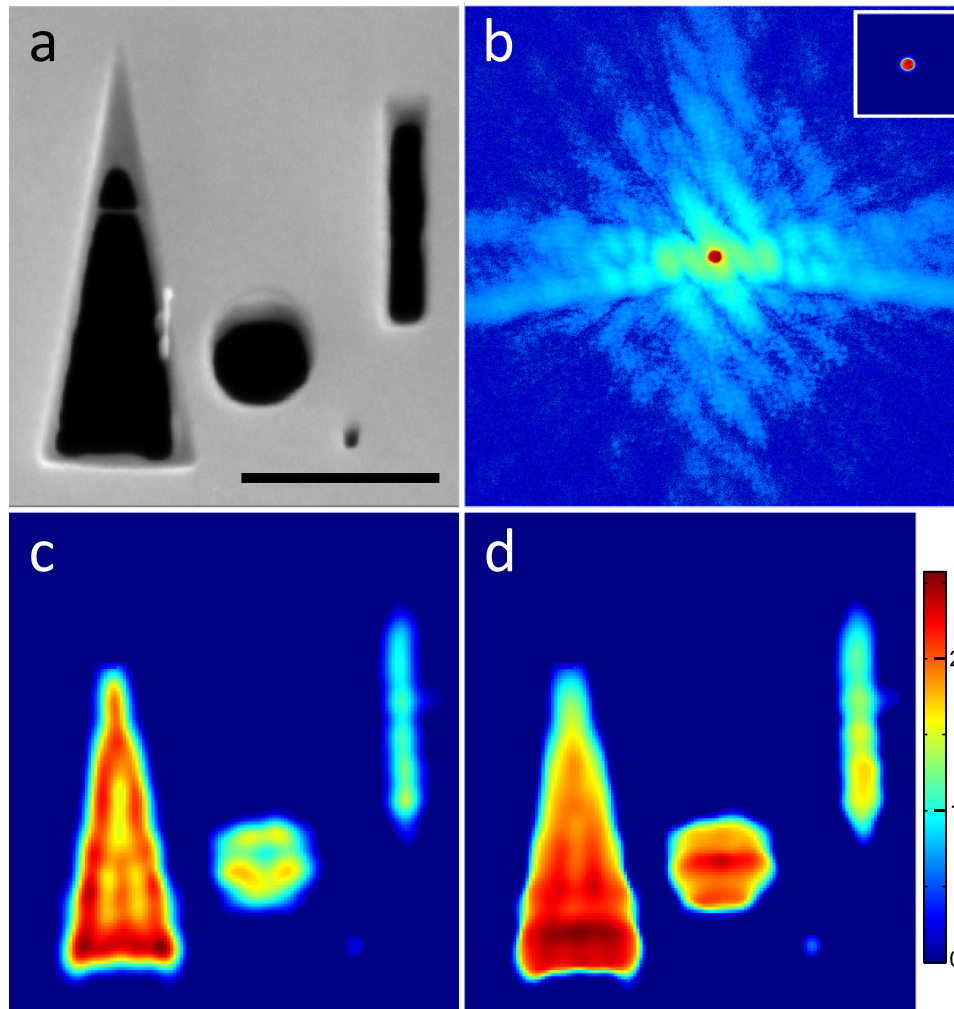


Figure 4.18: (a) Test pattern fabricated using focused ion beam. The scale bar has width $1\ \mu\text{m}$. (b) Diffraction pattern obtained using the test pattern shown in (a), scaled to the $1/4$ power. The inset shows the unscattered beam. (c),(d) Reconstructed amplitude (c) and phase (d) of the test pattern, with the unscattered reference beam subtracted as discussed in the text. The scale bar in (a) is shared with (c) and (d). Figure adapted from Zhang et al. [182].

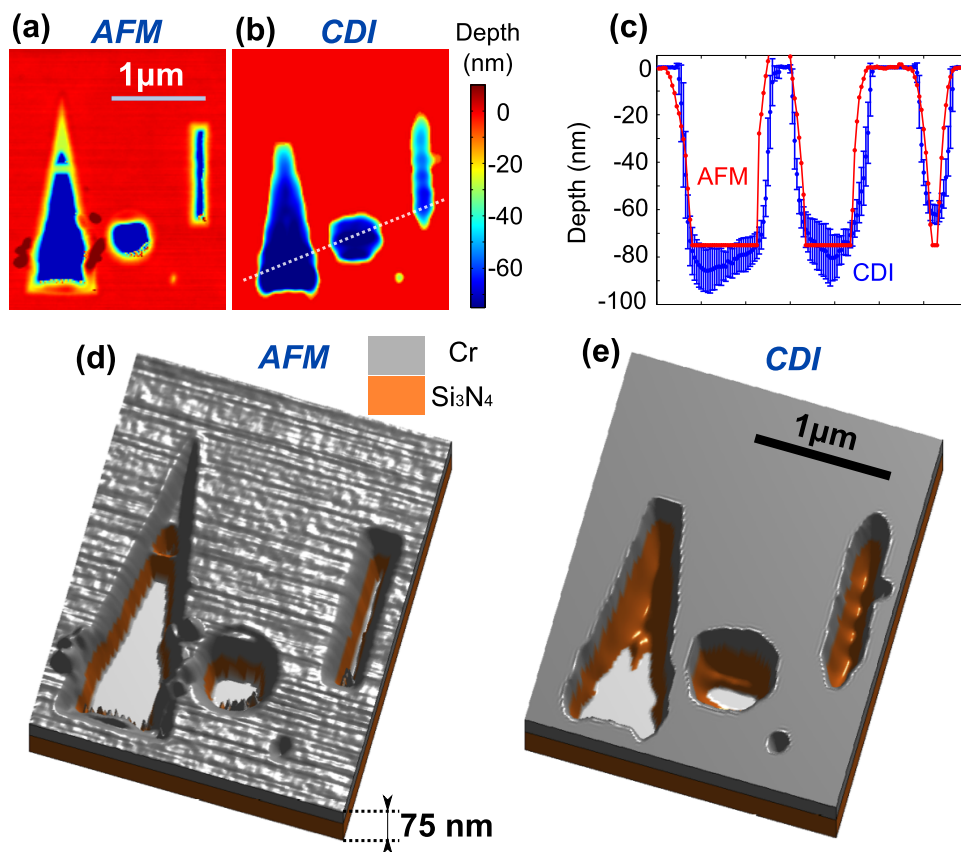


Figure 4.19: (a),(b) Depth profiles from (a) AFM and (b) CDI. The colorbar to the right of (b) is shared with (a). (c) Lineout along the dashed white line shown in (b), showing good quantitative agreement between AFM and CDI. (d),(e) 3D profiles of the test pattern based on (d) AFM and (e) CDI measurements. The chromium and silicon nitride layers are shown in different colors. Figure adapted from Zhang et al. [182].

While the initial demonstrations of tabletop keyhole CDI, presented in Section 4.2, were at lower resolution, they represent the capability to image more complex samples than was previously possible. The keyhole technique has more demanding requirements on source stability and coherence, so the successful results presented are further evidence of the laser-like properties of the high harmonic source. In the future, the keyhole technique will allow for time resolved imaging of real, complex nano-systems for the study of topics such as spin and energy transport at the nanoscale.

Chapter 5

Coherent Diffractive Imaging in a Reflection Geometry

Up to this point, the potential for harnessing the power of CDI for imaging complex nanostructured surfaces, which requires the use of a reflection geometry for imaging, has been largely ignored. Surfaces are critical in nanoscience and nanotechnology, for example in catalysis, energy harvesting systems or nanoelectronics. A few successful demonstrations have applied CDI to reflection-mode imaging. However, work to date has either been limited to highly reflective EUV lithography masks in a normal incidence geometry [226], restricted to low numerical aperture through the use of a transmissive mask [227], or restricted to isolated objects [228, 229].

5.1 First attempts at tabletop reflection mode imaging

Our first experiment towards reflection mode imaging involved keeping the experimental geometry as simple as possible. This meant placing a sample at 45° angle of incidence near the focus of the EUV beam, with the detector placed immediately after the sample as before. A schematic diagram of the experimental geometry is shown in Fig. 5.1. Similar to what is described in previous chapters, the high harmonic source was generated using a Ti:sapphire amplifier system (KMLabs DragonTM, 3 kHz repetition rate, 2 mJ pulse energy, 25 fs pulse duration, centered at 785 nm). The laser was coupled into the EH_{11} mode of a 5 cm-long, 150 μm -ID hollow-core waveguide filled with ≈ 60 torr of argon, producing several high harmonics near 29 nm. After blocking the fundamental laser light with two 200 nm-thick Al filters, two Mg/SiC multilayer mirrors select the 27th harmonic at 29 nm and focus the EUV beam onto the sample. The sample used for this experiment was a

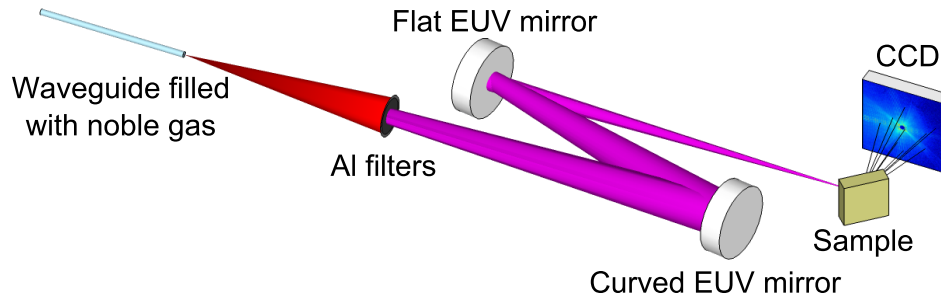


Figure 5.1: Schematic for initial reflection mode experiments. The 29 nm EUV beam was focused onto the sample using two multilayer mirrors, with 45° angle of incidence on the sample. The detector was placed directly after the sample, so that the detector plane was oriented normal to the specular reflection. Figure adapted from Gardner et al. [193].

periodic array of identical nickel nano-pillars patterned on a sapphire substrate. The nano-pillars were each $2 \mu\text{m}$ square and 20 nm tall. The detector was placed 4.5 cm away from the sample, oriented so that its surface was normal to the specular reflection of the beam.

As usual, the diffraction pattern is proportional to the Fourier transform of the scatterer in the far field. However, the non-zero angle of incidence on the two-dimensional grating sample distorts the scatter pattern (see Fig. 5.2(a)). Fortunately, these distortions can be taken into account using a coordinate transformation termed tilted plane correction (described in Ch. 3), which corrects the distortion to yield a pattern proportional to the actual Fourier transform of the nano-patterned array. The corrected pattern is shown in Fig. 5.2(b). In this case, the corrected scatter pattern is the product of a sampling comb whose spacing is set by the period of the nano-pillar spacing with the average of the Fourier transform of all of the illuminated pillars.

The intensity value at each peak in the corrected diffraction pattern was sampled and placed onto a new, coarser, grid, producing an oversampled diffraction pattern that represents the Fourier amplitude of the averaged pillars, shown in Fig. 5.2(c). In this case, the oversampling ratio is ≈ 4 , set by the inverse of the duty cycle of the pillars. Notice that the bright central peaks of the diffraction patterns shown in Fig. 5.2 were blocked in order to collect high angle scattering within the dynamic range of the CCD. During the iterative phase retrieval process, the algorithm was

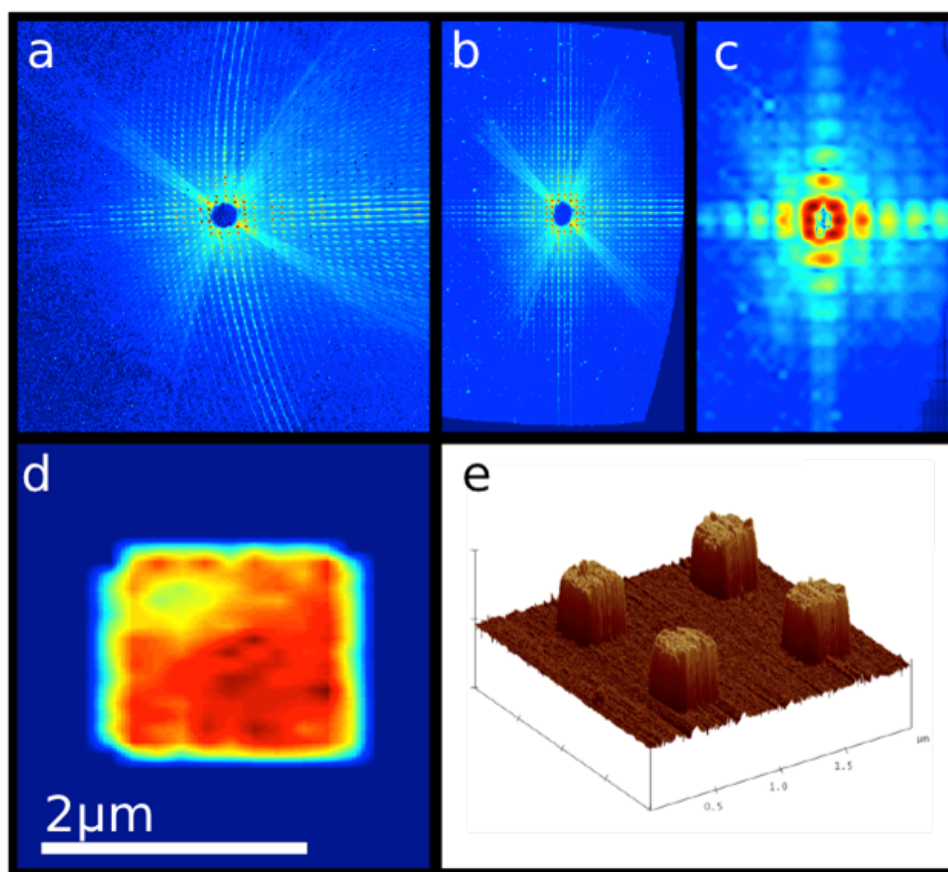


Figure 5.2: (a) Raw diffraction pattern, with noticeable conical diffraction. (b) Pattern after tilted plane correction, with the data sampled on a grid linear in spatial frequency. (c) Downsampled pattern obtained by sampling the peaks of the pattern in (b). (d) Reconstructed average pillar, based on the downsampled pattern in (c). (e) AFM image representative of the Ni nanopillars that were used as the sample. Figure adapted from Gardner et al. [193].

allowed to solve for both the amplitude and the phase of this region of the pattern. After the phase of the diffraction pattern was retrieved, an averaged image of the pillars with ≈ 100 nm resolution was formed by taking the inverse Fourier transform of the complex diffracted amplitudes, shown in Fig. 5.2(d).

While this was only a first step towards general reflection-mode imaging, it was nevertheless important. This data represented an experimental validation of the tilted plane correction interpolation method [193]. Additionally, this experiment laid the foundation for further work towards local imaging of non-periodic surfaces. Rather than resampling the diffraction peaks onto a coarser grid, the full, corrected pattern can be processed using an iterative phase retrieval algorithm in order to retrieve a quantitative phase-contrast image of the surface, with spatial resolution and phase sensitivity limited only by the wavelength of the illumination and the collected NA.

5.1.1 Reflection keyhole data

The next step towards reflection mode imaging involved moving toward a keyhole geometry similar to that described in Ch. 4. The geometry only differed from that shown in Fig. 4.16 in that the sample was again placed at 45° angle of incidence, and the detector was oriented with its surface normal to the specular reflection. As described in Section 4.2.2, two pinholes were used to remove any background light as well as to place a sharper edge on the beam. The sample used for this experiment again consisted of an array of nano-pillars, this time $1\ \mu\text{m}$ in diameter, $30\ \text{nm}$ tall, and cylindrical instead of square.

Raw diffraction data from this sample is shown in Fig. 5.3(a). Using tilted plane correction, the pattern was interpolated onto a grid linear in spatial frequency, shown in Fig. 5.3(b). However, attempts to retrieve the phase of this data were unsuccessful. This was likely due to the fact that the multilayer mirrors used for the experiment had a broader reflectivity bandwidth than expected. As can be seen in the diffraction shown in Fig. 5.3, 3 harmonics are clearly visible at each diffraction order. This is especially apparent at high diffraction angles.

Additionally, the need for accurate knowledge of the incident illumination in keyhole CDI [201]

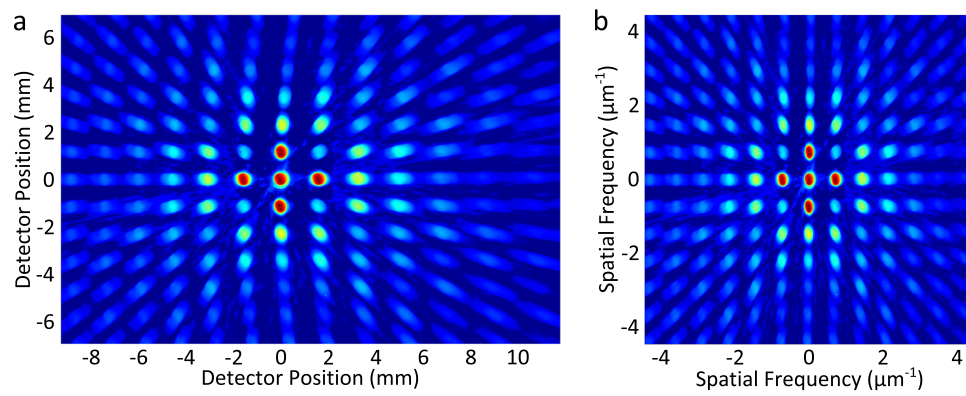


Figure 5.3: (a) Raw diffraction pattern from $1\ \mu\text{m}$ diameter cylindrical nano-pillars, using “keyhole” illumination as described in the previous chapter. (b) Pattern from (a) after tilted plane correction. Note that due to broad mirror bandwidth, 3 separate harmonics are apparent in the diffraction pattern.

presents significant difficulties in reflection mode. Furthermore, it is difficult to apply phase (non-negativity) constraints in the sample plane in reflection, which is an important component of many phase retrieval algorithms [73, 77]. This difficulty comes from the fact that for short wavelengths, even few-nanometer surface height variation within the illuminated field of view can produce large phase differences in reflection. Imperfect knowledge of the incident beam only exacerbates this issue.

Fortunately, a phase retrieval technique known as ptychography, which has the capability to reconstruct both the diffracting object as well as the incident illumination, has seen rapid progress over the past several years [85, 86]. The technique is described in detail in Ch. 3. In addition to the capability to retrieve the incident beam, there is no need for a phase constraint in the sample plane, making this technique ideal for overcoming the difficulties associated with reflection CDI. This extra information comes at a price; many diffraction patterns must be collected as the illumination is scanned across the sample in an overlapping grid pattern. The algorithm also requires precise knowledge of the relative distances between scan positions, meaning that high resolution, closed-loop stages must be used for sample positioning. New algorithms able to solve for the scan positions relax this requirement slightly [230, 231]. The successful application of ptychography to reflection CDI is described in the following section.

5.2 Ptychography in reflection mode

Here we demonstrate the most general reflection-mode coherent diffractive imaging to date using any light source, by combining the extended ptychographical iterative engine (ePIE) [86] with curved wavefront illumination [232]. This allows extended (non-isolated) objects to be imaged at any angle, which will enable tomographic imaging of surfaces. This work also represents the first non-isolated-object, high fidelity, tabletop coherent reflection imaging, which expands the scope of applications for CDI significantly to a very broad range of science and technology. First, our approach removes restrictions on the numerical aperture, sample, or angle, so that general extended objects can be imaged in reflection mode at any angle of incidence. Second, illumination of the

sample with a strongly curved wavefront removes the need for a zero-order beam-stop by reducing the dynamic range of the diffraction patterns. The curved illumination also allows the size of the beam to vary according to the sample size, alleviating the need for a large number of scan positions. This also results in fewer necessary scan positions when imaging a large field of view. Third, reflection ptychography produces surface images containing quantitative amplitude and phase information about the sample that are in excellent agreement with atomic force microscopy (AFM) and scanning electron microscopy (SEM) images, and also removes all negative effects of non-uniform illumination of the sample or imperfect knowledge of the sample position as it is scanned [231]. The result is a general and extensible imaging technique that can provide a comprehensive and definitive characterization of how light at any wavelength scatters from an object, with resolution limited only by the wavelength and the numerical aperture of the system. This complete amplitude and phase characterization thus is fully capable of pushing full field optical imaging to its fundamental limit. Finally, because we use a tabletop high harmonic generation (HHG) 30 nm source [31], in the future it will be possible to image energy, charge and spin transport with nm spatial and fs temporal resolution on nanostructured surfaces or buried interfaces, which is a grand challenge in nanoscience and nanotechnology [233, 234].

5.2.1 Experimental geometry

The experimental geometry for reflection mode Fresnel ptychography is shown in Fig. 5.4. A Ti:sapphire laser beam with wavelength ≈ 785 nm (1.5 mJ pulse energy, 22 fs pulse duration, 5 kHz repetition rate) is coupled into a 5 cm-long, 200 μm inner diameter, hollow waveguide filled with 60 torr of argon. Bright harmonics of the fundamental laser are produced near a center wavelength of 29.5 nm (27th harmonic) since the high harmonic generation process is well phase-matched [92], ensuring strong coherent signal growth and high spatial coherence. The residual fundamental laser light, which is collinear with the high harmonic beam, is filtered out using a combination of two silicon mirrors (placed near Brewsters angle for 785 nm light) and two 200 nm-thick aluminum filters. A pair of Mg/SiC multilayer mirrors then select the 27th harmonic of the Ti:sapphire laser

at 29.5 nm. The first mirror is flat, while the second mirror has a radius of curvature of 10 cm. This mirror pair focuses the HHG beam onto the sample at an angle of incidence of 45° . The focus position is 300 μm downstream of the sample, so that the HHG beam wavefront at the sample plane has significant curvature. The angle of incidence on the curved mirror is approximately 2° , which introduces small amounts of astigmatism and coma onto the HHG beam.

An adjustable ≈ 1 mm aperture is placed in the beam path ≈ 1 m upstream of the sample, to remove any stray light outside the beam radius. Here, only one aperture was used, in contrast to the two apertures that were necessary for the experiment described in Section 4.2.1. This simpler geometry is made possible by the fact that with such a large distance between the aperture and the spherical multilayer mirror, the majority of the scattered light from the aperture diffracts outside the diameter of the mirror. In this case, the finite mirror diameter serves the same purpose as the second aperture described in Section 4.2.1.

5.2.2 Sample fabrication

The sample used in the experiment was fabricated on a super-polished silicon wafer. The wafer was rinsed with acetone, isopropanol, and methanol, and baked on a hotplate for 20 minutes at 250°C . It was then spin-coated with Microchem 2% PMMA in anisole, molecular weight 950 at 4000 r.p.m. for 45 seconds. Afterwards it was baked at 180°C for 90 seconds. Electron beam lithography was performed using a FEI Nova NanoSEM 640, using Nanometer Pattern Generation System (NPGS) software and patterns. The resist was then developed by immersion in a 1:3 solution of methyl-isobutyl-ketone:isopropanol for 30 seconds. Approximately 30 nm of titanium was evaporated onto the surface using a CVC SC3000 3-boat thermal evaporator. The lift-off step was accomplished in acetone using a sonicator. A scanning electron microscope (SEM) image of resulting object is shown in Fig. 5.5(b).

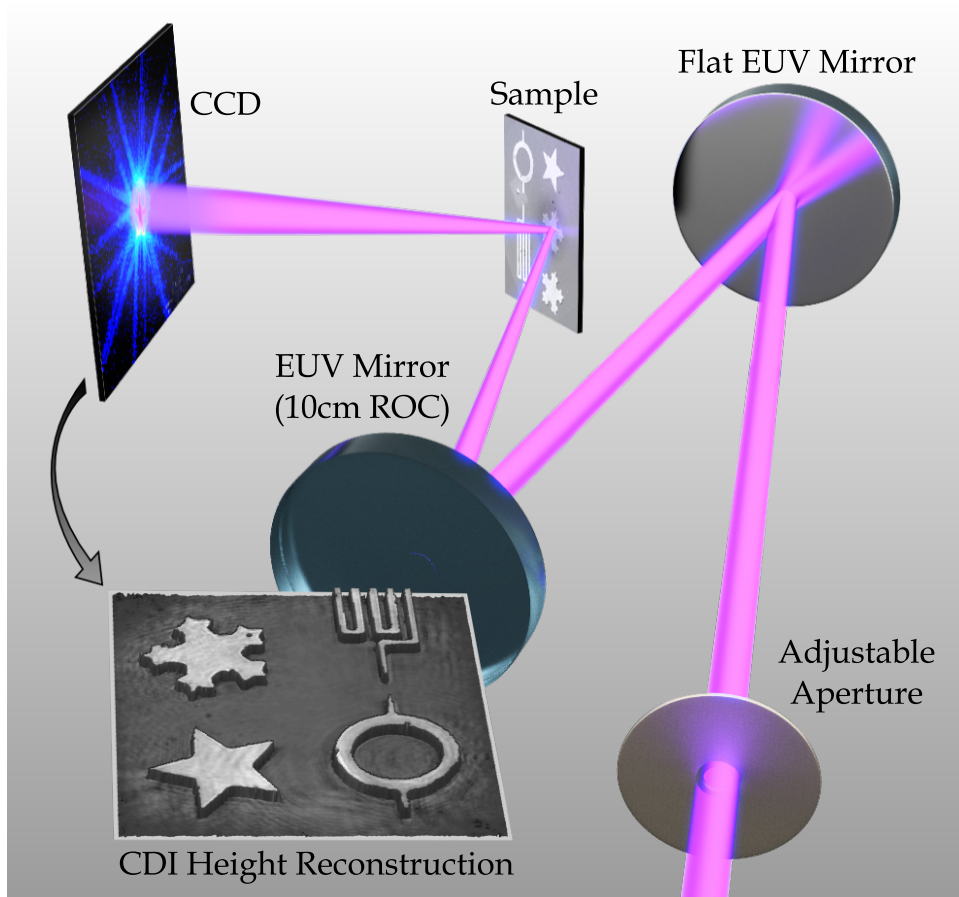


Figure 5.4: Experimental setup for reflection mode Fresnel ptychography. The EUV beam propagates through an adjustable ≈ 1 mm aperture; a single harmonic is selected using a pair of multilayer mirrors centered at 29.5 nm and focused onto the sample. The scattered light is collected on a CCD detector placed directly after the sample. The inset shows a height profile reconstructed through ptychography.

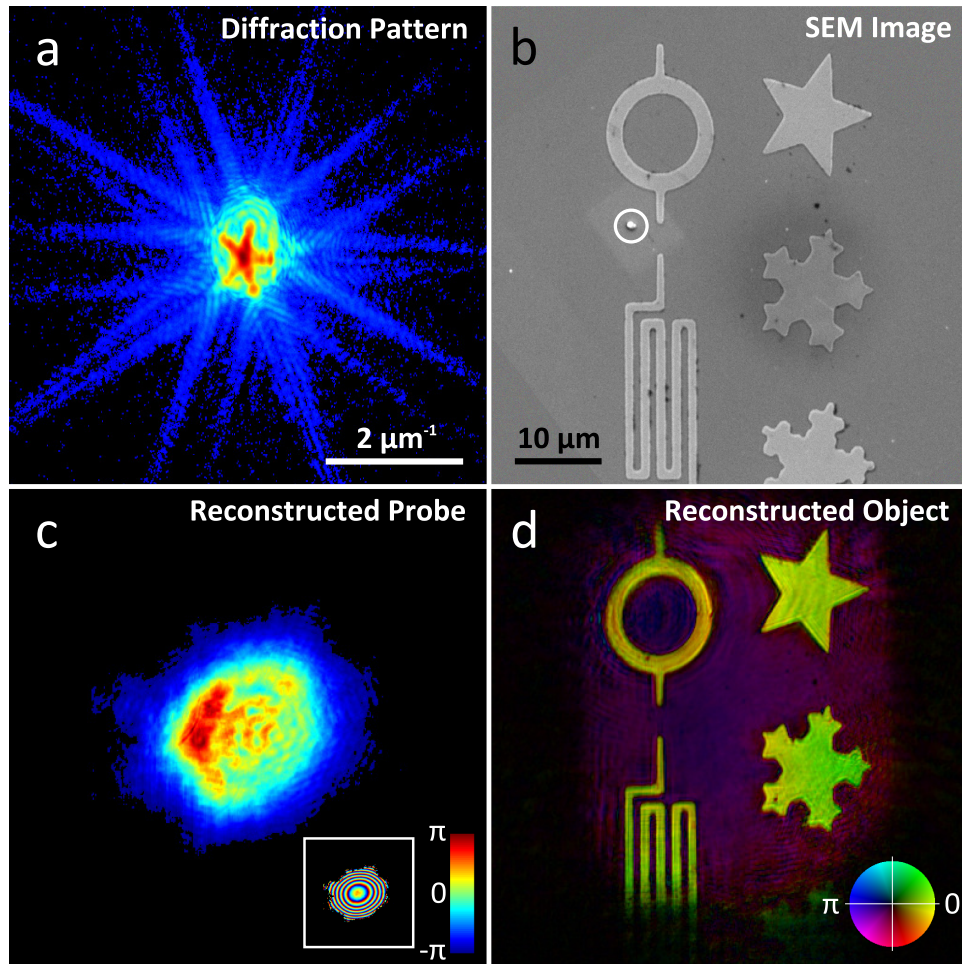


Figure 5.5: Diffraction data and ptychographic reconstruction. (a) Representative diffraction pattern, scaled to the $1/4$ power, taken from the 90-scan dataset. (b) SEM image of the Ti patterned Si sample. Note that the large defect circled in the SEM image resulted from contamination after the ptychography measurement. (c) Reconstructed amplitude (thresholded at 5%) of the HHG beam. The inset shows the reconstructed phase (displayed modulo- 2π). (d) Ptychographic reconstruction of the object shown in (b). The reconstruction is plotted as the complex amplitude, where brightness represents reflected amplitude and hue represents the phase of the reconstruction. Note that the majority of defects seen in the SEM image of the Ti nanostructures are reproduced in the ptychographic reconstruction. The scale bar in (b) is shared among (b)-(d).

5.2.3 Results and Discussion

The scattered light from the object is measured using an EUV-sensitive CCD detector (Andor iKon, 2048×2048 , $13.5 \mu\text{m}$ square pixels), placed 67 mm from the object, and oriented so that the detector surface was normal to the specular reflection of the beam. The sample was positioned $300 \mu\text{m}$ before the circle of least confusion along the beam axis, so that the beam diameter incident on the sample was approximately $10 \mu\text{m}$. Diffraction patterns were measured at each position of 10 adjacent 3×3 grids, with $2.5 \mu\text{m}$ step size between positions. The positions were randomized by up to $1 \mu\text{m}$ in order to prevent periodic artifacts from occurring in the ptychographic reconstruction [89].

Due to the non-normal angle-of-incidence on the sample, the patterns must be remapped onto a grid that is linear in spatial frequencies of the sample plane, in order to use fast Fourier transforms (FFTs) in the data analysis. We used tilted plane correction to accomplish this [193]. An example of a corrected diffraction pattern is shown in Fig. 5.5(a). The diffraction patterns were cropped such that the effective numerical aperture was 0.1, enabling a half-pitch resolution of 150 nm. The image was reconstructed using the ePIE, along with the sub-pixel position determination method [208, 231]. The full process for obtaining the reconstruction shown in Fig. 5.5(d) was as follows:

- (1) Tilted plane correction was applied to each of the 90 diffraction patterns in the full dataset.
- (2) The standard ePIE algorithm [86] was applied to the corrected data, with subpixel scan position precision handled as in Maiden *et al.* [208]. A starting guess for the probe was calculated using knowledge of the sample-to-focus distance ($300 \mu\text{m}$). The object starting guess was set to unity and the probe guess was normalized to contain the same energy as the average diffraction pattern in the dataset. The algorithm was allowed to update the probe guess in parallel with the object guess at each sub-iteration. The algorithm was run in this way for 20 full ptychographic iterations, at which point the probe guess had made much more progress towards convergence than the object guess. The object guess

was reinitialized to unity, and the algorithm was restarted using the new probe guess, and allowed to run for 100 iterations, long enough for both the object and probe to converge to stable solutions.

- (3) The object guess was re-initialized as described in step 2, and the probe guess was set to that found at the end of step 2. The subpixel position correction method [231] was applied to the ePIE, and the overlap constraint was applied with subpixel shifts of the probe [208]. The position correction feedback parameter β was started at a value of 50, and automated as in Zhang *et al.* [231]. The probe guess was not allowed to update during this step. Again, the algorithm was run for 100 iterations, until the position corrections converged to < 0.1 pixel.
- (4) Finally, using the probe found in step 2 and the corrected scan positions found in step 3, and with the object guess reinitialized to unity, the algorithm was run for 200 iterations to achieve the final reconstruction.

Each full iteration (cycling through all 90 diffraction patterns) took approximately 30 seconds on a personal computer, leading to a total reconstruction time of 3.5 hours.

As mentioned above, the algorithm was used to further solve for the complex amplitude of the probe as well, resulting in the illumination shown in Fig. 5.5(c). As discussed in Section 5.2.4, the reconstructed probe is completely consistent with a measurement of the unscattered beam at the detector. The high fidelity of the CDI reconstruction is evident by the fact that the majority of small defects visible in the SEM image of the Ti patterns (Fig. 5.5(b)) are also clearly visible in the CDI reconstruction (Fig. 5.5(d)). Note that the large defect circled in the SEM image in Fig. 5.5(b) was the result of sample contamination after the ptychography measurement. Section 5.2.5 contains a more detailed comparison between the defects seen in the CDI reconstruction, and those seen in the SEM and AFM images (Fig. 5.9).

Ptychography solves for the complex amplitudes of both the object and the probe (or incident beam) simultaneously [86, 89]. As a result, reliable quantitative information about the object can

be obtained from the reconstruction, since the effect of the probe on the diffraction patterns is essentially divided out. Quantitative surface relief information can be obtained from the phase of the reconstructed object as well. The titanium was patterned at a thickness of approximately 30 nm. The round trip path difference of the reflected light is $-2h \cos \theta$, where h is the height above a reference (such as the substrate) and θ is the angle of incidence. At 45° angle of incidence for a feature thickness of 30 nm, the round trip path length difference between the silicon substrate and the patterned titanium features is 42.4 nm. At 29.5 nm wavelength, this corresponds to between 1 and 2 wavelengths path length difference. Additionally, the phase change upon reflection can be highly variable for absorbing materials. In the case of this sample, both silicon and titanium have native oxide layers which must be taken into account when calculating this phase change. Thus, some prior knowledge is required in order to retrieve the absolute height of the features. The method for calculating the phase change upon reflection from a thin-film system with complex indices of refraction is described in Born and Wolf [200]. The indices of refraction at 29.5 nm wavelength necessary for this calculation were obtained from the Center for X-Ray Optics (CXRO) [40].

The thickness of the oxide layer on the Si wafer used for sample fabrication was determined through ellipsometry (Gaertner Scientific L117F300). The measurements were made at 70° angle of incidence using a He-Ne laser at 632.8 nm. The ellipsometric angles ψ and Δ were determined to be $10.20(4)^\circ$ and $171.00(7)^\circ$, respectively. The angles are defined as

$$\frac{r_p}{r_s} = \tan \psi e^{-i\Delta} \quad (5.1)$$

where r_p and r_s are the complex reflectivity coefficients for p - and s -polarized light, respectively. The thickness of the oxide layer was calculated by numerically solving the argument of Eq. (5.1), assuming an index of refraction for the oxide layer of $1.474(3)$ and an index of refraction for the silicon substrate of $3.89(2) + i0.011(9)$ at 632.8 nm wavelength. The result was an oxide layer thickness of $3.0(1)$ nm.

The thickness of the titanium oxide layer was assumed to be $2.9(2)$ nm based on the literature [235, 236]. For the SiO_2/Si region, the phase change δ_{Si} was calculated to be $-1.22(3)$ radians and

the theoretical reflectivity was calculated to be 0.33%. For the TiO_2/Ti patterns, the phase change δ_{Ti} was calculated to be $-1.92(9)$ radians and the theoretical reflectivity was calculated to be 10.9%. The object reconstruction shows a ratio of ≈ 17 between the reflectivity of the titanium and the silicon surfaces based on a histogram of the reconstructed amplitude, in reasonably good agreement with the calculated values, which assumed no surface roughness.

A flattening method was applied to the reconstructed phase of the silicon substrate, similar to that used in atomic force microscopy, due to some residual phase curvature reconstructed on the flat substrate. The peak-to-valley height variation of the subtracted surface fit was < 4 nm over the full $35 \times 40 \mu\text{m}^2$ field of view. After flattening, the reconstruction shows an average of 4.26 radians of phase difference between the titanium and silicon surfaces, corresponding to a 46.2(7) nm path length difference (when 2π is added and after taking the phase changes upon reflection into account). This corresponds to a 32.7(5) nm average thickness of the titanium patterns. A height map of the sample could then be produced by assuming that 2π should be added to any part of the reconstruction that exhibited an amplitude above 25% of the maximum (based on the relative reflectivities of titanium and silicon, as discussed above). Additionally, the reflection phases δ_{Si} and δ_{Ti} were subtracted from the Si and Ti regions using the same criteria. The result of this analysis is displayed in Fig. 5.6(a), and represents a significant improvement in image quality compared with all tabletop coherent reflective imaging to date. After the ptychography measurements were taken, an independent height map of the sample was obtained using a Digital Instruments Dimension 3100 AFM. The resulting AFM height map is shown in Fig. 5.6(b), after applying the same flattening method as that used for the CDI reconstruction. The AFM measurement shows an average height for the titanium features of 32.7 nm, which agrees exactly with the ptychography result within error bars.

Many small pieces of debris are visible in the AFM image shown in Fig. 5.6(b), with heights above that of the patterned titanium. None of the EUV work was done in a cleanroom environment. The reason these are not visible in the CDI height map (Fig. 5.6(a)) is that the 3D information relies on the phase difference of light reflecting from the substrate versus the features (at 45°)

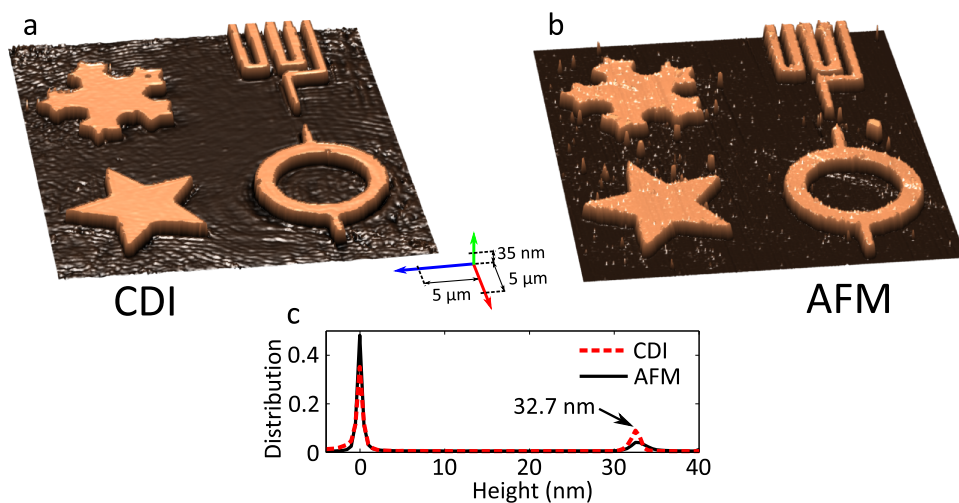


Figure 5.6: Height profile comparison between CDI and AFM. (a) 3D profile of the object based on ptychographic reconstruction. (b) 3D profile of the object based on an AFM measurement. Any features taller than 40 nm were thresholded to 40 nm for the 3D rendering. (c) Histograms of the height profiles shown in (a) and (b). The histograms were used to calculate the average feature thickness of 32.7 nm based on the both the CDI and AFM measurements. The scale axis shown in (a) is shared by both (a) and (b). Note that the large debris spot on the right of the AFM image was introduced after the CDI image was taken.

and not on the absolute height difference. While the debris locations are still evident in the CDI reconstruction (Fig. 5.5(d)), the modulo 2π ambiguity of the phase information combined with the very short wavelength prevents us from extracting the absolute height information of all features. However, a tomographic or multi-wavelength approach would enable full 3D reconstructions of all features on a surface [91].

Finally, we note that previously it was believed that full knowledge of the probe was necessary when using Fresnel (curved wavefront) ptychography for phase retrieval [232]. However, we find that for ptychographic grids of 3×3 and larger with sufficient overlap between adjacent probe positions (60-70% area overlap [86]), the algorithm converges to a consistent result for the probe provided that the phase curvature of the starting guess differs by no more than 50% of the actual phase curvature. Even this condition is relaxed entirely in the case of isolated objects. To demonstrate this, we performed a separate ptychographic retrieval of the probe by scanning a $5 \mu\text{m}$ diameter pinhole across the beam near the focus. The probe that is retrieved using this method can be propagated to the sample plane for comparison to the probe found in the course of the sample reconstruction. We found very good agreement between the two probe reconstructions, independent of the accuracy of the starting guess for the probe. More details of this comparison can be found in Section 5.2.4.

5.2.4 High Harmonic Beam Characterization Through Ptychography

To ensure that our recovery algorithm as discussed in the main text was correctly retrieving the probe illumination, we first characterized the extreme ultraviolet (EUV), high harmonic generation (HHG) beam by scanning a $5 \mu\text{m}$ diameter pinhole across the beam near its focus and reconstructed the illumination using ptychography. In this case, the pinhole can be thought of as the probe, while the beam is an effective object. The scan consisted of a 6×6 grid with $1 \mu\text{m}$ step size between adjacent scan positions. The reconstructed beam is shown in Fig. 5.7(a).

The reconstructed beam was propagated to the sample position ($200 \mu\text{m}$ upstream of the pinhole probe location) and calculated on the tilted plane (at 45°) using tilted plane correction,

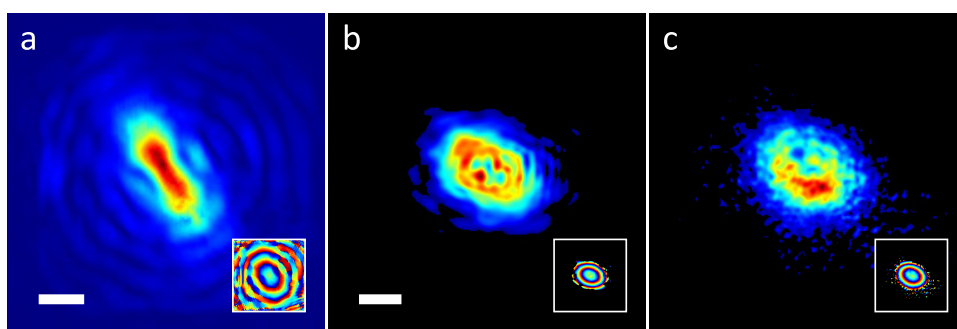


Figure 5.7: A comparison of separate reconstructions of the HHG illumination beam, using the beam as the object in one case and as the probe in the second case. (a) Reconstruction of the HHG beam near the focus using a $5\ \mu\text{m}$ diameter pinhole probe. The main image displays the amplitude and the inset displays the phase. The scale bar has width $2\ \mu\text{m}$. (b) The result of propagating the reconstructed beam from (a) to the tilted sample plane. Again, the main image shows the amplitude and the inset shows the phase. The scale bar has width $5\ \mu\text{m}$. (c) The amplitude (main image) and phase (inset) of the reconstructed probe based on a 3×3 ptychographic scan across the one of the features on the titanium sample discussed in the text. The scale bar is shared with (b). Note that the beam amplitudes in (b) and (c) are displayed in the tilted sample coordinates, resulting in elongation in the horizontal direction.

shown in Fig. 5.7(b). Immediately after this ptychography scan, the pinhole probe was removed and the sample was translated such that the beam illuminated one of the star patterns on the sample (with reconstruction shown in Fig. 5.5(d)). We performed a 3×3 ptychographic scan across the star feature, with $2.5 \mu\text{m}$ step size. In this case, a probe starting guess consisting of a Gaussian amplitude profile with random phase sufficed to consistently retrieve the probe amplitude shown in Fig. 5.7(c). As can be seen by comparison of Figs. 5.7(b) and (c), the two beam characterization methods show very good agreement between both the phase and the amplitude. It should be noted that the HHG beam drifted slightly inside the adjustable aperture during the course of the two scans, resulting in slightly different beam structure during the two measurements.

As a further consistency check, the probe reconstruction discussed in the main text (shown in Fig. 5.5(c)) was propagated to the detector, and the tilted plane correction was undone in order to examine the result in the real coordinates of the detector. The result of these steps is shown in Fig. 5.8(a). A comparison was made with a direct measurement of the unscattered beam by translating the sample to a featureless region of the silicon substrate, shown in Fig. 5.8(b). As can be seen in Figs. 5.8(a) and (b), while it is evident that, as in the above sample plane comparison, some beam drift occurred during the course of the ptychographic scan, the reconstructed probe is entirely consistent with the high harmonic beam used to illuminate the sample.

5.2.5 Comparison between CDI reconstruction and SEM and AFM images

As mentioned in Section 5.2.3, there are a number of defects visible in the sample image reconstructed through ptychographic coherent diffractive imaging (CDI) which are also visible in scanning electron microscope (SEM) and atomic force microscope (AFM) images. A visual comparison between the three techniques is shown in Fig. 5.9. Of the 7 defects pointed out in the figure, only defects 1-5 are visible in all of the images. The 6th and 7th defects are only visible in the CDI phase image and the AFM image. This is a demonstration of the fact that CDI has both amplitude contrast (analogous to SEM) and phase/height contrast (analogous to AFM).

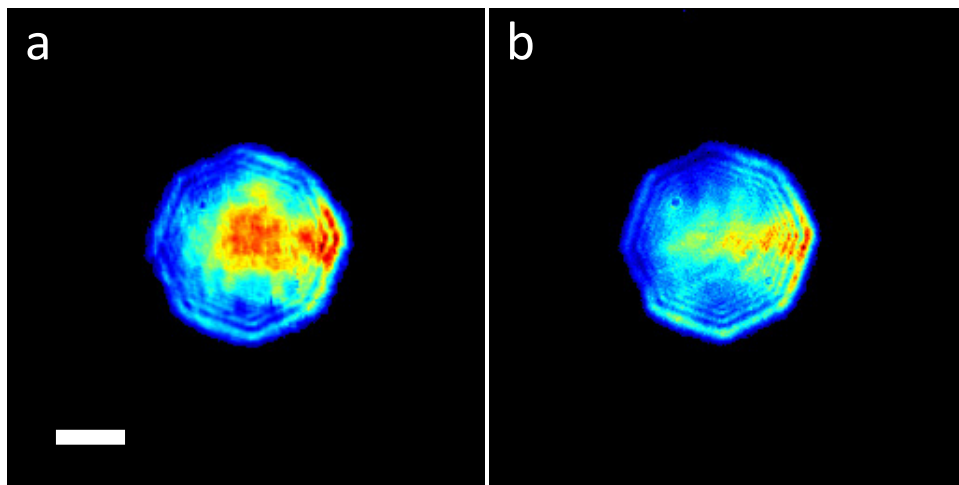


Figure 5.8: Comparison between the illumination reconstructed as a ptychographic probe and propagated to the detector, and the unscattered illumination measured directly on the detector (raw data). (a) The probe reconstruction from Fig. 5.5, propagated to the detector plane. (b) The HHG beam measured directly on the detector by translating the sample to a featureless region of the silicon substrate. The scale bar in (a) has width 1 mm and is shared by (a) and (b).

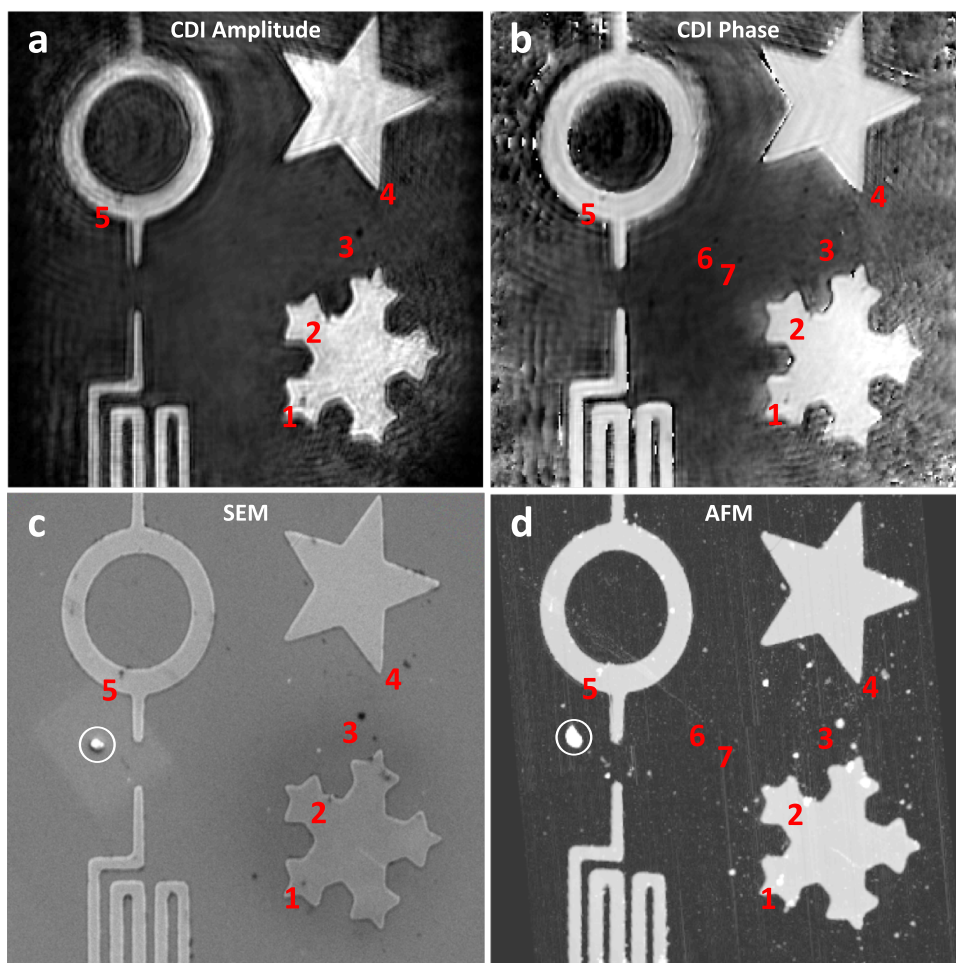


Figure 5.9: A visual comparison between the reconstructed CDI amplitude and phase with images obtained using SEM and AFM. (a) Reconstructed CDI amplitude image of the sample. (b) Phase of the reconstructed image. (c) SEM image of the sample. (d) AFM image of the sample. In the above images, seven defects have been pointed out (located above and to the right of each number). Defects 1-5 are visible in all of the images, whereas defects 6 and 7 are only visible in the reconstructed phase and in the AFM image. The circled defect in (c) and (d) was a result of contamination after the CDI measurements were taken.

5.3 Conclusions

We have demonstrated the first general, tabletop, full field reflection mode CDI microscope, capable of imaging extended nanosurfaces at arbitrary angles in a non-contact, non-destructive manner. This technique is directly scalable to shorter wavelengths and higher spatial and temporal resolution, as well as tomographic imaging of surfaces. By combining reflection-mode CDI with HHG sources in the keV photon energy region, it will be possible to capture nanoscale surface dynamics with femtosecond temporal and nanometer spatial resolution. Moreover, full characterization of the curved wavefront of the illuminating HHG beam at the sample plane through ptychography opens up the possibility for reflection keyhole CDI [182, 201]. This is significant for dynamic studies, since in contrast to ptychography CDI which requires overlapping diffraction patterns, keyhole CDI needs only one diffraction pattern, and therefore requires no scanning of the sample.

Chapter 6

Future Work

One of the main motivations for the work presented in this thesis is to enable scientific study at the intersection of the nanoscale and ultrafast. The CDI-based microscope presented in this thesis is now ready to move in this direction. The HHG source described in Ch. 2 has the capability for femto- to atto-second time resolution, which can be combined with the nanoscale resolution of the microscope to study ultrafast processes in an imaging modality.

The high time resolution can be achieved most easily in one of two ways. In both cases it is assumed that the dynamics are instigated with a femtosecond “pump” pulse, in order to achieve the highest time resolution. First, in cases where the process is predicted to be repeatable, the diffraction measurement for each time delay between the pump and the probe can be made stroboscopically over the course of many laser shots. In the case where the process is not repeatable (either the sample relaxation time is too long, the process is random, or the sample is damaged after only a few shots), the diffraction measurement for each time delay must be made during the course of a single shot. This second case requires a high number of HHG photons per laser shot, but is not unprecedented [237–239]. This chapter will outline specific potential routes towards dynamic imaging, in addition to a number of proposed experiments. The potential for applying these techniques at higher photon energies will also be discussed.

6.1 Methods for dynamic imaging experiments

This section will describe two new approaches which will find application to dynamic imaging. First, the keyhole CDI technique can be used generally. In cases where the process being studied is not repeatable, diffraction patterns can be measured in a single shot for each time delay (enabled by high-flux HHG sources). Second, a new hyperspectral extension to ptychography will enable dynamic EUV imaging spectroscopy. However, this technique will require a full ptychographic dataset at each time delay, meaning it can only be applied to repeatable processes in a stroboscopic manner. The following descriptions of both techniques include experimental requirements and methods as well as proof-of-principle demonstrations of each technique applied to EUV reflection-mode imaging.

As demonstrated in Ch. 5 and in other published experiments [61, 240–242], ptychography has become an excellent method for characterization of a focused EUV or X-ray beam. Aside from the fact that this is the most comprehensive way to measure nano-focused illumination to date, this is also extremely useful from an imaging point of view. The implication in ptychography is that it is possible to divide out non-uniformities in the illumination from the object reconstruction, resulting in images that more faithfully reproduce sample structure. In addition, full knowledge of the illumination is necessary in order to use keyhole CDI-based techniques [201]. Thus, it is possible to fully characterize the incident illumination using ptychography and subsequently use that information to perform single-pattern keyhole reconstructions at each time delay of a dynamic imaging experiment. This will be extremely useful, in particular for dynamic experiments which require single-shot imaging.

While the keyhole algorithm is not as powerful as ptychography, progress towards implementation of this approach has already been made. A single diffraction pattern taken from the ptychographic dataset described in Section 5.2 is displayed in Fig. 6.1(a). The reconstructed probe shown in Fig. 5.5(c) was used to reconstruct an image from this single diffraction pattern using keyhole CDI. The result is shown in Fig. 6.1(b). The image fidelity is not as high as the full

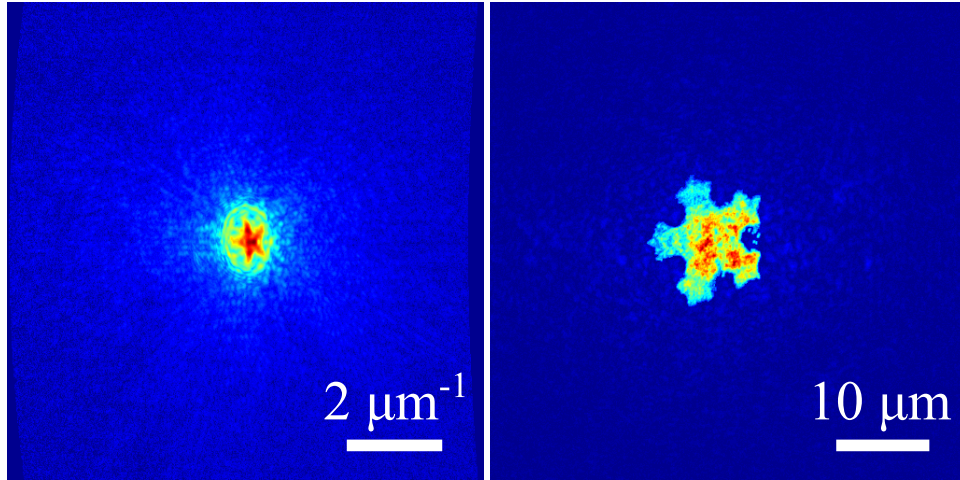


Figure 6.1: Keyhole reconstruction using knowledge of probe based on a ptychographic reconstruction. (a) Single diffraction pattern taken from the ptychographic dataset described in Section 5.2, after tilted plane correction. (b) Keyhole CDI reconstruction using the reconstructed probe shown in Fig. 5.5(c) combined with the diffraction pattern in (a).

ptychographic result shown in Fig. 5.5(d). This is likely due to low signal to noise ratio (SNR) at high angles of the diffraction pattern measurement. Keyhole CDI is more sensitive to noise than ptychography, due to the lack of redundant information as compared with ptychography. If this approach is taken for a dynamic experiment, the SNR will need to be higher. Higher SNR can be achieved by further optimization of the HHG flux, by longer integration times, or with improvements to detector technology.

Another technique that will be very useful for dynamic imaging is a new extension to ptychography called ptychographical information multiplexing (PIM) [91]. This technique was developed very recently at visible wavelengths and takes advantage of the vast amount of information in a ptychographic dataset to reconstruct independent images at multiple wavelengths. While the full potential for this technique is still unknown, we can make some brief comments here. A reasonable criterion for being able to distinguish a multi-wavelength diffraction pattern from a monochromatic pattern is to require that the n th peak of one constituent wavelength should overlap with the $(n + 1)$ th peak of the adjacent wavelength. This is related to the idea of the temporal coherence length discussed in Section 3.2.2, except here we want to detect scattering at angles beyond that

allowed by the coherence length of the source. The required NA to meet this criterion is

$$\text{NA} > \frac{\lambda_1 \lambda_2}{D \Delta \lambda}, \quad (6.1)$$

where D now represents the probe diameter. In the case of HHG, we are likely interested in distinguishing adjacent harmonics. It is interesting to note that in this case, the above requirement can be written simply in terms of the wavelength of the driving laser, as

$$\text{NA} > \frac{\lambda_0}{2D} \quad (6.2)$$

where λ_0 is the fundamental laser wavelength. This criterion is equivalent to requiring that the probe diameter differs by at least one pixel (based on the image resolution) in object space. The information multiplexing in ptychography can be understood to come from the fact that the overlap constraint is wavelength-dependent. It is important to note that in order to take advantage of this, the full range of the ptychography scan must span the diameter of the probe. If this is not the case, D in Eqs. (6.1) and (6.2) must be replaced with the scan range.

We have extended this approach to the EUV to image an object with four harmonics simultaneously. Thus far we have only achieved a proof-of-principle experiment, but the initial results are very promising. We have replaced the EUV multilayer mirrors that were used for the previous imaging experiments with a nickel-coated elliptical mirror at 5° glancing incidence. A schematic of the modified experimental geometry is shown in Fig. 6.2(a). The HHG spectrum used for the experiment is shown in Fig. 6.2(b). It is important to note that the harmonics are actually very narrow. The blurring between peaks in Fig. 6.2(b) is caused by low spectral resolution in the diagnostic spectrometer. The sample that was imaged is the same as that used for the experiment described in Section 5.2. The single-color ptychographic reconstruction is reproduced in Fig. 6.2(c). Finally, the retrieved images for each harmonic are shown in Figs. 6.2(d)-(g); the corresponding peaks are labeled accordingly in Fig. 6.2(b). Note that the best reconstructions were achieved for the two brightest harmonics.

Both of these techniques will be very useful as the microscope is applied to dynamic imaging experiments. There are many exciting experiments which can make use of this microscope to probe

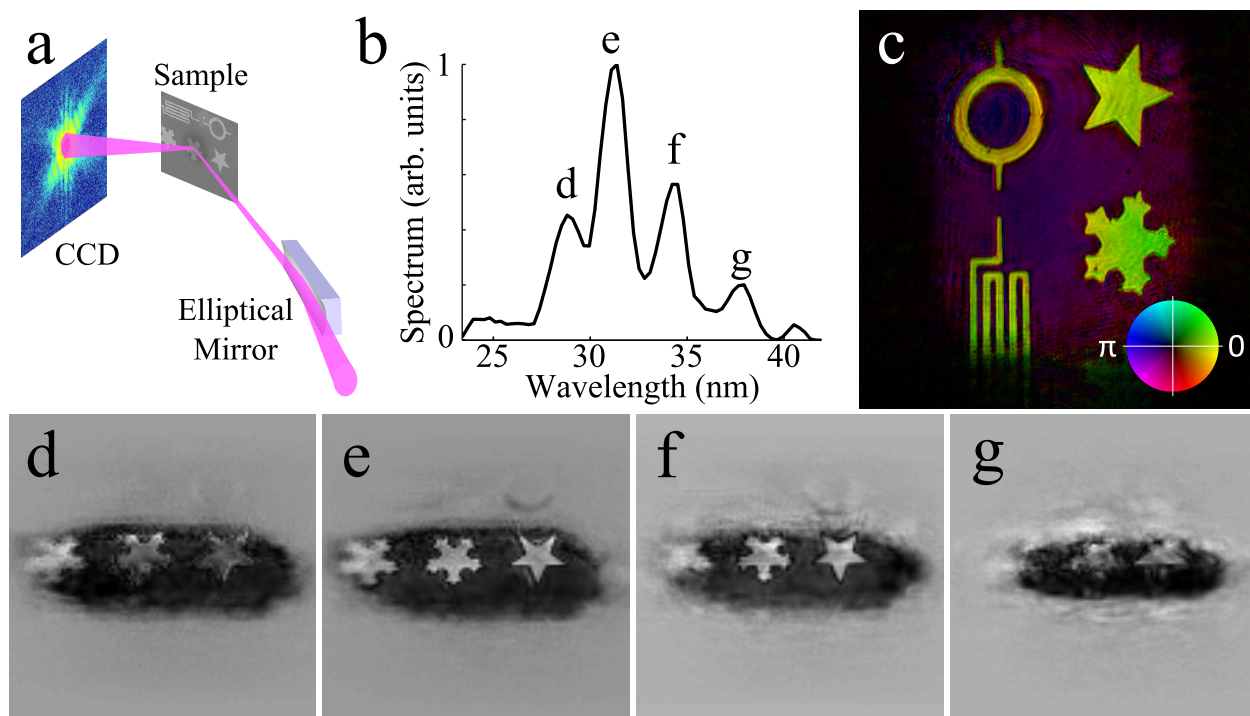


Figure 6.2: First EUV hyperspectral images based on ptychographical information multiplexing (PIM). (a) Schematic for PIM with multiple harmonics. Four bright, phase-matched harmonics are all refocused using a glancing incidence elliptical mirror. The sample is placed at the focus, where the beam diameter is $\approx 10 \mu\text{m}$. (b) Phase-matched harmonic spectrum. The harmonic peaks are blurred due to low spectral resolution in the diagnostic spectrometer. In actuality the peaks are much narrower and do not overlap. (c) Ptychographic reconstruction of the sample used for this experiment, reproduced from Fig. 5.5(c). (d)-(g) Independent PIM reconstructions at each harmonic shown in (b), where the harmonic peaks are labeled correspondingly.

short length and time scales simultaneously. To name a few, ideas for first experiments include imaging ballistic heat transfer dynamics and surface acoustic waves [233,243], demagnetization dynamics and spin transport [1,234], or imaging nano-plasmonic dynamics using the varying electron density as a contrast mechanism [244,245]. Of course, it will be very important moving forward to open new collaborations with experts in a variety of dynamic nanosystems, who likely have more concrete ideas concerning the most relevant scientific questions to address.

6.2 Imaging with keV harmonics

This microscope is also poised to move towards shorter wavelengths. Recently, phase-matched HHG sources have been extended all the way to photon energies > 1 keV [31]. This has been made possible through the use of longer wavelength driving lasers (up to $3.9 \mu\text{m}$ [184]), motivated by the single atom cutoff scaling with λ^2 described by Eq. (2.13). Figure 6.3 depicts HHG spectra obtained using a variety of driving laser wavelengths. As the driving laser wavelength becomes longer, the spectrum becomes a supercontinuum. Pushing these long-wavelength lasers to kHz repetition rates is the subject of current research. HHG sources capable of producing water window ($300 - 500$ eV) photons at kHz repetition rates are very nearly ready to apply towards imaging.

The PIM technique discussed in the previous section combined with the very broad phase-matched bandwidths produced with long-wavelength driving lasers represents potential for nanoscale spectro-microscopy. This type of spectro-microscopy at keV photon energy may be several years away as we wait for bright enough sources. However, water window spectro-microscopy may be a very useful tool for biological imaging applications.

6.3 Concluding remarks

This thesis describes the development of a general microscopy technique based on coherent diffractive imaging with a high harmonic source. First, we demonstrated the high resolution potential for this microscope by obtaining 22 nm resolution with a 13 nm light source [185]. Second, the microscope was generalized to image more complex, extended objects using the keyhole CDI

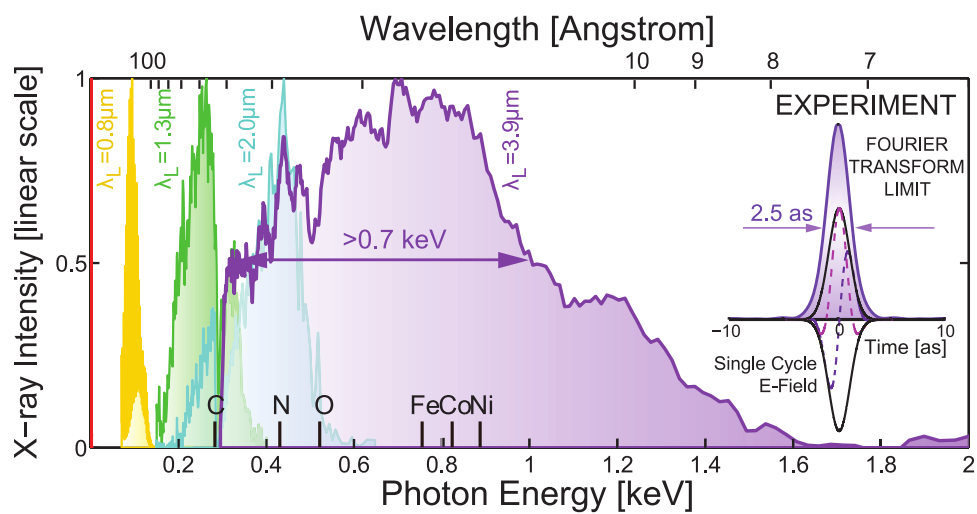


Figure 6.3: HHG spectra for a variety of driving laser wavelengths. Note that it is possible to generate phase-matched harmonics above 1 keV using a 3.9 μm few-cycle driving laser. Figure reproduced from [31].

technique [182]. Finally, general EUV reflection mode CDI was demonstrated, extending the utility of the CDI technique to image a wide variety of surface systems [183]. There are many exciting and interesting scientific directions that this microscope can be applied towards. HHG sources are becoming more reliable and are being extended to higher and higher photon energies, and can only be expected to improve further. The high spatio-temporal resolution of this versatile microscopy tool is sure to enable the study of many interesting systems, with promise for probing new nanoscale physics as a result.

Bibliography

- [1] E. Turgut, C. La-o-vorakiat, J. M. Shaw, P. Grychtol, H. T. Nembach, D. Rudolf, R. Adam, M. Aeschlimann, C. M. Schneider, T. J. Silva, M. M. Murnane, H. C. Kapteyn, and S. Mathias. Controlling the Competition between Optically Induced Ultrafast Spin-Flip Scattering and Spin Transport in Magnetic Multilayers. Phys. Rev. Lett., 110(19):197201, 2013.
- [2] M. E. Siemens, Q. Li, R. Yang, K. A. Nelson, E. H. Anderson, M. M. Murnane, and H. C. Kapteyn. Quasi-ballistic thermal transport from nanoscale interfaces observed using ultrafast coherent soft X-ray beams. Nat. Mater., 9(1):26–30, 2010.
- [3] G. Binnig, C. F. Quate, and C. Gerber. Atomic Force Microscope. Phys. Rev. Lett., 56(9):930–933, 1986.
- [4] G. Binnig, H. Rohrer, C. Gerber, and E. Weibel. Surface Studies by Scanning Tunneling Microscopy. Phys. Rev. Lett., 49(1):57–61, 1982.
- [5] D. McMullan. Scanning electron microscopy 1928-1965. Scanning, 17(3):175–185, 2006.
- [6] V. M. Hallmark, S. Chiang, J. F. Rabolt, J. D. Swalen, and R. J. Wilson. Observation of atomic corrugation on Au (111) by scanning tunneling microscopy. Phys. Rev. Lett., 59(25):2879–2882, 1987.
- [7] W. A. Hofer, A. S. Foster, and A. L. Shluger. Theories of scanning probe microscopes at the atomic scale. Rev. Mod. Phys., 75(4):1287–1331, 2003.
- [8] S. Yoshida, Y. Terada, M. Yokota, O. Takeuchi, H. Oigawa, and H. Shigekawa. Optical pump-probe scanning tunneling microscopy for probing ultrafast dynamics on the nanoscale. Eur. Phys. J. Spec. Top., 222(5):1161–1175, 2013.
- [9] B. A. Nechay, U. Siegner, M. Achermann, H. Bielefeldt, and U. Keller. Femtosecond pump-probe near-field optical microscopy. Rev. Sci. Instrum., 70(6):2758–2764, 1999.
- [10] R. Erni, M. Rossell, C. Kisielowski, and U. Dahmen. Atomic-Resolution Imaging with a Sub-50-pm Electron Probe. Phys. Rev. Lett., 102(9):096101, 2009.
- [11] A. H. Zewail. Four-dimensional electron microscopy. Science, 328(5975):187–93, 2010.
- [12] W. R. Zipfel, R. M. Williams, and W. W. Webb. Nonlinear magic: multiphoton microscopy in the biosciences. Nat. Biotechnol., 21(11):1369–77, 2003.

- [13] T. Klar, E. Engel, and S. Hell. Breaking Abbes diffraction resolution limit in fluorescence microscopy with stimulated emission depletion beams of various shapes. Phys. Rev. E, 64(6):1–9, 2001.
- [14] T. A. Klar, S. Jakobs, M. Dyba, A. Egner, and S. W. Hell. Fluorescence microscopy with diffraction resolution barrier broken by stimulated emission. Proc. Natl. Acad. Sci. U. S. A., 97(15):8206–10, 2000.
- [15] R. Henriques, C. Griffiths, E. H. Rego, and M. M. Mhlanga. PALM and STORM: unlocking live-cell super-resolution. Biopolymers, 95(5):322–331, 2011.
- [16] M. J. Rust, M. Bates, and X. Zhuang. Sub-diffraction-limit imaging by stochastic optical reconstruction microscopy (STORM). Nat. Methods, 3:793–796, 2006.
- [17] J. Squier and M. Muller. High resolution nonlinear microscopy: A review of sources and methods for achieving optimal imaging. Rev. Sci. Instrum., 72(7):2855, 2001.
- [18] J.-X. Cheng and X. S. Xie. Coherent Anti-Stokes Raman Scattering Microscopy: Instrumentation, Theory, and Applications. J. Phys. Chem. B, 108:827–840, 2004.
- [19] W. Chao, B. D. Harteneck, J. A. Liddle, E. H. Anderson, and D. T. Attwood. Soft X-ray microscopy at a spatial resolution better than 15 nm. Nature, 435:1210–3, 2005.
- [20] D. Y. Parkinson, G. McDermott, L. D. Etkin, M. A. Le Gros, and C. A. Larabell. Quantitative 3-D imaging of eukaryotic cells using soft X-ray tomography. J. Struct. Biol., 162(3):380–6, 2008.
- [21] C. A. Larabell and M. A. L. Gros. X-ray Tomography Generates 3-D Reconstructions of the Yeast, *Saccharomyces cerevisiae*, at 60-nm Resolution. Mol. Biol. Cell, 15:957–962, 2004.
- [22] J. Nelson, X. Huang, J. Steinbrener, D. Shapiro, J. Kirz, S. Marchesini, A. M. Neiman, J. J. Turner, and C. Jacobsen. High-resolution x-ray diffraction microscopy of specifically labeled yeast cells. PNAS, 107(16):7235–9, 2010.
- [23] D. H. Bilderback, P. Elleaume, and E. Weckert. Review of third and next generation synchrotron light sources. J. Phys. B At. Mol. Opt. Phys., 38(9):S773–S797, 2005.
- [24] J. Feldhaus, J. Arthur, and J. B. Hastings. X-ray free-electron lasers. J. Phys. B At. Mol. Opt. Phys., 38(9):S799–S819, 2005.
- [25] J. J. Rocca, V. Shlyaptsev, F. G. Tomasel, O. D. Cortázar, D. Hartshorn, and J. L. A. Chilla. Demonstration of a discharge pumped table-top soft-x-ray laser. Phys. Rev. Lett., 73(16):2192–2196, 1994.
- [26] J. J. Rocca. Table-top soft x-ray lasers. Rev. Sci. Instrum., 70(10):3799, 1999.
- [27] Y. Wang, M. Larotonda, B. Luther, D. Alessi, M. Berrill, V. Shlyaptsev, and J. Rocca. Demonstration of high-repetition-rate tabletop soft-x-ray lasers with saturated output at wavelengths down to 13.9nm and gain down to 10.9nm. Phys. Rev. A, 72(5):053807, 2005.
- [28] L. Rymell and H. M. Hertz. Droplet target for low-debris laser-plasma soft X-ray generation. Opt. Commun., 103(1-2):105–110, 1993.

- [29] J. de Groot, O. Hemberg, A. Holmberg, and H. M. Hertz. Target optimization of a water-window liquid-jet laserplasma source. J. Appl. Phys., 94(6):3717, 2003.
- [30] A. Mcpherson, G. Gibson, H. Jara, U. Johann, T. S. Luk, I. A. McIntyre, K. Boyer, and C. K. Rhodes. Studies of multiphoton production of vacuum-ultraviolet radiation in the rare gases. J. Opt. Soc. Am B, 4(4):595–601, 1987.
- [31] T. Popmintchev, M.-C. Chen, D. Popmintchev, P. Arpin, S. Brown, S. Alisauskas, G. Andriukaitis, T. Balciunas, O. D. Mücke, A. Pugzlys, A. Baltuska, B. Shim, S. E. Schrauth, A. Gaeta, C. Hernández-García, L. Plaja, A. Becker, A. Jaron-Becker, M. M. Murnane, and H. C. Kapteyn. Bright coherent ultrahigh harmonics in the keV x-ray regime from mid-infrared femtosecond lasers. Science, 336(6086):1287–91, 2012.
- [32] W. Friedrich, P. Knipping, and M. von Laue. Interferenz-Erscheinungen bei Röntgenstrahlen. Sitzungsberichte der Math. Cl. der Königlich-Bayerischen Akad. der Wissenschaften zu München, pages 303–322, 1912.
- [33] P. Kirkpatrick and A. V. Baez. Formation of Optical Images by X-Rays. J. Opt. Soc. Am., 38(9):766–774, 1948.
- [34] G. Schmahl and D. Rudolph. Lichtstarke Zonenplatten als abbildende Systeme für weiche Röntgenstrahlen. Optik (Stuttg.), 29:577–585, 1969.
- [35] B. Niemann, D. Rudolph, and G. Schmahl. Soft X-ray Imaging Zone Plates with Large Zone Numbers for Microscopic and Spectroscopic Applications. Opt. Commun., 12(2):160–163, 1974.
- [36] J. Kirz. Phase zone plates for x rays and the extreme uv. J. Opt. Soc. Am., 64(3):301–309, 1974.
- [37] J. N. Cederquist, J. R. Fienup, J. C. Marron, and R. G. Paxman. Phase retrieval from experimental far-field speckle data. Opt. Lett., 13(8):619–621, 1988.
- [38] J. Miao, P. Charalambous, and J. Kirz. Extending the methodology of X-ray crystallography to allow imaging of micrometre-sized non-crystalline specimens. Nature, 400:342–344, 1999.
- [39] J. R. Fienup. Reconstruction of an object from the modulus of its Fourier transform. Opt. Lett., 3(1):27–29, 1978.
- [40] B. L. Henke, E. M. Gullikson, and J. C. Davis. X-Ray Interactions: Photoabsorption, Scattering, Transmission, and Reflection at $E = 50\text{--}30,000$ eV, $Z = 1\text{--}92$. At. Data Nucl. Data Tables, 54:181–342, 1993.
- [41] T. W. Barbee, S. Mrowka, and M. C. Hettrick. Molybdenum-silicon multilayer mirrors for the extreme ultraviolet. Appl. Opt., 24(6):883, 1985.
- [42] D. G. Stearns, R. S. Rosen, and S. P. Vernon. Multilayer mirror technology for soft-x-ray projection lithography. Appl. Opt., 32(34):6952–60, 1993.
- [43] C. Wagner and N. Harned. EUV lithography: Lithography gets extreme. Nat. Photonics, 4(1):24–26, 2010.

- [44] Y. U. Spenskii, D. B. Urenkov, T. H. Atano, and M. Y. Amamoto. Optimal Design of Multilayer Mirrors for Water-Window Microscope Optics. *14(1):64–73*, 2007.
- [45] R. Kodama, N. Ikeda, Y. Kato, Y. Katori, T. Iwai, and K. Takeshi. Development of an advanced Kirkpatrick-Baez microscope. *Opt. Lett.*, 21(17):1321–3, 1996.
- [46] S. Matsuyama, N. Kidani, H. Mimura, Y. Sano, Y. Kohmura, K. Tamasaku, M. Yabashi, T. Ishikawa, and K. Yamauchi. Hard-X-ray imaging optics based on four aspherical mirrors with 50 nm resolution. *Opt. Express*, 20(9):10310–9, 2012.
- [47] A. S. Bakulin, S. M. Durbin, T. Jach, and J. Pedulla. Fast imaging of hard x rays with a laboratory microscope. *Appl. Opt.*, 39(19):3333–7, 2000.
- [48] S. Yi, B. Mu, X. Wang, J. Zhu, L. Jiang, Z. Wang, and P. He. A four-channel multilayer KB microscope for high-resolution 8-keV X-ray imaging in laser-plasma diagnostics. *Chinese Opt. Lett.*, 12(1), 2014.
- [49] S. Matsuyama, Y. Emi, H. Kino, Y. Sano, Y. Kohmura, K. Tamasaku, M. Yabashi, T. Ishikawa, and K. Yamauchi. Development of achromatic full-field x-ray microscopy with compact imaging mirror system. In Barry Lai, editor, *SPIE X-Ray Nanoimaging*, volume 8851, 2013.
- [50] D. T. Attwood. *Soft X-Rays and Extreme Ultraviolet Radiation: Principles and Applications*. Cambridge Univ. Press, Cambridge, 1999.
- [51] D.-H. Kim, P. Fischer, W. Chao, E. Anderson, M.-Y. Im, S.-C. Shin, and S.-B. Choe. Magnetic soft x-ray microscopy at 15 nm resolution probing nanoscale local magnetic hysteresis (invited). *J. Appl. Phys.*, 99(8):08H303, 2006.
- [52] W. Chao, P. Fischer, T. Tyliczszak, S. Rekawa, E. Anderson, and P. Naulleau. Real space soft x-ray imaging at 10 nm spatial resolution. *Opt. Express*, 20(9):9777–83, 2012.
- [53] J. Vila-Comamala, K. Jefimovs, J. Raabe, T. Pilvi, R. H. Fink, M. Senoner, A. Maassdorf, M. Ritala, and C. David. Advanced thin film technology for ultrahigh resolution X-ray microscopy. *Ultramicroscopy*, 109(11):1360–4, 2009.
- [54] J. Vila-Comamala, S. Gorelick, E. Färm, C. M. Kewish, A. Diaz, R. Barrett, V. A. Guzenko, M. Ritala, and C. David. Ultra-high resolution zone-doubled diffractive X-ray optics for the multi-keV regime. *Opt. Express*, 19(1):175–84, 2011.
- [55] Y. Liu, J. Nelson, C. Holzner, J. C. Andrews, and P. Pianetta. Recent advances in synchrotron-based hard x-ray phase contrast imaging. *J. Phys. D. Appl. Phys.*, 46(49):494001, 2013.
- [56] F. Zernike. Phase Contrast, A New Method for the Microscopic Observation of Transparent Objects. *Physica*, 9(7):686–698, 1942.
- [57] A. Sakdinawat and Y. Liu. Phase contrast soft x-ray microscopy using Zernike zone plates. *Opt. Express*, 16(3):1559–64, 2008.
- [58] T.-Y. Chen, Y.-T. Chen, C.-L. Wang, I. M. Kempson, W.-K. Lee, Y. S. Chu, Y. Hwu, and G. Margaritondo. Full-field microimaging with 8 keV X-rays achieves a spatial resolutions better than 20 nm. *Opt. Express*, 19(21):19919–24, 2011.

- [59] Y. Wang, W. Yun, and C. Jacobsen. Achromatic Fresnel optics for wideband extreme-ultraviolet and X-ray imaging. *Nature*, 424(July):50–53, 2003.
- [60] K. Yamauchi, H. Mimura, T. Kimura, H. Yumoto, S. Handa, S. Matsuyama, K. Arima, Y. Sano, K. Yamamura, K. Inagaki, H. Nakamori, J. Kim, K. Tamasaku, Y. Nishino, M. Yabashi, and T. Ishikawa. Single-nanometer focusing of hard x-rays by Kirkpatrick-Baez mirrors. *J. Phys. Condens. matter*, 23:394206, 2011.
- [61] X. Huang, H. Yan, E. Nazaretski, R. Conley, N. Bouet, J. Zhou, K. Lauer, L. Li, D. Eom, D. Legnini, R. Harder, I. K. Robinson, and Y. S. Chu. 11 nm hard X-ray focus from a large-aperture multilayer Laue lens. *Sci. Rep.*, 3:3562, 2013.
- [62] A. Snigirev, V. Kohn, I. Snigireva, and B. Lengeler. A compound refractive lens for focusing high-energy X-rays. *Nature*, 384:49–51, 1996.
- [63] C. G. Schroer, O. Kurapova, J. Patommel, P. Boye, J. Feldkamp, B. Lengeler, M. Burghammer, C. Riekkel, L. Vincze, A. van der Hart, and M. Kuchler. Hard x-ray nanoprobe based on refractive x-ray lenses. *Appl. Phys. Lett.*, 87(12):124103, 2005.
- [64] C. J. R. Sheppard and T. Wilson. On the equivalence of scanning and conventional microscopes. *Optik (Stuttg.)*, 73(1):39–43, 1986.
- [65] C. Holzner, M. Feser, S. Vogt, B. Hornberger, S. B. Baines, and C. Jacobsen. Zernike phase contrast in scanning microscopy with X-rays. *Nat. Phys.*, 6(11):883–887, 2010.
- [66] H. Kang, J. Maser, G. Stephenson, C. Liu, R. Conley, A. Macrander, and S. Vogt. Nanometer Linear Focusing of Hard X Rays by a Multilayer Laue Lens. *Phys. Rev. Lett.*, 96(12):127401, 2006.
- [67] H. Yan, J. Maser, A. Macrander, Q. Shen, S. Vogt, G. B. Stephenson, and H. Kang. Takagi-Taupin description of x-ray dynamical diffraction from diffractive optics with large numerical aperture. *Phys. Rev. B*, 76(11):115438, 2007.
- [68] H. Jiang, H. Wang, C. Mao, A. Li, Y. He, Z. Dong, and Y. Zheng. Optimization of a multilayer Laue lens system for a hard x-ray nanoprobe. *J. Opt.*, 16(1):015002, 2014.
- [69] F. Döring, A. L. Robisch, C. Eberl, M. Osterhoff, A. Ruhlandt, T. Liese, F. Schlenkrich, S. Hoffmann, M. Bartels, T. Salditt, and H. U. Krebs. Sub-5 nm hard x-ray point focusing by a combined Kirkpatrick-Baez mirror and multilayer zone plate. *Opt. Express*, 21(16):19311–19323, 2013.
- [70] G. Pavlov, I. Snigireva, a. Snigirev, T. Sagdullin, and M. Schmidt. Refractive X-ray shape memory polymer 3D lenses with axial symmetry. *X-Ray Spectrom.*, 41(5):313–315, 2012.
- [71] F. Seiboth, A. Schropp, R. Hoppe, V. Meier, J. Patommel, H. J. Lee, B. Nagler, E. C. Galtier, B. Arnold, U. Zastrau, J. B. Hastings, D. Nilsson, F. Uhlén, Ulrich Vogt, H. M. Hertz, and C. G. Schroer. Focusing XFEL SASE pulses by rotationally parabolic refractive x-ray lenses. *J. Phys. Conf. Ser.*, 499:012004, 2014.
- [72] J. R. Fienup. Phase retrieval algorithms: a comparison. *Appl. Opt.*, 21(15):2758–69, 1982.

- [73] S. Marchesini. Invited article: a unified evaluation of iterative projection algorithms for phase retrieval. *Rev. Sci. Instrum.*, 78(1):011301, 2007.
- [74] H. N. Chapman, A. Barty, S. Marchesini, A. Noy, S. P. Hau-riege, C. Cui, M. R. Howells, R. Rosen, H. He, J. C. H. Spence, U. Weierstall, T. Beetz, C. Jacobsen, and D. Shapiro. High-resolution ab initio three-dimensional x-ray diffraction microscopy. *J. Opt. Soc. Am. A*, 23(5):1179–1200, 2006.
- [75] Y. Takahashi, Y. Nishino, R. Tsutsumi, H. Kubo, H. Furukawa, H. Mimura, S. Matsuyama, N. Zettsu, E. Matsubara, T. Ishikawa, and K. Yamauchi. High-resolution diffraction microscopy using the plane-wave field of a nearly diffraction limited focused x-ray beam. *Phys. Rev. B*, 80(5):1–5, 2009.
- [76] Y. Takahashi, N. Zettsu, Y. Nishino, R. Tsutsumi, E. Matsubara, T. Ishikawa, and K. Yamauchi. Three-dimensional electron density mapping of shape-controlled nanoparticle by focused hard X-ray diffraction microscopy. *Nano Lett.*, 10(5):1922–6, 2010.
- [77] V. Elser. Phase retrieval by iterated projections. *J. Opt. Soc. Am. A. Opt. Image Sci. Vis.*, 20(1):40–55, 2003.
- [78] R. W. Gerchberg and W. O. Saxton. A practical algorithm for the determination of phase from image and diffraction plane pictures. *Optik (Stuttg.)*, 35:227–246, 1972.
- [79] T. B. Edo, D. J. Batey, A. M. Maiden, C. Rau, U. Wagner, Z. D. Pešić, T. A. Waigh, and J. M. Rodenburg. Sampling in x-ray ptychography. *Phys. Rev. A*, 87(5):053850, 2013.
- [80] J. Miao, T. Ishikawa, E. Anderson, and K. Hodgson. Phase retrieval of diffraction patterns from noncrystalline samples using the oversampling method. *Phys. Rev. B*, 67(17):1–6, 2003.
- [81] B. Chen, R. Dilanian, S. Teichmann, B. Abbey, A. Peele, G. Williams, P. Hannaford, L. Van Dao, H. Quiney, and K. Nugent. Multiple wavelength diffractive imaging. *Phys. Rev. A*, 79(2):3–6, 2009.
- [82] J. N. Clark and A. G. Peele. Simultaneous sample and spatial coherence characterisation using diffractive imaging. *Appl. Phys. Lett.*, 99(15):154103, 2011.
- [83] B. Chen, B. Abbey, R. Dilanian, E. Balaur, G. van Riessen, M. Junker, C. Q. Tran, M. W. M. Jones, A. G. Peele, I. McNulty, D. J. Vine, C. T. Putkunz, H. M. Quiney, and K. A. Nugent. Diffraction imaging: The limits of partial coherence. *Phys. Rev. B*, 86(23):235401, 2012.
- [84] J. N. Clark, X. Huang, R. Harder, and I. K. Robinson. High-resolution three-dimensional partially coherent diffraction imaging. *Nat. Commun.*, 3:993, 2012.
- [85] P. Thibault, M. Dierolf, A. Menzel, O. Bunk, C. David, and F. Pfeiffer. High-resolution scanning x-ray diffraction microscopy. *Science*, 321:379–82, 2008.
- [86] A. M. Maiden and J. M. Rodenburg. An improved ptychographical phase retrieval algorithm for diffractive imaging. *Ultramicroscopy*, 109(10):1256–62, 2009.
- [87] W. Hoppe. Beugung im inhomogenen Primärstrahlwellenfeld. I. Prinzip einer Phasenmessung von Elektronenbeugungsinterferenzen. *Acta Crystallogr. Sect. A*, 25(4):495–501, 1969.

- [88] P. D. Nellist, B. C. McCallum, and J. M. Rodenburg. Resolution beyond the ‘information limit’ in transmission electron microscopy. *Nature*, 374:630–632, 1995.
- [89] P. Thibault, M. Dierolf, O. Bunk, A. Menzel, and F. Pfeiffer. Probe retrieval in ptychographic coherent diffractive imaging. *Ultramicroscopy*, 109(4):338–43, 2009.
- [90] A. M. Maiden, M. J. Humphry, and J. M. Rodenburg. Ptychographic transmission microscopy in three dimensions using a multi-slice approach. *J. Opt. Soc. Am. A. Opt. Image Sci. Vis.*, 29(8):1606–14, 2012.
- [91] D. J. Batey, D. Claus, and J. M. Rodenburg. Information multiplexing in ptychography. *Ultramicroscopy*, 138:13–21, 2014.
- [92] R. A. Bartels, A. Paul, H. Green, H. C. Kapteyn, M. M. Murnane, S. Backus, I. P. Christov, Y. Liu, D. Attwood, and C. Jacobsen. Generation of Spatially Coherent Light at Extreme Ultraviolet Wavelengths. *Science*, 297:376–378, 2002.
- [93] Y. Wang, E. Granados, F. Pedaci, D. Alessi, B. Luther, M. Berrill, and J. J. Rocca. Phase-coherent, injection-seeded, table-top soft-X-ray lasers at 18.9nm and 13.9nm. *Nat. Photonics*, 2(2):94–98, 2008.
- [94] E. D. Courant, M. S. Livingston, and H. S. Snyder. The Strong-Focusing Synchrotron - A New High Energy Accelerator. *Phys. Rev.*, 88(5):1190–1196, 1952.
- [95] F. R. Elder, A. M. Gurewitsch, R. V. Langmuir, and H. C. Pollock. Radiation from Electrons in a Synchrotron. *Phys. Rev.*, 71:829–830, 1947.
- [96] C. Kunz. Synchrotron radiation: third generation sources. *J. Phys. Condens. Matter*, 13:7499–7510, 2001.
- [97] J. D. Jackson. *Classical Electrodynamics*. John Wiley & Sons, Inc., Hoboken, NJ, 3rd edition, 1999.
- [98] S. Khan, K. Holldack, T. Kachel, R. Mitzner, and T. Quast. Femtosecond Undulator Radiation from Sliced Electron Bunches. *Phys. Rev. Lett.*, 97(7):074801, 2006.
- [99] E. L. Saldin, E. A. Schneidmiller, and M. V. Yurkov. *The Physics of Free Electron Lasers*. Springer, Berlin, 2000.
- [100] L. R. Elias, W. M. Fairbank, J. M. J. Madey, H. A. Schwettman, and T. I. Smith. Observation of Stimulated Emission of Radiation by Relativistic Electrons in a Spatially Periodic Transverse Magnetic Field. *Phys. Rev. Lett.*, 36(13):717–720, 1976.
- [101] P. Emma, R. Akre, J. Arthur, R. Bionta, C. Bostedt, J. Bozek, A. Brachmann, P. Bucksbaum, R. Coffee, F. Decker, Y. Ding, D. Dowell, S. Edstrom, A. Fisher, J. Frisch, S. Gilevich, J. Hastings, G. Hays, Ph. Hering, Z. Huang, R. Iverson, H. Loos, M. Messerschmidt, A. Miahnahri, S. Moeller, H. Nuhn, G. Pile, D. Ratner, J. Rzepiela, D. Schultz, T. Smith, P. Stefan, H. Tompkins, J. Turner, J. Welch, W. White, J. Wu, G. Yocky, and J. Galayda. First lasing and operation of an ångstrom-wavelength free-electron laser. *Nat. Photonics*, 4:641–647, 2010.

- [102] J. Amann, W. Berg, V. Blank, F.-J. Decker, Y. Ding, P. Emma, Y. Feng, J. Frisch, D. Fritz, J. Hastings, Z. Huang, J. Krzywinski, R. Lindberg, H. Loos, A. Lutman, H.-D. Nuhn, D. Ratner, J. Rzepiela, D. Shu, Y. Shvyd'ko, S. Spampinati, S. Stoupin, S. Terentyev, E. Trakhtenberg, D. Walz, J. Welch, J. Wu, A. Zholents, and D. Zhu. Demonstration of self-seeding in a hard-X-ray free-electron laser. *Nat. Photonics*, 6(10):693–698, 2012.
- [103] T. Sato, A. Iwasaki, S. Owada, K. Yamanouchi, E. J. Takahashi, K. Midorikawa, M. Aoyama, K. Yamakawa, T. Togashi, K. Fukami, T. Hatsui, T. Hara, T. Kameshima, H. Kitamura, N. Kumagai, S. Matsubara, M. Nagasono, H. Ohashi, T. Ohshima, Y. Otake, T. Shintake, K. Tamasaku, H. Tanaka, T. Tanaka, K. Togawa, H. Tomizawa, T. Watanabe, M. Yabashi, and T. Ishikawa. Full-coherent free electron laser seeded by 13th- and 15th-order harmonics of near-infrared femtosecond laser pulses. *J. Phys. B At. Mol. Opt. Phys.*, 46(16):164006, 2013.
- [104] T. Maltezopoulos, M. Mittenzwey, A. Azima, J. Bödewadt, H. Dachraoui, M. Rehders, C. Lechner, M. Schulz, M. Wieland, T. Laarmann, J. Roßbach, and M. Drescher. A high-harmonic generation source for seeding a free-electron laser at 38 nm. *Appl. Phys. B*, 115(1):45–54, 2013.
- [105] S. Ackermann, A. Azima, S. Bajt, J. Bödewadt, F. Curbis, H. Dachraoui, H. Delsim-Hashemi, M. Drescher, S. Düsterer, B. Faatz, M. Felber, J. Feldhaus, E. Hass, U. Hipp, K. Honkavaara, R. Ischebeck, S. Khan, T. Laarmann, C. Lechner, Th. Maltezopoulos, V. Miltchev, M. Mittenzwey, M. Rehders, J. Rönsch-Schulenburg, J. Rossbach, H. Schlarb, S. Schreiber, L. Schroedter, M. Schulz, S. Schulz, R. Tarkeshian, M. Tischer, V. Wacker, and M. Wieland. Generation of Coherent 19- and 38-nm Radiation at a Free-Electron Laser Directly Seeded at 38nm. *Phys. Rev. Lett.*, 111(11):114801, 2013.
- [106] L. H. Yu. Generation of intense uv radiation by subharmonically seeded single-pass free-electron lasers. *Phys. Rev. A*, 44(8):5178–5193, 1991.
- [107] E. Allaria, A. Battistoni, F. Bencivenga, R. Borghes, C. Callegari, F. Capotondi, D. Castonovo, P. Cinquegrana, D. Cocco, M. Coreno, P. Craievich, R. Cucini, F. D’Amico, M. B. Danailov, A. Demidovich, G. De Ninno, A. Di Cicco, S. Di Fonzo, M. Di Fraia, S. Di Mitri, B. Diviacco, W. M. Fawley, E. Ferrari, A. Filipponi, L. Froehlich, A. Gessini, E. Giangristotomi, L. Giannessi, D. Giuressi, C. Grazioli, R. Gunnella, R. Ivanov, B. Mahieu, N. Mahne, C. Masciovecchio, I. P. Nikolov, G. Passos, E. Pedersoli, G. Penco, E. Principi, L. Raimondi, R. Sergo, P. Sigalotti, C. Spezzani, C. Svetina, M. Trovò, and M. Zangrando. Tunability experiments at the FERMI@Elettra free-electron laser. *New J. Phys.*, 14(11):113009, 2012.
- [108] T. Hara. Free-electron lasers: Fully coherent soft X-rays at FERMI. *Nat. Photonics*, 7(11):852–854, 2013.
- [109] D. L. Matthews, P. L. Hagelstein, M. D. Rosen, M. J. Eckart, N. M. Ceglio, A. U. Hazi, H. Medeck, B. J. Macgowan, J. E. Trebes, B. L. Whitten, E. M. Campbell, C. W. Hatcher, A. M. Hawryluk, R. L. Kauffman, L. D. Pleasance, G. Rambach, J. H. Scofield, G. Stone, and T. A. Weaver. Demonstration of a Soft X-Ray Amplifier. *Phys. Rev. Lett.*, 54(2):110–113, 1985.
- [110] D. Alessi, Y. Wang, B. M. Luther, L. Yin, D. H. Martz, M. R. Woolston, Y. Liu, M. Berrill, and J. J. Rocca. Efficient Excitation of Gain-Saturated Sub-9-nm-Wavelength Tabletop Soft-X-Ray Lasers and Lasing Down to 7.36nm. *Phys. Rev. X*, 1(2):021023, 2011.

- [111] S. Heinbuch, M. Grisham, D. Martz, and J. J. Rocca. Demonstration of a desk-top size high repetition rate soft x-ray laser. Opt. Express, 13(11):4050–4055, 2005.
- [112] M. Berrill, D. Alessi, Y. Wang, S. R. Domingue, D. H. Martz, B. M. Luther, Y. Liu, and J. J. Rocca. Improved beam characteristics of solid-target soft x-ray laser amplifiers by injection seeding with high harmonic pulses. Opt. Lett., 35(14):2317–9, 2010.
- [113] L. M. Meng, D. Alessi, O. Guilbaud, Y. Wang, M. Berrill, B. M. Luther, D. H. Martz, D. Joyeux, S. De Rossi, J. J. Rocca, and A. Klisnick. Temporal coherence and spectral linewidth of an injection-seeded transient collisional soft x-ray laser. Opt. Express, 19(13):12087–12092, 2011.
- [114] L. Li, Y. Wang, S. Wang, E. Oliva, L. Yin, T. T. T. Le, S. Daboussi, D. Ros, G. Maynard, S. Sebban, B. Hu, J. J. Rocca, and P. Zeitoun. Wavefront improvement in an injection-seeded soft x-ray laser based on a solid-target plasma amplifier. Opt. Lett., 38(20):4011–4014, 2013.
- [115] J. Bokor, P. H. Bucksbaum, and R. R. Freeman. Generation of 35.5-nm coherent radiation. Opt. Lett., 8(4):217–219, 1983.
- [116] M. Lewenstein, P. Balcou, M. Y. Ivanov, A. L. Huillier, and P. B. Corkum. Theory of high-harmonic generation by low-frequency laser fields. Phys. Rev. A, 49(3):2117–2132, 1994.
- [117] P. B. Corkum. Plasma Perspective on Strong-Field Multiphoton Ionization. Phys. Rev. Lett., 71(13):1994–1997, 1993.
- [118] A. Rundquist, C. G. Durfee, Z. Chang, C. Herne, S. Backus, M. M. Murnane, and H. C. Kapteyn. Phase-Matched Generation of Coherent Soft X-rays. Science, 280:1412–1415, 1998.
- [119] C. G. Durfee, A. R. Rundquist, S. Backus, C. Herne, M. M. Murnane, and H. C. Kapteyn. Phase Matching of High-Order Harmonics in Hollow Waveguides. Phys. Rev. Lett., 83(11):2187–2190, 1999.
- [120] F. Krausz. Attosecond physics. Rev. Mod. Phys., 81(1):163–234, 2009.
- [121] O. Kfir, P. Grychtol, E. Turgut, R. Knut, D. Zusin, D. Popmintchev, T. Popmintchev, H. Nembach, J. M. Shaw, A. Fleischer, H. Kapteyn, M. Murnane, and O. Cohen. Generation of bright circularly-polarized extreme ultraviolet high harmonics for magnetic circular dichroism spectroscopy. [arXiv:1401.4101 \[physics.optics\]](https://arxiv.org/abs/1401.4101), pages 1–15, 2014.
- [122] A. L. Schawlow and C. H. Townes. Infrared and Optical Masers. Phys. Rev., 112(6):1940–1949, 1958.
- [123] T. H. Maiman. Stimulated Optical Radiation in Ruby. Nature, 187:493–494, 1960.
- [124] F. J. McClung and R. W. Hellwarth. Giant Optical Pulsations from Ruby. J. Appl. Phys., 33(3):828, 1962.
- [125] A. J. DeMaria, W. H. Glenn, M. J. Brienza, and M. E. Mack. Picosecond laser pulses. Proc. IEEE, 57(1):2–25, 1969.
- [126] L. E. Hargrove, R. L. Fork, and M. A. Pollack. Locking of He-Ne Laser Modes Induced by Synchronous Intracavity Modulation. Appl. Phys. Lett., 5(1):4, 1964.

- [127] H. W. Mocker and R. J. Collins. Mode Competition and Self-Locking Effects in a Q-Switched Ruby Laser. Appl. Phys. Lett., 7(10):270, 1965.
- [128] A. J. DeMaria. Self Mode-Locking of Lasers With Saturable Absorbers. Appl. Phys. Lett., 8(7):174, 1966.
- [129] P. M. French, J. A. Williams, and J. R. Taylor. Femtosecond pulse generation from a titanium-doped sapphire laser using nonlinear external cavity feedback. Opt. Lett., 14(13):686–8, 1989.
- [130] D. E. Spence, P. N. Kean, and W. Sibbett. 60-fsec pulse generation from a self-mode-locked Ti:sapphire laser. Opt. Lett., 16(1):42–4, 1991.
- [131] U. Keller, G. W. 'tHooft, W. H. Knox, and J. E. Cunningham. Femtosecond pulses from a continuously self-starting passively mode-locked Ti:sapphire laser. Opt. Lett., 16(13):1022–1024, 1991.
- [132] J. Zhou, G. Taft, C. P. Huang, M. M. Murnane, H. C. Kapteyn, and I. P. Christov. Pulse evolution in a broad-bandwidth Ti:sapphire laser. Opt. Lett., 19(15):1149–51, 1994.
- [133] R. L. Fork, O. E. Martinez, and J. P. Gordon. Negative dispersion using pairs of prisms. Opt. Lett., 9(5):150–2, 1984.
- [134] T. Brabec, C. Spielmann, P. F. Curley, and F. Krausz. Kerr lens mode locking. Opt. Lett., 17(18):1292–4, 1992.
- [135] M. T. Asaki, C. P. Huang, D. Garvey, J. Zhou, H. C. Kapteyn, and M. M. Murnane. Generation of 11-fs pulses from a self-mode-locked Ti:sapphire laser. Opt. Lett., 18(12):977–9, 1993.
- [136] E. P. Ippen. Principles of Passive Mode Locking. Appl. Phys. B, 58:159–170, 1994.
- [137] S. T. Cundiff. Phase stabilization of ultrashort optical pulses. J. Phys. D. Appl. Phys., 35:R43–R59, 2002.
- [138] H. Rabitz. Whither the Future of Controlling Quantum Phenomena? Science, 288(5467):824–828, 2000.
- [139] M. Dantus and V. V. Lozovoy. Experimental coherent laser control of physicochemical processes. Chem. Rev., 104(4):1813–59, 2004.
- [140] R. J. Jones, K. Moll, M. Thorpe, and J. Ye. Phase-Coherent Frequency Combs in the Vacuum Ultraviolet via High-Harmonic Generation inside a Femtosecond Enhancement Cavity. Phys. Rev. Lett., 94(19):193201, 2005.
- [141] D. C. Yost, T. R. Schibli, and J. Ye. Efficient output coupling of intracavity high-harmonic generation. Opt. Lett., 33(10):1099–101, 2008.
- [142] S. Backus, C. G. Durfee, M. M. Murnane, and H. C. Kapteyn. High power ultrafast lasers. Rev. Sci. Instrum., 69(3):1207, 1998.
- [143] O. E. Martinez. Design of High-Power Ultrashort Pulse Amplifiers by Expansion and Recompression. IEEE J. Quantum Electron., QE-23(8):1385–1387, 1987.

- [144] S. Backus, R. Bartels, S. Thompson, R. Dollinger, H. C. Kapteyn, and M. M. Murnane. High-efficiency, single-stage 7-kHz high-average-power ultrafast laser system. Opt. Lett., 26(7):465–467, 2001.
- [145] M. V. Ammosov, N. B. Delone, and V. P. Krainov. Tunnel ionization of complex atoms and of atomic ions in an alternating electromagnetic field. Sov. Phys. JETP, 64(6):1191–1194, 1986.
- [146] X. M. Tong and C. D. Lin. Empirical formula for static field ionization rates of atoms and molecules by lasers in the barrier-suppression regime. J. Phys. B At. Mol. Opt. Phys., 38(15):2593–2600, 2005.
- [147] R. W. Boyd. Nonlinear Optics. Elsevier Science, San Diego, CA, 2nd edition, 2003.
- [148] E. Constant, D. Garzella, P. Breger, E. Mével, C. Dorrer, C. Le Blanc, F. Salin, and P. Agostini. Optimizing High Harmonic Generation in Absorbing Gases: Model and Experiment. Phys. Rev. Lett., 82(8):1668–1671, 1999.
- [149] E. A. J. Marcatili and R. A. Schmeltzer. Hollow Metallic and Dielectric Waveguides for Long Distance Optical Transmission and Lasers. Bell Syst. Tech. J., 43:1783–1809, 1964.
- [150] M.-C. Chen, P. Arpin, T. Popmintchev, M. Gerrity, B. Zhang, M. Seaberg, D. Popmintchev, M. Murnane, and H. Kapteyn. Bright, Coherent, Ultrafast Soft X-Ray Harmonics Spanning the Water Window from a Tabletop Light Source. Phys. Rev. Lett., 105(17):1–4, 2010.
- [151] J.-F. Hergott, M. Kovacev, H. Merdji, C. Hubert, Y. Mairesse, E. Jean, P. Breger, P. Agostini, B. Carré, and P. Salières. Extreme-ultraviolet high-order harmonic pulses in the microjoule range. Phys. Rev. A, 66(2):021801, 2002.
- [152] E. Takahashi, Y. Nabekawa, M. Nishida, and K. Midorikawa. Generation of high-energy high-order harmonics by use of a long interaction medium. J. Opt. Soc. Am. B, 20(1):158, 2003.
- [153] W. Boutu, T. Auguste, J. P. Caumes, H. Merdji, and B. Carré. Scaling of the generation of high-order harmonics in large gas media with focal length. Phys. Rev. A, 84(5):053819, 2011.
- [154] A. L’Huillier, K. J. Schafer, and K. C. Kulander. High-Order Harmonic Generation in Xenon at 1064 nm: The Role of Phase Matching. Phys. Rev. Lett., 66(17):2200–2203, 1991.
- [155] I. P. Christov, J. Zhou, J. Peatross, A. Rundquist, M. M. Murnane, and H. C. Kapteyn. Nonadiabatic Effects in High-Harmonic Generation with Ultrashort Pulses. Phys. Rev. Lett., 77(9):1743–1746, 1996.
- [156] A. M. Weiner. Femtosecond pulse shaping using spatial light modulators. Rev. Sci. Instrum., 71(5):1929, 2000.
- [157] C. Froehly, B. Colombeau, and M. Vampouille. Shaping and Analysis of Picosecond Light Pulses. In E. Wolf, editor, Prog. Opt. XX, pages 63–153. 1983.
- [158] A. M. Weiner, J. P. Heritage, and E. M. Kirschner. High-resolution femtosecond pulse shaping. J. Opt. Soc. Am. B, 5(8):1563, 1988.

- [159] A. M. Weiner. Ultrafast optical pulse shaping: A tutorial review. Opt. Commun., 284(15):3669–3692, 2011.
- [160] A. M. Weiner, D. E. Leaird, J. S. Patel, and J. R. Wullert. Programmable femtosecond pulse shaping by use of a multielement liquid-crystal phase modulator. Opt. Lett., 15(6):326, 1990.
- [161] E. Zeek, K. Maginnis, S. Backus, U. Russek, M. Murnane, G. Mourou, H. Kapteyn, and G. Vdovin. Pulse compression by use of deformable mirrors. Opt. Lett., 24(7):493–5, 1999.
- [162] R. Trebino, K. W. DeLong, D. N. Fittinghoff, J. N. Sweetser, M. A. Krumbugel, B. A. Richman, and D. J. Kane. Measuring ultrashort laser pulses in the time-frequency domain using frequency-resolved optical gating. Rev. Sci. Instrum., 68(9):3277, 1997.
- [163] D. Meshulach, D. Yelin, and Y. Silberberg. Adaptive ultrashort pulse compression and shaping. Opt. Commun., 138:345–348, 1997.
- [164] D. Yelin, D. Meshulach, and Y. Silberberg. Adaptive femtosecond pulse compression. Opt. Lett., 22(23):1793–5, 1997.
- [165] R. Bartels, S. Backus, E. Zeek, L. Misoguti, G. Vdovin, I. P. Christov, M. M. Murnane, and H. C. Kapteyn. Shaped-pulse optimization of coherent emission of high-harmonic soft X-rays. Nature, 406(6792):164–6, 2000.
- [166] M. C. Chen, J. Y. Huang, Q. Yang, C. L. Pan, and J.-I. Chyi. Freezing phase scheme for fast adaptive control and its application to characterization of femtosecond coherent optical pulses reflected from semiconductor saturable absorber mirrors. J. Opt. Soc. Am. B, 22(5):1134, 2005.
- [167] V. V. Lozovoy, I. Pastirk, and M. Dantus. Multiphoton intrapulse interference. IV. Ultrashort laser pulse spectral phase characterization and compensation. Opt. Lett., 29(7):775–7, 2004.
- [168] M. C. Chen, J. Y. Huang, and L. J. Chen. Coherent control multiphoton processes in semiconductor saturable Bragg reflector with freezing phase algorithm. Appl. Phys. B, 80(3):333–340, 2004.
- [169] J. K. Ranka, A. L. Gaeta, A. Baltuska, M. S. Pshenichnikov, and D. A. Wiersma. Autocorrelation measurement of 6-fs pulses based on the two-photon-induced photocurrent in a GaAsP photodiode. Opt. Lett., 22(17):1344–6, 1997.
- [170] R. Bartels, S. Backus, I. Christov, H. Kapteyn, and M. Murnane. Attosecond time-scale feedback control of coherent X-ray generation. Chem. Phys., 267(1-3):277–289, 2001.
- [171] T. Pfeifer, D. Walter, C. Winterfeldt, C. Spielmann, and G. Gerber. Controlling the spectral shape of coherent soft X-rays. Appl. Phys. B, 80(3):277–280, 2005.
- [172] S. Grafstrom, U. Harbarth, J. Kowalski, R. Neumann, and S. Noehte. Fast Laser Beam Position Control With Submicroradian Precision. Opt. Commun., 65(2):121–126, 1988.
- [173] F. Breitling, R. S. Weigel, M. C. Downer, and T. Tajima. Laser pointing stabilization and control in the submicroradian regime with neural networks. Rev. Sci. Instrum., 72(2):1339, 2001.

- [174] T. Kanai, A. Suda, S. Bohman, M. Kaku, S. Yamaguchi, and K. Midorikawa. Pointing stabilization of a high-repetition-rate high-power femtosecond laser for intense few-cycle pulse generation. *Appl. Phys. Lett.*, 92(6):061106, 2008.
- [175] Y. Kida, K. Okamura, J. Liu, and T. Kobayashi. Sub-10-fs deep-ultraviolet light source with stable power and spectrum. *Appl. Opt.*, 51(26):6403–10, 2012.
- [176] G. Genoud, F. Wojda, M. Burza, A. Persson, and C.-G. Wahlström. Active control of the pointing of a multi-terawatt laser. *Rev. Sci. Instrum.*, 82(3):033102, 2011.
- [177] A. Stalmashonak, N. Zhavoronkov, I. V. Hertel, S. Vetrov, and K. Schmid. Spatial control of femtosecond laser system output with submicroradian accuracy. *Appl. Opt.*, 45(6):1271–4, 2006.
- [178] L. Kral. Automatic beam alignment system for a pulsed infrared laser. *Rev. Sci. Instrum.*, 80(1):013102, 2009.
- [179] R. Singh, K. Patel, J. Govindarajan, and A. Kumar. Fuzzy logic based feedback control system for laser beam pointing stabilization. *Appl. Opt.*, 49(27):5143–7, 2010.
- [180] A. Tustin. A method of analysing the behaviour of linear systems in terms of time series. *J. Inst. Electr. Eng.*, 94(1):130–142, 1947.
- [181] A. Fix and C. Stöckl. Investigations on the beam pointing stability of a pulsed optical parametric oscillator. *Opt. Express*, 21(9):10720–10730, 2013.
- [182] B. Zhang, M. D. Seaberg, D. E. Adams, D. F. Gardner, E. R. Shanblatt, J. M. Shaw, W. Chao, E. M. Gullikson, F. Salmassi, H. C. Kapteyn, and M. M. Murnane. Full field tabletop EUV coherent diffractive imaging in a transmission geometry. *Opt. Express*, 21(19):21970–21980, 2013.
- [183] M. D. Seaberg, B. Zhang, D. F. Gardner, E. R. Shanblatt, M. M. Murnane, H. C. Kapteyn, and D. E. Adams. Tabletop Nanometer Extreme Ultraviolet Imaging in an Extended Reflection Mode using Coherent Fresnel Ptychography. *arXiv:1312.2049*, pages 1–9, 2013.
- [184] G. Andriukaitis, T. Balčinas, S. Ališauskas, A. Pugžlys, A. Baltuška, T. Popmintchev, M.-C. Chen, M. M. Murnane, and H. C. Kapteyn. 90 GW peak power few-cycle mid-infrared pulses from an optical parametric amplifier. *Opt. Lett.*, 36(15):2755–7, 2011.
- [185] M. D. Seaberg, D. E. Adams, E. L. Townsend, D. A. Raymondson, W. F. Schlotter, Y. Liu, C. S. Menoni, L. Rong, C.-C. Chen, J. Miao, H. C. Kapteyn, and M. M. Murnane. Ultrahigh 22 nm resolution coherent diffractive imaging using a desktop 13 nm high harmonic source. *Opt. Express*, 19(23):22470–9, 2011.
- [186] H. Jiang, C. Song, C.-C. Chen, R. Xu, K. S. Raines, B. P. Fahimian, C.-H. Lu, T.-K. Lee, A. Nakashima, J. Urano, T. Ishikawa, F. Tamanoi, and J. Miao. Quantitative 3D imaging of whole, unstained cells by using X-ray diffraction microscopy. *Proc. Natl. Acad. Sci. U. S. A.*, 107(25):11234–9, 2010.
- [187] J. N. Clark, L. Beitra, G. Xiong, A. Higginbotham, D. M. Fritz, H. T. Lemke, D. Zhu, M. Chollet, G. J. Williams, M. Messerschmidt, B. Abbey, R. J. Harder, A. M. Korsunsky, J. S. Wark, and I. K. Robinson. Ultrafast three-dimensional imaging of lattice dynamics in individual gold nanocrystals. *Science*, 341(6141):56–9, 2013.

- [188] J. J. Turner, X. Huang, O. Krupin, K. A. Seu, D. Parks, S. Kevan, E. Lima, K. Kisslinger, I. McNulty, R. Gambino, S. Mangin, S. Roy, and P. Fischer. X-Ray Diffraction Microscopy of Magnetic Structures. Phys. Rev. Lett., 107(3):033904, 2011.
- [189] R. Xu, H. Jiang, C. Song, J. A. Rodriguez, Z. Huang, C.-C. Chen, D. Nam, J. Park, M. Gallagher-Jones, S. Kim, A. Suzuki, Y. Takayama, T. Oroguchi, Y. Takahashi, J. Fan, Y. Zou, T. Hatsui, Y. Inubushi, T. Kameshima, K. Yonekura, K. Tono, T. Togashi, T. Sato, M. Yamamoto, M. Nakasako, M. Yabashi, T. Ishikawa, and J. Miao. Single-shot 3D structure determination of nanocrystals with femtosecond X-ray free electron laser pulses. 2013.
- [190] A. C. Thompson, D. T. Attwood, E. M. Gullikson, M. R. Howells, J. B. Kortright, A. L. Robinson, J. H. Underwood, K.-J. Kim, J. Kirz, I. Lindau, P. Pianetta, H. Winick, G. P. Williams, and J. H. Scofield. X-RAY DATA BOOKLET. Berkeley, California, second edition, 2001.
- [191] The Center for X-Ray Optics. <http://www.cxro.lbl.gov/>.
- [192] J. M. Cowley. Diffraction Physics. Elsevier Science B.V., Amsterdam, third edition, 1995.
- [193] D. F. Gardner, B. Zhang, M. D. Seaberg, L. S. Martin, D. E. Adams, F. Salmassi, E. Gullikson, H. Kapteyn, and M. Murnane. High numerical aperture reflection mode coherent diffraction microscopy using off-axis apertured illumination. Opt. Express, 20(17):19050–9, 2012.
- [194] M. G. Moharam, E. B. Grann, and D. A. Pommet. Formulation for stable and efficient implementation of the rigorous coupled-wave analysis of binary gratings. J. Opt. Soc. Am. A, 12(5):1068–1076, 1995.
- [195] H. Jiang, R. Xu, C.-C. Chen, W. Yang, J. Fan, X. Tao, C. Song, Y. Kohmura, T. Xiao, Y. Wang, Y. Fei, T. Ishikawa, W. L. Mao, and J. Miao. Three-Dimensional Coherent X-Ray Diffraction Imaging of Molten Iron in Mantle Olivine at Nanoscale Resolution. Phys. Rev. Lett., 110(20):205501, 2013.
- [196] K. S. Raines, S. Salha, R. L. Sandberg, H. Jiang, J. A. Rodríguez, B. P. Fahimian, H. C. Kapteyn, J. Du, and J. Miao. Three-dimensional structure determination from a single view. Nature, 463(7278):214–7, 2010.
- [197] G. Wang, H. Yu, W. Cong, and A. Katsevich. Non-uniqueness and instability of ankylography. Nature, 480:E2–E3, 2011.
- [198] J. W. Cooley and J. W. Tukey. An Algorithm for the Machine Calculation Complex Fourier Series. Math. Comp., 19:297–301, 1965.
- [199] D. Sayre. Some implications of a theorem due to Shannon. Acta Crystallogr., 5:843, 1952.
- [200] M. Born and E. Wolf. Principles of Optics. 7th edition, 1999.
- [201] B. Abbey, K. A. Nugent, G. J. Williams, J. N. Clark, A. G. Peele, M. A. Pfeifer, M. de Jonge, and I. McNulty. Keyhole coherent diffractive imaging. Nat. Phys., 4(5):394–398, 2008.
- [202] T. Harada, J. Kishimoto, T. Watanabe, H. Kinoshita, and D. G. Lee. Mask observation results using a coherent extreme ultraviolet scattering microscope at NewSUBARU. J. Vac. Sci. Technol. B Microelectron. Nanom. Struct., 27(6):3203, 2009.

- [203] B. Abbey, L. W. Whitehead, H. M. Quiney, D. J. Vine, G. A. Cadenazzi, C. A. Henderson, K. A. Nugent, E. Balaur, C. T. Putkunz, A. G. Peele, G. J. Williams, and I. McNulty. Lensless imaging using broadband X-ray sources. *Nat. Photonics*, 5(7):420–424, 2011.
- [204] D. R. Luke. Relaxed averaged alternating reflections for diffraction imaging. *Inverse Probl.*, 21(1):37–50, 2005.
- [205] S. Marchesini, H. He, H. Chapman, S. Hau-Riege, A. Noy, M. Howells, U. Weierstall, and J. Spence. X-ray image reconstruction from a diffraction pattern alone. *Phys. Rev. B*, 68(14):1–4, 2003.
- [206] G. J. Williams, H. M. Quiney, A. G. Peele, and K. A. Nugent. Fresnel coherent diffractive imaging: treatment and analysis of data. *New J. Phys.*, 12(3):035020, 2010.
- [207] A. P. Mancuso, M. R. Groves, O. E. Polozhentsev, G. J. Williams, I. McNulty, C. Antony, R. Santarella-Mellwig, A. V. Soldatov, V. Lamzin, A. G. Peele, K. A. Nugent, and I. A. Vartanyants. Internal structure of an intact *Convallaria majalis* pollen grain observed with X-ray Fresnel coherent diffractive imaging. *Opt. Express*, 20(24):26778–85, 2012.
- [208] A. M. Maiden, M. J. Humphry, F. Zhang, and J. M. Rodenburg. Superresolution imaging via ptychography. *J. Opt. Soc. Am. A. Opt. Image Sci. Vis.*, 28(4):604–12, 2011.
- [209] X. Zhang, A. R. Libertun, A. Paul, E. Gagnon, S. Backus, I. P. Christov, M. M. Murnane, H. C. Kapteyn, R. A. Bartels, Y. Liu, and D. T. Attwood. Highly coherent light at 13 nm generated by use of quasi-phase-matched high-harmonic generation. *Opt. Lett.*, 29(12):1357–9, 2004.
- [210] R. Sandberg, A. Paul, D. A. Raymondson, S. Hädrich, D. Gaudiosi, J. Holtsnider, R. I. Tobey, O. Cohen, M. M. Murnane, H. C. Kapteyn, Changyong Song, Jianwei Miao, Yanwei Liu, and Farhad Salmassi. Lensless Diffractive Imaging Using Tabletop Coherent High-Harmonic Soft-X-Ray Beams. *Phys. Rev. Lett.*, 99(9):1–4, 2007.
- [211] R. L. Sandberg, D. A. Raymondson, C. La-o-vorakiat, A. Paul, K. S. Raines, J. Miao, M. M. Murnane, H. C. Kapteyn, and W. F. Schlotter. Tabletop soft-x-ray Fourier transform holography with 50 nm resolution. *Opt. Lett.*, 34(11):1618–20, 2009.
- [212] D. A. Raymondson. Tabletop Coherent Diffractive Microscopy with Soft X-Ray Illumination from High Harmonic Generation at 29 nm and 13.5 nm. PhD thesis, University of Colorado at Boulder, 2010.
- [213] Y. Nagata, Y. Nabekawa, and K. Midorikawa. Development of high-throughput, high-damage-threshold beam separator for 13 nm high-order harmonics. *Opt. Lett.*, 31(9):1316–8, 2006.
- [214] R. W. Falcone and J. Bokor. Dichroic beam splitter for extreme-ultraviolet and visible radiation. *Opt. Lett.*, 8(1):21–3, 1983.
- [215] V. Elser. Random projections and the optimization of an algorithm for phase retrieval. *J. Phys. A. Math. Gen.*, 36(12):2995–3007, 2003.
- [216] M. Guizar-Sicairos, S. T. Thurman, and J. R. Fienup. Efficient subpixel image registration algorithms. *Opt. Lett.*, 33(2):156–8, 2008.

- [217] J. Steinbrener, J. Nelson, X. Huang, S. Marchesini, D. Shapiro, J. J. Turner, and C. Jacobsen. Data preparation and evaluation techniques for x-ray diffraction microscopy. Opt. Express, 18(18):18598–614, 2010.
- [218] R. L. Sandberg, C. Song, P. W. Wachulak, D. A. Raymondson, A. Paul, B. Amirbekian, E. Lee, A. E. Sakdinawat, C. La-o-vorakiat, M. C. Marconi, C. S. Menoni, M. M. Murnane, J. J. Rocca, H. C. Kapteyn, and J. Miao. High numerical aperture tabletop soft x-ray diffraction microscopy with 70-nm resolution. Proc. Natl. Acad. Sci. U. S. A., 105(1):24–7, 2008.
- [219] T. A. Pitts and J. F. Greenleaf. Fresnel transform phase retrieval from magnitude. IEEE Trans. Ultrason. Ferroelectr. Freq. Control, 50(8):1035–45, 2003.
- [220] M. Sivis, M. Duwe, B. Abel, and C. Ropers. Nanostructure-enhanced atomic line emission. Nature, 485:E1–2, 2012.
- [221] L. Minnhagen. Accurately Measured and Calculated Ground-Term Combinations of Ar II*. J. Opt. Soc. Am., 61(9):1257–1262, 1971.
- [222] J. E. Sansonetti and W. C. Martin. Handbook of Basic Atomic Spectroscopic Data. J. Phys. Chem. Ref. Data, 34(4):1559–2259, 2005.
- [223] M. Sivis, M. Duwe, B. Abel, and C. Ropers. Extreme-ultraviolet light generation in plasmonic nanostructures. Nat. Phys., 9(5):304–309, 2013.
- [224] H. M. Quiney, A. G. Peele, Z. Cai, D. Paterson, and K. A. Nugent. Diffractive imaging of highly focused X-ray fields. Nat. Phys., 2(2):101–104, 2006.
- [225] G. Williams, H. Quiney, B. Dhal, C. Tran, K. Nugent, A. Peele, D. Paterson, and M. de Jonge. Fresnel Coherent Diffractive Imaging. Phys. Rev. Lett., 97(2):1–4, 2006.
- [226] T. Harada, M. Nakasuji, Y. Nagata, T. Watanabe, and H. Kinoshita. Phase Imaging of Extreme-Ultraviolet Mask Using Coherent Extreme-Ultraviolet Scatterometry Microscope. Jpn. J. Appl. Phys., 52:06GB02, 2013.
- [227] S. Roy, D. Parks, K. A. Seu, R. Su, J. J. Turner, W. Chao, E. H. Anderson, S. Cabrini, and S. D. Kevan. Lensless X-ray imaging in reflection geometry. Nat. Photonics, 5(4):243–245, 2011.
- [228] M. Zürch, C. Kern, and C. Spielmann. XUV coherent diffraction imaging in reflection geometry with low numerical aperture. Opt. Express, 21(18):21131–47, 2013.
- [229] T. Sun, Z. Jiang, J. Strzalka, L. Ocola, and J. Wang. Three-dimensional coherent X-ray surface scattering imaging near total external reflection. Nat. Photonics, 6:586–590, 2012.
- [230] A. M. Maiden, M. J. Humphry, M. C. Sarahan, B. Kraus, and J. M. Rodenburg. An annealing algorithm to correct positioning errors in ptychography. Ultramicroscopy, 120:64–72, 2012.
- [231] F. Zhang, I. Peterson, J. Vila-Comamala, A. Diaz, R. Bean, B. Chen, A. Menzel, I. K. Robinson, and J. M. Rodenburg. Translation position determination in ptychographic coherent diffraction imaging. Opt. Express, 21(11):13592–13606, 2013.

- [232] D. J. Vine, G. J. Williams, B. Abbey, M. A. Pfeifer, J. N. Clark, M. D. de Jonge, I. McNulty, A. G. Peele, and K. A. Nugent. Ptychographic Fresnel coherent diffractive imaging. *Phys. Rev. A*, 80(6):063823, 2009.
- [233] D. Nardi, M. Travaglini, M. E. Siemens, Q. Li, M. M. Murnane, H. C. Kapteyn, G. Ferrini, F. Parmigiani, and F. Banfi. Probing thermomechanics at the nanoscale: impulsively excited pseudosurface acoustic waves in hypersonic phononic crystals. *Nano Lett.*, 11(10):4126–33, 2011.
- [234] S. Mathias, C. La-o-vorakiat, J. M. Shaw, E. Turgut, P. Grychtol, R. Adam, D. Rudolf, H. T. Nembach, T. J. Silva, M. Aeschlimann, C. M. Schneider, H. C. Kapteyn, and M. M. Murnane. Ultrafast element-specific magnetization dynamics of complex magnetic materials on a table-top. *J. Electron Spectros. Relat. Phenomena*, 189:164–170, 2013.
- [235] T. Ohtsuka, M. Masuda, and N. Sato. Ellipsometric Study of Anodic Oxide Films on Titanium in Hydrochloric Acid, Sulfuric Acid, and Phosphate Solution. *J. Electrochem. Soc.*, 132(4):787–792, 1985.
- [236] M. Advincula, X. Fan, J. Lemons, and R. Advincula. Surface modification of surface sol-gel derived titanium oxide films by self-assembled monolayers (SAMs) and non-specific protein adsorption studies. *Colloids Surf. B. Biointerfaces*, 42(1):29–43, 2005.
- [237] A. Ravasio, D. Gauthier, F. Maia, M. Billon, J-P. Caumes, D. Garzella, M. Géléoc, O. Gobert, J-F. Hergott, A-M. Pena, H. Perez, B. Carré, E. Bourhis, J. Gierak, A. Madouri, D. Mailly, B. Schiedt, M. Fajardo, J. Gautier, P. Zeitoun, P. Bucksbaum, J. Hajdu, and H. Merdji. Single-Shot Diffractive Imaging with a Table-Top Femtosecond Soft X-Ray Laser-Harmonics Source. *Phys. Rev. Lett.*, 103(2):1–5, 2009.
- [238] D. Gauthier, M. Guizar-Sicairos, X. Ge, W. Boutu, B. Carré, J. Fienup, and H. Merdji. Single-shot Femtosecond X-Ray Holography Using Extended References. *Phys. Rev. Lett.*, 105(9):1–4, 2010.
- [239] X. Ge, W. Boutu, D. Gauthier, F. Wang, A. Borta, B. Barbreil, M. Ducouso, A. I. Gonzalez, B. Carré, D. Guillaumet, M. Perdrix, O. Gobert, J. Gautier, G. Lambert, F. R. N. C. Maia, J. Hajdu, P. Zeitoun, and H. Merdji. Impact of wave front and coherence optimization in coherent diffractive imaging. 21(9):11441–11447, 2013.
- [240] S. Hönig, R. Hoppe, J. Patommel, A. Schropp, S. Stephan, S. Schöder, M. Burghammer, and C. G. Schroer. Full optical characterization of coherent x-ray nanobeams by ptychographic imaging. *Opt. Express*, 19(17):16324–9, 2011.
- [241] C. G. Schroer, F.-E. Brack, R. Brendler, S. Hönig, R. Hoppe, J. Patommel, S. Ritter, M. Scholz, A. Schropp, F. Seiboth, D. Nilsson, J. Rahomäki, F. Uhlén, U. Vogt, J. Reinhardt, and G. Falkenberg. Hard x-ray nanofocusing with refractive x-ray optics: full beam characterization by ptychographic imaging. In Ali Khounsary, Shunji Goto, and Christian Morawe, editors, *Proc. SPIE Adv. X-ray/EUV Opt. Components VIII*, volume 8848, page 884807, 2013.
- [242] A. Schropp, R. Hoppe, V. Meier, J. Patommel, F. Seiboth, H. J. Lee, B. Nagler, E. C. Galtier, B. Arnold, U. Zastrau, J. B. Hastings, D. Nilsson, F. Uhlén, U. Vogt, H. M. Hertz, and C. G.

- Schroer. Full spatial characterization of a nanofocused x-ray free-electron laser beam by ptychographic imaging. Sci. Rep., 3:1633, 2013.
- [243] Q. Li, K. Hoogeboom-Pot, D. Nardi, M. M. Murnane, H. C. Kapteyn, M. E. Siemens, E. H. Anderson, O. Hellwig, E. Dobisz, B. Gurney, R. Yang, and K. A. Nelson. Generation and control of ultrashort-wavelength two-dimensional surface acoustic waves at nanoscale interfaces. Phys. Rev. B, 85(19):195431, 2012.
- [244] M. I. Stockman, M. F. Kling, U. Kleineberg, and F. Krausz. Attosecond nanoplasmonic-field microscope. Nat. Photonics, 1(9):539–544, 2007.
- [245] J. A. Schuller, E. S. Barnard, W. Cai, Y. C. Jun, J. S. White, and M. L. Brongersma. Plasmonics for extreme light concentration and manipulation. Nat. Mater., 9(3):193–204, 2010.